Advancing optical lattice clocks: From cryogenic silicon cavities to superexchange interactions

by

William Richard Milner

B.A., University of Wisconsin-Madison, 2017

A thesis submitted to the

Faculty of the Graduate School of the

University of Colorado in partial fulfillment

of the requirements for the degree of

Doctor of Philosophy

Department of Physics

2024

Committee Members:

Jun Ye, Chair

Ana Maria Rey

Adam Kaufman

Eric Cornell

Marco Nicotra

Milner, William Richard (Ph.D., Physics)

Advancing optical lattice clocks: From cryogenic silicon cavities to superexchange interactions

Thesis directed by Prof. Jun Ye

Optical lattice clocks provide a testbed for a wide range of science spanning from studies of fundamental physics to probing novel many-body states. To improve clock precision, probing increasingly many atoms for the longest coherence times affordable is necessary. In this thesis, we summarize coherently interrogating atoms trapped in a three-dimensional optical lattice via an ultrastable laser to understand and advance clock precision. With a Fermi-degenerate gas of strontium atoms, we perform seconds long clock spectroscopy to probe Fermi-Hubbard physics and thus understand the effects of superexchange interactions on our coherence time. Along with advancing clock metrology, this work provides a groundwork for using optical lattice clocks to probe quantum magnetism and spin entanglement.

Dedication

To my family, old and new.

Acknowledgements

JILA is a special place. During my Ph.D. I was lucky enough to work with some of the smartest and most generous people I have ever met. Thanking everyone would be impossible, so I will just try to keep it brief:

First, the Boss. Simply put, the work reported in this thesis would not have been possible without the singular guidance of my Ph.D. advisor Prof. Jun Ye. Endless funding, Christmas day paper meetings, an infinite fount of brilliant ideas, and an assembled team of incredible scientists transformed ideas scribbled on whiteboards into fruition. Behind the glitter of journal covers and prized talks, those of us lucky enough to be taken under Jun's wing saw firsthand the dedication and hard work required to become a world-renowned physicist. For all of this and much more, thank you Jun.

I was lucky to join the Ye lab in July 2017 at a very exciting time. Our cryogenic, thermal noise-limited cavity 'Si3' was coming online, the new Fermi-degenerate clock 'Sr2' had published a first set of ground-breaking results, and the workhorse 'Sr1' machine was gearing up for a clock comparison with NIST. Somehow as a young student I found myself in the fray of all three experiments.

My first project was studying the long term instability of Si3 with the hopes of advancing timekeeping with optical technology. This work was chiefly carried out with postdoc Eric Oelker. Along with providing invaluable guidance with the timescale work, as a young student Eric's rigorous approach to research left a deep impression on me. To achieve the requisite cavity stability, long days and evenings were spent with senior graduate student

John Robinson 'noise hunting' aka surrounding laser systems with layers-upon-layers of boxes and foil. With John and Eric doing essentially all the heavy lifting,[1] we ended up with a nice set of results in the end. Dhruv Kedar took over the experiment and transformed hasty plans for a new, all-crystalline cavity 'Si6' into a state-of-the-art cavity system, discovering new birefringent noise associated with these crystalline coatings. The newest cavity system 'Si7'[2] aiming to enable $\mathcal{O}(100\text{ s})$ clock coherence times is in good hands with Ben Lewis, Zoey Hu, and Dahyeon Lee leading the experiment.

With some laser stabilization experience, I joined Sr2 following the optical timescale work and quickly realized my atomic physics knowledge was fairly limited. Christian Sanner deserves a special mention: despite having an encyclopedic knowledge of all things 'A', 'M', and 'O' Christian was always willing to patiently explain everything from thermal management to Roulette secrets to Fourier optics. I fondly remember the long nights we spent together mystified by Pauli Blocking data, and I will always appreciate his continued support for me as a physicist. Lindsay Sonderhouse was the leading graduate student for our Pauli blocking effort and taught me all about Fermi gases and frequency combs. Her SU(N) and spin-polarized Fermi gas work was the first step towards our future lattice experiments in the band insulating regime. Ross Hutson was the super-senior graduate student in terms of height, tenure, and experimental physics knowledge. After many, many late nights taking data, playing pool, and god-only-knows-what hopefully some of his expertise in atomic physics has rubbed off on me. To the original Sr2 members Sara Campbell, Ed Marti, and Aki Goban who I only briefly overlapped with, thank you for building such an amazing experiment! I am proud of all the results we accomplished as a team in the face of a global pandemic.

The experiment in headed towards distinguished and exciting research directions thanks to the new, talented Sr2gang. Lingfeng Yan was closely involved in the previous studies and

[1] Both figuratively and literally.

[2] We are very creative with naming cavity and clock systems around here.

is now one of the leaders of the experiment. Lingfeng was always willing to stay late to ensure the job is done and brings a positive spirit that is crucial when the going gets tough. Stefan Lannig joined in the midst of our superexchange experiment and was immediately instrumental in understanding our apparent contrast oscillations. Stefan's broad physics knowledge and outstanding calculation skills will keep the experiment pointed in the right direction. Max Frankel is the newest team member and has a great, hard-working attitude paired with a close eye to detail. I enjoyed teaching Max how to run the experiment, almost as much as singing karaoke on the Gold Hill bus. Ben Lewis' experimental prowess was critical when MOSFETs died or sensitivity functions needed to be determined. The skills everyone brings to the team are very complementary and mesh well together. So the future is very bright on Sr2 and I will keenly follow the all the future developments.

I worked closely with the 1D lattice clock Sr1 throughout my Ph.D. First I collaborated with Toby Bothwell, Dhruv Kedar, and Colin Kennedy on the dark matter search, clock comparison, and timescale work. As a young student, I was really impressed by how many projects they could juggle at once. Although there is still no BBR evaluation planned, I believe year-by-year we get closer to shrugging Toby's skepticism about our 3D lattice clock. The new Sr1 team of Alex Aeppli, Kyungtae Kim, and Will Warfield has been amazingly successful. Alex has been a close friend over the past years and we have many great memories together. Sequestering 4 am IHOP runs and DAMOP poolside adventures, Alex is a very methodical scientist whose careful scrutiny ensured the recent Sr1 success. Kyungtae is a walking Zotero library and selflessly jumps in whenever the 'postdoc touch' is required. Kyungtae's wisdom was helpful in the face of making big, tough career decisions and when things are really broken, you should call Kyungtae. 'Little Will'[3] Warfield brought his Boulder native street-credibility, general relativity knowledge, and hard-working attitude to the team. We are only slightly jealous about your coherence times over here on Sr2 and I am looking forward to many exciting results ahead.

[3] I did not come up with this nickname and I have no idea what big and little means here.

Sr3 is the newest clock experiment, introducing everyone to a whole new world of cavity QED physics. John Robinson, Maya Miklos, and Ming Tso constructed the experiment in lighting speed and quickly got ground-breaking results. I really enjoyed physics conversations with John during their construction period, talking for hours while watching John wave his hands attempting to embody a human Bloch sphere. Maya has an amazingly deep knowledge of physics and always provided great ideas when we were frequently stuck on Sr2 - Emmy the cQED canine brought a pacifying presence to group meetings too. Ming is a focused scientist who always seemed undeterred by the challenges to achieve squeezing; I guess it's a piece of cake compared to some of his culinary creations. Benedikt Heizenreder was a visiting student for 6 months, who possessed an interesting blend of MPQ rigor and Bavarian recklessness that made for some fun adventures on the slopes of Mt. Elbert. With postdocs Joonseok Hur and Tony Yang on the team, the standard quantum limit is no longer regarded as so 'standard' anymore.

KRb were always a fun group. I suppose the camaraderie of struggling on another Fermi gas platform meant many evenings were spent at the Dark Horse to commiserate together. The old crew of Giacomo Valtolina, Will Tobias, Jun-Ru Li, Luigi De Marco, and Kyle Matsuda impressed us with their amazing results, second only to their Jazz skills. Cal Miller, Junyu Lin, Henrik Hirzler, and Annie Carroll are quickly pushing the experiment in new, exciting directions. Annie and Stephen Gill deserve special mention as both next-door neighbors and close friends who were always eager to plan fun outings.

Adam Kaufman's group built a new tweezer clock platform across the hall that is both fairly complementary to Sr2 and has been incredibly prolific during my Ph.D. Aaron Young shared a lot of insights about lattice physics and I enjoyed conversations with Nathan Schine and Will Eckner. Currently lead by a jolly German with a laugh you can hear from the other side of JILA, I am excited to see what Prof. Dr. Herr Nelson Darkwah Oppong, Will E., Alec Cao, and Theo Lukin Yelin will do next.[4]

[4] Sorry, you will need to find a new guy to call at 11 pm if the clock laser is unlocked.

Ana Maria Rey has been our principal theory collaborator for much of the work during my Ph.D. While profiting from directly learning about atomic physics through an expert in the field, I also appreciated Ana Maria's optimism about the capabilities our experiment. Her insights on our superexchange experiment with her students Mikhail Mamaev and Anjun Chu were invaluable. The constant stream of good ideas and capable researchers from her group will certainly continue to benefit our experiment.

There is a long list of JILA staff to thank, and I won't pretend to fully do their contributions justice. The machine shop built much of the critical infrastructure on our experiment, including our custom Sr2 imaging mount and the alignment rig for optically contacting Si6. Todd Ascinar, Kyle Thatcher, Kim Hagen, Adam Ellzey, James Uhrich, and Hans Green all deserve thanks. JILA profits from a highly unique electronics shop with a history of designing custom electronics to solve the toughest problems. Terry Brown deserves special mention for patiently teaching me all about electronics and feedback systems, along with Carl Sauer and James Fung-A-Fat. Dave Alchenberger from the Keck lab provided us with AR coated diodes and custom, dispersive imaging optics. The supply office ensures that all purchasing hurdles are distanced from students and the Si3 dewar runneth over thanks to Brian Lynch, Jen Eriksson, Karen Lichtfuss, and Randall Holliness. Computing gurus J.R Raith, Corey Keasling, and Jim McKown always fixed any computing issues we encountered and never admonished our ethernet cabling practices too harshly. Agnieszka Lynch ensured I was paid, thus keeping a roof over my head. Krista Beck and Amy Allison were the administrative assistants in the group and Krista was absolutely instrumental in organizing my thesis defense.

There is an even longer list of Ye Lab researchers and collaborators over the years I owe thanks to and if I tried to single out everyone the acknowledgements section would be longer than the thesis. On the Mid-IR and XUV frequency comb experiments: Lee Liu, Bryan Changala, Chuankun Zhang, Dina Rosenberg, Jake Higgins, and Tian Ooi. On the directly-cooled molecule experiments: Kameron Mehling, Justin Burau, Yewei Wu, Dave Reens, Hao

Wu, and Shiqian Ding. Older-generation strontium scientists: Shimon Kolkowitz and Wei Zhang. Our PTB collaborators who generously hosted me in 2018: Thomas Legero, Uwe Sterr, and Fritz Riehle. Our NIST collaborators for the timescale and clock comparison work: Jeff Sherman, Judah Levine, Jian Yao, Michele Guinta, Tara Fortier, Holly Leopardi, Dave Hume, and Andrew Ludlow. Finally, thank you to my Ph.D. committee members not already mentioned: Eric Cornell and Marco Nicotra.

I lived with some amazing housemates during my time in grad school: Shawn Geller, whose eclectic friends, ability to drive to Denver in 20 minutes, and vast quantum information knowledge made for some serious fun. Hannah Knaack, who is actually doing quantum gates, shared some of her cryogenics lore, and made amazing bread weekly. And Aaron Young, who has provided years of stimulating conversations about physics that almost make up for the fact that he's actually an engineer. Someday I will forgive you for building that automatic, clip-loaded Nerf gun. My old roommates from Madison, Phil Buelow and Ian Hill, lived in Nederland and brought me outdoor climbing, backcountry skiing, and reminded me that there is life in Colorado outside Boulder. I will fondly remember late nights climbing with all of you guys, 'small' house parties that inevitably got out of hand, and watching battlebots together in the penthouse on our paunchy bean bag.

Throughout the ups and downs of grad school, I always had the support of my immediate family. My younger brother David has been a close friend and him moving to Boulder in the middle of COVID sparked a new, exciting chapter here. The time we spent together watching Boston sports teams consistently disappoint us, climbing at the Spot, and hearing about your budding career and life with Ellie always cheered me up. Unbeknownst to my twin brother Sam, he was a critical component of the only Ye labs startup to-date 'Quantwinuum' and I always enjoyed learning about his exciting research solving DMRG Hamiltonians. Finally, my parents have been my strongest advocate for truly as long as I can remember. Seeing their unwavering hard work and enthusiasm for my happiness has always inspired me to work a little harder and be a lot more humble. I am looking forward

to seeing you more often soon.

I spent countless days and nights over the past 7 years with everyone in these acknowledgements chasing after the results in this thesis. More often than not, I could probably be seen with an exasperated look on my face. But even if we never could resolve those dipole-dipole frequency shifts, and even if the silicon cavity long-term stability never surpassed the hydrogen maser, and even if we never saw superexchange interactions: the love and support I received from you all would have been more than enough for me.

Contents

Chapter

Tables

Table

Figures

Figure

Chapter 1

Introduction

1.1 Background

Quantum physics experiments with cold atoms and molecules have progressed enormously over recent decades. To highlight a few examples outside the focus of this thesis: Neutral atoms have cemented themselves as a leading candidate for developing a quantum computer achieving entangling fidelites $> 99\%$ and using error correction for large-scale processing [1, 2]. Quantum simulation studies now probe magnetism and many-body physics at the microscopic level [3, 4]. Fundamental physics studies with laser cooled molecules have placed bounds on the existence of a electron electric dipole moment [5, 6] and atom-interferometer platforms have measured the fine structure constant α at the part-per-trillion level [7]. The list of exciting results goes on and on...[1]

While aspects of this field are quickly changing, some simple ideas connect all sub-disciplines. Much of the attraction to this research is rooted in the capability to build pristine quantum systems from the ground up. Here, the internal degrees of freedom of particles can generally be well-approximated as a conceptually simple two-level system. Denoted as a qubit, a quantum spin, or a clock even small systems of these two-level particles gives rise to remarkable phenomena - particularly when interactions are introduced [8, 9] and spin-statistics are considered [10, 11]. Introducing quantum correlations via spin entanglement

[1] To further exemplify the quick pace of the field: this list will likely be outdated by the time a future reader picks up this thesis.

between constituent particles provides an exciting vista for creating systems of increasing size while maintaining high fidelity entanglement [12, 13, 14].

Clocks embody this idea by precisely controlling all external perturbations to our two-level system. With laboratory perturbations meticulously controlled, clocks offer the capability of realizing a quantum *sensor* sensitive to perturbations of interest [15, 16]. First and foremost, this has opened the door for tests of fundamental physics [17, 18, 19, 20, 21, 22]. By the nature of clock spectroscopy, studies of interactions at high density also provides a probe to understand the physics of coherent atom-light interactions in a new regime of many emitters [23, 24]. Improving clocks will thus pay dividends by further expanding the scope of these studies and ultimately lead to a redefinition of the SI second [25].

1.2 Why an *optical lattice* clock?

How do we improve a clock? First, we need to quantitatively evaluate its 'performance'. A reasonable place to start is to characterize the clock *stability* - the statistical frequency uncertainty of our clock when it is averaged over a time period τ.

Before divulging into a discussion about uncertainty, let's emphasize why measurement noise is so important. First, the essential quantity a physics experiment outputs is a measured signal with a corresponding uncertainty. Quoting either a signal or noise independently is not so relevant - practically one can either amplify or attenuate either of these values in the lab while the underlying physics process is unchanged. Secondly, the magnitude and time-dependence of noise is generally more insightful. Whether technical noise like camera readout noise, or fundamental noise like Brownian motion and quantum projection noise, characterizing these noise terms is generally much more important to either understand or improve a physics experiment than tuning a parameter to make a signal as large as possible. Thus, developing tools to quantitatively apprehend noise is imperative.

To characterize a clock's error, we start by defining a fractional error $y(t) \equiv (f(t) - f_R)/f_R$ corresponding to deviations of our clock's frequency $f(t)$ from a reference frequency

f_R [2] . A natural next step would be to calculate the variance of our frequency errors $\mathbb{V}(y) = \sum_i^N (y_i - \overline{y})^2/N$. However, for many noise terms relevant to clocks (e.g. Brownian motion in optical cavities displaying $1/f$ frequency noise), the mean $\overline{y}$ does not converge in the limit of large samples. Thus a metric that captures the *time-dependence* associated with noise, while making minimal assumptions about the functional form of the underlying noise process is more appropriate. Here, we define the Allan variance: [26, 27]

$$\sigma_y^2(\tau) = \frac{1}{2(N-1)} \sum_{i=1}^{N-1} \left[\tilde{y}(\tau)_{i+1} - \tilde{y}(\tau)_i\right]^2 \tag{1.1}$$

The conceptual difference here is that we evaluate deviations from measurements $(\tilde{y}(\tau)_{i+1} - \tilde{y}(\tau)_i)$, binned over averaging intervals τ rather than deviations of individual datum from the sample mean $\overline{y}$. This gives us a versatile tool to evaluate the time-dependent stability of our clock.

In addition, the *accuracy* of an atomic clock, or how our clock's absolute frequency f deviates from the reference frequency f_R, is of importance. One could envision f_R as the unperturbed transition frequency of a particle fully decoupled from its environment [28]. Practically, an experimenter needs to tabulate all systematic shifts from f_R with corresponding uncertainties to evaluate a clock's accuracy. We briefly detail the predominant systematic shifts for our clock in the coming page.

Next, we turn our eye to the fundamental noise terms for a clock's stability; this will guide our choice of clock design after all. Given that our two-level quantum system is fundamentally discretized, this gives rise to the so-called *quantum projection noise* (QPN) [29]. Consider a single particle, placed in an initial state $|\psi\rangle = \alpha\,|\downarrow\rangle + \beta\,|\uparrow\rangle$ [3] . Using spectroscopy techniques [30], coherences of our system containing information are encoded in the populations of $|\downarrow\rangle$ and $|\uparrow\rangle$. Yet any measurement will project this particle into $|\uparrow\rangle$ or

[2] One might question the validity of eliciting a perfect frequency reference f_R for this calculation. Indeed, this is just to simplify our explanation of clock stability. Any practical measurement requires a comparison of multiple independent clocks, each with finite noise. In chapter 3, we will detail how > 2 independent oscillators is required to triangulate the noise of individual clocks.

[3] $|\alpha|^2 + |\beta|^2 = 1$

$|\downarrow\rangle$. Other than the trivial case α or $\beta = 1$, where we have no interferometer sensitivity, a single measurement of $|\psi\rangle$ is indeterminant no matter how accurately the state is prepared or read out. To achieve the best clock stability, the task is immediately clear - make many identical copies of our particle and rather perform N projective measurements in parallel.

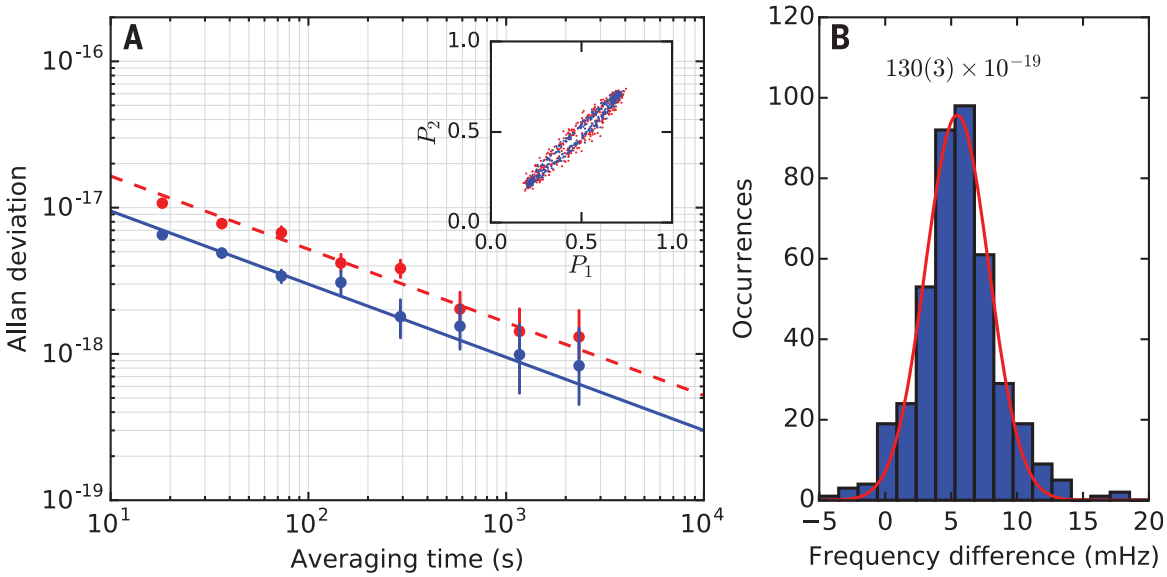

Figure 1.1: Synchronous clock comparison. Probing $\mathcal{O}(1000)$ atoms for $\mathcal{O}(1)$ second interrogation times, optical lattice clocks measure differential frequency shifts with statistical uncertainties at the 10^{-19} level in ~ 1 hour timescales. The blue (red) data points use 3000 (1000) atoms and direct observe a factor of $\sqrt{3}$ improvement in stability according to the reduction in quantum projection noise from Eq. 1.2. 19 digits of precision (≈ 100 μHz/ 429 THz) is the same order of magnitude as the accuracy budgets of the most accurate clocks worldwide [31, 32]. Figure reproduced from [33].

$$\sigma_{QPN}(\tau) = \frac{1}{2\pi f_0 \sqrt{NT\tau}}. \tag{1.2}$$

The Allan deviation corresponding to quantum projection noise is displayed in Eq. 1.2. We provide a detailed discussion of the clock spectroscopy techniques to arrive at this formula in Chapter 3 and rather use this section to conceptually emphasize the three key quantities to improve clock stability: one wants to maximize the total atom number N, the coherent spectroscopy time T, and the clock oscillation frequency f_0.

Let's start with f_0 - clocks that oscillate 'faster' at higher frequency have improved stability. To operate a clock with a large oscillation frequency f_0, we need to pick a two-level system where the energy separation is large. Historically this decision was largely dictated by engineering constraints, given we need coherent radiation at our atomic energy splitting to manipulate our particle of choice. Thus, microwaves were a natural choice of local oscillator and fountain clocks probing GHz-level hyperfine splitting of alkali atoms like cesium were the state-of-the-art [34, 35].

The past 30 years has seen a revolution of optical technology, pioneered by groups at JILA, NIST and other metrology labs worldwide, opening the door to realize clocks operating at optical frequencies. Lasers locked to Fabry-Pérot cavities routinely achieve Hz-level linewidths [36, 37, 38], with cryogenic silicon cavities emerging as the frontrunner in recent years [39, 40]. The challenge to count optical frequencies oscillating at hundreds of THz was solved in the early 21st century via elegant techniques to downconvert optical signals to the microwave domain [41, 42, 43, 44, 45, 46]. These two technological advances have distinguished two clock candidates with suitable optical transitions: neutral atoms and ions. With microwave clocks now in the rearview mirror, even 'XUV' transitions are actively being explored with a similar technological revolution ongoing [47, 48]. Currently the low-lying Thorium isomer transition has been identified as the most promising candidate and investigations to spectroscopically identify the transition with increasing precision are ongoing [49, 50, 51]. Currently the JILA XUV frequency comb experiment has the most stringent measurement of this transition, achieving 300 kHz-level precision and measuring the ratio of the ^{229}Th and ^{87}Sr transitions [52].

With our design of clock platform narrowed to ions and neutral atoms, our next task to optimize clock stability is to use as many particles as possible. Here, the choice is clear. The strong Coulomb interactions that enable robust ion trapping and interactions for quantum gates [53, 54] makes scalability beyond tens of ions very challenging [55]. Although efforts are ongoing [56], many ions trapped in a single Paul trap essentially behave as a 'crystal' [57]

where collective modes introduce challenging motional systematic effects. Comparatively, trapping neutral atoms in *optical lattices* formed with standing waves of light provides a robust, scalable confinement where $N > 10^4$ is straightforwardly achieved. We will detail the progress and challenges of confining atoms with optical lattices in the coming pages.

We have narrowed our search for achieving the optimal clock stability to trapping neutral atoms in optical lattices. The final optimization parameter in Eq. 1.2 is the coherent interrogation time T. Although up to now we have treated our stability parameters f_0 and N as independent variables, here we already face the first challenge: even the earliest clock studies showed that coherent interrogation times depended strongly on the number of atoms [58]. Naive approximations of spin-polarized, non-interacting fermions were insufficient, motivating subsequent studies to understand collisions with increasing precision [59]. Recent work demonstrated elegant techniques to cancel s and p-wave interactions in a one dimensional lattice clock, strongly diminishing collisional shifts [60]. We immediately see that optical lattice clocks occupy a unique space, lying at an intersection of precision measurement and many-body physics.

The continued improvements of 1D lattice clocks over the past 20 years appears to be a perpetual success story: Recent upgrades to our 1D lattice clock utilizing an in-vacuum buildup cavity have enabled optical lattices with a very large mode volume, achieving record stability of mid-10^{-18} level at 1 second [21]. Differential AC stark shifts between the electronic ground and clock state are addressed by use of 'magic wavelength' traps, where the ground and excited state polarizabilities are exactly matched [61]. The relatively simple AC stark shift model in a 1D lattice has allowed these shifts to be systematically characterized at the low-10^{-19} level [62]. Tabulating all systematic shifts including blackbody radiation, these 1D clocks are highly accurate at the high 10^{-19} level [32]. Leveraging the relatively robust design and operation of 1D lattice clocks has opened the door for dark matter studies [19] and new timekeeping techniques [63]. Looking to the future, current explorations are ongoing to study quantum enhanced metrology on these platforms [64]. For future studies, notions of

proper time [65] and time dilation [66] might even be required to quantitatively understand millimeter separated clouds studied at the 10^{-21} level.

In summary, loading into a single standing-wave optical lattice one can trap hundreds of thousands of atoms and probe them for tens of seconds. In terms of both clock stability and accuracy this clock platform is clearly the winner, with no apparent end in sight to the exciting vista of physics ahead.

1.3 Why a *Fermi-degenerate three-dimensional* optical lattice clock?

Yet, this thesis describes operating a clock using a Fermi-degenerate gas loaded into a three dimensional lattice. The technical requirements to realize this system are necessarily much more demanding: To achieve Fermi degeneracy, the experiment cycle time is longer due to evaporative cooling. Twice as many lasers are required for our narrow-line cooling and trapping procedure. Contact interactions are $\approx \times 10^3$ stronger in 3D confinement. The density is comparatively so high, that nearly all the atoms in our sample fit into a single 10 μm^2 camera pixel on the 1D lattice experiment. In the face of all these technical hurdles, what is the motivation to build this experiment?

In the previous section, we motivated our clock as a quantum sensor. One would naturally ask next: what regimes can we place our sensor to probe the most interesting physics? While there is great interest in studying clock operation at large distances where gravitational effects may be enhanced [15], there is an equally exciting frontier exploring clock operation at the very highest atomic densities. Indeed, the canonical formulas for atom-light interactions that we provide in Chapters 2 and 3 fall to the wayside when the spacing between atoms is commensurate with the light wavelength λ. Rather, concepts like the excited lifetime Γ must be regarded as *collective* and may be tuned based on system parameters like the confinement geometry [67]. When motion is introduced to atoms in the 3D lattice, tunable anisotropic spin models emerge between strongly interacting fermions that can be probed via clock spectroscopy [68]. Controlling these interactions at high density will

open the door to engineer quantum enhanced sensors with clock stability exceeding the QPN bounds detailed above [12, 13, 14].

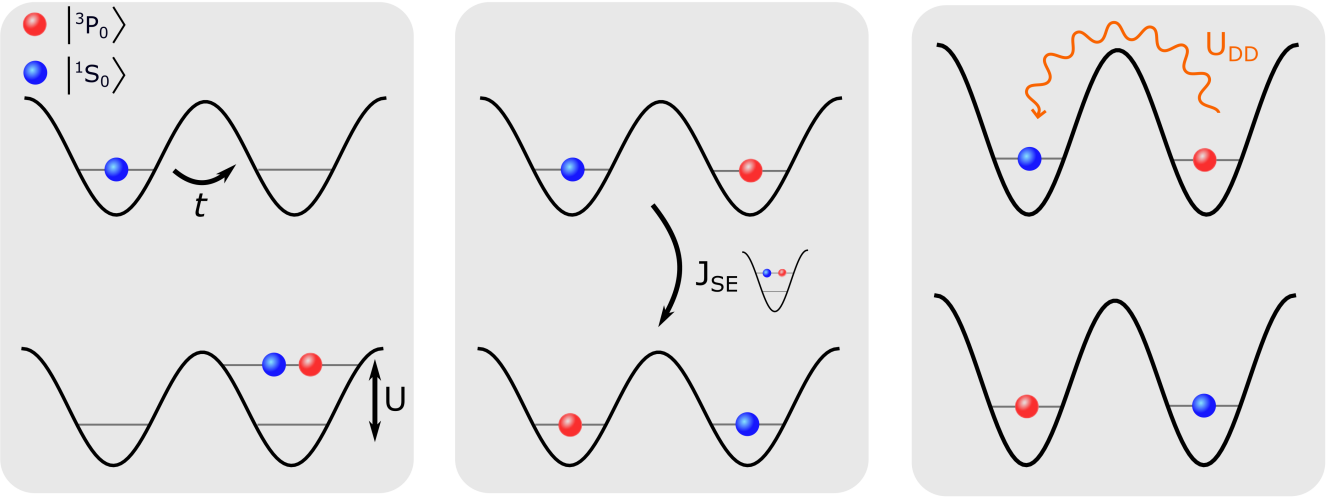

Figure 1.2: Illustration of interactions probed on this experiment. Consider the hierarchy of energy scales decreasing from left to right. **Left**: The basic ingredients of our three-dimensional lattice are captured by the *Fermi-Hubbard* model. Atoms may tunnel to neighboring sites at a rate t, at the cost of an interaction energy U if the site is occupied. **Middle**: At half filling in the Mott-insulating regime, atoms interact via superexchange interactions. These dynamics are modelled by a *Heisenberg* Hamiltonian. **Right**: In a deep lattice where motion is restricted, atoms interact via weak, long-range *dipole-dipole* interactions. The coherent portion can be understood as a exchange of photons.

Energy scales of experiment	
On-site contact energy U	1 kHz
Rabi frequency Ω	100 Hz
Tunneling t	25 Hz
Superexchange $J_{SE} \propto t^2/U$	1 Hz
Dipolar coupling $U_{DD} \propto \Gamma_0$	1 mHz

Table 1.1: Interaction scales in our optical lattice. These values are all tunable, and thus the order of magnitude of these parameters is most important.

The interaction landscape in our 3D optical lattice contains a hierarchy of energy scales as depicted in Fig. 1.2. The basic ingredients of our three-dimensional lattice are first

captured by the *Fermi-Hubbard* model:

$$\hat{H}_{\mathrm{FH}} = -t \sum_{j,\sigma\in\{g,e\}} (\hat{\tilde{c}}^{\dagger}_{j,\sigma}\hat{\tilde{c}}_{j+1,\sigma} + H.c.) + U\sum_{j} \hat{\tilde{c}}^{\dagger}_{j,e}\hat{\tilde{c}}_{j,e}\hat{\tilde{c}}^{\dagger}_{j,g}\hat{\tilde{c}}_{j,g}. \tag{1.3}$$

Here, $\hat{\tilde{c}}^{\dagger}_{j,\sigma}(\hat{\tilde{c}}_{j,\sigma})$ creates (annihilates) a fermion on site j with state σ in the lab frame. Atoms may tunnel to neighboring sites at a rate t, at the cost of an interaction energy U if the site is occupied [69]. Owing to the Pauli exclusion, two atoms may only occupy the same site if they are different electronic states, denoted $|g\rangle = {}^1S_0$ and $|e\rangle = {}^3P_0$ for the ground and clock states respectively. Both t [70] and U [71] can be directly probed via clock spectroscopy and play an important role in clock operation. As we will detail in Chapter 6, tunneling places stringent limitations on clock coherence [72, 73]. Given $U \approx$ kHz is the dominant interaction energy scale and much larger than our clock drive Ω, doubly occupied sites can be spectrally removed from our atomic ensemble [71]. Thus, the door is opened to prepare many-body states in lattice that are less sensitive to decoherence from contact interactions [33].

At high filling in the Mott-insulating regime ($U \gg t$), motion is restricted as doubly occupied sites are highly energetically unfavorable. Rather, the dynamics of atoms are characterized by *superexchange* interactions where perturbative spin exchange processes occur at a rate $J_{\mathrm{SE}} = 4t^2/U$ [74, 75, 76]. These dynamics are modelled by a quantum *Heisenberg* Hamiltonian:

$$\hat{H}_{\mathrm{Heis.}} = \sum_{j} J_{\mathrm{SE}}(j)\hat{\tilde{\mathbf{s}}}_j \cdot \hat{\tilde{\mathbf{s}}}_{j+1}. \tag{1.4}$$

Here, we introduce spin operators $\hat{\tilde{s}}^{\alpha}_j$ for $\alpha \in \{X, Y, Z\}$ referring to Pauli matrices for atoms on sites indexed by j. This Hilbert space is simplified compared to the Fermi-Hubbard Hamiltonian as we only consider states below the energy gap $\approx U$. More importantly, the Heisenberg Hamiltonian is a canonical spin model of interest in understanding quantum magnetism. The physics of superexchange is central to describing magnetic phenomena such as antiferromagnetism [77, 78] and is believed to play a role in superconductiv-

ity [79]. Several ultracold atom experiments have employed optical lattices to explore low-temperature bosonic ferromagnetic and fermionic antiferromagnetic correlations induced by superexchange [80, 81, 82, 83, 3, 84, 85, 86]. In our clock platform, we gain the flexibility to tune the initial state evolving under $\hat{H}_{\text{Heis.}}$ with our clock drive. As we will explain in Chapter 6, we use this tunability to realize an XXZ-style Hamiltonian that can be directly employed for the generation of large scale quantum entanglement over the entire 3D lattice system [87, 88, 89, 68].

In concept, the lattice depth can be made sufficiently deep that the superexchange interaction strength J_{SE} is much smaller than any parameter in Table 1.1. Here, atoms are pinned in place and at first glace one may assume that our atomic ensemble would finally be devoid of any many-body interactions. Astonishingly, atoms still interact via weak, long-range *dipole-dipole* interactions that are proportional to the single-body decay rate Γ_0. The coherent portion of these interactions can be understood as a exchange of photons:

$$\hat{H}_{\text{DD}} = \sum_j \sum_{i \neq j} U_{\text{DD}}^{ij} \hat{\hat{s}}_i^+ \hat{\hat{s}}_j^- . \tag{1.5}$$

Here the spin flip operators are $\hat{\hat{s}}_j^{\pm} = \hat{\hat{s}}_j^X \pm i\hat{\hat{s}}_j^Y$. These collective dynamics are now solved via examining the populations and coherences of the atomic density matrix $\hat{\rho}$ evolving under a master equation $d\hat{\rho}/dt = -\frac{i}{\hbar}[\hat{H}_{\text{DD}}, \hat{\rho}] + \mathcal{L}[\hat{\rho}]$ including non-Hermitian, dissipative interactions $\mathcal{L} \propto \Gamma_0$. $\hat{H}_{\text{DD}}$ is anisotropic spin model that can admit squeezing [90] just like our Heisenberg Hamiltonian $\hat{H}_{\text{DD}}$. In contrast to the superexchange interactions, the dipole-dipole interactions U_{DD}^{ij} are long-range, extending beyond the nearest neighbor coupling, and contain terms proportional to both $1/r$ and $1/r^3$. As we will detail in Chapter 7, the relative orientation of the optical lattice and clock beam dramatically modifies U_{DD}^{ij} via constructive interference of atomic dipoles. These dipole-dipole interactions also represent a systematic clock shift of order $\approx 10^{-18}$ at the same level as current state-of-the-art accuracy evaluations for optical lattice clocks [32]. Although 1D clocks are not operating at a high enough density that these

dipolar shifts currently present a limitation, our 3D clock platform can still be posed as an apparatus to explore a next generation of clock systematics that will be increaingly relevant as clock stability continues to improve.

We now see that there are a number of different interaction mechanisms in our 3D lattice, each admitting rich Hamiltonians that we directly probe with clock spectroscopy. During the course of my Ph.D., we investigated each of these models and proposed solutions to minimize the deleterious aspects of these interactions to improve clock performance. Looking to the future with a firm understanding of these interactions in hand, we can set more ambitious sights. One goal is to use these tunable, anisotropic spin models to generate entanglement for improved clock stability. These anisotropic spin models can be likened as a one axis twisting Hamiltonian to intuit the squeezing dynamics, where the metrological gain depends weakly on the range of interactions [91]. By introducing quantum correlations via these interactions, our ensemble of N atoms are no longer identical and the $1/\sqrt{N}$ scaling in Eq. 1.2 is surpassed.

A different perspective is to use our clock to probe these interactions at finer energy scales and with increasing complexity to reveal novel physics. For the superexchange study reported in Chapter 6, the clock dynamics are well modelled by approximating our ensemble as piecewise chains where small clusters of atoms separated by holes interact. For future studies, using box potentials to remove the external harmonic confinement and pushing to lower temperatures could realize sufficiently large uninterrupted chains of atoms that dynamics become computationally intractable. The dipole-dipole interactions on the clock transition that we studied were in the perturbative regime, where the coherent interrogation times T were much shorter than the interaction timescale $1/\Gamma_0$. For this, the modelling of these dynamics could be strongly simplified from a full master equation treatment and effects like excited state decay changing the $\langle \hat{\hat{s}}^z \rangle$ projection could be ignored. As we will detail in Chapter 7, using dressing lasers to mix states with larger dipole moments enables entering the regime $\tilde{\Gamma}\ T \approx 1$ where once again theory breaks down and the dynamics are

much richer. To use these dipole-dipole interactions for spin squeezing, ensuring that the interaction strength is at least commensurate with the interrogation time is also a necessary prerequisite.

In summary while our 3D lattice clock requires a demanding overhead of technical resources for operation, it also opens the door for explorations into the physics of atoms and light in a novel regime. Although the next steps to further control these interactions will be challenging, these future studies will undoubtedly pay dividends in advancing the capabilities of optical lattice clocks operating at the state-of-the-art.

1.4 Outline of thesis

First in Chapter 2, we give an overview of our atom of choice: fermionic ^{87}Sr. The unique properties of alkaline-earth atoms give rise to a versatile experimental toolbox, including novel laser cooling techniques, enhanced evaporative cooling, and most importantly narrow-linewidth transitions for clock spectroscopy. Starting with chunk of metal heated to 460° C, we detail how we combine these cooling techniques to realize a nuclear spin-polarized Fermi gas of ^{87}Sr atoms.

Next in Chapter 3, we outline the requirements for achieving clock operation in a three-dimensional optical lattice. Using our Fermi gas, we load atoms into the ground motional band of our lattice. Combined with our cryogenic silicon cavity, we perform seconds-long, coherent interrogation of our confined atoms.

In Chapter 4, we describe the realization of the first all-optical timescale, surpassing the performance of state-of-the-art microwave timescales. Here, we leverage the excellent stability of our silicon cavity at both short and long averaging times to achieve superior timing error over month-long timescale operation.

Next in Chapter 5, we detail the progress and challenges of operating clocks at high density. Specifically, achieving high fidelity *in situ* imaging, required for imaging spectroscopy of clock systematics, mandates a new set of imaging techniques. Using highly saturated

imaging, we confirm filling fractions $> 90\%$ in the band-insulating regime.

Finally in Chapter 6, we combine all pieces to study the atomic coherence time in our 3D optical lattice. We identify *superexchange* interactions as an important clock systematic, and quantitatively study the effect of these interactions on Ramsey fringe contrast.

In conclusion, we provide an outlook for future studies in Chapter 7. We provide preliminary data for ongoing experiments and share future exciting research directions on this experimental platform.

The central results of this thesis are summarized in the following published works and preprints:

- **W. R. Milner**, S. Lannig, M. Mamaev, L. Yan, A. Chu, B. Lewis, M. N. Frankel, R. B. Hutson, A. M. Rey, and J. Ye, arXiv (2024).
- **W. R. Milner**, L. Yan, R. B. Hutson, C. Sanner, and J. Ye, Phys. Rev. A **107**, 063313 (2023).
- **W. R. Milner**, J. M. Robinson, C. J. Kennedy, T. Bothwell, D. Kedar, D. G. Matei, T. Legero, U. Sterr, F. Riehle, H. Leopardi, T. M. Fortier, J. A. Sherman, J. Levine, J. Yao, J. Ye, and E. Oelker, Phys. Rev. Lett. **123**, 173201 (2019).

Additional published work I contributed to during the course of my thesis:

- R. B. Hutson, **W. R. Milner**, L. Yan, J. Ye, C. Sanner, Science **383**, 384 (2024).
- W. J. Eckner, N. D. Oppong, A. Cao, A. W. Young, **W. R. Milner**, J. M. Robinson, J. Ye, and A. M. Kaufman, Nature **621**, 734 (2023).
- D. Kedar, J. Yu, E. Oelker, A. Staron, **W. R. Milner**, J. M. Robinson, T. Legero, F. Riehle, U. Sterr, and J. Ye, Optica, **10** 464 (2023).
- T. Bilitewski, A. Piñeiro Orioli, C. Sanner, L. Sonderhouse, R. B. Hutson, L. Yan, **W. R. Milner**, J. Ye, and A. M. Rey, Phys. Rev. Lett. **128**, 093001 (2022).

- C. Sanner, L. Sonderhouse, R. B. Hutson, L. Yan, **W. R. Milner**, and J. Ye, Science **374**, 979 (2021).
- BACON Collaboration, Nature **591**, 564 (2021).
- J. M. Robinson, E. Oelker, **W. R. Milner**, D. Kedar, W. Zhang, T. Legero, D. G. Matei, S. Hafner, F. Riehle, U. Sterr, and J. Ye, Optics Letters **46**, 592 (2021).
- H. Leopardi *et al.*, Metrologia **58**, 015017 (2021).
- A. W. Young, W. J. Eckner, **W. R. Milner**, D. Kedar, M. A. Norcia, E. Oelker, N. Schine, J. Ye, and A. M. Kaufman, Nature **588**, 408 (2020).
- Sonderhouse L., C. Sanner, R. B. Hutson, A. Goban, T. Bilitewski, L. Yan, **W. R. Milner**, A. M. Rey, and J. Ye, Nature Physics **16**, 1216 (2020).
- C. J. Kennedy, E. Oelker, J. M. Robinson, T. Bothwell, D. Kedar, **W. R. Milner**, G. E. Marti, A. Derevianko, and J. Ye, Phys. Rev. Lett. **125**, 201302 (2020).
- M. Bodine *et al.*, Phys. Rev. Research **2**, 033395 (2020).
- J. M. Robinson, E. Oelker, **W. R. Milner**, W. Zhang, T. Legero, D. G. Matei, F. Riehle, U. Sterr, and J. Ye, Optica **6**, 240 (2018).

Chapter 2

Ultracold strontium

In Chapter 1, we motivated the design of our 3D optical lattice clock based on elegant spin models we can realize with fermions at high density. To achieve this in the laboratory, we need to prepare ensembles with a sufficiently low temperature to achieve these high filling fractions in our 3D optical lattice. As we will explain in this chapter, fermionic ^{87}Sr is very well suited for this task. The atomic properties of strontium allow for laser cooling to near quantum degeneracy, efficient evaporative cooling to prepare highly degenerate Fermi gases, and spin-polarizing techniques to ultimately realize a nuclear spin-polarized, degenerate Fermi gas.

Previously described as an exploratory atomic species in earlier Ph.D. thesis' from the Ye lab [92, 93], strontium is now a workhorse element for ultracold atom experiments featuring many attractive properties. This includes electronic transitions at visible and near-IR wavelengths spanning a wide range of different linewidths, and both abundant bosonic and fermionic isotopes. We leverage the combination of these properties to prepare a degenerate Fermi gas of ^{87}Sr. This Fermi gas is the linchpin of our 3D optical lattice clock experiment, and the starting point for all results in this thesis. The goal of this chapter is thus to provide a broad overview of the experimental techniques and physics insights required to prepare this Fermi gas starting from a chunk of metal heated to 460° C.

2.1 Strontium

Much of the relevant atomic physics of strontium stems from the fact it is in the 'alkaline-earth' family, meaning it has two valence electrons. This should be contrasted to the standard hydrogen-like 'alkali' atoms with a single valence electron including cesium, rubidium, potassium, lithium. Here both the spatial and spin portions of the wavefunction for the two valence electrons can either be parallel (triplet state) or anti-parallel (singlet state). Just like the ground state of helium ('parahelium'), the spins of the strontium electronic ground state is a singlet state [94].

2.1.1 Properties

We define the total spin $\mathbf{S}$, which is the vector sum of the two electron spins $\mathbf{S} = \mathbf{s}_1 + \mathbf{s}_2$. We also define a similar orbital angular momentum operator $\mathbf{L} = \mathbf{l}_1 + \mathbf{l}_2$, and the total angular momentum $\mathbf{J} = \mathbf{L} + \mathbf{S}$ [95]. The energy levels are then described by the standard Russell-Saunders notation ($^{2S+1}L_J$). Our singlet electronic ground state has by definition $\mathbf{S} = 0$, and is also the lowest orbital angular momentum state $L = 0$.[1] Thus we arrive at the starting point: the electronic ground state $^1S_0$.

Before diving into transitions from our ground state, it is insightful to consider some of the properties of this state. The presence of the nuclear spin $\mathbf{I}$ introduces a hyperfine interaction with an additional quantum number $\mathbf{F} = \mathbf{I} + \mathbf{J}$. It turns out, only the fermionic isotope ^{87}Sr has a nuclear spin $I = 9/2$. This can be understood by the nuclear shell model, where owing to the Pauli exclusion principle nucleons are well described as non-interacting fermions occupying increasing energy states. For ^{87}Sr Z = 38, A = 49 and there is an unpaired neutron in the $1g_{9/2}$ level [96]. For the bosonic isotopes, A = 46, 48, 50 and due to an even number of neutrons paired off they have no nuclear spin $(I = 0)$[2] . These hyperfine

[1] The historical, spectroscopic notation for L takes the form 0 → S, 1 → P, 2 → D, 2 → F, then alphabetical ordering.

[2] This is referred to an 'even-even' nucleus where generally $I = 0$.

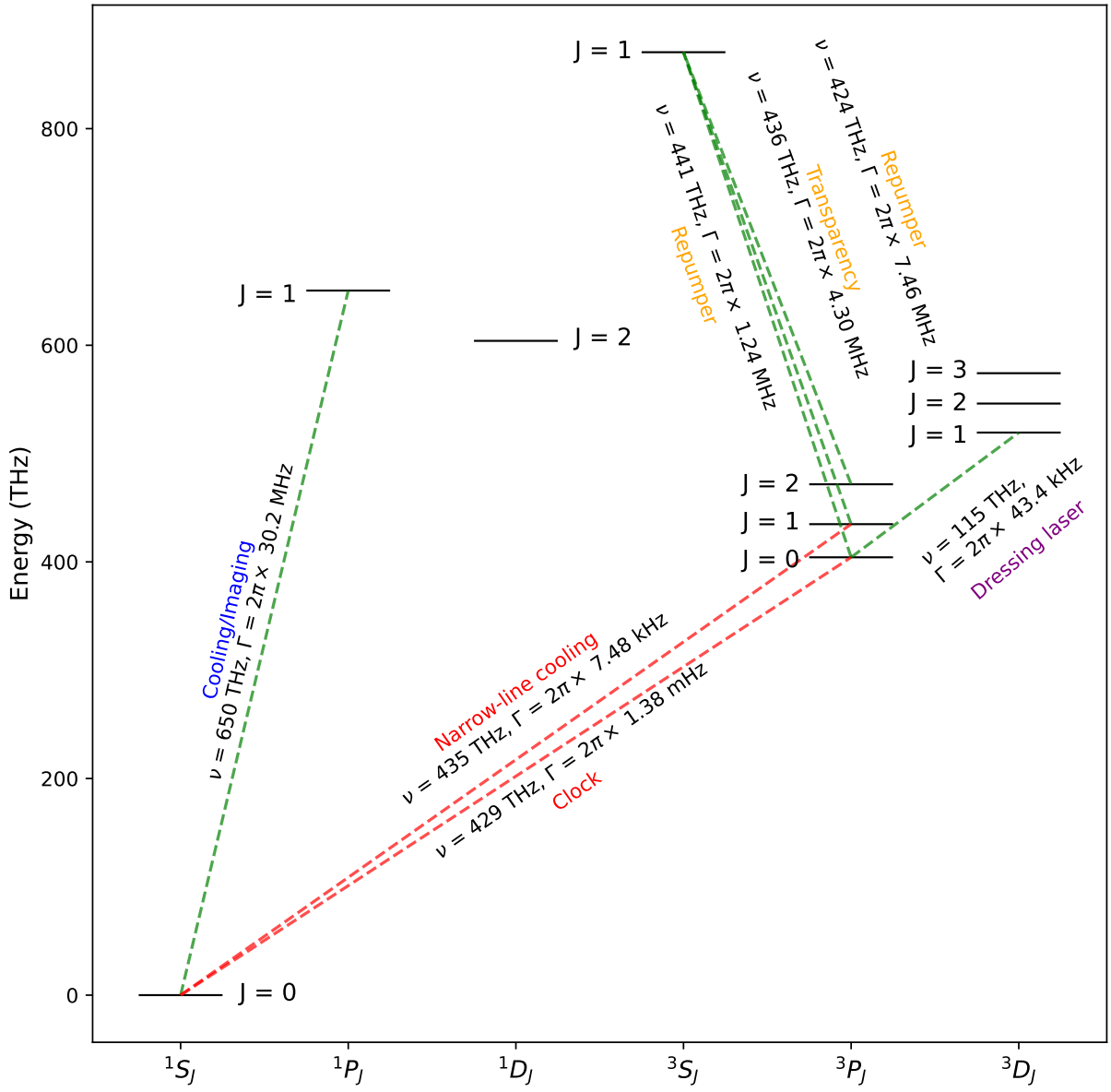

Figure 2.1: Level structure of ^{87}Sr. Dipole-allowed transitions where $\Delta\mathbf{L} = \pm 1$ and $\Delta\mathbf{S} = 0$ are shown in green. Dipole-forbidden, *intercombination* transitions between singlet ($\mathbf{S} = 0$) and triplet ($\mathbf{S} = 1$) states are shown in red. ^3P_J and ^3D_J energies are broadened to make the plot more readable.

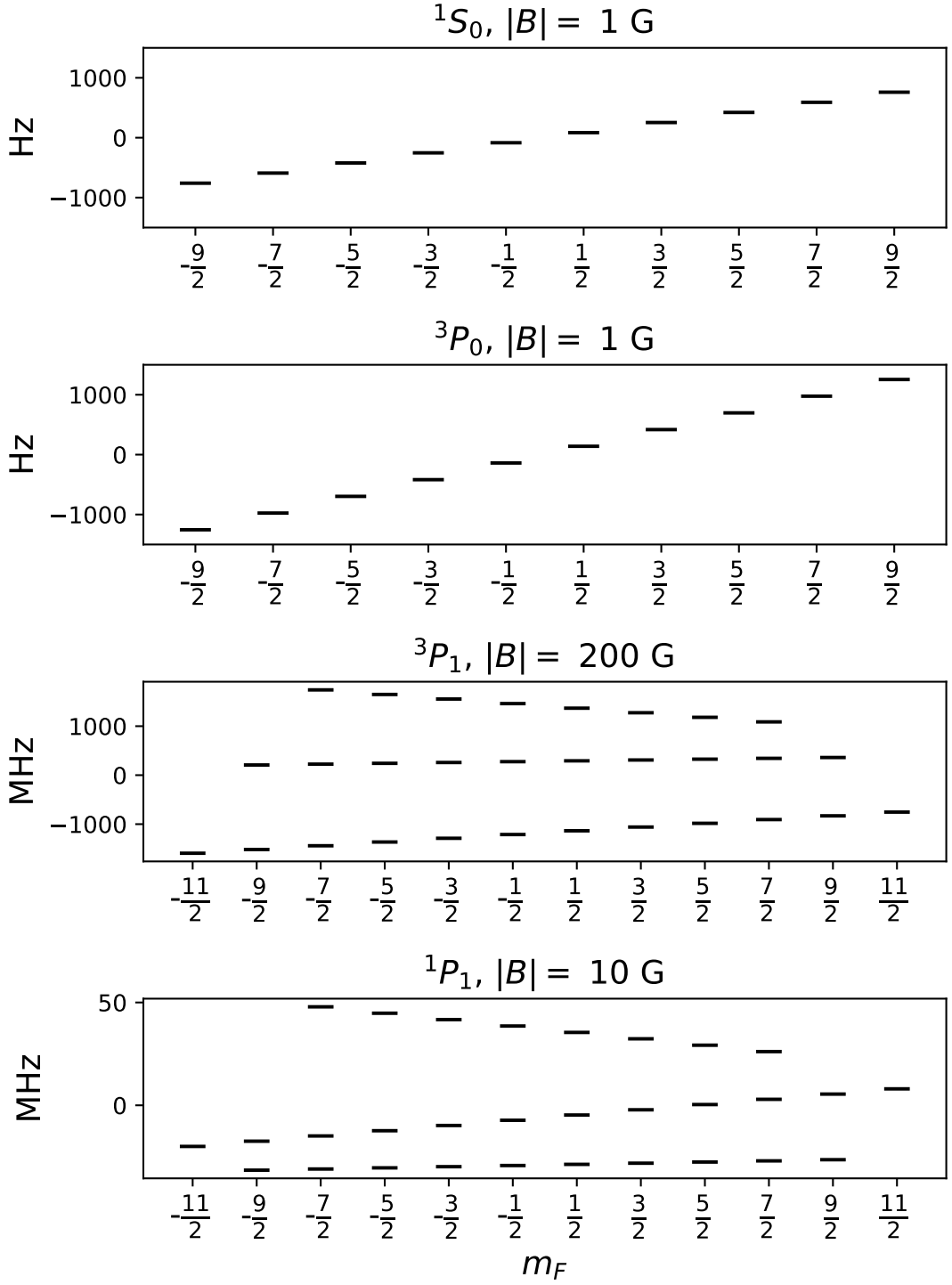

Figure 2.2: Zeeman shifts of relevant states in ^{87}Sr. For the $J \neq 0$ states with hyperfine structure, an external B field was chosen for each plot so the Zeeman shifts are commensurate with the hyperfine splitting.

states are shifted in energy by

$$\Delta E_{HF}/h = \frac{A}{2}K + \frac{Q}{2}\frac{\frac{3}{4}K(K+1) - I(I+1)J(J+1)}{I(2I-1)J(2J-1)}, \tag{2.1}$$

where A and Q are the magnetic dipole and electric quadrupole constants for a given electronic state and $K = F(F+1) - J(J+1) - I(I+1)$. Their values are tabulated here for the two predominant higher lying states in Table 2.1.

Hyperfine splitting			
State	A (MHz)	Q (MHz)	Shift (MHz)
$^3P_1, F = 7/2$			1414
$^3P_1, F = 9/2$	260.084 [97]	35.658 [97]	284
$^3P_1, F = 11/2$			-1174
$^1P_1, F = 7/2$			37
$^1P_1, F = 9/2$	-3.4 [98]	39 [98]	-29
$^1P_1, F = 11/2$			-6

Table 2.1: Hyperfine splitting for $^1P_1$ and $^3P_1$ states.

With a basic understanding of the different electronic states, we next turn our attention to *transitions* between these states. For a given transition between electronic states, much of the physics is encoded in the transition frequency ν and the linewidth Γ. It is difficult to calculate these values ab initio [99] but these quantities can be straighforwardly measured in the laboratory. The first transitions to discuss are electric dipole-allowed[3] transition according to $\Delta L = 1$ and $\Delta S = 0$. The relevant electronic transitions on our experiment are plotted in Fig. 2.1, with dipole-allowed transitions in green. The $^1S_0 \rightarrow {}^1P_1$ transition with $\Gamma = 2\pi \times 30.2$ MHz is the predominant dipole-allowed transition used on our experiment for fast imaging and initial cooling of our thermal gas.

Intercombination transitions ($\Delta S = 1$) between singlet and triplet states are nominally dipole forbidden and thus require state mixing processes to be driven. These mixing processes

[3] This selection rule can be understood by parity arguments where the dipole operator $d \propto x$ and the only non-zero matrix elements are $\Delta L = 1$.

are comprehensively described in the following work from our group [100]. In brief summary, the $^3P_1$ state has an admixture of the $^1P_1$ state owing to 'spin-orbit' coupling of the form $l_i \cdot s_i$. In addition, the hyperfine interaction also provides a state mixing mechanism providing a weak admixture of $^1P_1$ in $^3P_0$. Thus, these dipole-forbidden transitions $^1S_0 \rightarrow {}^3P_1$ and $^1S_0 \rightarrow {}^3P_0$ have correspondingly smaller linewidths of $\approx 2\pi \times 7$ kHz and $\approx 2\pi \times 1$ mHz respectively owing to admixture of the $^1P_1$ state. The magnetic structure of each of these states is plotted in Fig. 2.2. Additionally, the linear magnetic field sensitivities are tabulated in Table 2.2.

B-field sensitivity	
$^1S_0, F = 9/2$	$168.8 \times m_F$ Hz/G
$^3P_0, F = 9/2$	$278.8 \times m_F$ Hz/G
$^3P_1, F = 7/2$	$-467 \times m_F$ kHz/G
$^3P_1, F = 9/2$	$85 \times m_F$ kHz/G
$^3P_1, F = 11/2$	$381 \times m_F$ kHz/G
$^1P_1, F = 7/2$	$-311 \times m_F$ kHz/G
$^1P_1, F = 9/2$	$57 \times m_F$ kHz/G
$^1P_1, F = 11/2$	$254 \times m_F$ kHz/G

Table 2.2: Linear sensitivities at low magnetic field in the absence of quadratic shifts.

The $^1S_0 \rightarrow {}^3P_0$ 'clock' transition with a linewidth of $\approx 2\pi \times 1$ mHz forms the basis for essentially all the scientific explorations detailed in Chapter 1. To gain some intuition about the spectroscopy of this transition, we plot the transitions between magnetic sublevels of $^1S_0$ and $^3P_0$ in Fig. 2.3. Note, this is simply the differences of the energy levels plotted in Fig. 2.2. Interestingly the minimally magnetically-sensitive transition is $|m_F| = \frac{5}{2} \rightarrow |m_{F'}| = \frac{3}{2}$, owing to a fortuitous cancellation of the differential sensitivities. For all clock spectroscopy in this thesis, we drive the $|m_F| = \frac{9}{2} \rightarrow |m_{F'}| = \frac{9}{2}$, although it may be worthwhile to use more magnetically insensitive transitions for future studies. The magnetically insensitive properties of this $|m_F| = \frac{5}{2} \rightarrow |m_{F'}| = \frac{3}{2}$ transition was first employed to achieve record stability between independent optical lattice clocks [40].

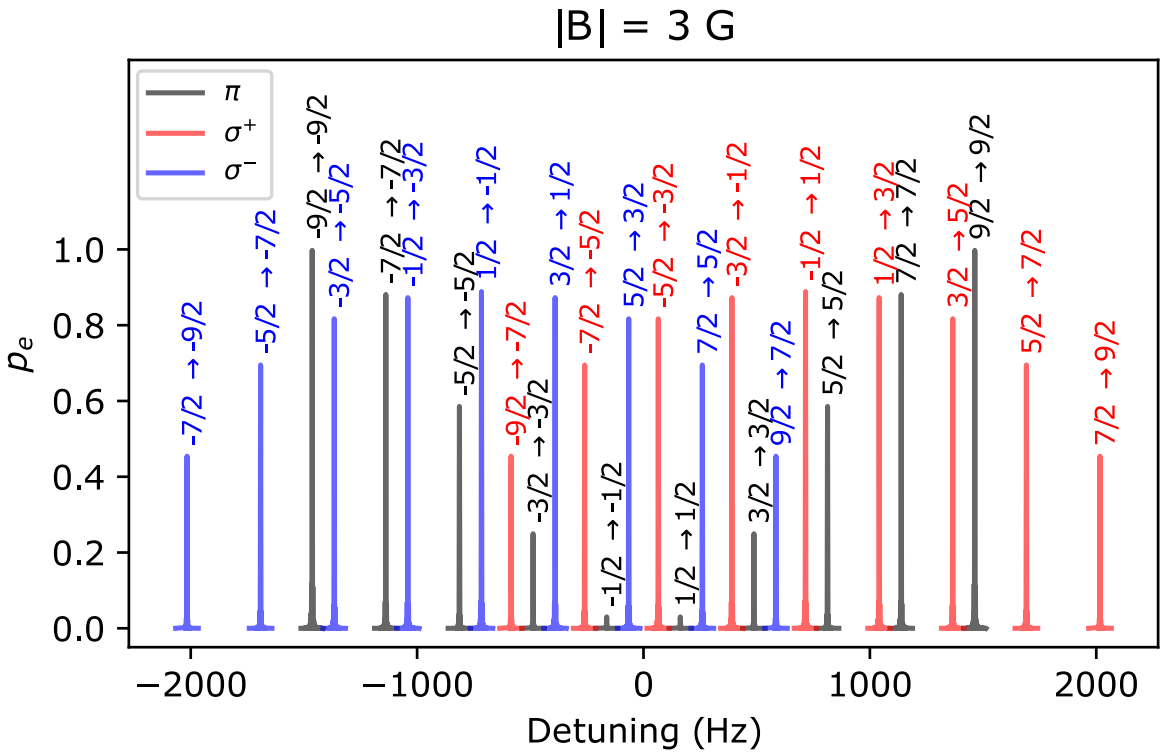

Figure 2.3: Zeeman splitting for ${}^1S_0 \rightarrow {}^3P_0$ transition. Pulse duration for all transitions corresponds to a π pulse for $|m_F| = \frac{9}{2} \rightarrow |m_{F'}| = \frac{9}{2}$ with peak excitation fraction $p_e = 1$. Note the minimally magnetically-sensitive transition is $|m_F| = \frac{5}{2} \rightarrow |m_{F'}| = \frac{3}{2}$ in the center of the plot.

2.1.2 Experimental apparatus

With a basic understanding of the strontium level structure in hand, we next focus on an overview of the experimental apparatus to coherently probe these various transitions. In summary, a UHV vacuum system is required so the background-gas-collision limited lifetime is much longer than any clock dynamics we wish to study. As we detail in Chapter 3, loss measurements of atoms trapped in our lattice bound our vacuum lifetime to > 100 s. The efforts to assemble this vacuum system and characterize it's performance are detailed in Sara Campbell's Ph.D thesis [101]. A schematic of the apparatus is depicted in Fig. 2.4. Pumping to achieve UHV is done with a 150 L/s ion pump on main chamber and 3 L/s pump on oven

assembly. Strontium atoms are heated to 460° C in the AOSense atom source, then cooled with a Zeeman slower stage as detailed in Section 2.2.1. In the science chamber, multiple stages of cooling and trapping are implemented to ultimately achieve Fermi degeneracy. In many respects, this vacuum system is fairly simple with no atomic transport of cold atoms, and thus all laser cooling, trapping, and clock spectroscopy is done at the center of the chamber. It has also been incredibly reliable and is essentially the only part of the experiment untouched during the course of my Ph.D.

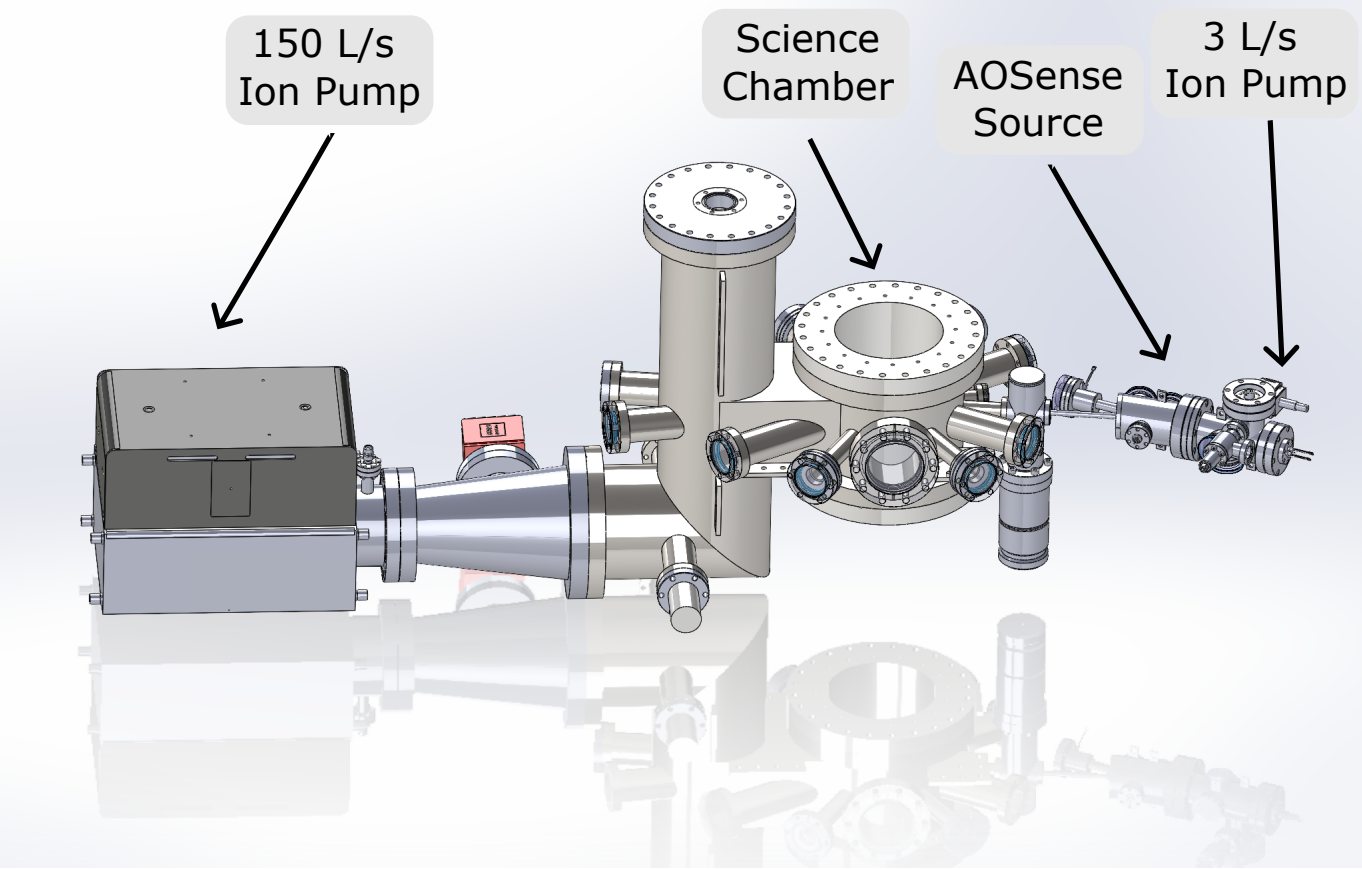

Figure 2.4: Vacuum chamber for the experiment. Commercial AOSense atomic source delivers a collimated beam of ^{87}Sr that is laser cooled to Fermi degeneracy in the Science chamber. We use a 150 L/s ion pump on the main chamber to achieve UHV and 3 L/s pump on the oven assembly.

A cross-section of the 'science' chamber is depicted in Fig. 2.5. The obvious downside to avoiding transport is that every single laser beam addressing the atoms must enter a

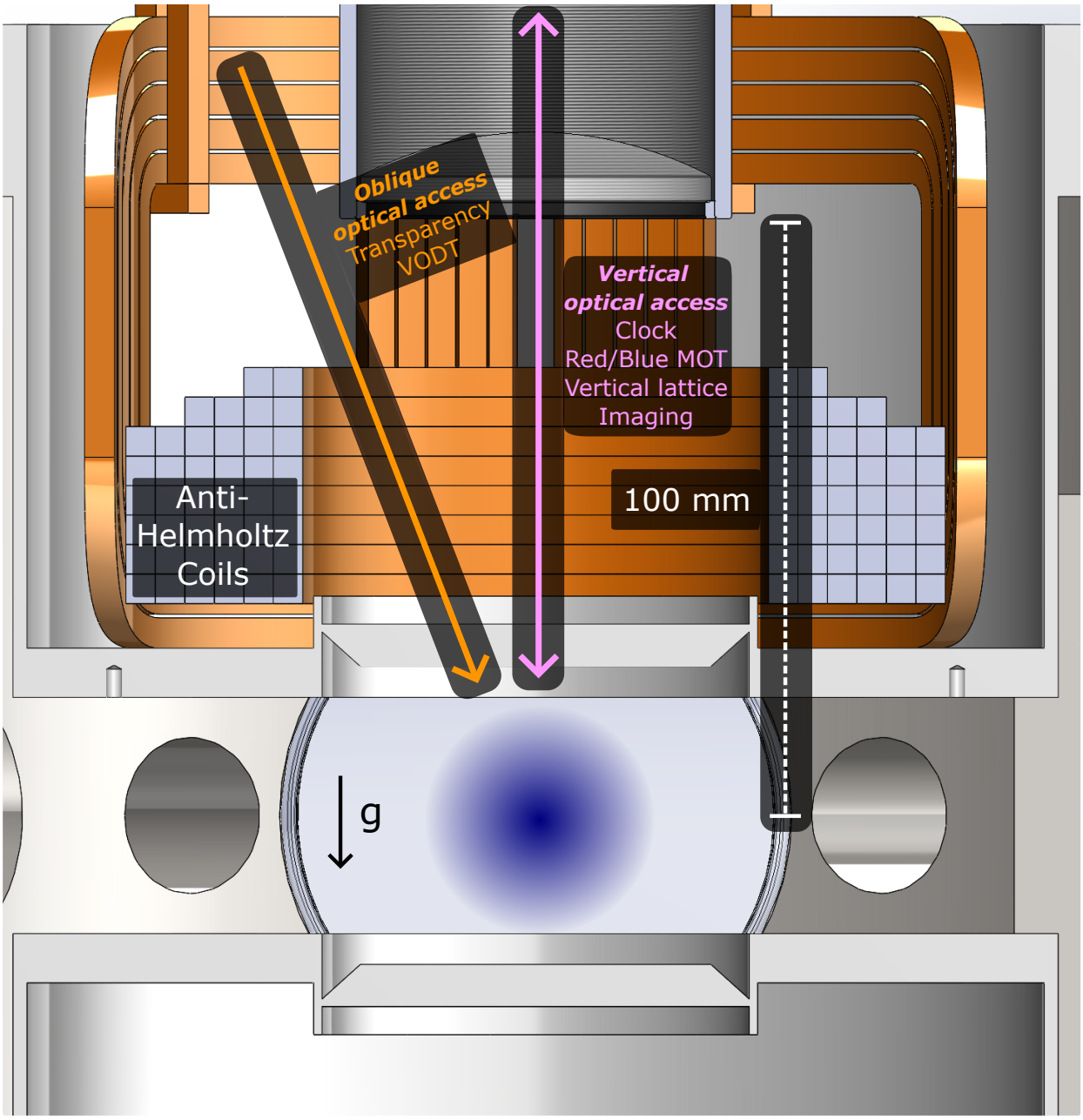

Figure 2.5: Cross-section of science chamber. The imaging objective lens is positioned 100 mm from the atoms. Our vertical clock laser, red and blue MOT beams, vertical lattice, and imaging beams all go through this imaging system oriented along gravity. A full description of this setup is provided in Chapter 3. Between the objective lens and anti-Helmholtz coils is optical access for an oblique optical path $\approx 10^\circ$ tiled from the vertical path, including our vertical optical dipole trap and transparency beam. Compensation coils are farther away from the chamber, thus not in view, providing weak (< 10 G) fields to establish a quantization axis.

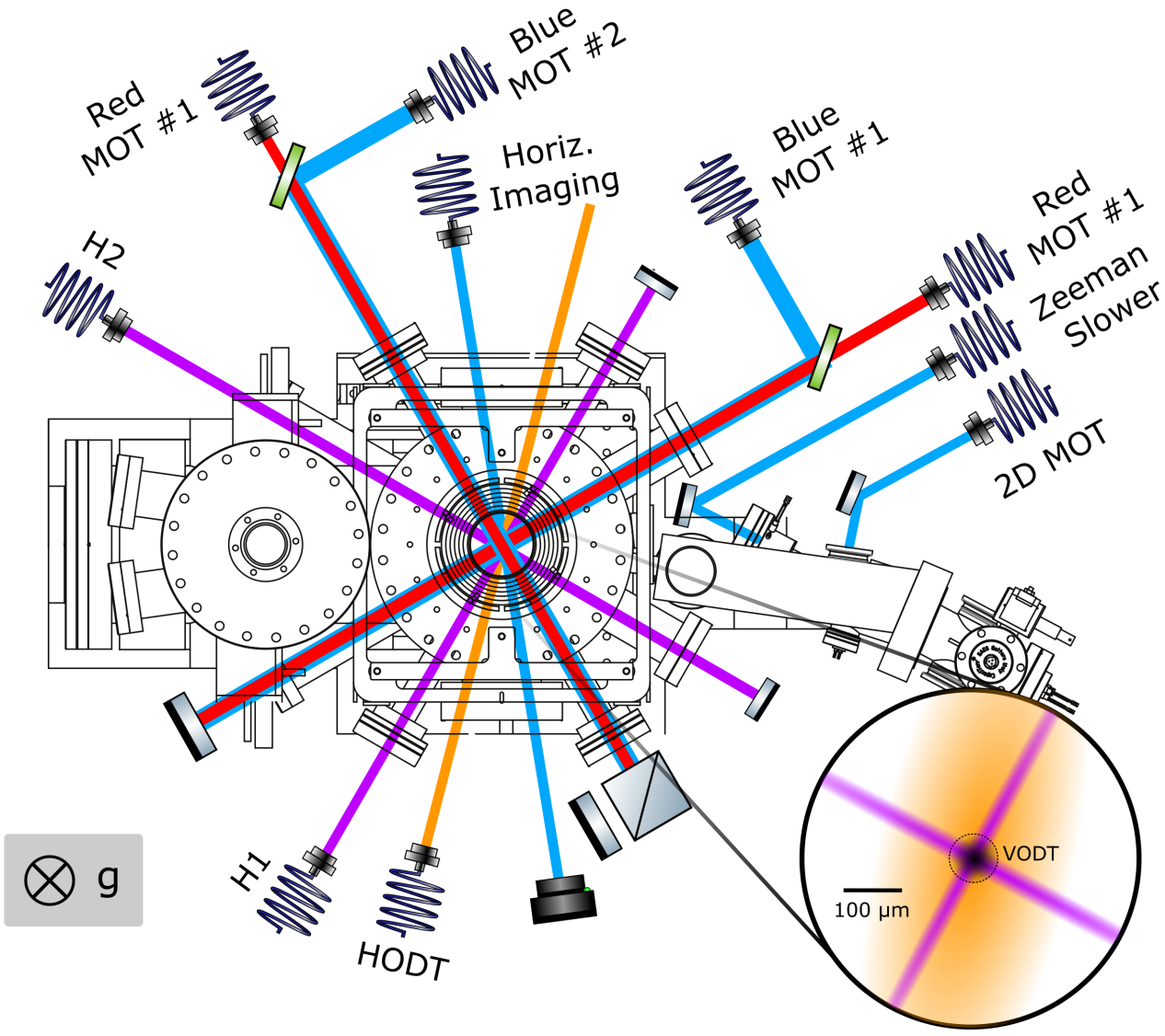

Figure 2.6: Schematic of trapping and cooling lasers on the main breadboard surrounding the science chamber. Most optical elements are omitted for clarity. Each of these lasers plays a crucial role for both cooling atoms to quantum degeneracy and for loading into our 3D optical lattice. **Inset:** Intensity (proportional to the confinement strength) of the ODT and optical lattice lasers is plotted.

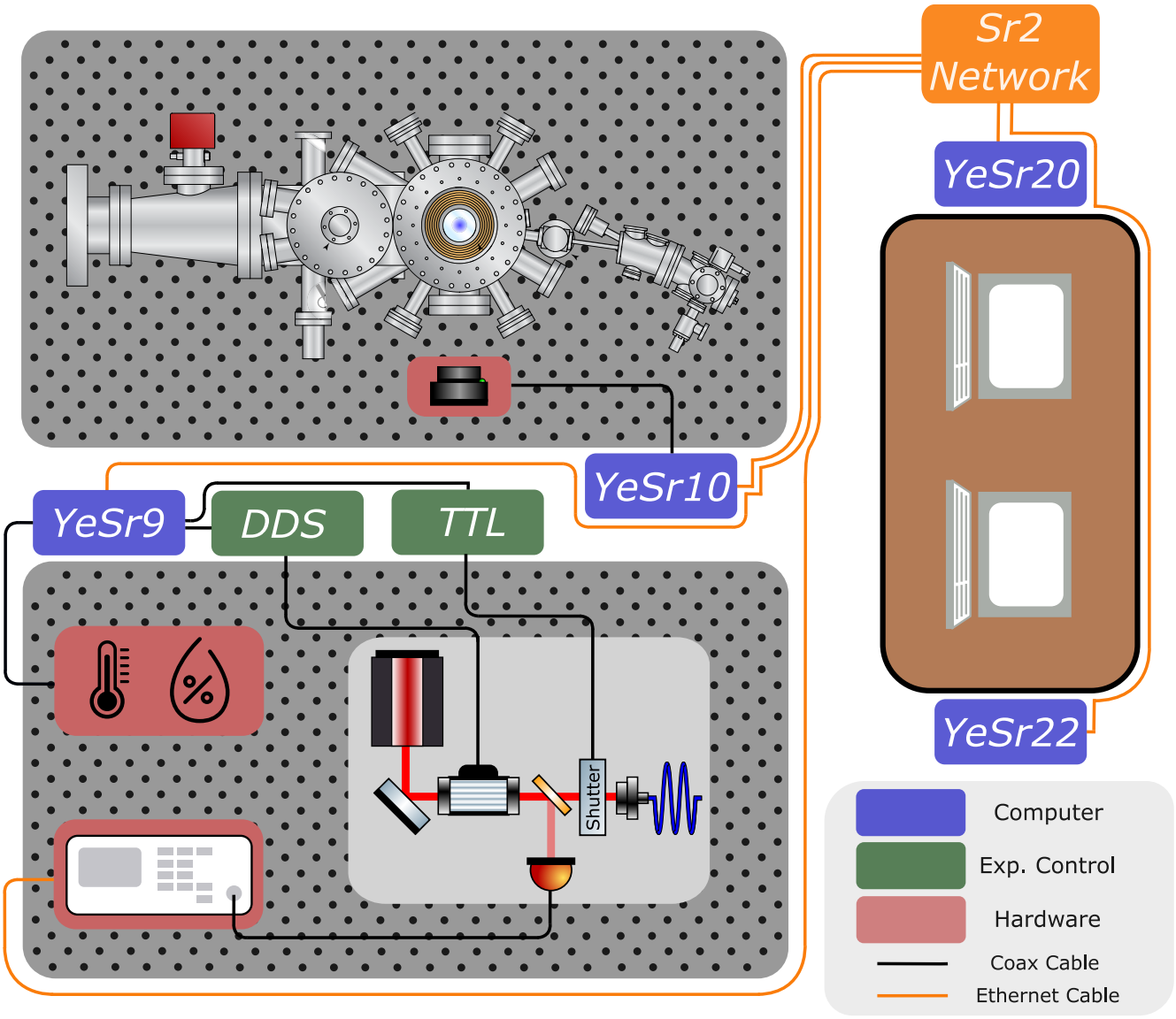

Figure 2.7: Layout of the Sr2 control system. Computers are interfaced over the Sr2 network. Experimental hardware is either directly connected to the network (orange) or connected to computers (black). By design, any computer can then communicate with any piece of experimental hardware.

single chamber of the vacuum system with finite optical access. This technical hurdle is exemplified fairly well in this figure. The vertical optical path includes an intricate design to accommodate laser cooling, trapping, clock spectroscopy, and a high-resolution imaging system. The details of this optical design are summarized in Chapter 5. We also have an 'oblique' optical path tilted $\approx 10^\circ$ used for auxiliary beams including our vertical dipole trap. A schematic of the many lasers surrounding our vacuum chamber is shown Fig. 2.6. By the end of Chapter 3, a reader will be familiar with all of these lasers!

Before diving into the details of all the laser systems on Sr2, it is useful to give a broad overview of the experimental control and data storage/analysis. How do we engineer and control dozens of DAC analog voltages, TTL digital signals, and lasers systems separated across different rooms in an organized and flexible way? And how do we turn this complicated sequence into a meaningful measurement of our atomic ensemble to learn some physics? The essence of our experimental control, developed by previous Ph.D. student Ross Hutson, is based on a network protocol called *Labrad* designed to communicate with equipment over a lab network.

To gain some intuition about the functionality of our experimental control, a simplified schematic is depicted in Fig. 2.7. All computers, denoted *YeSrX*, are connected to the Sr2 network and can communicate with each other. Similarly all lab hardware is either directly connected to these computers or to the lab network. One immediately sees the implementation of this design: via *Labrad* any computer can talk to any piece of hardware (e.g. '*YeSr9*' can tell '*YeSr10*' to take an image of the atoms). The remaining challenge is thus programming and synchronizing in hardware all equipment to run a tailored experimental sequence of choice. Here, python servers called the *sequencer* and *conductor* servers allow a user to program a choice sequence with a flexible graphical user interface (GUI) and then ensure that all lab hardware is appropriately programmed.[4] The real power in this home-

[4] Postdoc Eric Oelker did a nice job of summarizing these servers in more detail here: https://github.com/PickyPointer/SrE/wiki

built design is that essentially all software is written in python and the setup is designed to be modular. Thus, there are seemingly no constraints on the amount of hardware or compatible devices to use. For example, we routinely use spectrum analyzers to coarsely log the locking performance of the lasers on our experiment and environmental sensors to monitor the temperature and humidity at various locations on our experiment as depicted in Fig. 2.7. The main drawback is also in the nature of a home-built solution - cryptic errors occasionally arise that require the user to have some literacy in python debugging. The sequencer GUI is displayed on our analysis computer *YeSr20*, and the *conductor* and *sequencer* servers are physically executed on *YeSr10*. All data storage is on the computer *YeSr22*, where cameras save compressed images in *.hdf5* format. All-in-all, this *Labrad* and python based experimental control works very well for Sr2.

2.2 Fermi-degenerate ^{87}Sr

We summarize the process of making a nuclear spin-polarized Fermi gas, step-by-step in this section.

2.2.1 Broadband laser cooling

In this section, we briefly summarize our 'Blue' Magneto-Optical Trap (MOT) operating at $\approx$ 461 nm employing the $^1S_0 \rightarrow {}^1P_1$ transition. Given the large linewidth $\Gamma = 2\pi \times 30.2$ MHz, this transition is used to effectively capture atoms over a wide velocity range. Using a commercial atom source from AOSense strontium atoms are sublimated at 460° C, then cooled with a Zeeman slower and two-dimensional MOT. Given that the hyperfine splitting for $^1P_1$ is commensurate with transition linewidth, spectroscopy is in a somewhat peculiar regime where hyperfine splitting is resolved (i.e. $F = 7/2, 9/2, 11/2$ manifolds) but individual m_F states are not. A 50 G/cm magnetic field gradient from the anti-Helmholtz coils depicted in Fig. 2.5 is used for Blue MOT operation. With a cooling laser intensity $I/I_{sat} \approx 1$, we trap $\approx$ 100 million atoms with a temperature $\approx$ 1 mK close to

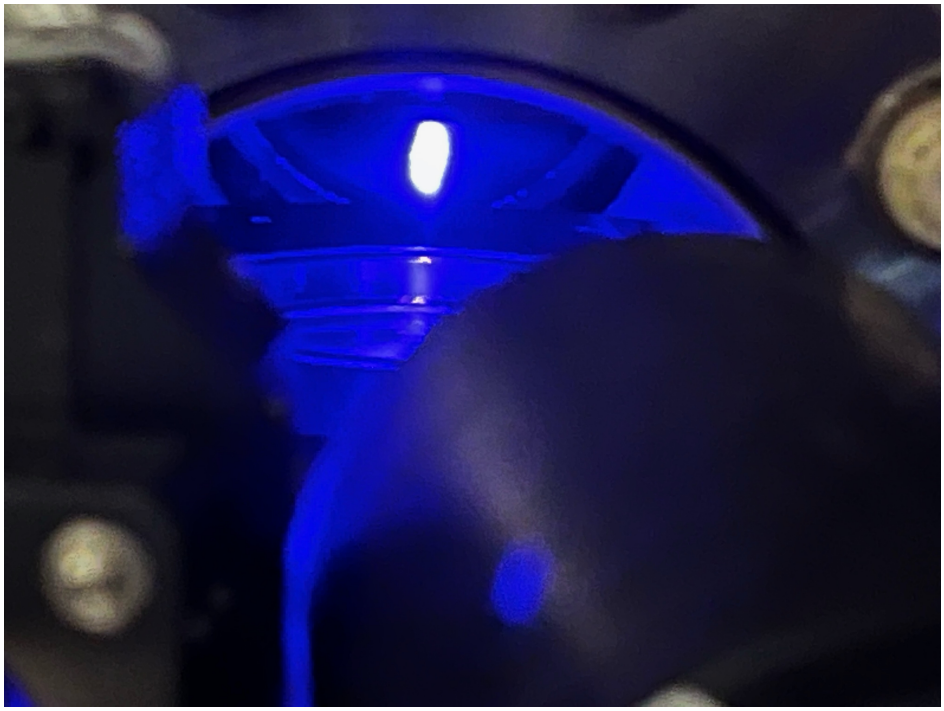

Figure 2.8: Photo of blue MOT. The only stage of the experiment that can be seen by the naked eye!

Doppler temperature of $\frac{\hbar\Gamma}{2k_B} = 725\ \mu$K [102]. This is nearly a closed, cycling transition with 1:40000 probability atoms decays to the $^1D_2$ state, which then decay to the $^3P_2$ state or the $^3P_1$ state with 1:2 probability. The $^3P_2$ state is very long lived ($2\pi \times \Gamma \ll 1$ Hz), so to address this dark state we turn on repumping lasers that cycle the $^3P_2 \rightarrow {}^3S_1$ and $^3P_0 \rightarrow {}^3S_1$ dipole-allowed transitions and pump atoms back to $^1S_0$ via the $^3P_1$ state. Trapping ≈ 100 million atoms may sound like a very large number, but as we will detail in the coming sections the different cooling steps to achieve Fermi degeneracy and dramatically increase the phase space density are unavoidably lossy. A photo of our blue MOT is shown in Fig. 2.8. The only stage of the experiment where imaging the atoms with an iPhone is conceivable!

2.2.2 Narrow-linewidth laser cooling

The cooling techniques described in Section 2.2.1 are similar to standard Doppler cooling methods used in alkali experiments where temperatures of ≈ 1 mK are readily achieved.

Next these alkali experiments typically use 'sub-Doppler' cooling techniques to circumvent the Doppler temperature limit. Strontium offers a drastically different perspective, using narrow-line cooling transitions where the Doppler limit prescribed by the linewidth Γ is not the limitation, but rather the photon recoil energy. For the ${}^1S_0 \rightarrow {}^3P_1$ transition where $\Gamma \approx 2\pi \times 7$ kHz, the Doppler temperature is $\frac{\hbar\Gamma}{2k_B} = 179$ nK [103], while the recoil temperature $\frac{\hbar^2 k^2}{2m} = 460$ nK where the wavevector $k = 2\pi/\lambda$. This opens the door to laser cooling gases to near quantum degeneracy, and also conveniently allows all-optical evaporative cooling.[5] An additional limitation to consider is the maximum laser cooling force, given by $F_{max} = \hbar k \Gamma/2$. For this transition in strontium $F_{max} \approx 16$ mg, meaning transitions with $\Gamma \ll 2\pi \times 1$ kHz are generally ineffective to support atoms against the force of gravity. For example, this was problematic in the alkaline-earth species calcium, necessitating quenching the transition with the ${}^1D_2$ state to enhance Γ [105]. As we will detail in this section, we even use additional techniques making spatial regions of our atom cloud 'transparent' to cooling light to address limitations imposed by the recoil temperature [106, 107].

Before diving into the details of narrow-line cooling and trapping, this is a good opportunity here to briefly overview some of the properties of trapping atoms with light fields. We blend a number of very good references in this section here [108, 109, 75, 110]. Neutral atoms interact with light because they are *polarizable*. That is, an oscillating electric field directed at an atom will cause it's charge distribution to oscillate. A semi-classical treatment captures much of the physics, where a two-level quantum system interacts with a classical electric field $\mathbf{E}(\mathbf{r},t) = \hat{\mathbf{e}}\tilde{E}(\mathbf{r})\exp(-i\omega t) + \text{c.c.}$, inducing a dipole $\mathbf{p}(\mathbf{r},t)$ with magnitude $\mathbf{p} = \alpha\mathbf{E}$ according to a complex polarizability α depending on the external drive frequency ω. We classically solve the equations of motion to gain some intuition about the functional form of $\alpha(\omega)$. Here we model our system as a driven, classical harmonic oscillator

[5] $U_{trap} \approx \mu$K deep optical dipole traps are straightforward to realize with commercial fiber lasers, but the transfer to this trap will be very lossy unless $U_{trap} \gg T$ where T is the atomic ensemble temperature. A rule of thumb is that the equilibrium temperature $T = U_{trap}/\eta$ where $\eta = 10$ [104]. For alkali experiments with high magnetic sensitivity as the ground state is $J = 1/2$, magnetic trapping can be employed and $U_{trap} \approx 1$ mK may be used.

$$\ddot{x} + \Gamma\dot{x} + \omega_0^2 x = -e\tilde{E}/m \tag{2.2}$$

with damping rate Γ and resonance frequency ω_0. With the ansatz $x(t) = x_0 e^{-i\omega t}$, we solve

$$ex_0 = \frac{e^2/m}{\omega_0^2 - \omega^2 - i\Gamma\omega}\tilde{E} \quad \rightarrow \quad \alpha(\omega) = \frac{e^2/m}{\omega_0^2 - \omega^2 - i\Gamma\omega}. \tag{2.3}$$

Next we solve for the potential depth U, often referred as an *AC stark shift*, and scattering rate Γ_{sc} for our harmonic oscillator. Substituting $\Gamma = \frac{e^2\omega^2}{6\pi\epsilon_0 mc^3}$:[6]

$$U = -\mathbf{p}\cdot\mathbf{E} = -\frac{1}{2\epsilon_0 c}\mathrm{Re}(\alpha)I = -\frac{3\pi c^2}{2\omega_0^3}\left(\frac{\Gamma}{\omega_0 - \omega} + \frac{\Gamma}{\omega_0 + \omega}\right)I, \tag{2.4}$$

$$\Gamma_{sc} = \dot{\mathbf{p}}\cdot\mathbf{E} = \frac{\omega}{\epsilon_0 c}\mathrm{Im}(\alpha)I = \frac{3\pi c^2}{2\hbar\omega_0^3}\left(\frac{\Gamma}{\omega_0 - \omega} + \frac{\Gamma}{\omega_0 + \omega}\right)^2 I. \tag{2.5}$$

Here, I is the intensity of our applied field. If we operate near resonance, $\omega_0 \approx \omega$ and the 'counter-rotating term' $\omega_0 + \omega$ can be omitted. Then, Eq. 2.5 and Eq. 2.4 is simplified to $\Gamma_{sc} = \frac{3\pi c^2}{2\hbar\omega_0^3}\left(\frac{\Gamma}{\Delta}\right)^2 I$ and $U = -\frac{3\pi c^2}{2\omega_0^3}\frac{\Gamma}{\Delta}I$ where $\Delta \equiv \omega - \omega_0$.

There are two important points to make on our formulas for U and Γ_{sc}. First, the sign of trap depth U depends on detuning Δ, where atoms are attracted to light fields 'red-detuned' ($\Delta < 0$) and repelled when 'blue-detuned' ($\Delta > 0$). This can be intuited as our dipole $p \cdot E$ oscillating in-phase or out-of-phase with respect to the applied field. Secondly, $\Gamma_{sc} \propto 1/\Delta^2$ while $U \propto 1/\Delta$ motivating operating at large detuning Δ to fractionally minimize scattering. This technique of using far-off resonance traps (FORT) works remarkably well and is generally applicable for essentially all atomic species using telecommunication wavelength lasers that are commercially available with high optical power (> 10 W). Operating at $\lambda \approx 1$ μm, these lasers are highly red-detuned from visible and near-IR resonances. This principle is the basis for our 813 nm optical lattice and 1064 nm optical dipole traps that we will detail in the coming chapters.

[6] This expression comes from the Larmor formula for the radiative power of an oscillating dipole. Also, SI units are used for this derivation.

While this semi-classical derivation gives us a nice introduction to trapping atoms, it leaves out a few important details that we will revisit later. First, we do not address saturation effects in our treatment here. Based on Eq. 2.5, one would conclude that the scattering rate Γ_{sc} is limited only by the available laser intensity I. In reality, the scattering rate is limited by the transition linewidth and the maximum scattering rate is $\Gamma/2$.[7] Thus, Eqs. 2.5 and 2.4 are only strictly correct in the highly detuned regime at low saturation where $\Gamma \gg \Gamma_{sc}$ and thus the population of the excited state is negligible. We employ the effects of saturation to achieve quantitative imaging at high density in Chapter 5. Second, this semi-classical derivation does not capture coherent atom-light interactions again due to the fact the population of the excited state is always negligibly small. We detail this theoretical framework in Chapter 3, which is critical to realize clock spectroscopy. Particularly with our clock transition, we largely neglect the contributions of dissipation ($\Gamma \approx 0$) and dynamically control the populations and coherences of our two-level quantum system with external fields.

To quantitatively understand trapping our strontium atoms, there are a few remaining pieces to add to arrive at a full expression for the polarizability $\alpha(\omega)$. There are many excellent resources that have derived $\alpha(\omega)$ in full detail [95, 111, 112], and the goal of this section is just to provide a reader with an intuitive overview for calculating the polarizability to finally arrive at an expression for the *scalar*, *vector*, and *tensor* shifts.

Our semi-classical expression for Γ is strictly not correct[8] and does not consider the dipole-selection rules presented above that strongly modify the coupling strength between different states. To properly address this, the coupling strength is prescribed by the dipole matrix element $\mathbf{d} = -e(\mathbf{x}_1 + \mathbf{x}_2)$ between two states $|g\rangle$ and $|e\rangle$.

$$\Gamma_{ge} = \frac{\omega_{ge}^3}{3\pi\epsilon_0\hbar c^3}\frac{2J_e+1}{2J_g+1}|\langle g|\,|\mathbf{d}|\,|e\rangle|^2. \tag{2.6}$$

[7] One perspective to understand saturation for an unfamiliar reader is the modelling of atomic populations via rate equations. Including the effects of saturation is necessary to understand phenomena like population inversion and lasing.

[8] For the dipole allowed alkali transitions (i.e. the D lines), the semi-classical calculation for Γ actually agrees within a few percent [108].

Here the double lines ||.|| denote the so-called *reduced* dipole matrix element that only depends on the radial portion of the electron wavefunction.[9] Additionally, to properly determine the polarizability, we need to tabulate *all* states. As we saw in the level diagram from Fig. 2.1, there are contributions from many different electronic states denoted $|e'\rangle$. Considering these two effects, the polarizability $\alpha(\omega)$ is now expressed as:

$$\alpha(\omega) \propto \sum_{e'} \frac{\omega_{ge'} |\langle g| |\mathbf{d}| |e'\rangle|^2}{\hbar(\omega_{ge'}^2 - \omega^2)}. \tag{2.7}$$

To fully determine $\alpha(\omega)$ we need sum over different m_F values. We next simplify Eq. 2.7 by breaking $\alpha(\omega)$ in individual terms based on m_F dependence:

$$\alpha(\omega) = \alpha_s(\omega) + \alpha_v(\omega)\frac{m_F}{2F}\xi \mathbf{k}\cdot\mathbf{B} + \alpha_t(\omega)\frac{3m_F^2 - F(F+1)}{2F(2F-1)}(3|\boldsymbol{\epsilon}\cdot\mathbf{B}|^2 - 1). \tag{2.8}$$

The prefactors $\alpha_i(\omega)$ are dependent on Wigner-j symbols and are derived in [95, 111, 112]. We see that Eq. 2.8 is dramatically simplified with respect to Eq. 2.7 and just depends on the frequency of our external light field ω, some basic properties of the light field like the k-vector $\mathbf{k}$ and polarization $\boldsymbol{\epsilon}$ and on the direction of the magnetic field $\mathbf{B}$ which sets the quantization axis for our experiment. From Eq. 2.8 the AC stark shift of a given state $|i\rangle$ from an external field with intensity I and frequency ω is: $\Delta\nu^i = \alpha^i(\omega)I/h$.

There are a few key insights to gain from Eq. 2.8. The 'Scalar' shift $\alpha_s(\omega)$ is just dependent on frequency of field ω and is devoid of any m_F dependence. The 'Vector' shift $\alpha_v(\omega)$, behaves like a fictitious magnetic field with a linear m_F dependence just like a Zeeman shift. It also depends on light polarization circularity ξ. We use linear light polarization in this chapter ($\xi = 0$) and thus neglect any vector shifts. Finally, the 'Tensor' shift is m_F^2 dependent. This m_F sensitivity is important for the spin selection techniques we use later in the chapter.

[9] The electron wavefunction is separable and can be decomposed into radial and angular portions. The overlap of the angular portion can be simplified in terms of selection rules and the exact coefficients are expressed in terms of Wigner symbols.

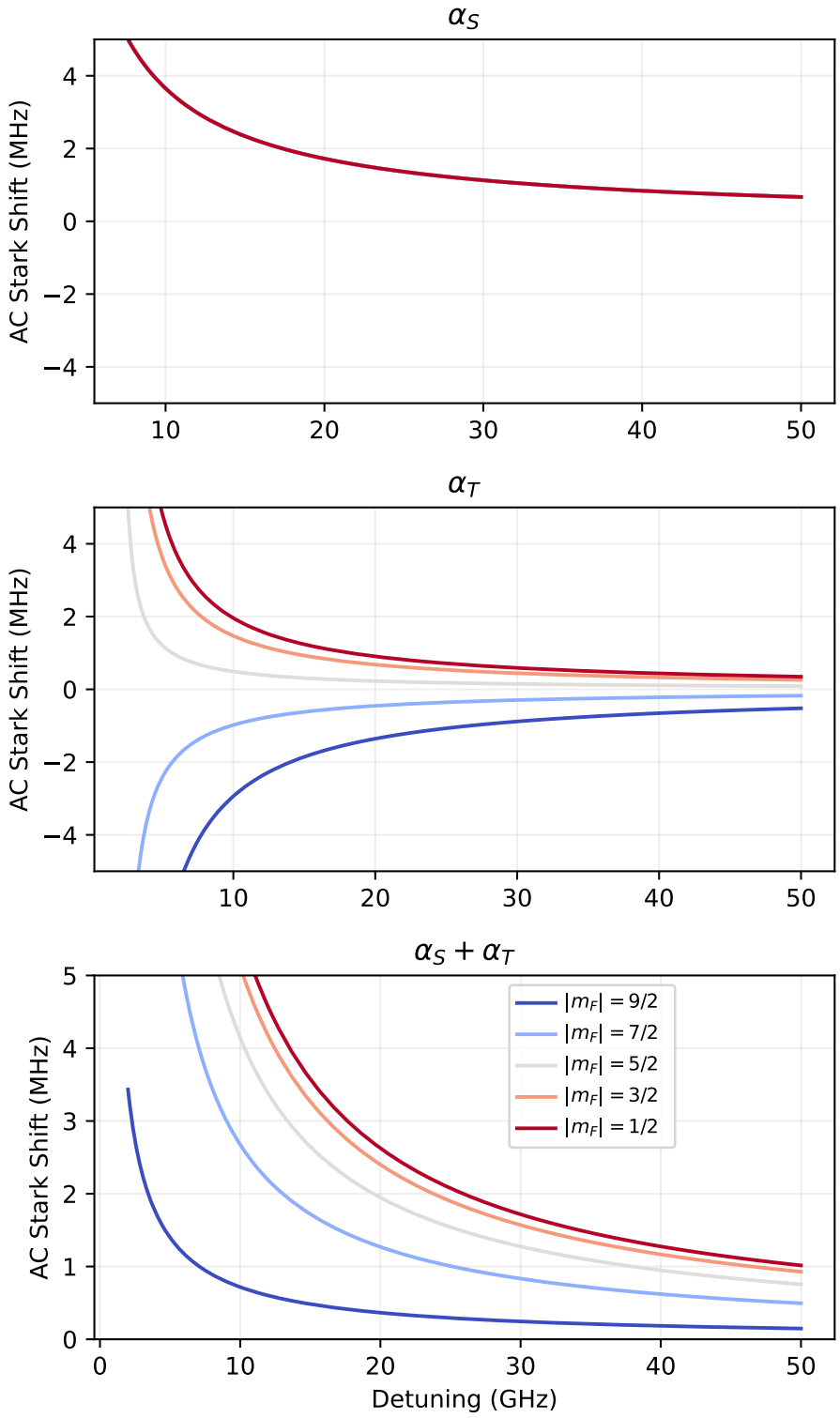

Figure 2.9: AC stark shifts for ${}^3P_1$ $F = 9/2$ states after application of transparency beam. Scalar (α_S), tensor (α_T), and combined ($\alpha_S + \alpha_T$) shifts are plotted. Detuning is plotted from bare ${}^3P_1 \rightarrow {}^3S_1$ transition omitting hyperfine structure. We operate with this beam ≈ 25 GHz detuned.

With a basic understanding of trapping atoms with light fields, we turn our attention back to narrow line cooling. To achieve the coldest temperatures possible, we wanted to address the limitations placed by the photon recoil temperature $\frac{\hbar^2 k^2}{2m} = 460$ nK. One method to achieve this is by intentionally introducing AC stark shifts leveraging the many different electronic states of ^{87}Sr. To shift the $^3P_1$ state, we use light detuned from the dipole-allowed $^3P_1 \rightarrow {}^3S_1$ transition. As we will detail, making the regions in the center of our dipole trap AC stark shifted from resonance creates a 'transparent' region at high density [106, 107]. This transparent region thermalizes with the edges of the cloud being actively laser cooled, with the conceptual idea of preparing of low entropy region at the center. We note that in addition to shielding the reabsorption of cooling photons, this technique also addresses light-assisted inelastic collisions that may lead to heating [113]. We plot the scalar shifts $\alpha_s(\omega)$, tensor shifts $\alpha_t(\omega)$ and the combined AC stark shift $\alpha(\omega) = \alpha_s(\omega) + \alpha_t(\omega)$ in Fig. 2.9. We operate with this beam ≈ 25 GHz detuned from the bare $^3P_1 \rightarrow {}^3S_1$ transition omitting hyperfine structure. Although the main effect is scalar shift from our blue detuned beam, including the tensor shift is necessary to fully calculate the AC stark shift.

To fully understand the effects of our transparency beam, including the spatial intensity distribution of the beam when modelling is also necessary. We first provide a quick overview on Gaussian beams before presenting this calculation. The transverse intensity profile of a coherent laser beam can be decomposed into Hermite-Gaussian (HG) modes which are solutions of the paraxial Helmholtz equation [114]. For essentially all the beams on our experiment, the intensity from the output of a single mode fiber is well approximated as the lowest order of these HG modes:

$$I(x,y,z) = \frac{2P}{\pi \mathrm{w}^2(z)} \exp\left(-2\frac{x^2+y^2}{\mathrm{w}^2(z)}\right), \quad \mathrm{w}(z) = \mathrm{w}_0\Big(1+\frac{z^2}{z_R^2}\Big), \quad z_R = \pi \mathrm{w}_0^2/\lambda. \tag{2.9}$$

Here x, y, and z are Cartesian coordinates and P is the total power in beam. We see the power in our beam falls off in the transverse direction with intensity $1/e^2$ at $r^2 = \mathrm{w}(z)^2$

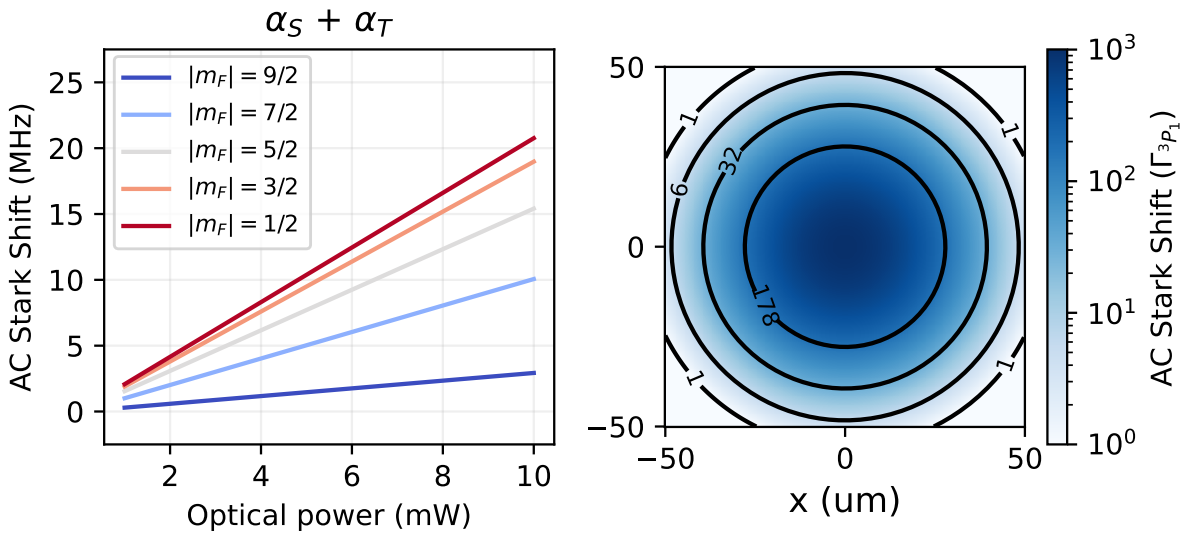

Figure 2.10: Spatial variation of transparency beam shifts. Plotted **left** is peak AC stark shifts for $^3P_1$ $F = 9/2$ states at the center of the Gaussian beam. Plotted **right** is spatial variations of these AC stark shifts for 5 mW power, 30 μm beam waist, 25 GHz detuning, and for the $m_F = |5/2|$ state. Shifts are normalized to the $^3P_1$ linewidth $\Gamma_{^3P_1} = 2\pi \times 7$ kHz. We see that $\Delta \geq \Gamma_{^3P_1}$ within a spatial extent of ≈ 50 μm.

where $r^2 = x^2 + y^2$. w_0, the width of the beam at its narrowest point at $z = 0$, is generally called the *waist*. This is reflected in Fig. 2.10, where the AC stark shift depends on the intensity $I(r)$. To gain some intuition, we normalize the AC stark shift to the $^3P_1$ linewidth. For 5 mW power, 30 μm beam waist, and the $m_F = |5/2|$ state, the AC stark shift is greater than $^3P_1$ linewidth Γ within a $\approx$ 50μm radius. Given the intensity of our cooling lasers $\ll I/I_{sat}$ at the end of our narrow-line cooling sequence, power-broadening effects are ignored and this area corresponds to the 'transparent' region where the detuning $\Delta \geq \Gamma$.[10]

These laser parameters were chosen so the transparent area roughly matches the waist of our VODT beam. We note that these transparency beam calculations do not include the AC stark shifts arising from the 1064 nm dipole trap. Although the AC stark shifts from the dipole trap are far less than the peak transparency beam shift of $\approx 1000\ \Gamma_{^3P_1}$, they are

[10] The exact definition of the 'transparent' region is a little ill-defined. Given the scattering rate $\Gamma \propto 1/\Delta^2$, so one might argue that a large detuning would be more appropriate (e.g. $\Delta \geq 10\,\Gamma$, $\Gamma \to \Gamma/100$).

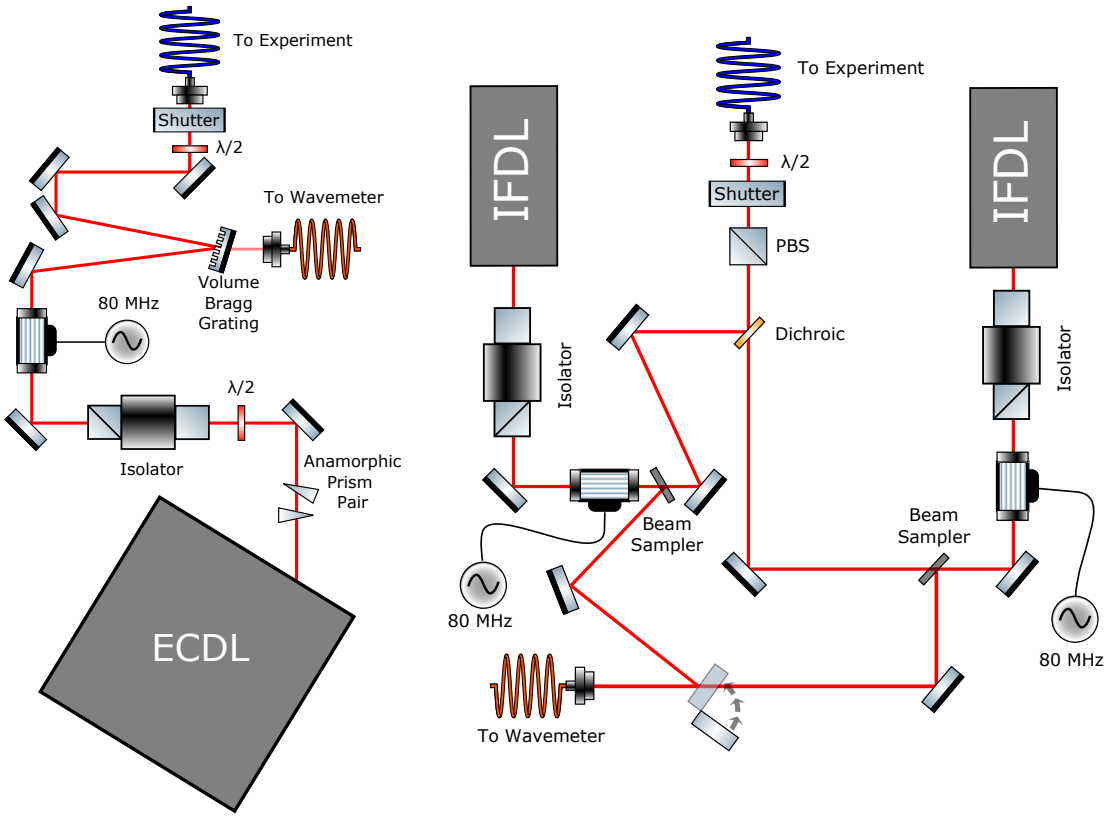

Figure 2.11: **Left:** Transparency beam setup. A volume Bragg grating is used to minimize resonant scatter from the 25 GHz detuned laser. **Right:** Repumper setup. These two lasers drive the transitions ${}^3P_0 \rightarrow {}^3S_1$ and ${}^3P_2 \rightarrow {}^3S_1$ respectively to deplete the metastable electronic states for readout and laser cooling purposes.

still $\approx \Gamma_{{}^3P_1}$. Similar to [115], we use circularly polarized light for our ODT to minimize differential shifts.

Our transparency laser setup is depicted in Fig. 2.11, along with our repumping laser system discussed in Section 2.2.1. These are fairly standard laser systems, where light from an External-Cavity Diode Laser (ECDL) [116] or Interference Filter Diode Laser (IFDL) [117] are coupled into a fiber. The cited papers nicely summarize the design of these lasers that we use. In essentially all laser systems, we use both an AOM and shutter to control the intensity of the light. This way the AOM is used for fast switching, while the shutter ensures

that the light is fully extinguished.[11] For the transparency beam, we use a Volume Bragg Grating (VBG) to ensure that residual, resonant light on our laser ≈ 25 GHz offset from the carrier is further filtered.

2.2.3 Evaporative cooling

We use the combination of narrow-line cooling and our transparency scheme to prepare a sample with temperature $T = 2\ \mu$K [107]. This section is a natural place to next outline the requirements to reach highly quantum degenerate gasses. As we will detail, the appropriate benchmark for our temperature T is the *Fermi temperature* T_F. We provide a detailed overview of the thermodynamics of Fermi gases in Appendix C, and use this section to briefly summarize the key points.

As we will detail, the physics of non-interacting Fermi gases can largely be encoded in a few, fairly simple equations. First, we write the Hamiltonian for our atoms trapped in a tightly focused Gaussian beam. This can be well-approximated as a quantum harmonic oscillator:

$$H = \frac{1}{2m}(p_x^2 + p_y^2 + p_z^2) + \frac{1}{2}m(\omega_x^2 x^2 + \omega_y^2 y^2 + \omega_z^2 z^2). \tag{2.10}$$

Practically, the *trapping frequencies* $\omega_x, \omega_y, \omega_z$ depend on the beam parameters of our optical dipole trap. The energy levels of this quantum harmonic oscillator are simple: $\epsilon(n_x, n_y, n_z) = \hbar(\omega_x n_x + \omega_y n_y + \omega_z n_z)$.

How do our atoms distribute themselves among the rungs of this quantum harmonic oscillator? This is elegantly captured by the Fermi-Dirac distribution, where the probability an atom occupies an energy level ϵ_i is:

[11] 1 mW of visible light contains $\approx 10^{15}$ photons and even a single resonant photon can dramatically affect the internal states of our atoms. For our imaging system, we use two cascaded AOMs to suppress any leakage light into the diffracted order.

$$n_i = \frac{1}{\frac{1}{\zeta}e^{\beta\epsilon_i} + 1}. \tag{2.11}$$

Here, $\beta = 1/k_B T$ and $\zeta = e^{\beta\mu}$ where μ is the chemical potential. This formula must naturally satisfy the following condition $\sum_i n_i = N$.[12] At $T = 0$, atoms fill up the harmonic oscillator states one-by-one up to Fermi-Energy $E_F = k_B T_F = \hbar\bar{\omega}(6N)^{1/3}$ where $\bar{\omega} = (\omega_x\omega_y\omega_z)^{1/3}$. This distribution is depicted in Fig. 2.12 for a $T = 0$ Fermi gas. At finite temperate, the degeneracy parameter T/T_F determines the population of states above E_F and thus the holes below E_F. This picture is exactly analogous in later chapters to the density distribution in the optical lattice, where the lattice filling and thus the fraction of holes is also dictated by the temperature. To enter the regime where holes are minimal, we must ensure $T \ll T_F$. Explicitly, the entropy scales as $S \approx k_B N \pi^2 T/T_F$, as derived in Appendix C.

After our narrowline laser cooling, our ensemble is at $T = 2$ μK corresponding to $T/T_F \approx 2.0$ [107]. Although direct laser cooling to degeneracy with bosons has been achieved [106, 118, 119], these schemes generally require compression and re-thermalization techniques analogous to evaporative cooling and to my knowledge deeply degenerate Fermi gases ($T/T_F \leq 0.1$) have not been produced via laser cooling. To reach $T/T_F \ll 1$ on this experiment, we employ *evaporative cooling.*

The details of our evaporative cooling scheme are outlined in [120], so we will just provide a brief overview. The basic idea behind evaporative cooling is conceptually fairly simple [121]. Reducing the trap depth U_{trap}, hot atoms spill out of the dipole trap. Ensuring the system remains in thermal equilibrium, entropy is carried away with these lost atoms. The first challenge encountered in evaporative cooling of fermions is the Pauli exclusion principle. In order to enjoy s-wave[13] collisions at low temperature, non-identical fermions are required. This is generally achieved using ensembles with mixtures with different hyperfine states [122]. The optimization of evaporative cooling also requires ensuring that the elastic

[12] The chemical potential μ is perhaps the one variable in this formula lacking an immediate intuition. One could argue μ is the normalization constant ensuring $\sum_i n_i = N$ is satisfied.

[13] The only partial wave not frozen out at low temperature.

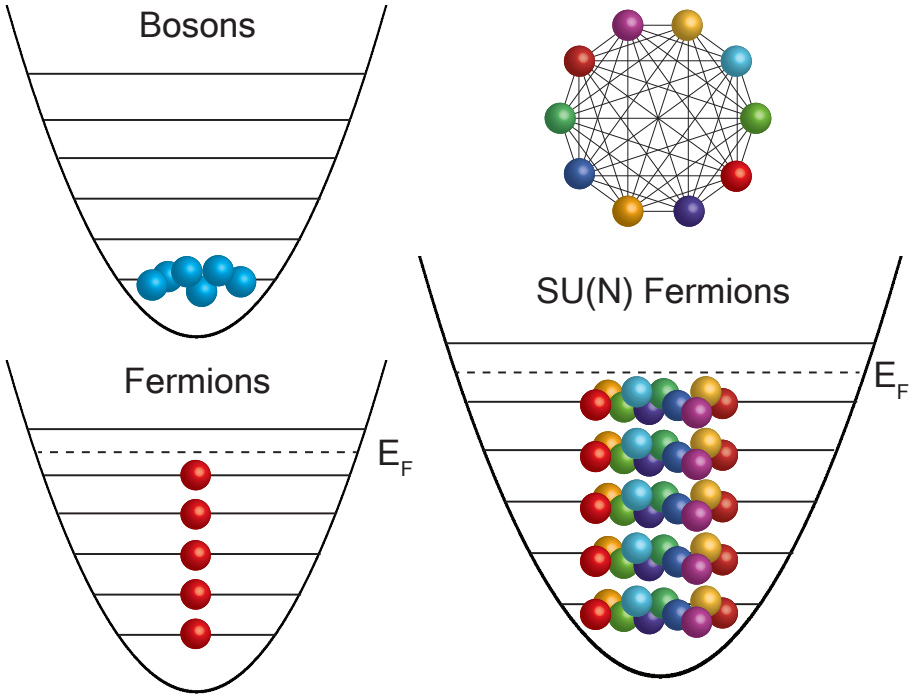

Figure 2.12: SU(N) fermions. For a $T = 0$ spin-polarized gas, bosons all occupy the ground motional state, while fermions occupy each rung of the harmonic oscillator up to the Fermi energy E_F. With an N-component Fermi gas, each spin component interacts with $N - 1$ collisional partners, strongly enhancing the interaction strength. Figure adapted from Ref. [107].

collision rate is large compared to any heating or loss rates in the system. This places an immediate additional challenge - the collision rate increases at high density but so does deleterious effects like the three-body loss rate. Strontium-87 is well suited to address both of these issues. First and foremost, the large nuclear spin manifold with ($N = 10$) states ensures that atoms have many different collisional partners as shown in Fig. 2.12. Second, the SU(N) symmetry from the $J = 0$ electronic ground state means that the nuclear and electronic degrees of freedom are decoupled and all nuclear spin states have an identical scattering length [123]. Finally, the three-body loss rate for ^{87}Sr in the electronic ground state is $K_3 = 2.0(0.2) \times 10^{-30}\text{cm}^3\ \text{s}^{-1}$ [71], lower than alkali counterparts like ^{87}Rb where $4.3(1.8) \times 10^{-29}\text{cm}^3\ \text{s}^{-1}$ [124]. Combining these pieces, highly degenerate Fermi gases can be prepared as depicted in Fig. 2.12. In addition, evaporative cooling with ^{87}Sr is highly

efficient and Fermi gases with $T/T_F \approx 0.2$ can be prepared with evaporation times < 1 second. This is highly relevant for optimizing clock stability, where dead time can limit clock stability.

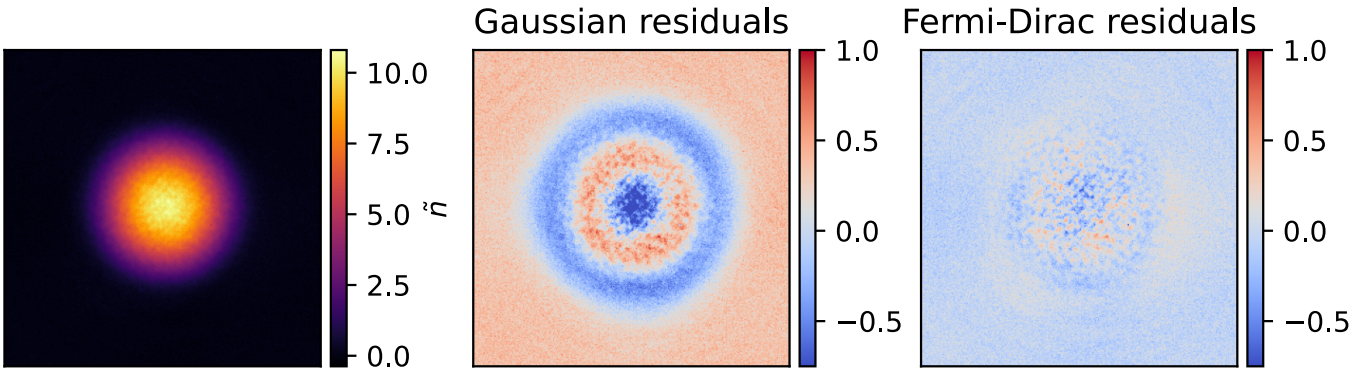

Figure 2.13: Non-interacting thermometry of an expanded Fermi gas. From the image in the left, we extract $T/T_F = 0.072(9)$. The 'ring' structure in the Gaussian residuals reflects the incompressible nature or Fermi pressure of the fermionic atoms; owing to the Pauli exclusion principle the density in the center of the cloud is smaller than prescribed by a Gaussian fit. When fit to the Fermi-Dirac distribution, residuals are strongly reduced.

Next we need to experimentally determine the degeneracy parameter T/T_F. Time-of-flight imaging provides a convenient, reliable method to extract this parameter. After ballistic expansion, the atomic distribution reflects the in-situ momentum distribution and the *shape* of the distribution determines T/T_F. To see this clearly, we write express the semi-classical phase-space distribution based on H defined above:

$$w(r,p;T,\mu) = \frac{1}{(2\pi)^3}\left\{\exp\left[\beta(\frac{p^2}{2m} + V_{har}(r) - \mu)\right]\right\}^{-1}. \tag{2.12}$$

This is a good approximation in the limit N is large and thus many states are occupied [125]. We note that the real space and momentum distributions can be determined from Eq. 2.12:

$$\begin{aligned} n(r;T,\mu) &= \int d^3p\; w(r,p;T,\mu), \\ p(r;T,\mu) &= \int d^3r\; w(r,p;T,\mu). \end{aligned} \tag{2.13}$$

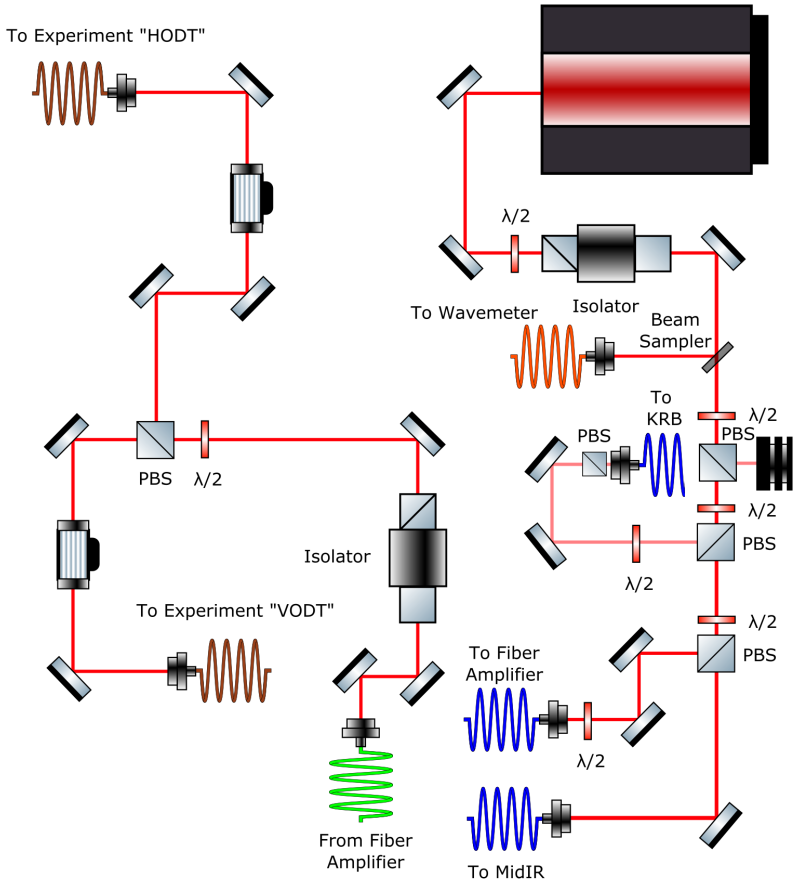

Figure 2.14: Optical dipole trapping laser system operating at 1064 nm. Given this laser is hundreds of THz detuned from any resonance and not applied during clock spectroscopy, it is one of the few lasers on the experiment that does not require frequency stabilization. We share this light with KRb and MidIR comb experiments in the Ye Lab. Photonic crystal fibers are important to ensure that stimulated Brilluoin scattering (SBS) is minimized.

We next consider ballistic expansion where $r \to r_0 - p_0\, t\,/\,m$ with r_0 and p_0 the trapped position and momentum of a particle and $V_{har} = \frac{1}{2} m\omega^2 r^2$. For simplicity, we just take the $r_0 = 0$ case. Then after expansion:

$$w(r,p;T,\mu) \quad \to \quad \frac{1}{(2\pi)^3}\left\{\exp\left[\beta\gamma(\frac{p^2}{2m} - \mu/\gamma)\right]\right\}^{-1}. \tag{2.14}$$

One sees the fugacity $\zeta = e^{\beta\mu}$ is unchanged under time-of-flight and rather the temperature and chemical potential μ are re-scaled by a factor $\gamma = 1 + \omega t^2$. Thus even in

time-of-flight measuring ζ can be used to determine in-situ degeneracy parameter T/T_F. Explicitly, $Li_3(-\zeta) = \frac{-1}{6(T/T_F)^3}$ and Li_n refers to a polylogarithmic function of order n. This re-scaling is more rigorously treated for all r in the following work [126].

We present time-of-flight images of our Fermi gas in Fig. 2.13. Here we use absorption imaging to extract the density distribution. We provide a detailed overview of imaging cold atoms in Chapter 5, including a description of the challenges of imaging dense clouds *in-situ*. We see that the atomic distribution after ballistic expansion is circular, reflecting the isotropic momentum distribution of non-interacting fermions. Note that the momentum distribution is completely independent of the trapping frequencies, unlike the *in situ* density distribution where the spatial aspect ratio of the cloud is determined by the ratio of trapping frequencies. Fitting ζ from the distribution in Fig. 2.13. we extract a $T/T_F = 0.072(9)$. In this analysis, we ignore interaction effects. These effects were modelled in [107], where interactions can be introduced to the Hamiltonian in Eq. 2.10 as a mean-field term of the form $V_{MF} = g(N-1)n(r)$ where $g = 4\pi\hbar^2 a/m$, $a = 97\mathrm{a}_0$ is the s-wave scattering length [127], $N = 10$, and $n(r)$ is from Eq. 2.13. Intuitively, the repulsive interactions mimic the Fermi pressure from quantum degeneracy and yield an erroneously low fitted T/T_F at the $10-20\%$ level for typical operating parameters. Thus a more conservative T/T_F to report would be < 0.1 for the data in Fig. 2.13. Exploring quantitative thermometry of interacting Fermi gases on this experiment with $T/T_F \ll 0.1$ could be a very fruitful future research direction.

To prepare our degenerate Fermi gas, we use the laser system depicted in Fig. 2.14. This laser system is very similar to those employed in many quantum gas experiments. We use a Mephisto NPRO to seed a fiber amplifier that can deliver 50 W of power at $\lambda = 1064\mathrm{nm}$. To avoid stimulated Brillouin scattering, we use photonic crystal fibers. Given this laser is hundreds of THz red-detuned from any resonance, there is no need to stabilize its frequency.

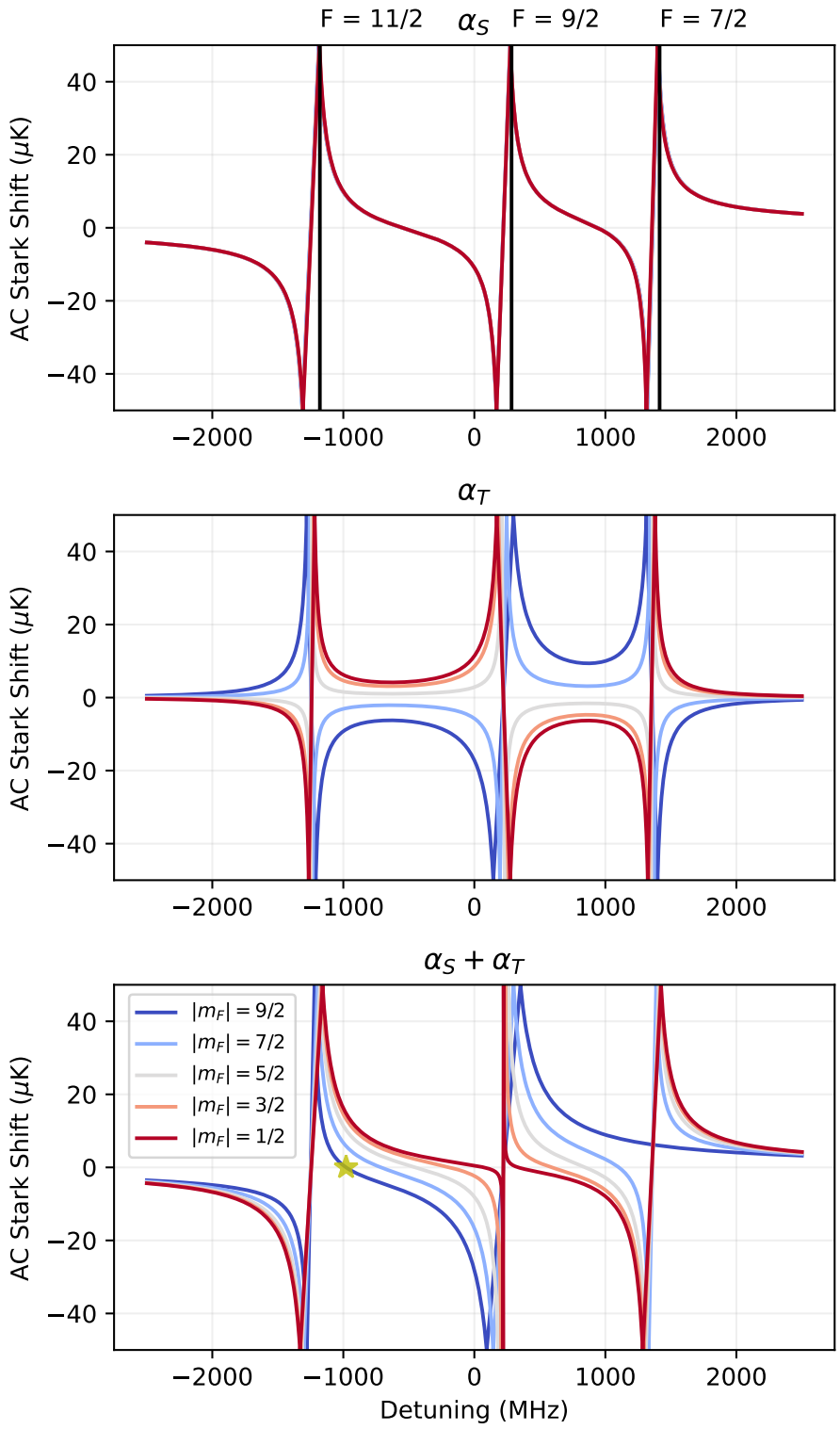

Figure 2.15: AC stark shifts from TenS^4 laser. Plot is centered around the bare $^3P_1$ transition in absence of hyperfine splitting. The net AC stark shift vanishes for the $m_F = 9/2$ state when the TenS^4 laser is ≈ 250 MHz blue-detuned from the F $= 11/2$ transition (highlighted with a gold star).

2.2.4 Nuclear-spin polarization

As displayed in Fig. 2.13, we nicely prepare highly degenerate Fermi gasses with $T/T_F \ll 0.1$ using all 10 nuclear spins. However, for the spin models in Chapter 1 we want to confine ourselves to a two-level system based on the ground ($^1S_0$) and clock ($^3P_0$) electronic states. Thus, we need to devise a scheme to *spin-polarize* our sample to have just a single nuclear spin state.

One option would be to turn on resonant light to pump the unwanted nuclear spins out of the trap. In concept, with a sufficiently large magnetic field that the Zeeman shifts between states are much larger than the $^3P_1$ linewidth, optical pumping might work. However, given $T/T_F \approx 0.1$, $T_F \approx 200$ nK and $T \approx 20$ nK, a single absorbed $^3P_1$ photon with $T_R = 460$ nK is disastrous! In practice, all attempts we made to achieve spin-polarizing with optical pumping resulted in substantial heating.

As we recall from Section 2.2.2, we can create blue-detuned traps that are highly repulsive. Thus another option is to design a potential that is highly repulsive for all m_F states except our target state. This can be achieved using the tensor shift m_F^2 dependence from Eq. 2.8 to get a strong, differential m_F shift. We call our spin-dependent potential, the 'Tensor Stark shift spin selector' (TenS^4).[14] To gain some intuition about how this scheme works, we plot the scalar and vector polarizabilities in Fig. 2.15. The scalar polarizability $\alpha_s(\omega)$ is fairly simple, and we see three discontinuities according to the three hyperfine manifolds calculated in Table 2.1. Including the tensor shifts $\alpha_t(\omega)$, we plot the total polarizability $\alpha(\omega) = \alpha_s(\omega) + \alpha_t(\omega)$. We see this admits a rich structure with many different zero-crossings in the total polarizability. For $|m_F| = 9/2$ state, $\alpha_s(\omega) = \alpha_t(\omega)$ at ≈250 MHz blue-detuned from the F $= 11/2$ transition, while the potential is strongly repulsive for other m_F states.

In practice, we found our TenS^4 scheme effectively removed $|m_F| = 5/2, 3/2, 1/2$ states

[14] 'Optical Stern Gerlach' is a more conventional name for this technique.

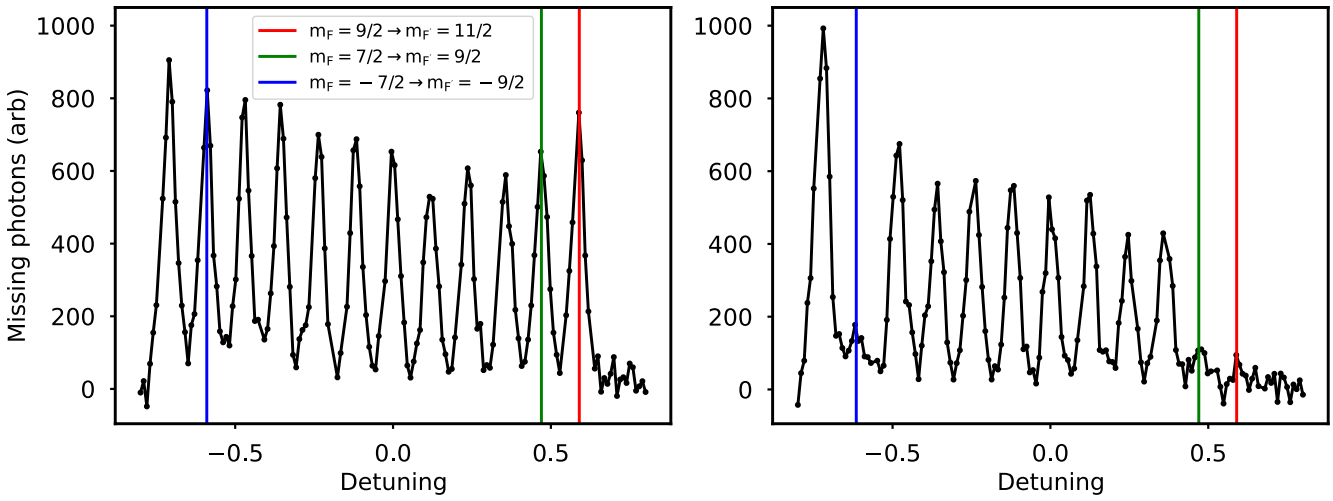

Figure 2.16: Absorption imaging on ${}^1S_0 \rightarrow {}^3P_1$ F $= 11/2$ transition. Spin populations are plotted **left** before and **right** after polarization via resonant pulses. We intentionally deplete the m_F states that experience a weak force from the TenS^4 potential.

with the strongest repulsive potential. We used optical pumping to remove the $|m_F| = 7/2$ and $m_F = 9/2$ states as depicted in Fig. 2.16. The spectroscopy presented here used red absorption imaging on ${}^1S_0 \rightarrow {}^3P_1$ transition, where application of a 5 G bias field allows individual m_F states to be spin resolved. Quantitative red absorption imaging is challenging, so the purpose of this measurement was just to ensure m_F populations are depleted. With $\approx$ kHz linewidth, untrapped atoms are quickly Doppler shifted out of resonance, requiring $I/I_{sat} \gg 1$ to scatter as many photons as possible. As detailed in Chapter 5, in this highly saturated regime the total atom number is just proportional to the number of 'missing' photons in the absorption beam.

While conceptually we have presented a dispersive, spin-polarized scheme, we still need to determine the residual heating from this potential and optimize its parameters to achieve the lowest T/T_F. This practically requires optimizing the pulse duration of our potential to balance fully depleting the unwanted m_F states and minimizing heating. This optimization is depicted in Fig. 2.17. The left panel shows the total atom number declining as atoms are pushed out of the ODT. The T/T_F as a function of pulse duration is plotted in the right

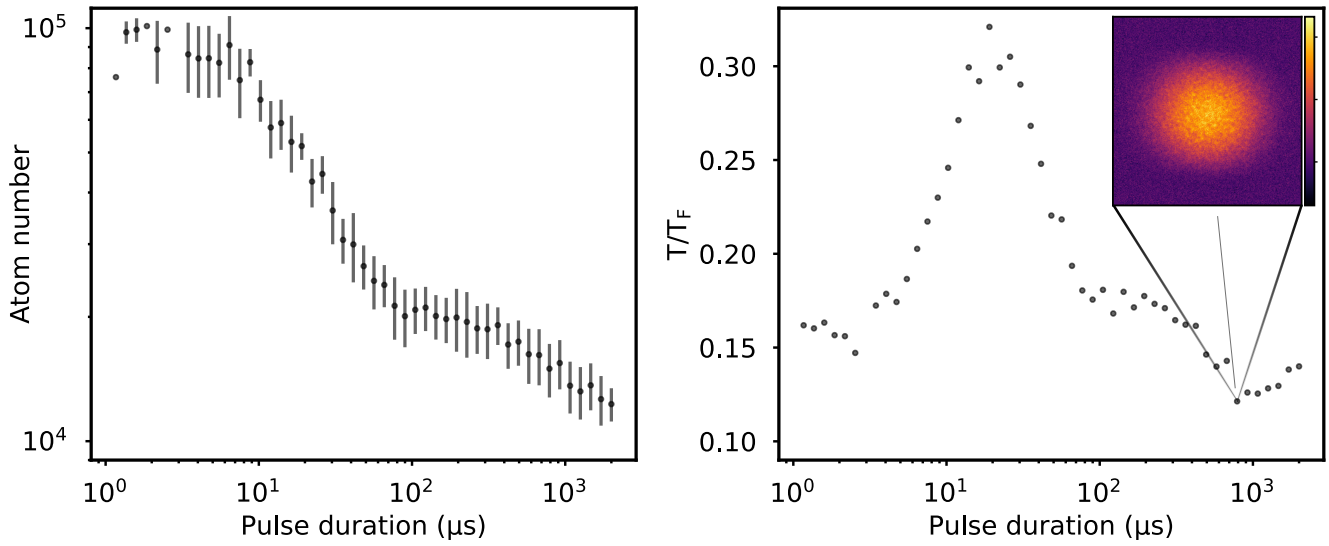

Figure 2.17: TenS^4 optimization as a function of pulse duration. If the pulse duration is not sufficiently long to fully deplete unwanted spins, they will remain trapped and collide with the $m_F = -9/2$ target state to cause heating. Choosing an optimal pulse duration of 750μs, we achieve $T/T_F = 0.15$.

panel. The peak in the T/T_F plot at intermediate pulse durations is a rethermalization effect - if the pulse is not sufficiently long to fully deplete unwanted spins, they will remain trapped and collide with the $m_F = -9/2$ target state to cause heating. Picking an optimal pulse duration of 750 μs, we achieve $T/T_F = 0.15$. As we will detail in Chapter 5, this T/T_F is sufficiently low entropy to admit lattice filling fractions $> 90\%$.

To create our TenS^4 potential, we use the laser system depicted in Fig. 2.18. The laser is a commercial Moglabs laser, that uses a high powered injection locked laser seeded by an IFDL. We lock the IFDL to a $\gamma \approx 1$ Hz linewidth laser stabilized to a ULE Fabry-Pérot cavity [37]. At slow timescales, we steer this laser to our silicon cavity via our frequency comb. A critical component of this laser system is a filter cavity to strip away resonant light ≈ 250 MHz detuned from the $F = 11/2$ transition. Given the frequency stability of our laser system is more than sufficient ($\gamma \ll \Gamma_{^3P_1}$)[15] , we lock the length of the filter cavity to our TenS^4 via a PDH feedback scheme [128] using the cavity piezo as the feedback actuator.

[15] As we are so detuned from resonance, this condition is likely not necessary.

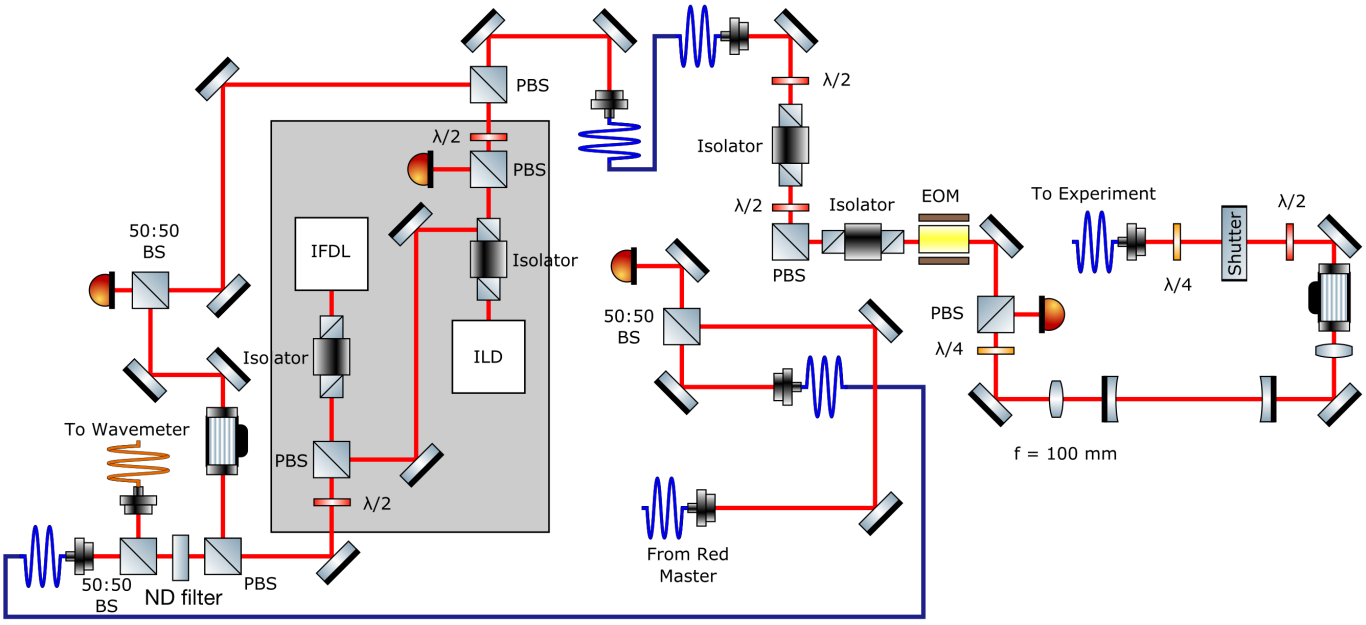

Figure 2.18: TenS^4 laser system. A Fabry-Pérot filter cavity is used to strongly suppress any residual light near resonance ≈ 250 MHz from the carrier. We lock the length of the filter cavity to our TenS^4 laser, prestabilized to a 1 Hz linewidth ULE stabilized laser [37], via a PDH feedback scheme using the cavity piezo as the feedback actuator.

We found that using this filter cavity was crucial to achieve $T/T_F = 0.15$.

Chapter 3

Three-dimensional optical lattice clock

In Chapter 2, we provided an account of the various trapping and cooling techniques required to prepare a highly degenerate Fermi gas. In this chapter, we can begin to focus on unique applications of our strontium quantum gas. As we will detail, trapping atoms in *optical lattices* formed with standing waves of light opens the door to study qualitatively new physics. Traditionally the so-called *Lamb-Dicke* regime was desired, where the lattice trapping frequency ν_{lat} is much larger than the recoil frequency shift ν_R allowing for coherent atom-light coupling without changing the atom's motional state. Alternatively, in real-space the motional extent of the atom's wavefunction $x_0 \approx \sqrt{h/m\nu_{lat}}$ is small compared to our clock probe wavelength.[1] However strictly speaking, so long as the sideband is spectroscopically resolvable ($\Omega \ll \nu_{lat}$), coherent electronic operations are still decoupled from changing the atom's motional state. Entering this tightly confined regime using optical lattices opens the door for coherent atom-light operations and motivates developing highly phase stable lasers to optimize interferometric sensitivity. As we will detail in this chapter, second-scale optical phase coherence requires lasers locked to ultrastable Fabry-Pérot cavities. The state-of-the-art optical phase stability to-date has been achieved with silicon cavities operating at cryogenic temperatures to minimize thermal-noise fluctuations [39, 40]. Combining these pieces, we demonstrate second-scale atom-light coherence using clock spectroscopy. These measurements motivated studies of atomic coherence in Chapter 6 to understand the inter-

[1] Yet another perspective is that the optical lattice and corresponding band structure strongly enhances the effective mass of the trapped atoms.

play of single-particle dephasing and interactions.

3.1 Overview

We use this section to provide an overview of the physics of atoms trapped in optical lattices. There are many excellent references that present the concepts of this section in full mathematical rigor [109, 75, 110]. Thus, the goal of this section is just to provide a conceptual physics intuition. The single-particle Hamiltonian is:

$$\hat{H}_{OL} = \frac{p^2}{2m} + U_0 \cos^2(kz). \tag{3.1}$$

U_0 is the lattice depth and typically expressed in units of the recoil energy $E_R = \frac{\hbar^2 k^2}{2m}$. One key assumption here is that this is a homogeneous system that extends to infinity. Extensions to the calculations in this chapter including effects of the harmonic confinement have been done [129]. $U_0 \cos^2(kz)$ is a periodic potential, allowing solutions for the wavefunction to be determined using Bloch's theorem. This tells us the solutions are of the form $\Psi_q^n(z) = e^{iqx}u^n(z)$. $u^n(z)$ is a function with the same periodicity as the lattice, and the values n and q refer to the Band index and quasimomentum respectively. These wavefunctions can be solved using the truncated Hamiltonian method from [130] and are plotted in Fig. 3.1. We see the solutions $\Psi_q^n(z)$ 'Bloch waves' are totally delocalized in real space.

Although we have arrived at the eigenstates of $\hat{H}_{OL}$, it is challenging to conceptually connect these delocalized Bloch waves to an intuitive picture of atoms in a lattice tunneling or colliding. A basis where atoms are localized to individual lattice sites indexed j would be more appropriate [110]. Here we transform to the Wannier basis:

$$W_j^n(z) = \frac{1}{C}\sum_q \Psi_q^n(z) e^{-iqj/\hbar}. \tag{3.2}$$

C is a normalization constant proportional to the number of quasimomentum q being summed. Although not eigenstates of $\hat{H}_{OL}$, this is still an orthonormal basis with only

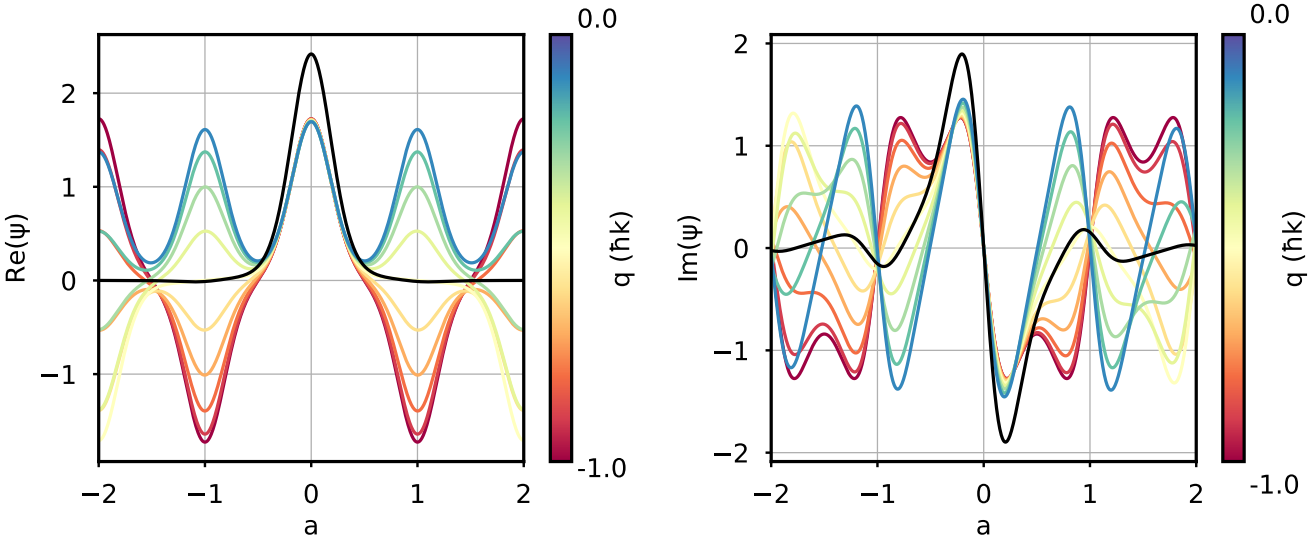

Figure 3.1: The solutions to the periodic potential in Eq. 3.1 are Bloch waves characterized by quasimomentum q. **Left** and **right** panels are wavefunctions for the ground band ($n = 0$) and first band ($n = 1$) respectively. Localized *Wannier* functions are plotted in black, arising from constructive and destructive interference of Bloch waves.

one Wannier function centered on a given lattice site. These Wannier functions are plotted in black in Fig. 3.1.

It is insightful to also examine the eigenenergies of Eq. 3.1. As plotted in Fig. 3.2, these eigenenergies form bands indexed n, each with a dispersion relation depending on q. We additionally plot the 'bandgap', the energy offset between bands, as a function of the lattice depth U_0. The bandgap increases and bands flatten (bandwidth is decreased) as lattice depth is increased. We compare the numerically solved bandgap with the trap frequency in the harmonic approximation $\nu_{lat,HO} = 2\nu_R\sqrt{\frac{U_0}{E_R}}$, in the conceptual limit that atoms are localized in deep, isolated traps. Although the harmonic approximation qualitatively captures the bandgap behavior, it misses an anharmonic correction of $-E_R(n+1)$ [131]. In the limit $U_0 \gg E_R$, this correction becomes increasingly negligible.

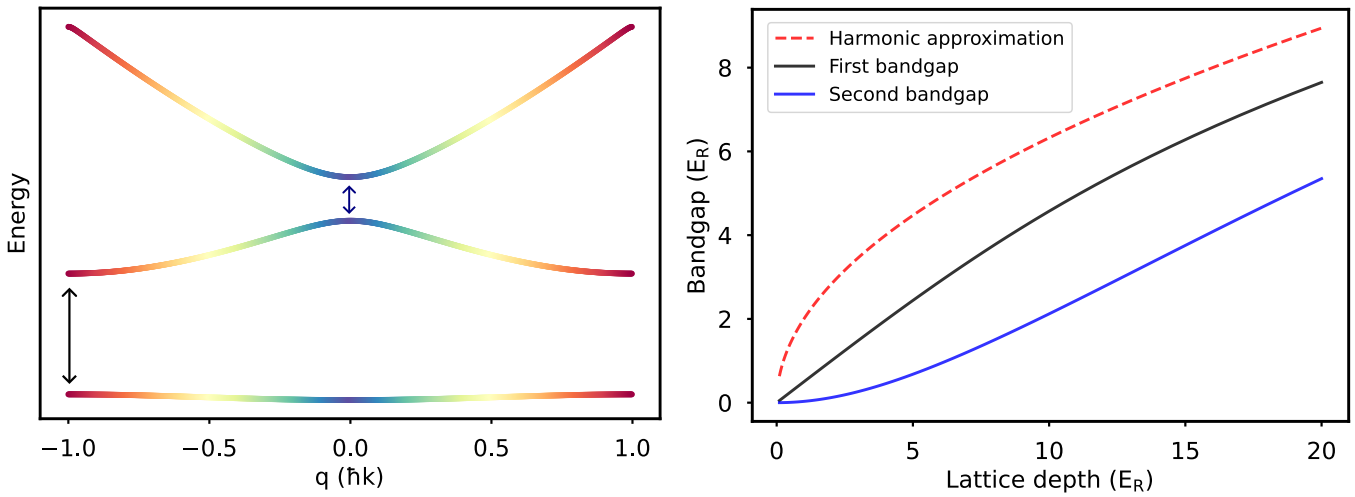

Figure 3.2: **Left:** Eigenenergies are plotted for wavefunctions in Fig. 3.1 for a lattice depth of 7 E_R. Energies have a dispersion relation depending on the quasimomenta q. **Right:** Bandgap is plotted as a function of lattice depth for the first (second) bandgap in black (blue). Bandgap increases and band flatten (bandwidth is decreased) as lattice depth is increased. The bandgap in the harmonic approximation $\nu_{lat,HO} = 2\nu_R\sqrt{\frac{U_0}{E_R}}$ is plotted with a red dashed line for comparison.

3.1.1 Lattice loading

From Fig. 3.1 and Fig. 3.2, we see optical lattices provide a geometry to confine atoms in localized traps where the motional extent of the atom's wavefunction is small compared to our clock probe wavelength. We also see in Fig. 3.1 that the $n = 0$ wavefunction is much more localized than the $n = 1$ band. In the optical lattice, ν_{lat} can easily exceed tens of kHz for realistic beam parameters, achieving the Lamb-Dicke condition $\nu_{lat} \gg \nu_R$. Transitioning from our Fermi gas where $\nu_{trap} \approx 100$ Hz to our optical lattice with $\nu_{lat} \approx 50$ kHz requires an involved adiabatic loading procedure to minimize heating and ensure all atoms are loaded into the ground $(n = 0)$ band.

Our evaporative cooling and lattice loading procedure is depicted in Fig. 3.3. In the top panel, we plot the trapping frequencies ν_{trap} of our horizontal and vertical dipole traps, HODT and VODT respectively. From $T = 0 \rightarrow 4$ seconds, we are performing a standard forced evaporation sequence arriving at a spin-polarized Fermi gas using the techniques

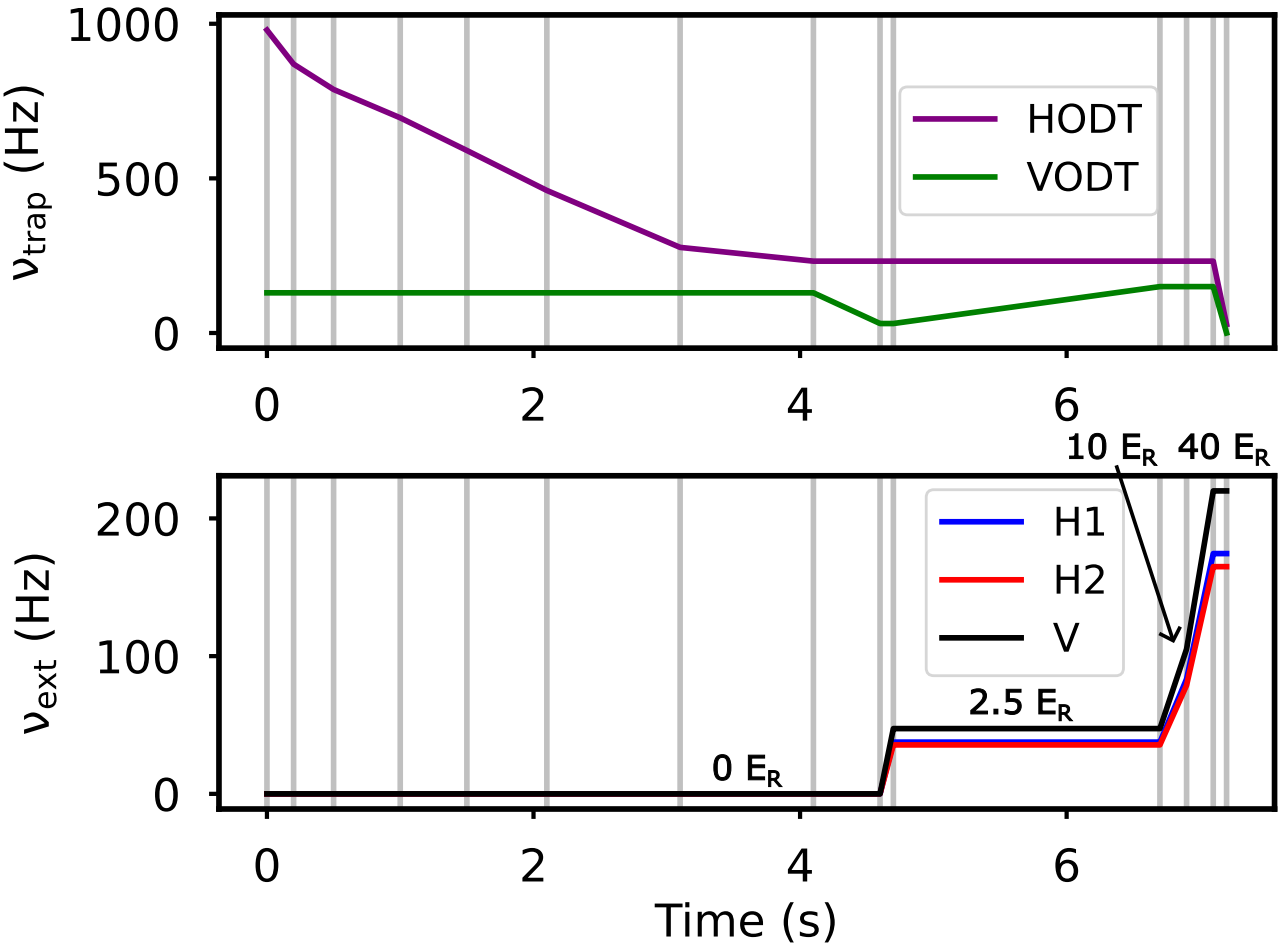

Figure 3.3: Lattice loading sequence. **Top:** Trapping frequencies ν_{trap} for our optical dipole trap during evaporative cooling and lattice loading. **Bottom:** External confinement frequencies ν_{ext} for lattice beams during loading. Trap depths in E_R are labelled in plot.

reported in Chapter 2. During this sequence, the optical lattice is turned off.

When turning on the lattice, we need to carefully consider the lattice band structure. The calculations above are for a 1D lattice (i.e. Eq. 3.1 is just a function of x). While the wavefunctions and eigenenergies are fully separable so the 3D wavefunction and eigenenergies are trivial to calculate[2] , one needs to be mindful that for the first excited band with two $n = 0$ and one $n = 1$ Bloch states the eigenenergy for certain quasimomenta is lower energy

[2] $|\psi\rangle = |\psi(x)\rangle \otimes |\psi(y)\rangle \otimes |\psi(z)\rangle$

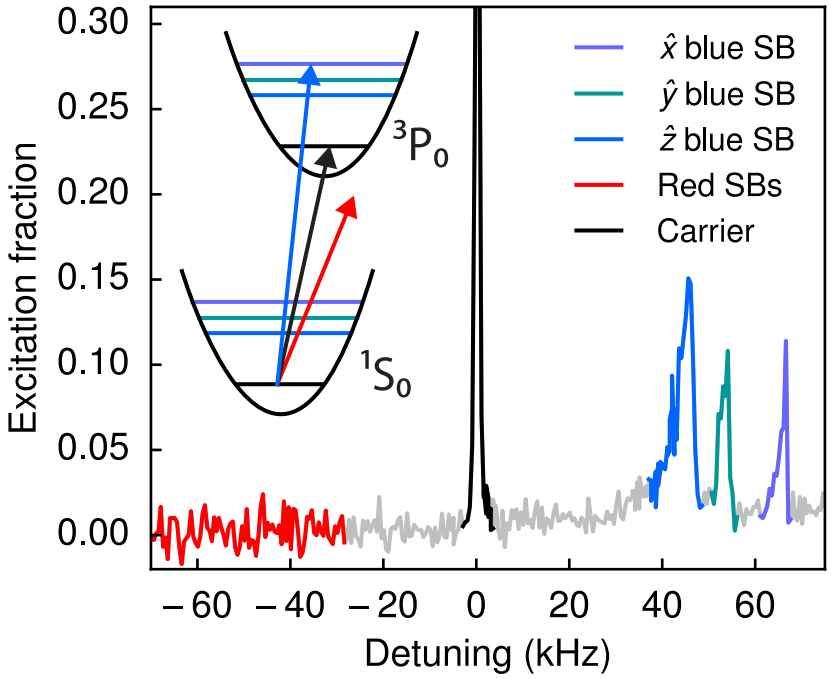

Figure 3.4: Sideband spectroscopy. No observable red sideband indicates atoms are nearly entirely in the ground motional state ($\bar{n}_x, \bar{n}_y, \bar{n}_z \approx 0$). Figure reproduced from [33].

than the ground band (all $n = 0$ Bloch states) [132]. Thus in a 3D lattice, the bandgap only starts to open at $2.24E_R$. To avoid populating higher bands, we strongly reduce the Fermi energy by decompressing the VODT before even turning the lattice on. Next, we ramp the lattice from $0E_R$ to $2.5E_R$. With the ground and first band no longer degenerate, we strongly compress the VODT to reach high density in the center of the combined dipole trap and lattice potential. This compression stage in the combined potential is motivated to 'mode-match' to the final density distribution in the lattice to minimize mass transport. Once the lattice depths are above $2.24E_R$, we are more flexible in terms of lattice ramping. We ramp to $10E_R$, then to the final operational trap depth, generally in 200 ms steps. Additionally, the Gaussian intensity profile of our transverse optical lattice beams $\mathrm{w}_j, \mathrm{w}_k$ introduces an 'external confinement': $\nu^2_{ext,i} = \frac{2E_R}{m}\left(\frac{2U_{0,j}-\sqrt{U_{0,j}}}{\mathrm{w}_j^2} + \frac{2U_{0,k}-\sqrt{U_{0,k}}}{\mathrm{w}_k^2}\right)$. This formula includes the change in ground state energy as the laser intensity decreases from the trap center, requiring

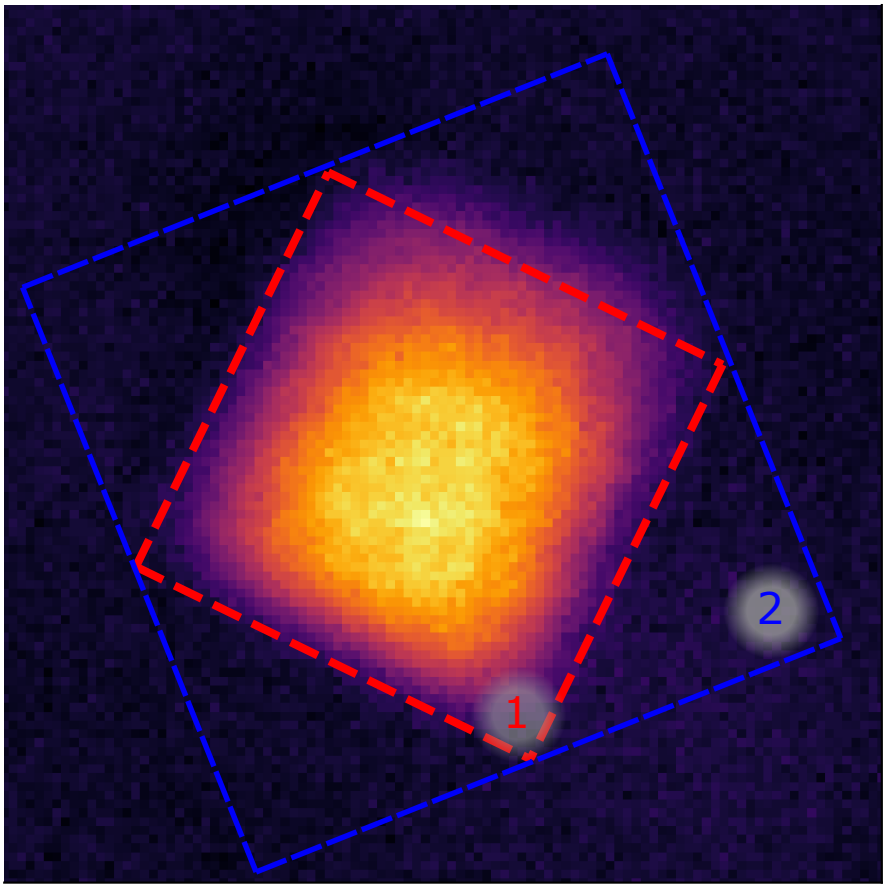

Figure 3.5: 'Band mapping' provides a complementary measurement to examine the band populations. Square density distribution indicates that atoms are in the ground band or '1st Brillouin Zone'. Slight assymetry is likely due to vertical lattice being tilted with respect to imaging system.

a $-\sqrt{U_0}$ correction. The external confinement frequencies ν_{ext} for lattice beams are plotted for comparison with ν_{trap} in Fig. 3.3.

Next we need to confirm if we populated any higher bands during our lattice loading procedure. 'Sideband' spectroscopy with our clock transition is a very convenient tool to quantitatively measure higher band populations. As depicted in Fig. 3.4, we drive trapped atoms on the ${}^1S_0 \rightarrow {}^3P_0$ transition. In addition to the $h\nu_{clock}$ energy required to excite an atom to ${}^3P_0$, an additional $+h\nu_{lat}$ ($-h\nu_{lat}$) of energy will drive a 'blue' ('red') sideband exciting an atoms to the $n+1$ ($n-1$) motional state. Atoms in the ground motional state

can only be driven by the blue sideband. No observable red sideband indicates atoms are nearly entirely in the ground motional state ($\bar{n}_x, \bar{n}_y, \bar{n}_z \approx 0$).

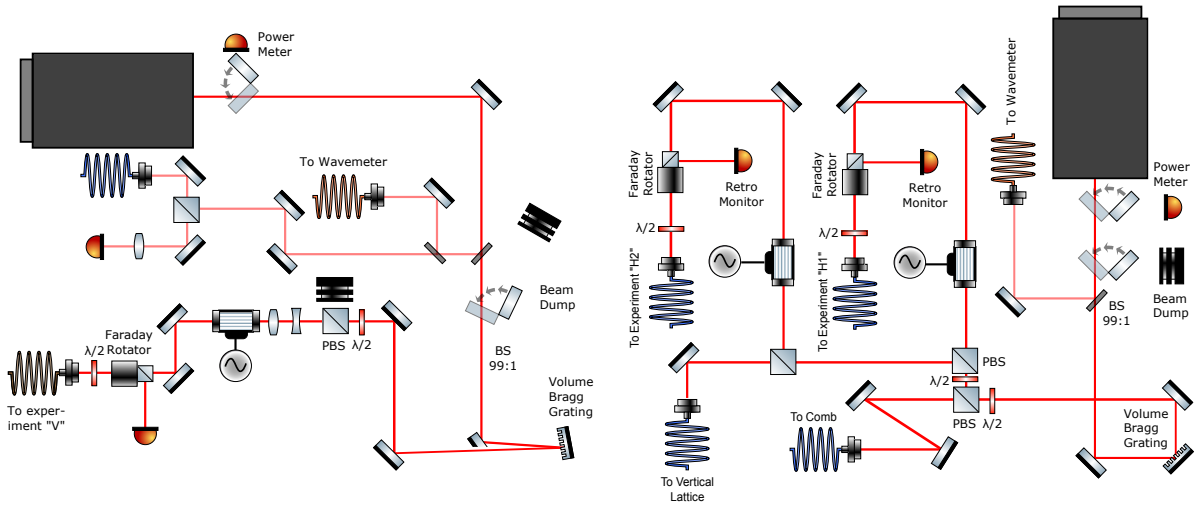

Figure 3.6: Lattice laser systems. Both vertical and horizontal lattices use commercial fiber lasers from Prescilaser. **Left:** Vertical lattice laser system. **Right:** Horizontal lattice laser system. Horizontal lattice is frequency stabilized to frequency comb referenced to silicon cavity. Vertical lattice laser is frequency stabilized to horizontal lattice laser via heterodyne detection. Volume Bragg Grating (VBG) is employed on both systems to remove any residual light that may cause detrimental AC stark shifts.

An alternative method called 'Band mapping' can also be used to examine the band populations. This is more conventionally employed on optical lattice experiments without the spectroscopy properties of strontium. We adiabatically lower the lattice depth so the quasimomentum q is conserved. After ballistic expansion we probe the momentum distribution as expressed in Chapter 2. As displayed in Fig. 3.5, the square shape reflects the maximum quasimomentum of $\pm\hbar k$ in the ground band. While this method is not as quantitative as using coherent spectroscopy in Fig. 3.4, it serves as an independent confirmation of our band populations. The laser systems used to create our optical lattice is displayed in Fig. 3.6.

Although we have confirmed that we load all atoms into the ground band, residual

heating processes can still drive atoms to higher motional states. These heating processes can place limitations on the achievable coherent spectroscopy times. The predominant mechanism is parametric heating from trapping laser intensity fluctuations:

$$\Gamma_{n\pm2\leftarrow n} = \frac{\pi^2}{8}\nu_{trap}^2 S_I(2\nu_{trap})(n+1\pm1)(n\pm1). \tag{3.3}$$

In Fig. 3.7, the parametric heating rates $\Gamma_{2\leftarrow0}$ are plotted for our optical dipole trap and optical lattice lasers. Following the techniques outlined in Ref. [133], we use low amplitude-noise VCOs to provide the RF drive for our trapping laser AOMs and tune the intensity feedback loop to avoid any appreciable servo bump near $2\nu_{trap}$. With some care to avoid technical resonances when lattice loading, $\Gamma_{2\leftarrow0}$ can be much less than any timescale of interest including the clock state $\Gamma_{^3P_0}$.

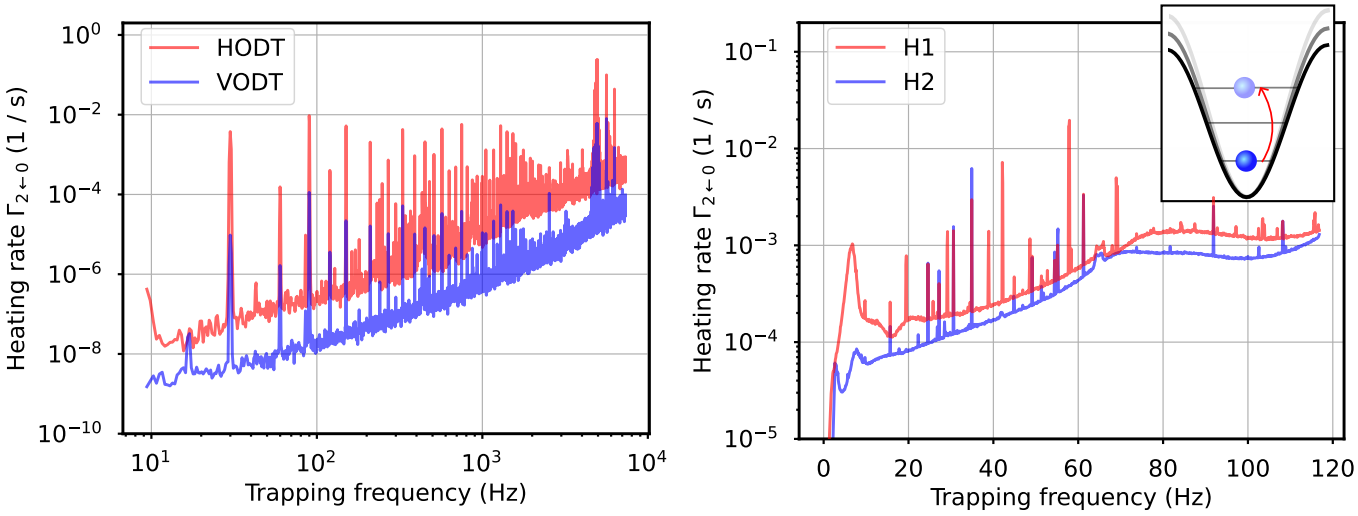

Figure 3.7: Parametric heating rates $\Gamma_{2\leftarrow0}$ are plotted for optical dipole trap **left** and optical lattice laser **right**. Note that given $\Gamma \propto \nu_{trap}^2$, the heating rates are substantially lower for the optical dipole trap.

As a final confirmation of our optical lattice performance, we measure the lifetime of trapped ground state atoms in Fig. 3.8. Parametric heating from our optical lattice lasers and the finite lifetime of our vacuum chamber can both lead to loss. The atoms are held in

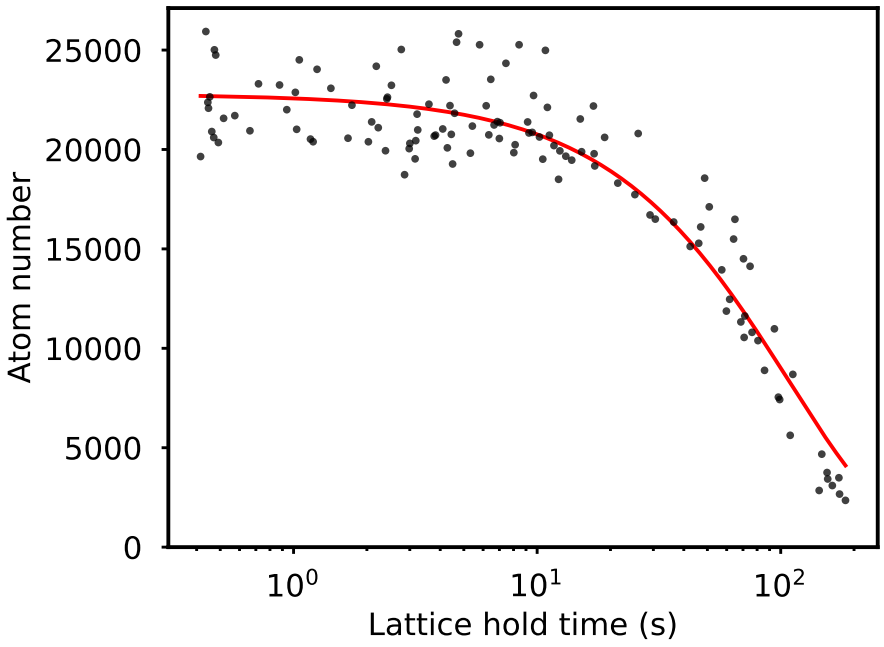

Figure 3.8: $^1S_0$ lattice lifetime. The atoms are held in a deep 3D lattice and the atom number loss is measured as a function of hold time. In this measurement $V_{\perp,1} = 66.5E_R$, $V_{\perp,2} = 69.9E_R$, and $V_z = 43.7E_R$. A 1/e time of 108(5) seconds is fit to the data. The atom loss is likely limited by a combination of parametric heating from the optical lattice and the vacuum lifetime. This technical loss timescale is long compared to all dynamics studied in this thesis.

a deep 3D lattice and the atom number loss is measured as a function of hold time. A 1/e time of 108(5) seconds is fit to the data.

3.2 Clock spectroscopy: Putting it all together

From the previous section, we confirmed that we load atoms into our 3D lattice in the ground motional band with high fidelity ($\bar{n}_x, \bar{n}_y, \bar{n}_z \approx 0$). This allows us to make a convenient assumption not afforded to 1D lattice clocks - all atoms are in an identical motional state. Next, we transition into a description of coherently addressing the electronic states of our strontium atoms. From Section 2.2.2, we discussed how the trapping for each electronic state $|i\rangle$ is dictated by the polarizability $\alpha_i(\omega)$. To achieve state insensitive trapping, we operate

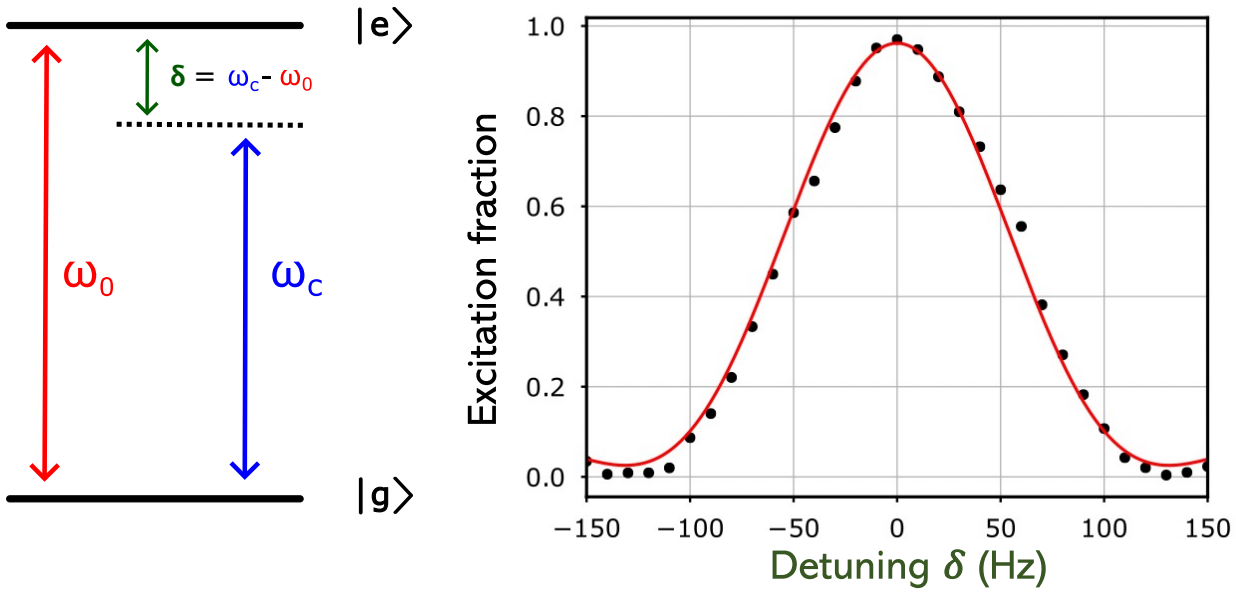

Figure 3.9: Rabi spectroscopy. Here ω_0 is the energy difference between our ground and clock states, and ω_c is the frequency of our optical local oscillator. Varying the detuning $\delta = \omega_c - \omega_0$ with a π pulse area, a spectroscopic feature is resolved with full-width at half-maximum inversely proportional to the pulse duration duration $\Delta\nu \approx 0.8/T_{pulse}$.

at the 'Magic' frequency where $\alpha_{^1S_0}(\omega) = \alpha_{^3P_0}(\omega)$ at $\lambda_{magic} = 813$ nm. Addressing the vector and tensor shifts in a 3D lattice was solved in [33], where a correct choice of lattice polarizations and detunings can cancel the scalar and tensor shifts for all beams. Vector shifts are nominally zero for all linear-polarized beams and further suppressed by the $\mathbf{k} \cdot \mathbf{B}$ term for two of the lattice beams. Operating at the magic wavelength allows another convenient assumption, as we can treat electronic and motional degrees of freedom as decoupled. That is we can write the wavefuction of all N atoms in the lattice as:

$$|\psi\rangle = \Big((\alpha\,|g\rangle + \beta\,|e\rangle) \otimes |n_x = 0, n_y = 0, n_z = 0\rangle \Big)^{\otimes N}. \tag{3.4}$$

With Eq. 3.4 in mind and the atoms prepared in our choice motional state, we next ask how we dynamically change the electronic portion of wavefunction? As depicted in Fig. 3.9, the dynamics with a coherent clock drive can be understood from a driven, two-level system.

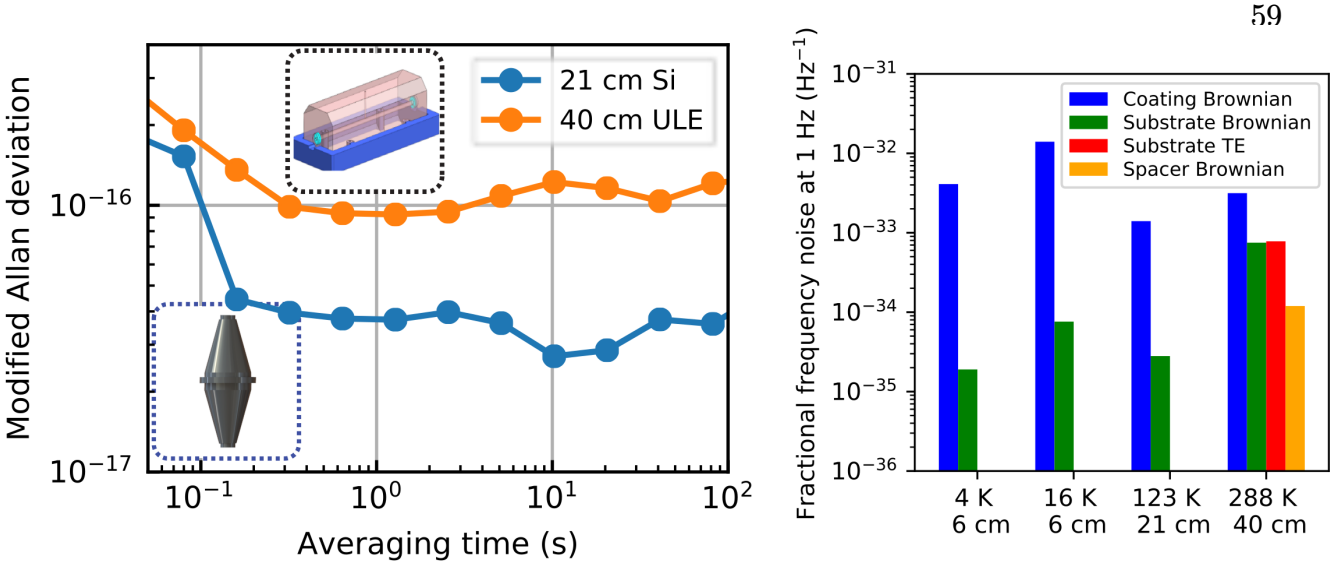

Figure 3.10: **Left:** Modified Allan deviation for both our room-temperature 40 cm ULE cavity and 21 cm silicon cavity operating at 124 K. Both cavity systems frequency noise is limited by thermal noise arising from Brownian motion of the amorphous (SiO_2/Ta_2O_5) mirror coatings. **Right:** Fundamental noise terms for ULE and Si cavities are tabulated for a number of system parameters. The improved mechanical properties of Si (i.e. Spacer Brownian, Subtrate Thermoelectric, Subtrate Brownian noise terms are negligible) and the reduced operational temperature compared to ULE realize a lower thermal noise floor as depicted **left**.

Here, ω_0 is the energy difference between our ground and clock states, ω_c is the frequency of our optical local oscillator, and the detuning $\delta = \omega_c - \omega_0$. The coupling between $|g\rangle$ and $|e\rangle$ is characterized by the Rabi frequency Ω_0. We judge the fidelity of rotations by the excitation fraction $p_e = \frac{N_g}{N_g+N_e}$, where N_g (N_e) refers to the number of atoms in the ground (excited) state satisfying $N = N_g + N_e$. On resonance ($\delta = 0$), we use a 'π pulse' duration T_{pulse} to achieve nearly unity excitation so $\Omega_0 T_{pulse} = \pi$. As a function of detuning, p_e varies as:

$$p_e(\delta) = \frac{\Omega_0^2}{\Omega_0^2 + \delta^2} \sin\left(\frac{\pi\sqrt{\Omega_0^2 + \delta^2}}{2\Omega_0}\right)^2. \tag{3.5}$$

In order to achieve high fidelity clock operations, minimizing temporal perturbations to both the atomic energy splitting ω_0 and the optical local oscillator frequency ω_c is imperative. We will detail studies of perturbations to the atomic resonance frequency ω_0 on this platform

in Chapter 6. The Rabi frequency Ω_n on the carrier transition ($|g,n\rangle \rightarrow |e,n\rangle$) depends explicitly on the motional state n and Lamb-Dicke parameter $\eta^2 = \frac{\nu_R}{\nu_{trap}}$ via:

$$\Omega_n = \Omega_0(1 - \eta^2 n) \tag{3.6}$$

We see from Eq. 3.5 that to optimize spectroscopy resolution, we need to extend our pulse duration T_{pulse}. Explicitly the full-width at half-maximum of our Rabi lineshape is $\Delta\nu = 0.8/T_{pulse}$. Practically this requires engineering lasers with optical coherence times commensurate with T_{pulse}. The purpose of this section is to outline synthesizing this optical local oscillator and delivering phase coherent light to atoms trapped in our 3D lattice.

3.2.1 Ultrastable laser systems

Currently, the state-of-the-art performance for optical local oscillators is achieved using lasers locked to Fabry-Pérot cavities. Using ultra-low-expansion (ULE) cavities, one can routinely achieve Hz-level linewidths [36, 37, 38]. Recently, cryogenic silicon cavities have surpassed these ULE cavities achieving linewidths as low as 8 mHz [39, 40]. Dating back to Eq. 1.1 in Chapter 1, we pointed out that the Allan deviation is an appropriate measure of a clock or local oscillator's frequency noise. In Fig. 3.10, we plot the modified Allan deviation for both our 40 cm ULE cavity and 21 cm silicon cavity operating at 124 K. Both of these cavities are *thermal-noise-limited*. That is, all technical noise terms have been sufficiently suppressed that the frequency noise is limited by thermal fluctuations of our mirror coatings. This 'thermal-noise' depends on the cavity temperature T, the coating loss angle $\phi_{coat.}$ and the Fourier frequency f and can be directly expressed in terms of a power spectral density: $S^{coat.}(f) \propto k_B T \phi_{coat.}/f$. Silicon has a coefficient of thermal expansion (CTE) zero-crossing at $T = 124$ K, and thus allows operation at lower temperatures than room temperature afforded to ULE cavities. This reduced thermal noise directly translates into extended light coherence times as quantitatively studied in [39].

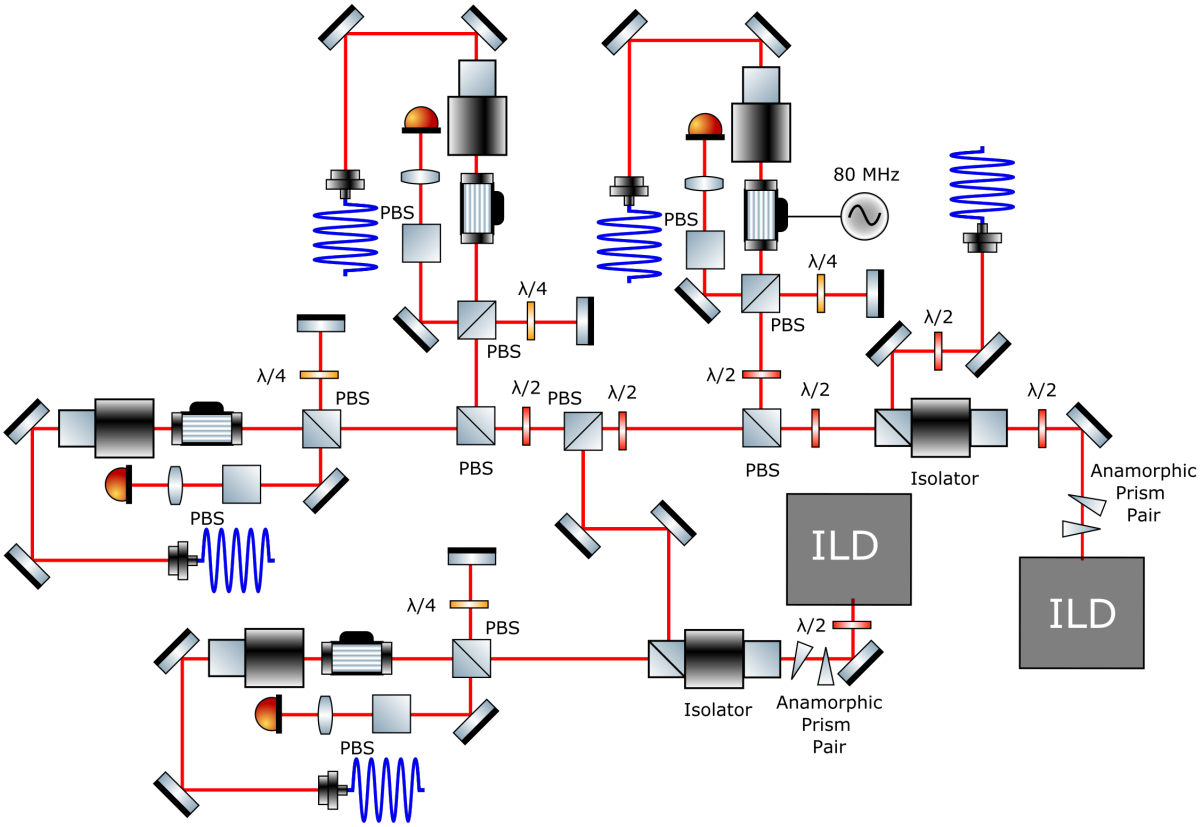

Figure 3.11: Distribution center layout is plotted. Light from the 40 cm ULE cavity seeds injection-locked diodes (ILD). Additive noise from injection locking is negligible with respect to the silicon cavity noise model as verified in Fig. 3.12. To distribute phase-stable laser light to many different experiments, fiber noise cancellation (FNC) is employed, where a Michelson interferometer is used to detect additive fluctuations to be removed via feedback.

Our 124 K silicon laser system along with the stability transfer to 698 nm is well documented in [40, 120]. In summary, although the strontium clock transition is at $\lambda_{clock} \approx$ 698 nm, silicon is opaque at this wavelength. However silicon is transparent at 1.5μm, where commercial telecommunication lasers with free-running linewidths of $\approx$ 1 Hz can be purchased. To transfer this frequency stability, we lock the repetition rate of a frequency comb to our silicon cavity. Thus the tooth of our comb closest to λ_{clock} is an optical tone with the stability properties of our silicon cavity. We can conveniently lock our 40 cm ULE system to this tone at low bandwidth. An overview of this stability transfer scheme is provided in

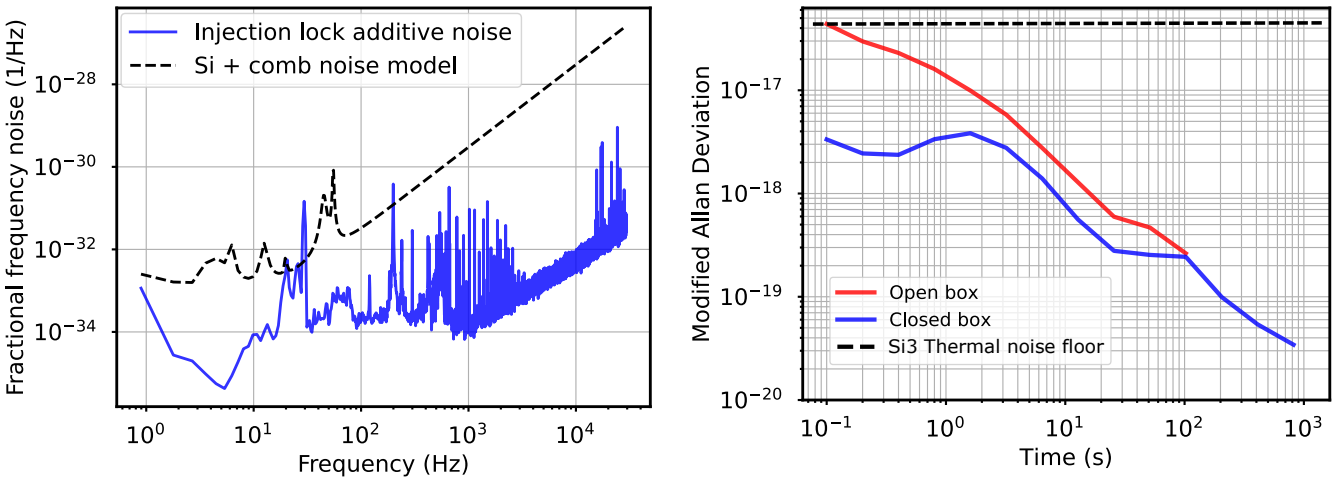

Figure 3.12: **Left:** The additive noise of injection locking was measured by beating the seed light with the output of the injection locked diode. An AOM was used to shift the frequency to enable a heterodyne measurement, avoiding technical noise close to DC. Additive noise is well below the silicon noise model from [40] for essentially all Fourier frequencies. **Right:** Measurement of additive noise from distribution center via beating two independent FNC loops. Closing the box surrounding the distribution center optics is important to fully suppress high frequency noise below the Si3 thermal noise floor.

Chapter 4.

While the excellent frequency stability of our silicon cavity is well-calibrated, the next task is to distribute this light to our experiment, as well as the other clocks in JILA. Distributing this light while adding negligible noise to our optical carrier is not trivial and each link of our frequency chain needs to be careful calibrated. The optical layout for our 'distribution center' is depicted in Fig. 3.11. Light from the 40 cm ULE cavity seeds injection-locked-diodes (ILD). To distribute phase-stable laser light to many different experiments, fiber noise cancellation (FNC) is employed, where a Michelson interferometer can be used to detect additive fluctuations through optical fibers to remove via feedback [134]. One of these paths is used to lock our 40 cm ULE cavity to the optical frequency comb [40].

The purpose of the injection locked diodes is to optically amplify our clock laser while adding minimal frequency noise. We measured the additive noise from the injection locking

process as plotted in Fig. 3.12. For this measurement, we beat the seeding light with the optically amplified light via a heterodyne beat offset with an AOM. Thus, any differential noise between the seed and amplified light will appear on this beat. This heterodyne technique is designed to decouple our measurement from different noise sources at low frequency (e.g. 60 Hz noise, ground loops, vibrations, temperature fluctuations). The additive noise is well below the silicon noise model from [40] for essentially all Fourier frequencies.

3.2.2 Vertical clock path

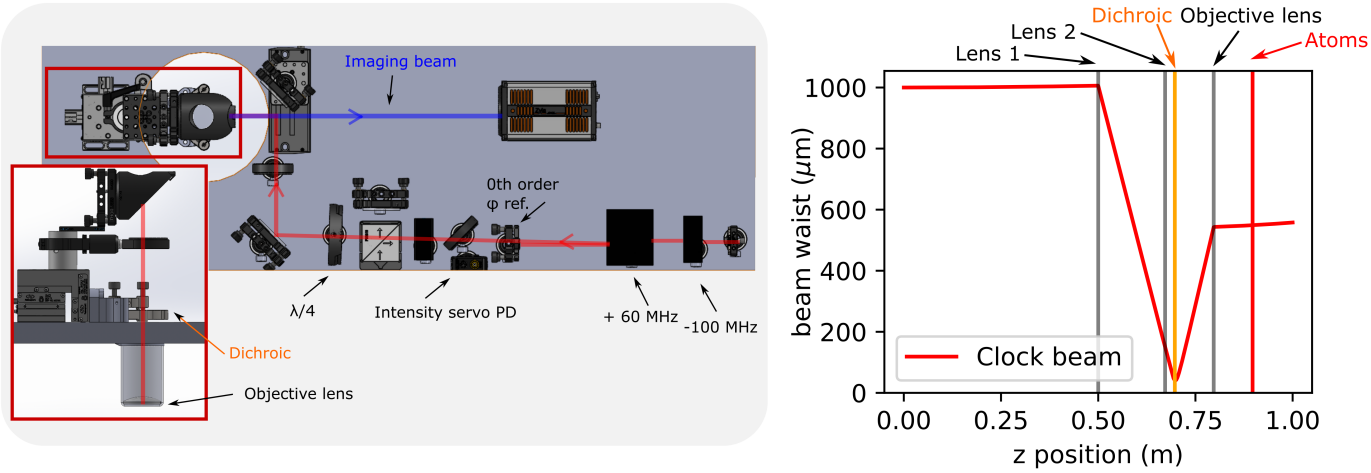

Figure 3.13: **Left:** The optics layout for our vertical clock laser. Clock light propagates colinear with the MOT and imaging beams. **Right:** Clock beam propagation. The Gaussian beam is focused at the dichroic to achieve the necessary retro condition for FNC. The laser beam size at the atoms is $\approx 300\mu$m, corresponding to a maximum Rabi frequency inhomogeneity of 1% across the cloud as confirmed in Fig. 6.27

We next need to deliver our amplified, phase-stable clock light to our trapped atoms. To remove any additive noise during the light delivery using the interferometer depicted in Fig. 3.11, we want to retro-reflect light from a phase reference as close to atoms as possible. We achieve this phase reference by using a single dichroic optic as both the lattice retro-reflector and clock reference. Our optics layout for our clock path is displayed in Fig. 3.13.

The clock beam is delivered to atoms by traversing through our vertical imaging system.[3] Both the 0th and 1st diffracted orders of our 60 MHz AOM are employed for FNC. The 1st order is the light that is ultimately shined on the atoms, while the 0th order provides an additional convenient phase reference that is never extinguished. We use a sample-and-hold technique detailed in [120] to engage the 1st order servo when turning on our clock drive.

One convenient attribute of our 3D lattice is that we achieve the Lamb-Dicke condition in all three axes, relaxing constraints about clock laser alignment. This can be contrasted to 1D lattice clocks, where atoms are very weakly confined ($\nu_{trap} \approx 100$ Hz) in the radial direction and great care must be taken to make the 1D lattice and clock highly co-linear [131]. We also plot the clock beam size in Fig. 3.13. To achieve the retro-reflection condition necessary for FNC, the beam must be focused at the dichroic. This leads to a beam size of $\approx 300\mu$m at atoms. Given a cloud size of 30μm, we expect a maximum Rabi frequency inhomogeneity of 1% across the cloud as confirmed with measurements in Chapter 6.

To judge the performance of our 1st order FNC, in Fig. 3.14 we plot the in-loop error signal with both feedback engaged and disengaged. When disengaged, we observe a large amount of low-frequency noise likely from path length fluctuations. Given our clock light is sent through a MOT optics path including optics on large posts 6" above the ground, this is perhaps not so surprising. When locked, we suppress this noise to well below the silicon noise model from [40].

For reference, the measured coating curves for the objective lens and dichroic are plotted in Fig. 3.15. Vertical lines are for 461, 689, 698, and 813 nm respectively. All beams are designed to pass through objective, with transmission $T > 99\%$. The dichroic was designed to retro-reflect the lattice light at 813 nm and transmit other beams. Thus, for our clock retro-reflection we rely on a percent-level reflection. While using a single optic as both the lattice and clock retros would appear to be a perfect solution, there is one technical constraint - the dynamic range of clock optical power is fairly limited, placing limitations

[3] A detailed description of this imaging system is provided in Chapter 5.

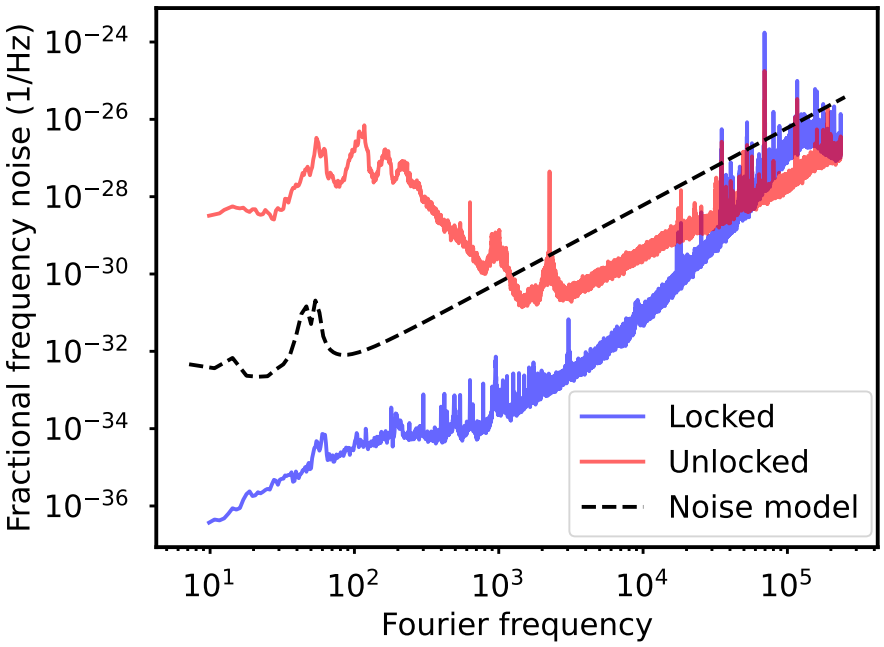

Figure 3.14: The in-loop error signal for our 1st order fiber noise cancellation setup. When disengaged, we observe a large amount of low-frequency noise from path length fluctuations. When the feedback loop is engaged the in-loop error signal, and thus any uncancelled noise, is well below the silicon noise model from [40].

on the usable Rabi frequency $\Omega \propto \sqrt{I}$. To achieve Hz-level clock spectroscopy, one needs to use optical powers $\ll 1$ nW while still retroing enough optical power to perform FNC with high SNR. Usually this is accomplished by having two distinct optics for the lattice retro and clock phase reference, placed in a hermetically sealed box so relative length fluctuations between them are negligible. Then, an ND filter can be inserted between these optics to attenuate the optical power as much as desired. A different spectroscopy method to achieve high sensitivity, which we will present in the next section, is *Ramsey* spectroscopy. Here the sensitivity is determined from the dark time T_{dark} where the light is extinguished, avoiding constraints for operating with a low Rabi frequency.

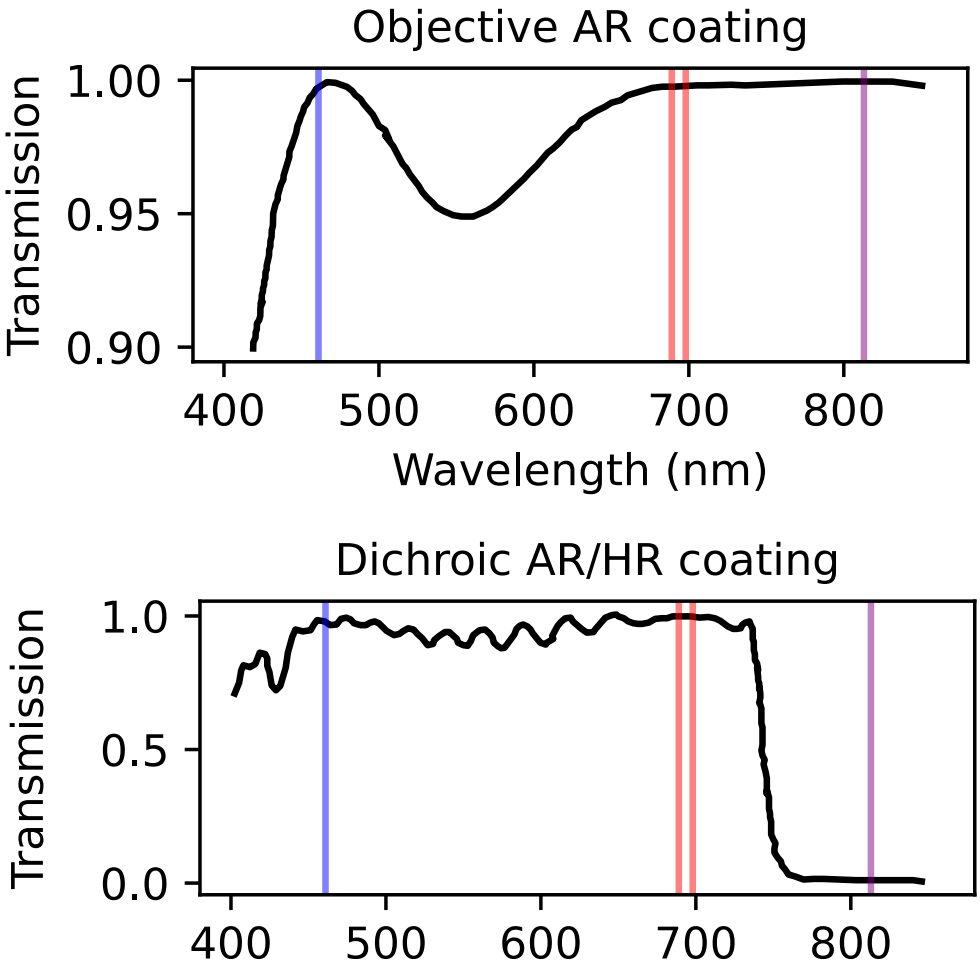

Figure 3.15: Measured coating curves for the objective lens and dichroic. Vertical lines are for 461, 689, 698, and 813 nm. All beams are designed to pass through objective with transmission $T > 99\%$ in **top**. The dichroic is designed to retro-reflect the lattice at 813 nm and transmit other beams as plotted in **bottom**.

3.2.3 Second-scale coherent spectroscopy

Finally, we combine the ground motional state lattice loading and ultrastable laser synthesis for clock spectroscopy. In Fig. 3.16, we present results coherently interrogating atoms over seconds-long timescales. For these measurements, we employ 'Ramsey spectroscopy'. While the conceptual idea of increasing the coherent interrogation time for increased sensitivity is exactly analogous to Rabi spectroscopy from Fig. 3.9, the details of this scheme

are slightly different. Atoms are first placed in a coherent superposition state with a '$\pi/2$ pulse' $\Omega_0 T_{pulse} = \pi/2$, so $|\psi\rangle = (|g\rangle + |e\rangle)/\sqrt{2} \equiv |X\rangle$. Next, the atoms precess over a dark time T_{dark} where the light is extinguished. The detuning $\Delta = \omega_c - \omega_0$ results in an accumulated phase shift $\phi_{total} = \Delta T_{dark} + \delta\phi$, including a random laser phase $\delta\phi$ that stocastically increases as the dark time is extended. As we will detail in future chapters, interactions between atoms may also lead to phase shifts that can be spectroscopically probed. This phase shift ϕ_{total} is mapped into the excitation fraction p_e in the final $\pi/2$ pulse. In this measurement, we intentionally step the laser frequency ω_c to scan out Ramsey 'fringes'. To study the limits of our atom-light coherence, we vary our dark time T_{dark} from 100 ms, to 1 s, to 4 s from top panel to bottom. Even up to 4 s dark time, we maintain atom-light coherence. We additionally see that the fringe visibility is decreased as T_{dark} is extended, strongly motivating the studies of 'atomic coherence' in Chapter 6.

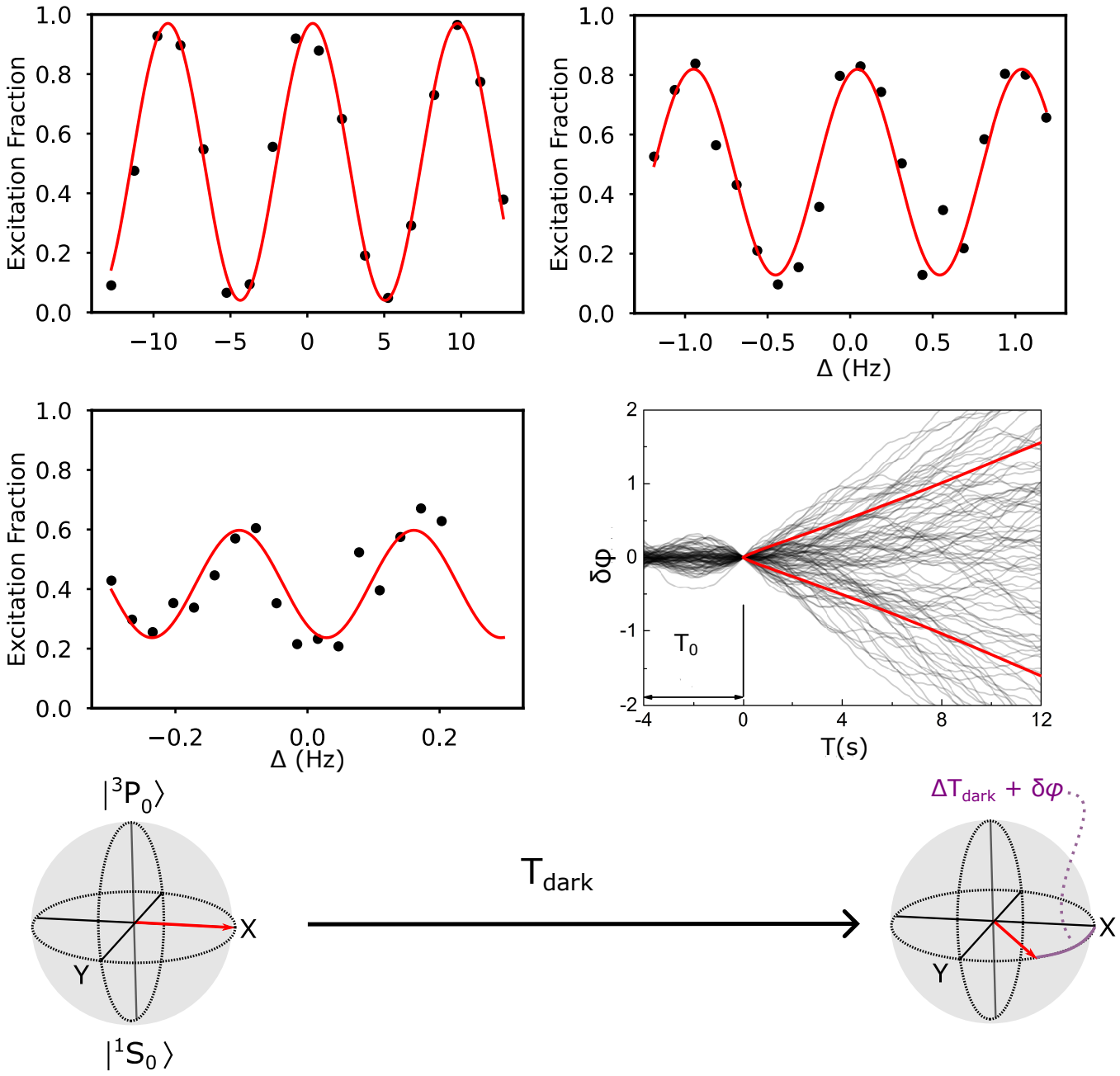

Figure 3.16: Probing atom-light coherence via Ramsey spectroscopy. For this sequence we employ dark times of **top left:** T_{dark} = 100 ms, **top right:** 1 s, and **middle left:** 4 s respectively. Red lines are sinusoidal fits. The loss of fringe visibility is discussed comprehensively in Chapter 6, due primarily to single-particle dephasing from lattice photon scattering at the deep lattice depths employed for this measurement. **Middle right**: Mean phase excursion between two silicon cavities at 1542 nm is plotted. Figure is adapted from Ref. [39]. **Bottom**: During the Ramsey dark time T_{dark}, a phase shift is accumulated due to both the laser detuning Δ intentionally applied for each experimental realization and a random phase $\delta\phi$ accumulated by the silicon cavity. This net phase shift is translated into a modification of the excitation fraction with a final $\pi/2$ pulse around the Y axis.

Chapter 4

Demonstration of an all-optical timescale

The research in this chapter is reported in the following publication: W. R. Milner, J. M. Robinson, C. J. Kennedy, T. Bothwell, D. Kedar, D. G. Matei, T. Legero, U. Sterr, F. Riehle, H. Leopardi, T. M. Fortier, J. A. Sherman, J. Levine, J. Yao, J. Ye, and E. Oelker, *Phys. Rev. Lett.* **123**, 173201 (2019).

4.1 Introduction

Time plays a vital role in day-to-day life. You look at your phone, see the time is 9:30 AM, and realize you only have 5 minutes before you are late for group meeting. Thus time is relative [135] and apparently unidirectional. But where does the time come from?

4.1.1 Why an *all-optical* timescale?

The worldwide time standard, Coordinated Universal Time (UTC), is synthesized from a global network of atomic clocks and disseminated at monthly intervals. [1] National metrology institutes bridge the gap between updates of UTC by broadcasting independent time scales derived from ensembles of microwave local oscillators steered to accurate atomic frequency standards [136, 137]. To advance the frontier of precision timekeeping, the development of both improved local oscillators and atomic frequency standards is imperative. This

[1] The monthly Circular T report from BIPM!

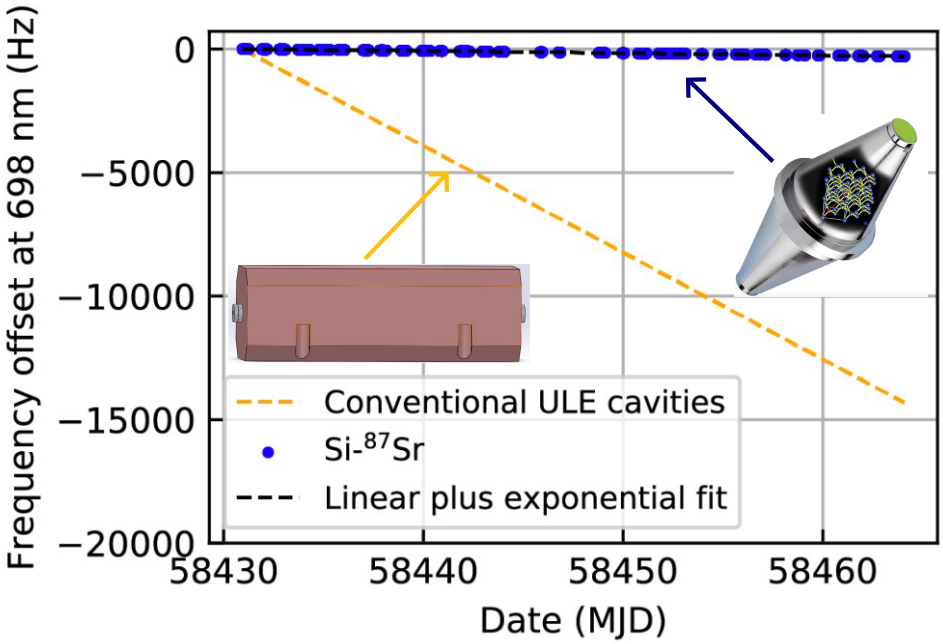

Figure 4.1: Cavity drift comparison between conventional ULE cavities and our 21 cm, cryogenic silicon cavity. In terms of cavity drift, the crystalline cavity outperforms the amorphous ULE cavity by many orders of magnitude.

will pay dividends for a wide array of applications, ranging from navigation and geodesy to studies of fundamental physics [138, 139, 140, 141, 142, 19].

Optical atomic clocks [143, 103, 144, 141, 145, 31], show promise as frequency standards for time scale applications. Recent efforts to incorporate optical clocks into existing microwave timescales have lead to improved performance [146, 147, 148]. However, despite the fact that optical clocks have demonstrated mid-10^{-17} level stability in one second of averaging [40, 149], time scales steered to optical standards have thus far required weeks of averaging to reach 10^{-16} level precision [150, 148]. This disparity in performance arises due to down conversion of noise from the local oscillator – a consequence of steering to an atomic standard in the presence of dead time – which degrades the long-term stability of the time scale [148]. This limitation motivates the development of local oscillators with improved stability, particularly at averaging times around the typical interval between clock measurements (10^3 to 10^5 s). Improvements in local oscillator stability allow a timescale to maintain a competitive level of performance even when relaxing the requirements on optical clock uptime.

After a decade of development [151, 152], cryogenic silicon reference cavities are now a proven platform for laser stabilization at the mid-10^{-17} level [153, 39]. The exceptional short-term stability of these local oscillators has enabled advances in optical clock stability [40]. These systems outperform all free-running local oscillators, both optical and microwave, at averaging times below 1×10^4 seconds [40]. Our silicon cavity also exhibits orders-of-magnitude lower frequency drift and superior long-term stability compared to all other OLOs [154, 153].

Despite the many attractive features of silicon cavities already characterized, the long term stability of these reference cavities was relatively unexplored. Historically, realizing a free-running Fabry-Pérot with long term stability commensurate with the best microwave local oscillators seemed impossible [150]. Rather, efforts were focused on improving cavity short-term stability (i.e. $0.5-10$ Hz frequency band) for optimal clock performance [40, 149].

Quantitatively characterizing the long-term frequency stability required either painstaking measurements over multiple weeks with our ^{87}Sr clock, or direct comparisons with an independent local oscillator exhibiting commensurate performance. As we will detail in the forthcoming chapters, both approaches were used to determine the cavity long-term stability in good agreement.

As plotted in Fig. 4.1, initial measurements of the silicon cavity frequency over long averaging times with our ^{87}Sr clock clearly demonstrated that our crystalline cavity had far lower drift than any amorphous ULE cavity by many orders of magnitude. However, additional work was required to ensure the instability, or the deviations from the linear drift, were sufficiently small to challenge the performance of hydrogen masers. To address this, we installed super-polished optics for all optics in our optical cavity setup, including windows in the cavity housing and the alignment mirrors incident to the cavity, along with improving the thermal control of the cavity environment. Both of these technical improvements were implemented to limit the effects of parasitic etalons on our cavity stability. Additionally, active optical power stabilization in cavity transmission was crucial to reduce frequency excursions arising from laser intensity fluctuations.

4.2 Realizing an all-optical timescale

In this thesis chapter we summarize the first realization of a time scale based on an optical local oscillator (OLO) which outperforms state-of-the-art microwave oscillators steered to either microwave or optical frequency standards. This all-optical time scale scale consists of an ultrastable laser based on a cryogenic silicon reference cavity that is steered daily to an accurate ^{87}Sr lattice clock [155] over a month-long campaign. During this period, the frequency stability of the OLO surpasses that of the hydrogen masers in the UTC(NIST) time scale at all averaging intervals up to multiple days, demonstrating the requisite stability for improved time scale performance. Our analysis indicates that daily steering of the OLO frequency with 50% clock uptime allows for a time scale instability below the 10^{-17} level

within 85 days of operation. Our local oscillator frequency is easily predictable using conventional time scale steering algorithms, allowing us to limit the estimated time error to only 48 ± 94 ps after 34 days of operation. The continuous availability of the OLO coupled with the on-demand performance of our optical clock make our system viable for future inclusion in UTC(NIST). This new variant of time scale harnesses both the improved accuracy and stability of optical standards and provides a viable blueprint for the upgrade of time scales worldwide.

4.2.1 Interface with optical clock

We combine our local oscillator with an accurate optical frequency standard to form an all-optical time scale. Over a 34 day interval, a strontium lattice clock with systematic uncertainty of 2.0×10^{-18} [155] is used to track the OLO frequency with 25 percent uptime. Daily measurements of the OLO allow us to build a reliable predictive model of its frequency evolution. As new frequency data become available, the model is updated to better reflect its current behavior. The OLO is steered using the model to correct for changes in its frequency over time, and any residual frequency fluctuations ultimately determine the time scale stability. The analysis required to realize the time scale was carried out in post-processing, though we emphasize that our approach is compatible with real-time implementation.

To track frequency excursions larger than the low-10^{-16} level during intervals when the optical clock is offline, the OLO must be compared with two independent ultrastable lasers based on a 6 cm silicon cavity operated at 4 K [153] and a 40 cm ultra-low expansion (ULE) cavity [156]. Because the three systems have comparable short-term stability, one can use a three-cornered hat analysis to identify any significant frequency jumps in the OLO and update the predictive model accordingly.

A schematic of our optical time scale is presented in Fig. 4.2a. In order to reference the ^{87}Sr clock laser to the 124 K silicon cavity, we transfer its optical stability from 1542 nm to a prestabilized laser at 698 nm using a femtosecond Er:fiber frequency comb with negligible

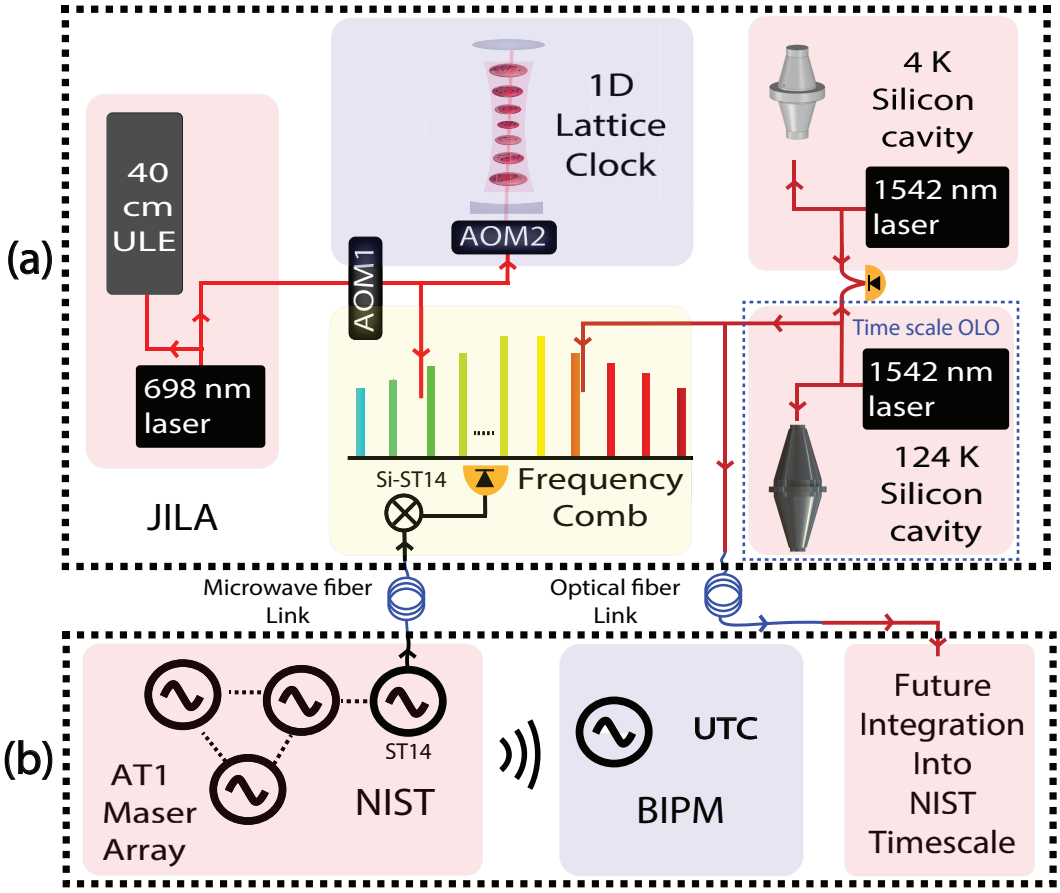

Figure 4.2: **(a)** An array of three lasers are locked to ultrastable Fabry-Pérot resonators. A femtosecond frequency comb transfers the stability of the OLO (124 K Si cavity) from 1542 nm to a prestabilized laser at 698 nm used to perform clock spectroscopy in a 1D ^{87}Sr lattice clock. **(b)** AT1, a free running microwave time scale at NIST is compared continuously against the OLO signal over a fiber optic link using a hydrogen maser (ST14) as a transfer oscillator. An optical fiber link between JILA and NIST allows for stable transfer of the optical time scale to NIST for future integration into UTC(NIST).

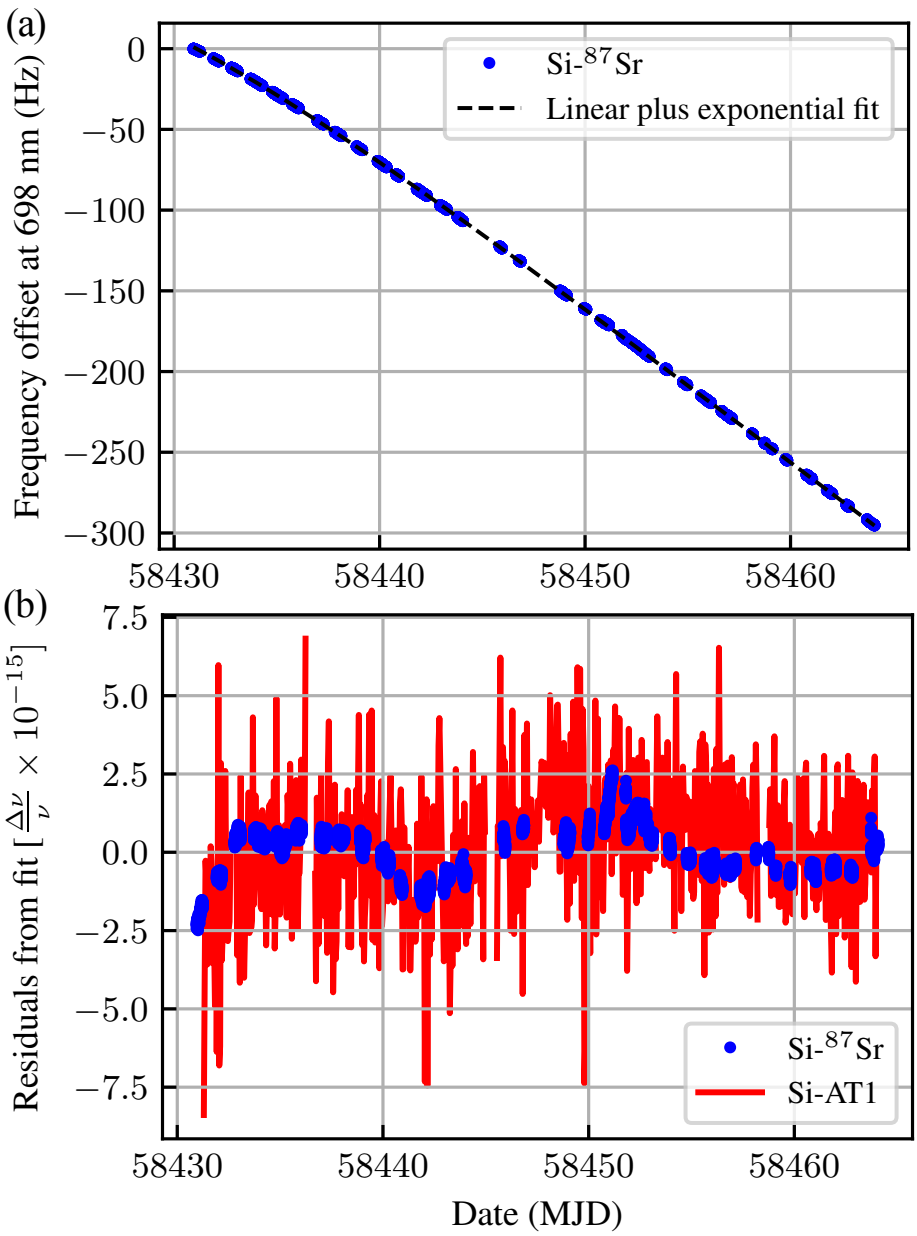

Figure 4.3: **(a)** The OLO frequency (Si) is measured at 698 nm using a ^{87}Sr lattice clock. A linear plus exponential trend, $a + bt + ce^{-\frac{t}{d}}$, agrees well with the raw frequency data. The fit parameters are $a = 24.16$ Hz, $b = -9.632$ Hz/day, $c = -23.17$ Hz, and $d = 7.813$ days. **(b)** The residuals of the OLO comparisons against the ^{87}Sr clock and the NIST AT1 time scale after subtracting the drift trend from (a) from both datasets.

additive instability [40]. The frequency corrections applied to AOM1 by the stability transfer servo are recorded to monitor the relative frequency fluctuations between the 40 cm ULE cavity and the OLO. The stabilized 698 nm light is then tuned to resonance for the ^{87}Sr clock transition using AOM2. The AOM2 correction signal is recorded and yields the OLO frequency relative to the ^{87}Sr transition. An optical beatnote at 1542 nm between the OLO and the 6 cm Si cavity serves as a continuous monitor of their frequency difference. Fig. 4.2b depicts AT1, a free running microwave time scale at NIST. Using a hydrogen maser as a transfer oscillator, AT1 is compared remotely with the local oscillator over a stabilized fiber-optic link. To enable this comparison, the OLO is down converted to the RF domain using a frequency comb. This provides an additional record of the long-term performance of the OLO that is nearly continuous (95% uptime) over the measurement campaign. We note that AT1 is chosen rather than UTC(NIST) due to its superior stability over the averaging intervals of relevance to this study.

A record of the OLO frequency during the data campaign spanning from a modified Julian date (MJD) of 58430 to 58464 is presented in Fig. 4.3a. The clock ran daily with the exception of MJD 58444 and 58447. Three days before the first measurement, the optical power incident on the cavity was changed to reset an intensity noise servo. Consistent with prior silicon cavity drift studies, the frequency evolution of the OLO after adjusting the incident optical power is well modeled by a constant linear drift plus an exponential relaxation term: $a + bt + ce^{-\frac{t}{d}}$ [153]. Fig. 4.3b shows the residuals of the OLO comparisons with the clock and AT1 after subtracting the modeled drift trend determined by a fit to the ^{87}Sr clock data. Perfect correlation between the two data sets is not expected as both AT1 and the microwave link contribute additional instability to the Si-AT1 record. During the interval between clock operation on MJD 58441 and 58442, two frequency jumps on the OLO were identified with a combined amplitude of 5.02×10^{-15}. For future applications of optical timescales, it is important to add redundancy in the form of multiple optical local oscillators with commensurate performance. A correction of the same magnitude is applied to all data

after this step when performing the analysis presented in this work. No significant change in the long-term drift trend of the local oscillator was observed following these excursions. Under real-time operating conditions, we anticipate an additional time error of less than 5 ps from these two jumps.

To realize a time scale, the OLO frequency record in Fig. 4.3a is steered using a predictive model to minimize its offset from the atomic frequency standard. The predictive model utilizes a Kalman filter to estimate the frequency of the OLO at a given time based on prior measurements with the clock. Kalman filtering techniques are commonly used in time scales to model the frequency of hydrogen masers [157, 158]. The drift in the OLO frequency between daily measurements is well approximated by a quadratic function: $k_0 + k_1 t + \frac{k_2 t^2}{2}$. The model prediction is determined by a state vector $[k_0, k_1, k_2]$ that is updated epoch-by-epoch when the ^{87}Sr clock is running. We stress that this technique does not utilize a priori knowledge of the drift coefficients from Fig. 4.3a. When the clock is online, the Kalman filter adapts rapidly to follow the current drift trend of the cavity and the prediction remains accurate provided the drift does not change significantly between daily measurements.

To evaluate the performance of a time scale, one typically compares it against a reference time scale with significantly lower timing uncertainty. To our knowledge, no such time scale at this performance level exists. Instead we treat the ^{87}Sr clock as an ideal frequency reference and examine the fractional frequency offset between the steered OLO record and the clock transition frequency, hereafter referred to as the prediction error. We define the time error of our time scale as the integral of the prediction error over time.

If the frequency record were continuous, the time error could be determined to within the measurement precision of the clock. However, a finite gap of time separates the frequency measurements in Fig. 4.3a, ranging from the 5 second interrogation cycle of our experiment to 24 hours between daily measurements. Most of the time error accumulates during the longer gaps, when the Kalman filter must accurately predict changes in the OLO frequency without new measurement data from the clock. The time error contribution from a gap

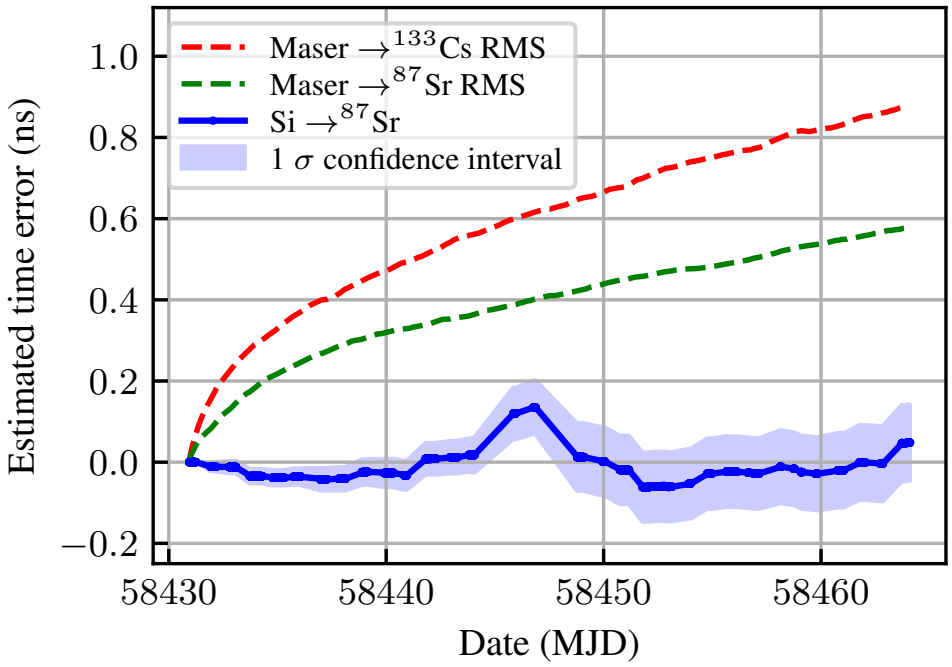

Figure 4.4: An estimate of the time error evolution of the optical time scale over the 34 day data campaign results in an integrated value of 48 ± 94 ps. The peak-to-peak value of 197 ps is dominated by a four day window that includes the two days when the ^{87}Sr clock was not operated. The RMS spread in time error for two time scales based on repeated simulations of a maser steered to either a microwave or optical frequency standard are shown for comparison.

is simply the gap duration multiplied by the mean prediction error during this interval. Instead, we estimate the mean prediction error by averaging the values before and after the gap and multiply by the gap duration to compute an estimated time error. We compute a 1σ confidence interval for the estimated time error through repeated simulations of the OLO frequency during each gap.

4.2.2 Optical timescale performance

An estimate of the integrated time error of our optical time scale is presented in Fig. 4.4. After 34 days of integration our time scale accumulates an error of 48 ± 94 ps. For comparison we simulate time scales consisting of a hydrogen maser steered to a ^{133}Cs fountain for 24 hours/day and a hydrogen maser steered to a ^{87}Sr optical clock for 6 hours/day using the same Kalman filter and noise models for the maser and fountain described in [150]. The typical performance of both time scales is assessed by computing time errors from repeated simulations, and their RMS spread over a 34 window is depicted in Fig. 4.4. Both exhibit a larger time error than the all-optical time scale.

Because the optical clock is run intermittently, the long-term stability of the time scale will be limited by a $1/\sqrt{\tau(s)}$ slope arising from aliased local oscillator noise akin to the Dick effect [150, 148]. Determining this stability limit requires an accurate characterization of the OLO. We evaluate the stability of our OLO by analyzing the frequency noise of the residuals in Fig. 4.3b. One complicating factor are the gaps in the frequency record during clock downtime. A gap-tolerant Allan variance similar to [159] is used to compute an estimated stability of the OLO out to multiple day averaging intervals.

The result of this analysis is plotted in Fig. 4.5. The OLO stability is fit to a noise model that includes the known thermal noise floor [40] and a random walk frequency noise term, resulting in an instability at long averaging times consistent with $\sigma_{RW} = 1.3\times\ 10^{-18}\sqrt{\tau(\mathrm{s})}$. The OLO maintains an instability below 10^{-15} out to 6×10^5 s, more than an order of magnitude improvement over the previous characterization of this system [39]. The frequency

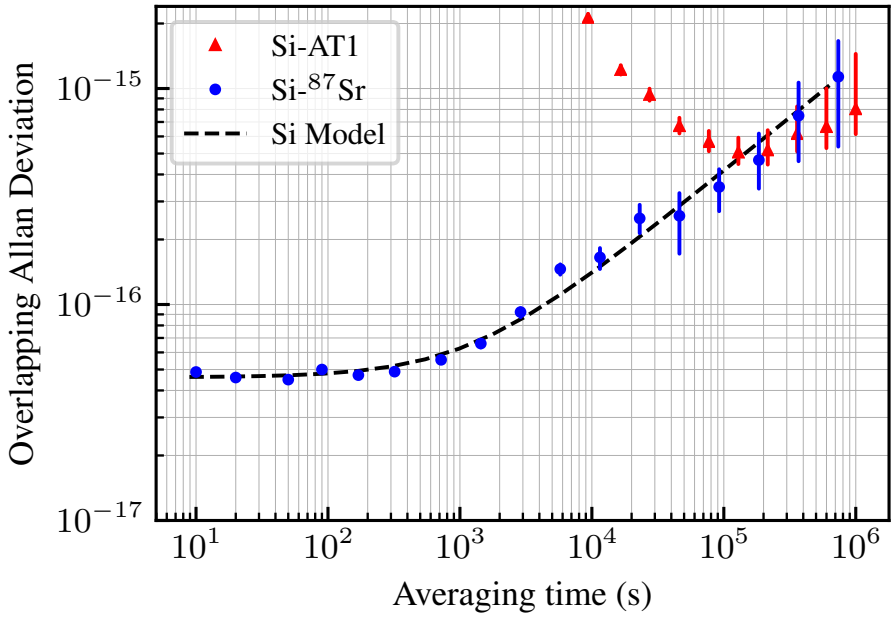

Figure 4.5: The silicon cavity stability is computed from the detrended ^{87}Sr data in Fig. 4.3b using a gap-tolerant Allan variance similar to [159]. The data is fit to a noise model with an instability of $\sigma = 1.3\times\ 10^{-18}\sqrt{\tau(\mathrm{s})}$ at long averaging times. The long-term stability of the OLO is also inferred from a continuous measurement against the NIST AT1 time scale.

stability of the Si-AT1 record is presented as well and its value at averaging times past 10^5 s agrees with the clock measurement within statistical uncertainty. At shorter averaging times, the stability is consistent with a noise model accounting for instability from the microwave link, the OLO, and AT1 [160].

With an accurate noise model for the OLO in hand, we now consider the anticipated long-term stability of our time scale as a function of optical clock duty-cycle. Similar to Refs. [148, 150], we simulate a lengthy local oscillator frequency record using the model presented in Fig. 4.5 with the drift trend from Fig. 4.3a added. This record is then steered to a simulated ^{87}Sr lattice clock for a fixed interval each day using the same Kalman filtering techniques described above. We compute an Allan deviation of the prediction error to determine the stability of the time scale. To quantify the impact of our improved local oscillator we carry out the same analysis for a similar time scale where the OLO has been substituted with a hydrogen maser. The noise model for the simulated hydrogen maser is based on the typical stability of the best performing masers in the UTC(NIST) time scale [150].

Fig. 4.6 shows the results of our analysis. As anticipated, the long-term stability of the time scale improves with increased clock uptime and reduced local oscillator noise and is reasonably consistent with the expected instability limit from aliased local oscillator noise past 10^6 s. When the optical clock is run with the same duty cycle, the steered OLO significantly outperforms a steered hydrogen maser at all averaging times. Even when steering one hour per day, our time scale is more stable than a hydrogen maser steered with a 50 percent duty cycle. This capability allows for competitive time scale performance with significantly relaxed uptime requirements. Based on this analysis, we expect a stability of approximately 1.8×10^{-17} after a 34 day campaign with an average clock uptime of 6 hours/day. This is in good agreement with the observed integrated time error of 48 ± 94 ps over 34 days, or $1.6 \pm 3.2 \times 10^{-17}$ in fractional units. When operating the clock 12 hours per day, our all-optical time scale remains at or below the 2×10^{-16} level at all averaging times

and is projected to reach a stability below 10^{-17} after only 85 days of operation. Additional effort on automation should allow for a clock duty cycle well above 50%.

4.2.3 Signal transfer overview

To supplement the intermittent frequency measurements of our optical local oscillator (OLO) with the ^{87}Sr lattice clock, the OLO frequency was also compared continuously with AT1, a free running microwave time scale operating at NIST. AT1 is chosen rather than UTC(NIST) because of its improved stability at averaging times below 10^6 s. To facilitate this comparison, the OLO frequency is down converted to the RF domain using a self-referenced Er:fiber frequency comb. The frequency difference (f_{beat}) between the OLO and the nearest comb tooth is stabilized to 35 MHz by actuating on the comb repetition rate ($f_{\mathrm{rep}} \approx 250$ MHz) as described by the relation: $f_{\mathrm{beat}} = f_{\mathrm{Si}} - n f_{\mathrm{rep}} - f_{\mathrm{ceo}}$. Here, f_{Si} is the OLO frequency, n is an integer, and f_{ceo} is stabilized to 35 MHz using an f-2f interferometer. The repetition rate, f_{rep} inherits the stability of the OLO and is used to synthesize an RF signal by measuring the optical beat between adjacent comb teeth. This signal is mixed down to 1 MHz using a RF signal synthesized from a NIST hydrogen maser, hereafter referred to as ST14, and counted with a 1 s gate time using a zero-dead-time lambda-type frequency counter. This allows us to continuously monitor $y_{\text{Si-ST14}}$, the fractional frequency difference between the OLO and ST14. The fractional frequency difference between ST14 and the AT1 timescale ($y_{\text{ST14-AT1}}$) is measured in tandem at NIST and we use both to compute the Si-AT1 beat as follows: $y_{\text{Si-AT1}} = y_{\text{Si-ST14}} + y_{\text{ST14-AT1}}$. Because the NIST time scale measurement system (TSMS) records $y_{\text{ST14-AT1}}$ in 720 s intervals, the Si-ST14 record is decimated in three steps by a factor of 720 and interpolated to the TSMS time stamps prior to computing $y_{\text{Si-AT1}}$. To transfer ST14 from NIST to JILA, a 1 GHz signal synthesized from ST14 is used to amplitude modulate a 1.3 micron wavelength laser which is transmitted over a group delay stabilized fiber-optic link [161]. Over the 34 day data campaign, the microwave fiber link and frequency comb located at JILA maintained a 95% uptime to determine the $y_{\text{Si-AT1}}$

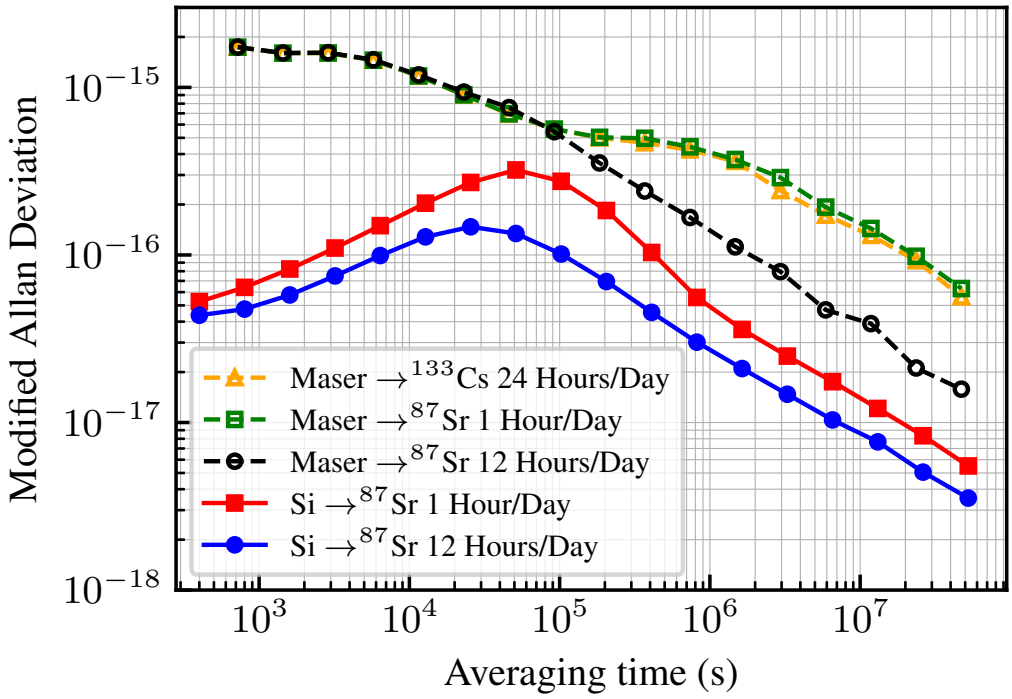

Figure 4.6: Expected fractional frequency stability of the optical time scale. The stability of our optical time scale is analyzed for two optical clock duty cycles. Our optical time scale is compared to a hydrogen maser based time scale steered to an optical lattice clock with identical uptime or a cesium fountain clock operating continuously.

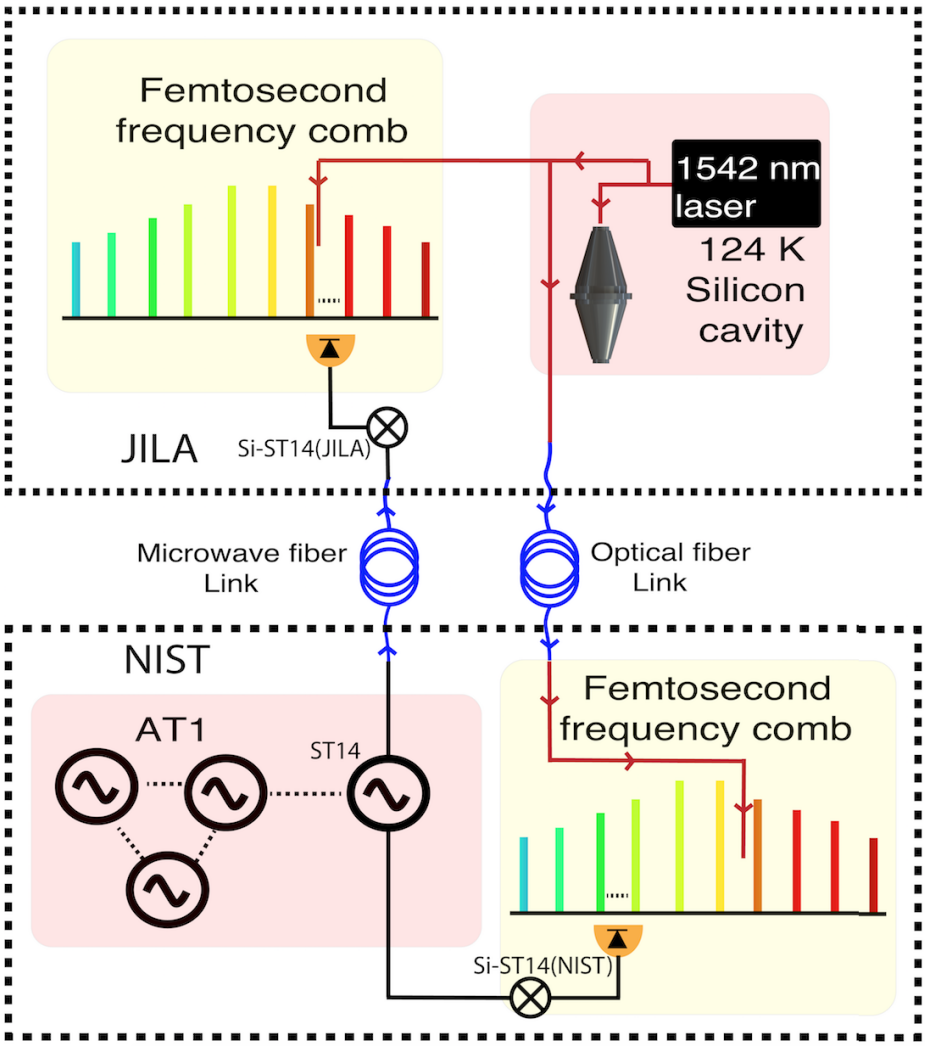

Figure 4.7: Schematic of the frequency comparison measurement between the OLO and the NIST AT1 time scale. A hydrogen maser, ST14, is used as a transfer oscillator. ST14 is compared locally with AT1 and remotely with the OLO using a stabilized fiber optic link and the Si-AT1 signal is computed from the two measurements. The OLO is down-converted to the microwave domain using a frequency comb. The analysis presented in Fig. 4.3b and Fig. 4.5 is generated by data from the frequency comb located at JILA. To characterize the noise added by the microwave link, a local measurement of Si-ST14 is performed at NIST over 5 days using a second frequency comb. This utilizes an existing phase-stabilized optical fiber link which adds negligible instability.

beat.

We note that drawing conclusions about the performance of the OLO from the Si-AT1 record is more nuanced than evaluating its stability directly using an optical clock. In this case, both the reference (AT1) and the link used to transfer microwave signals from NIST to JILA contribute appreciable instability to $y_{\text{Si-AT1}}$. Interpreting the stability of $y_{\text{Si-AT1}}$ requires comprehensive knowledge of these contributions. To estimate the instability added by AT1, we use the measurement of AT1 presented in Ref. [160]. The instability added by the microwave link is determined by performing a differential measurement. Over a 5 day interval during the data campaign (MJD 58438-58442), the OLO was transferred to NIST over a phase stabilized optical fiber link and measured against ST14 locally using a second Er:fiber frequency comb [162]. Because the optical link adds negligible noise to the OLO [163], we may estimate the noise added by the microwave link by examining the difference between these frequency records: $y_{\text{link}} = y_{\text{Si-ST14(JILA)}} - y_{\text{Si-ST14(NIST)}}$.

Fig. 4.8 depicts the time series of the three microwave signals after subtracting the linear frequency drift of ST14 and the OLO drift trend from Fig. 4.3a. Each signal has been decimated by an additional factor of 10 so that each is dominated by the long term performance of the oscillators rather than short term microwave link noise. This plot highlights the improved stability of the OLO in comparison with ST14.

The long term stability of the OLO can be inferred from the Allan deviation of the Si-AT1(JILA) record in Fig. 4.8. The plot also includes a model of the anticipated stability where the measured link noise, a noise model of AT1, and the OLO model from Fig. 4.5 are added in quadrature. Because of the shorter duration of the microwave link noise measurement, its magnitude is only known out to 10^5 s and its contribution to the model is set to zero at longer averaging times. At averaging times less than 10^5 seconds, the data is in good agreement with the model and is slightly below the model prediction at longer averaging times. This data suggests that the intermittent measurements of the OLO with the Sr clock provide an accurate picture of its true long-term performance.

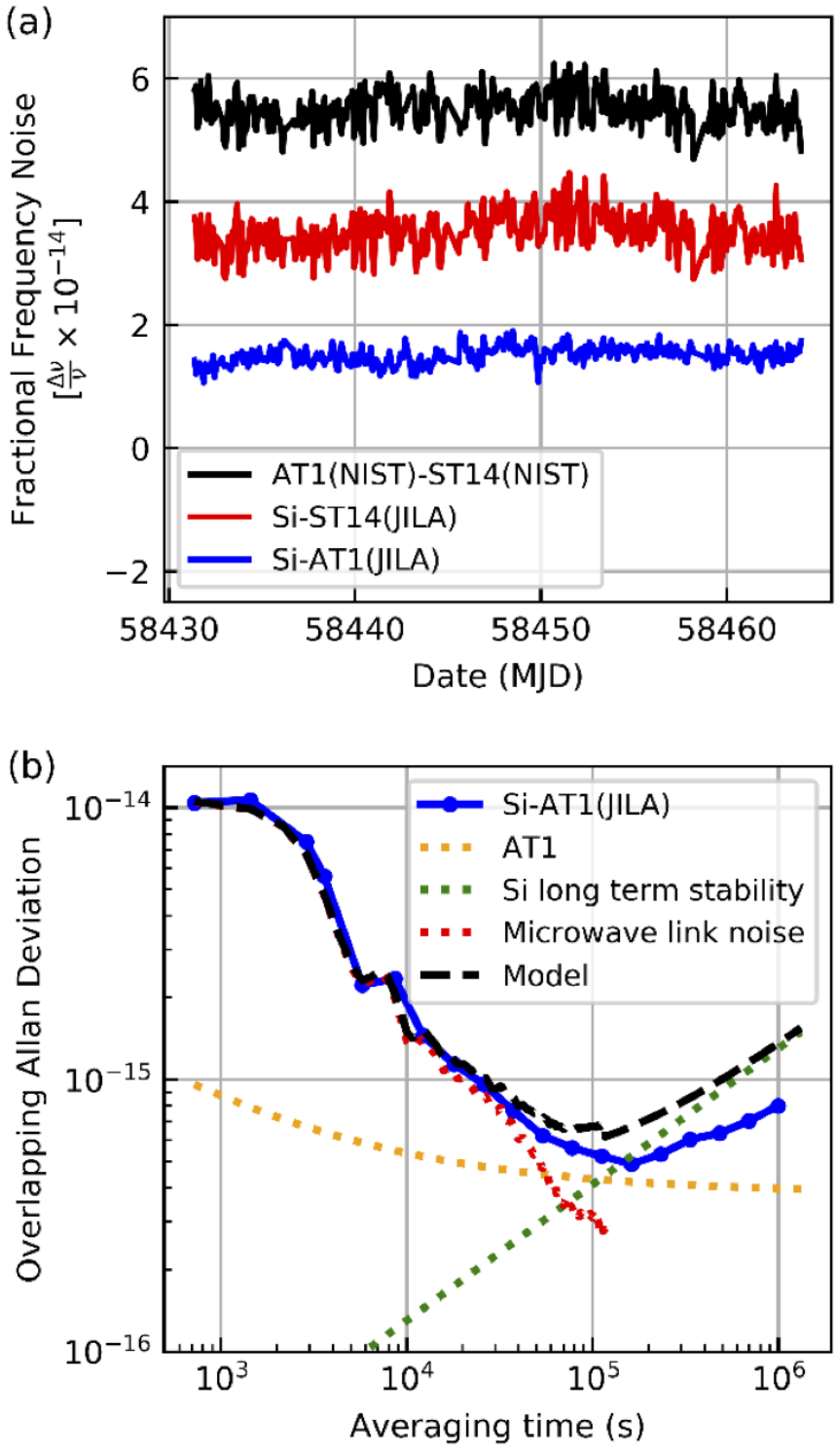

Figure 4.8: Frequency comparison between the OLO and the NIST AT1 time scale. **(a)** Time series of the beats between the various oscillators highlighting the improved stability of the OLO. The traces are labeled to indicate that they were measured either locally at NIST or remotely at JILA and are offset for clarity. **(b)** Fractional frequency stability of the Si-AT1(JILA) record. The data is compared against a model including contributions from AT1, microwave link noise, and the OLO model from Fig. 4.5

4.2.4 Kalman filter modeling

To minimize the time error during periods when an accurate frequency reference is unavailable, a time scale local oscillator must have a predictable frequency. The frequency of the local oscillator can then be steered using a predictive model to keep it as close to the value of the frequency reference as possible. Kalman filtering techniques are often used to construct such a model based on periodic measurements of the local oscillator frequency against an atomic frequency reference [150, 148]. For a hydrogen maser, a linear model of the form $f(t+\Delta t) = \hat{k}_0 + \hat{k}_1 \Delta t$ is typically used to track its frequency drift over time, where $\hat{k}_0$ is an estimate of the maser frequency at time t and $\hat{k}_1 = \frac{\mathrm{d}f}{\mathrm{d}t}(t)$ is an estimate of its linear frequency drift rate.

For the OLO, a linear model is sufficient to form a time scale with competitive performance. However, the presence of random walk frequency noise and the exponential term in its frequency drift tend to add a slight curvature to the OLO frequency evolution. We found that it was more optimal to model the OLO frequency using a quadratic function of the form $f(t+\Delta t) = \hat{k}_0 + \hat{k}_1 \Delta t + \frac{1}{2}\hat{k}_2 \Delta t^2$, where the additional term represents the estimate of the time derivative of the linear drift rate. As shown below, this function is typically written in matrix form, and the coefficients $\hat{k}_0, \hat{k}_1$, and $\hat{k}_2$ form what is known as the state estimate vector.

For the analysis presented in Fig. 4.4 the time separation between updates of the Kalman filter state vector was $\Delta t = 1$ s. For the nth epoch, the local oscillator frequency at time t_n is predicted using the state estimate vector at t_{n-1} and its expected evolution over the interval Δt.

$$\begin{pmatrix} \hat{k}_0[n|n-1] \\ \hat{k}_1[n|n-1] \\ \hat{k}_2[n|n-1] \end{pmatrix} = \begin{pmatrix} 1 & \Delta t & \frac{1}{2}\Delta t^2 \\ 0 & 1 & \Delta t \\ 0 & 0 & 1 \end{pmatrix} \begin{pmatrix} \hat{k}_0[n-1] \\ \hat{k}_1[n-1] \\ \hat{k}_2[n-1] \end{pmatrix} \tag{4.1}$$

The vector $\mathbf{k}[n|n-1]$ is known as the prior estimate of the state at epoch n. The local

oscillator frequency is steered by applying a frequency correction of $\hat{k}_0[n|n-1]$ during each epoch. In the event that no new measurement with the optical clock occurs during this epoch, the new state estimate vector is simply set equal to the prior estimate.

$$\begin{pmatrix} \hat{k}_0[n] \\ \hat{k}_1[n] \\ \hat{k}_2[n] \end{pmatrix} = \begin{pmatrix} \hat{k}_0[n|n-1] \\ \hat{k}_1[n|n-1] \\ \hat{k}_2[n|n-1] \end{pmatrix} \tag{4.2}$$

This is the behavior of the steering algorithm when the optical clock is offline. If the clock is operational and a new frequency measurement is available during epoch n, we may asses the fidelity of the model prediction by comparing the prior prediction of the local oscillator frequency, $\hat{k}_0[n|n-1]$, with the measurement:

$$\Delta f[n] = y[n] - \hat{k}_0[n|n-1] \tag{4.3}$$

where $y[n]$ is the measurement of the frequency detuning of the free-running local oscillator relative to the atomic transition and $\Delta f[n]$ is the prediction error (ie the residual detuning after steering the OLO). If the optical clock is viewed as an ideal frequency reference, $\Delta f[n]$ represents the residual frequency fluctuations of the local oscillator after steering. As described in the next section, this quantity can be analyzed to estimate the time error of the time scale. Following the measurement the state vector is updated as follows:

$$\begin{pmatrix} \hat{k}_0[n] \\ \hat{k}_1[n] \\ \hat{k}_2[n] \end{pmatrix} = \begin{pmatrix} \hat{k}_0[n|n-1] \\ \hat{k}_1[n|n-1] \\ \hat{k}_2[n|n-1] \end{pmatrix} + \Delta f[n]\mathbf{K}_n \tag{4.4}$$

The matrix $\mathbf{K}_n$ is known as the optimal Kalman filter gain for epoch n. The gain matrix $\mathbf{K}_n$ determines the relative weight of the measurement and the prior estimate when computing the new state estimate vector and is optimized using knowledge from past measurements and the known noise properties of the local oscillator. The procedure for calculating $\mathbf{K}_n$ is

beyond the scope of the current discussion. The reader is referred to the canonical text on this subject [164]. Nonetheless, we provide some of the parameters for tuning the Kalman filter below as a reference for readers with expertise in Kalman filtering who wish to reproduce the filter used in this work for steering a comparable local oscillator.

When computing the optimal Kalman filter gain, two co-variance matrices must be specified by the user corresponding to process noise and measurement noise. Process noise represents uncertainty in the future state of the local oscillator. For our system, this is dominated by the random-walk frequency noise which limits the local oscillator stability at 1-day averaging intervals. Measurement noise represents uncertainty in the current frequency measurement due to relative noise between the optical clock and the local oscillator.

The process noise in our Kalman filter is characterized by the Q matrix, defined as $[Q_{11}, 0, 0; 0, Q_{22}, 0; 0, 0, Q_{33}]$. Q_{11} corresponding to the random walk noise of silicon cavity, is set to be $5.1 \times 10^{-36}(s/s)^2$ which is based on the random walk coefficient from the local oscillator noise model in Fig. 4.5. Q_{22} and Q_{33}, corresponding to random run noise and higher-order noise, are negligible. In practice, these two values are set to $2.2 \times 10^{-46}(s/s^2)^2$ and $3.5 \times 10^{-57}(s/s^3)^2$ respectively. The prediction error is not particularly sensitive to the values of Q_{22} and Q_{33}. Only coarse tuning of these parameters is required to guarantee the performance of our filter. The measurement noise is characterized by the R matrix which has a value of $2.5 \times 10^{-33}(s/s)^2$ corresponding to the Allan variance of the thermal noise floor of the local oscillator. To test the robustness of the Kalman filter, the R matrix parameter was varied by an order of magnitude in either direction and the analysis presented in Fig.4.4 was recomputed. We found that this impacted the peak-to-peak time error over the 34 day campaign by less than 5 percent.

To minimize the time error, the time scale steering algorithm must accurately predict and correct for changes in the local oscillator frequency over time. If the exact frequency evolution of the local oscillator were somehow known, one could compute the time error over a given interval by multiplying the mean prediction error during this period by the elapsed

time Δt. In this work, a ^{87}Sr lattice clock with low-10^{-18} level systematic uncertainty [155] and mid-10^{-17} level stability at 1 s [40] serves as a nearly ideal reference for monitoring the frequency of the OLO. Due to the intermittency of the measurement record, the exact mean fractional error in the Kalman filter prediction during the gaps between measurements is not known. Instead, the mean prediction error is estimated by averaging the values immediately before and after the gap. This estimation is then multiplied by the gap duration to compute a time error for the gap in question. The contributions from each gap are integrated to produce the dark blue trace in Fig.4.4. Immediately following a longer gap, the prediction error may be appreciable due to a discrepancy between the predicted and actual drift of the OLO during the gap. The prediction error drops rapidly in the subsequent epochs as the state vector is adjusted to compensate according to Eq. 4.4.

There is inherent uncertainty in calculating the time error using this method, since the true mean prediction error during a gap likely differs from the estimated value. To estimate this uncertainty, we assume that during any long gaps between measurements the frequency corrections applied to the OLO by the steering algorithm are only effective in removing the linear plus exponential drift trend shown in Fig. 4.3a. The residuals are assumed to have a frequency stability identical to that of Fig. 4.3b and Fig. 4.5. Using the noise model from Fig. 4.5, we simulate a frequency record for each gap longer than 3 minutes during the 34 day campaign and compute both the mean prediction error for the entire gap and an estimate of the mean prediction error computed by averaging the prediction error for the first and final data points. By multiplying difference between the true and estimated means by the gap duration, we compute the uncertainty in the time error for the simulation. By running 1000 simulations, we compute a 1σ confidence interval for the time error by computing the standard deviation of the simulation result for each gap. Integrating this over the entire 34 day campaign, we calculate a time error uncertainty of $\pm$94 ps. The results of each simulation and the resulting 1σ confidence interval for the integrated time uncertainty are shown in Fig. 4.9. This 1σ confidence interval corresponds to the light blue shaded region

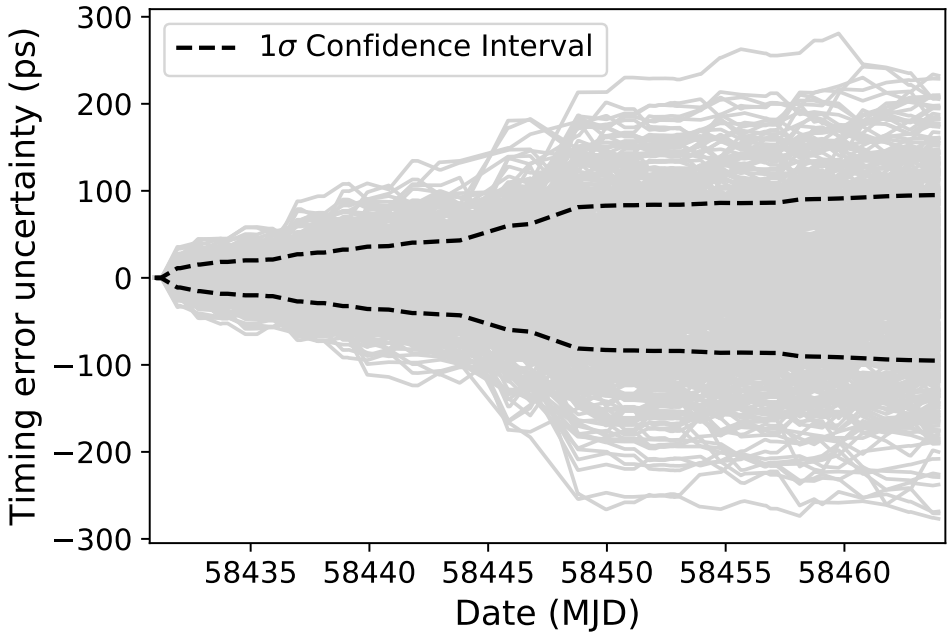

Figure 4.9: Time error uncertainty. Using the OLO noise model from Fig. 4.5, we simulate a frequency record for each gap between frequency measurements with the optical clock. We estimate the uncertainty in the time error calculated in Fig.4.4 by computing the difference between the estimated mean frequency and true mean frequency of the OLO during each gap and multiplying by the gap duration. The outcome of repeated simulations along with a 1σ confidence interval (dashed line) are depicted. This corresponds to a 1σ confidence interval of ± 94 ps over the 34 day campaign.

in Fig. 4.4.

4.2.5 Expected time scale instability

To determine the anticipated stability of the time scale, we simulate a lengthy frequency record for the OLO based on the noise model in Fig. 4.5 and the drift trend from Fig. 4.3a. This record is then steered using the Kalman filter described in Eqs. 4.1 through 4.4. To simulate the clock uptime, the state vector is updated according to Eq. 4.2 during epochs when the clock is offline and updated according to Eq. 4.4 when the clock is running. Unlike the case of a real data set, the true frequency of the local oscillator is known at all times. Therefore, the prediction error in Eq. 4.3 may be computed for every epoch, not just those when the clock is operating. This prediction error is simply the residual frequency noise of the simulated local oscillator after being steered to the clock. We then determine the expected fractional frequency stability of the time scale by taking an Allan deviation of these residuals.

Fig. 4.6 compares the anticipated stability of our all-optical timescale with that of a single Hydrogen maser from the UTC(NIST) time scale steered daily to an optical clock. Here, we extend this analysis by also considering time scale local oscillators from other metrology institutes [146, 147]. To explore the applicability of our OLO to these time scales, we repeat the analysis from Fig. 4.6 using an oscillator noise model that is representative of the Hydrogen masers in the UTC(PTB) time scale [147].

For the simulations in Fig. 4.6, the clock is operational for the same time window each day. In this case it is straightforward to compute the expected stability limit at long averaging times due to aliased noise from the local oscillator. This noise contribution, colloquially known as the Dick effect limit, is a well studied consequence of steering a local oscillator to an atomic reference in the presence of dead time [165, 150].

In Table 4.1, we consider the expected time scale stability when steering the three local oscillators assuming a single measurement per day ranging in length from 1 to 20 hours. The

	Si	NIST maser	PTB maser
1 hr/day	2.4×10^{-17}	2.8×10^{-16}	8.7×10^{-17}
6 hr/day	1.8×10^{-17}	1.2×10^{-16}	4.1×10^{-17}
12 hr/day	1.2×10^{-17}	7.0×10^{-17}	2.5×10^{-17}
20 hr/day	4.0×10^{-18}	3.0×10^{-17}	9.9×10^{-18}

Table 4.1: Expected time scale instability after 34 days (3×10^6 s) of averaging based on the Dick effect limit for steering each oscillator for different optical clock uptimes. This assumes that the uptime is grouped into a single run per day.

	Si	NIST maser	PTB maser
12 hr runs (1 run/day)	1.2×10^{-17}	7.0×10^{-17}	2.5×10^{-17}
6 hr runs (2 runs/day)	6.2×10^{-18}	6.6×10^{-17}	2.0×10^{-17}
3 hr runs (4 runs/day)	3.3×10^{-18}	6.1×10^{-17}	1.8×10^{-17}
1 hr runs (12 runs/day)	1.3×10^{-18}	4.1×10^{-17}	1.6×10^{-17}

Table 4.2: Expected time scale instability after 34 days (3×10^6 s) of averaging based on the Dick effect limit for steering each oscillator. We assume a total uptime of 12 hours/day distributed over a varying number of evenly spaced clock measurements per day. The all-optical time scale (Si) shows a significant improvement with increasing measurement frequency.

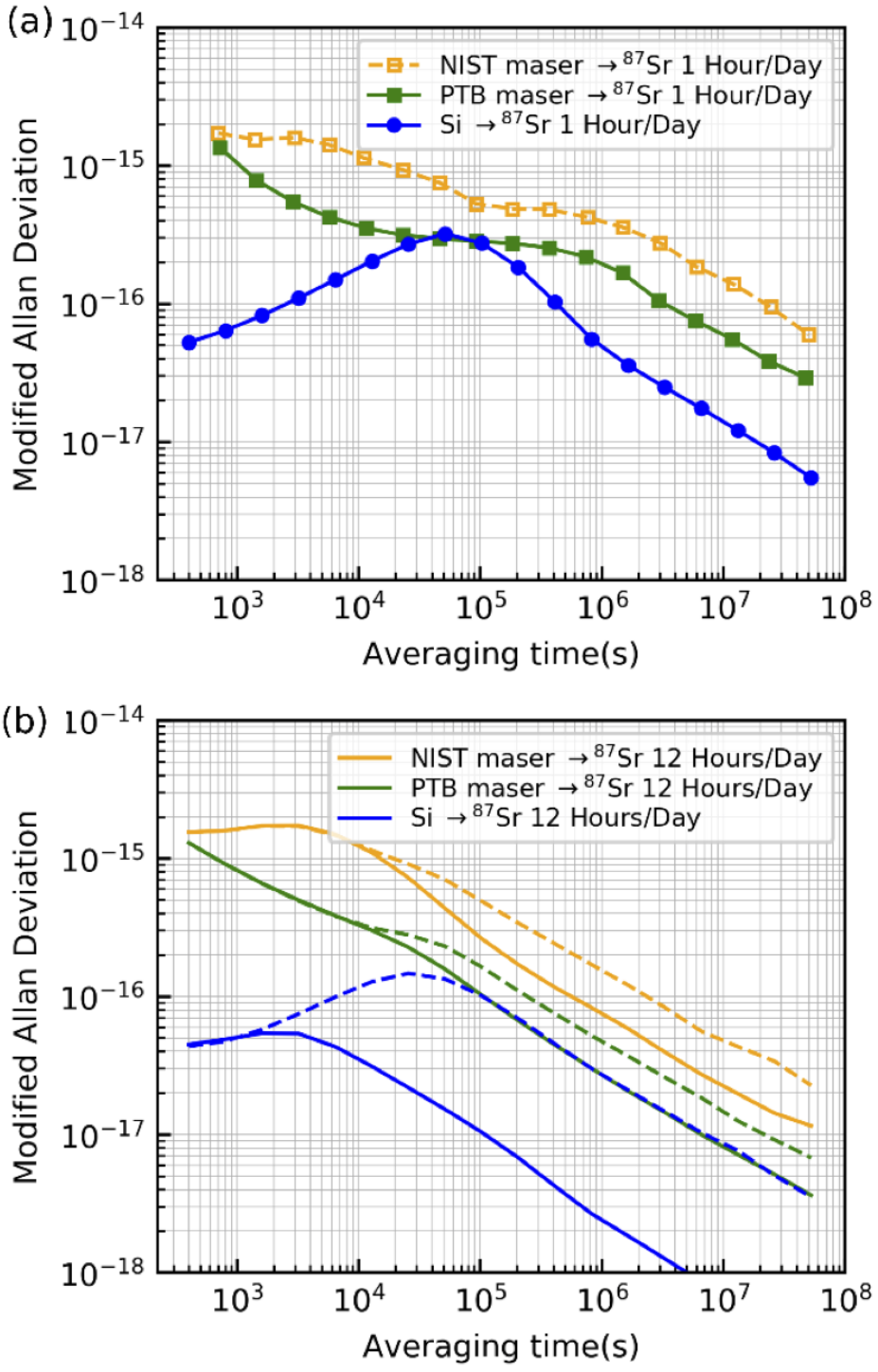

Figure 4.10: Anticipated fractional frequency stability of three different local oscillators steered to an optical clock with several uptime configurations. Panel **(a)** assumes a single 1 hour clock measurement per day. The dashed lines in panel **(b)** show the stability for a single 12 hour run per day, while the solid line assumes twelve 1 hour runs that are evenly spaced throughout the day.

Dick effect limit for the OLO is more than a factor of two better for all run configurations. As the reliability of optical clocks continues to improve, we anticipate that both the total uptime and the frequency of clock measurements will increase. Table 4.2 shows the expected performance for a 50% uptime when the clock is run multiple times per day at evenly spaced intervals. Increasing the measurement frequency results in a modest improvement for the two masers and a dramatic improvement for the OLO. This is a consequence of the local oscillator being limited by random walk frequency noise ($1/f^2$ slope in the frequency domain) at the Fourier frequencies that contribute to the Dick effect. The Dick limit, which depends on the local oscillator frequency noise at harmonics of the measurement frequency, falls off rapidly when more measurements are performed per day.

The results of time scale simulations for each oscillator are plotted in Fig 4.10. Fig 4.10(a) shows the anticipated time scale stability for a single 1 hour run per day. Fig 4.10(b) depicts the case of 50% uptime. Both the stability for a single 12 hour run per day and twelve evenly spaced 1 hour runs are shown for each oscillator. The stability of each simulation past 10^6 s agree well with the anticipated Dick effect limit from Table 4.1 and Table 4.2.

In Fig. 4.4, the performance of the all-optical time scale is compared against two simulated time scales consisting of a hydrogen maser steered to either a ^{87}Sr lattice clock or a ^{133}Cs fountain clock. The noise model for the hydrogen maser is based on the best performing oscillator in the UTC(NIST) time scale [150]. Both the instability and systematic uncertainty of a ^{133}Cs fountain are large enough to have a significant impact on the performance of the time scale over 34 days. The instability assumed for the fountain is identical to that in [150], while the systematic uncertainty is assumed to be 1.71×10^{-16} [166].

We repeatedly simulate a 34 day frequency record for the hydrogen maser and steer it to a simulated record of either a ^{87}Sr lattice clock or a ^{133}Cs fountain clock that accounts for their respective instability. The same Kalman filter described in [150] is used for the steering algorithm. To account for the systematic uncertainty of the fountain clock a constant frac-

tional frequency offset chosen from a normal distribution with a standard deviation equal to the assumed systematic uncertainty of the Cs fountain is added to the steered frequency record. The resulting fractional frequency record represents the exact mean fractional frequency offset from an ideal reference for every epoch and may be integrated to compute the time error for each simulation. We repeat the simulation 800 times and calculate the RMS value of the accumulated time error for each epoch to represent the typical performance of each time scale. The result is plotted in Fig. 4.4.

As depicted in Fig. 4.12, the OLO stability at short averaging intervals may also be inferred by measuring against two reference ultrastable lasers and performing a three-cornered hat analysis. The OLO and the reference systems based on a 4 K Si cavity and 40 cm ULE cavity are limited by their respective cavity thermal noise floor of $\sigma = 4.6 \times 10^{-17}$, 8.2×10^{-17}, and 1.1×10^{-16} [40, 153, 156]. Given their comparable short-term stability, one may easily identify any jumps in the OLO frequency larger than the mid 10^{-16} level by examining the time series of its frequency difference with the two reference systems. When a jump is detected, the predictive model of the OLO can be updated using this information.

Between evaluations with the optical clock on MJD 58442 and 58443, two jumps in the OLO frequency were observed using this technique. Fig. 4.11 displays beat between the OLO and the ultrastable laser based on the 4 K Si cavity, the reference laser with the lowest instability and frequency drift rate. A 15000 s interval around each frequency jump is fit to a linear plus Heaviside function: $ax + b + d[x > c]$. Here, the c fit coefficient determines the time of the jump in seconds, while the d fit coefficient determines the magnitude of the jump. Fig. 4.12 shows all three beats during this interval and confirms that both events were frequency jumps on the OLO as the beat between the two reference systems shows no frequency jumps.

The first jump was immediate and has a magnitude in fractional frequency units of 1.94×10^{-15}. The second jump occurred when the residual amplitude modulation (RAM) servo for the OLO ran out of range. At this time, we elected to change the sign of the

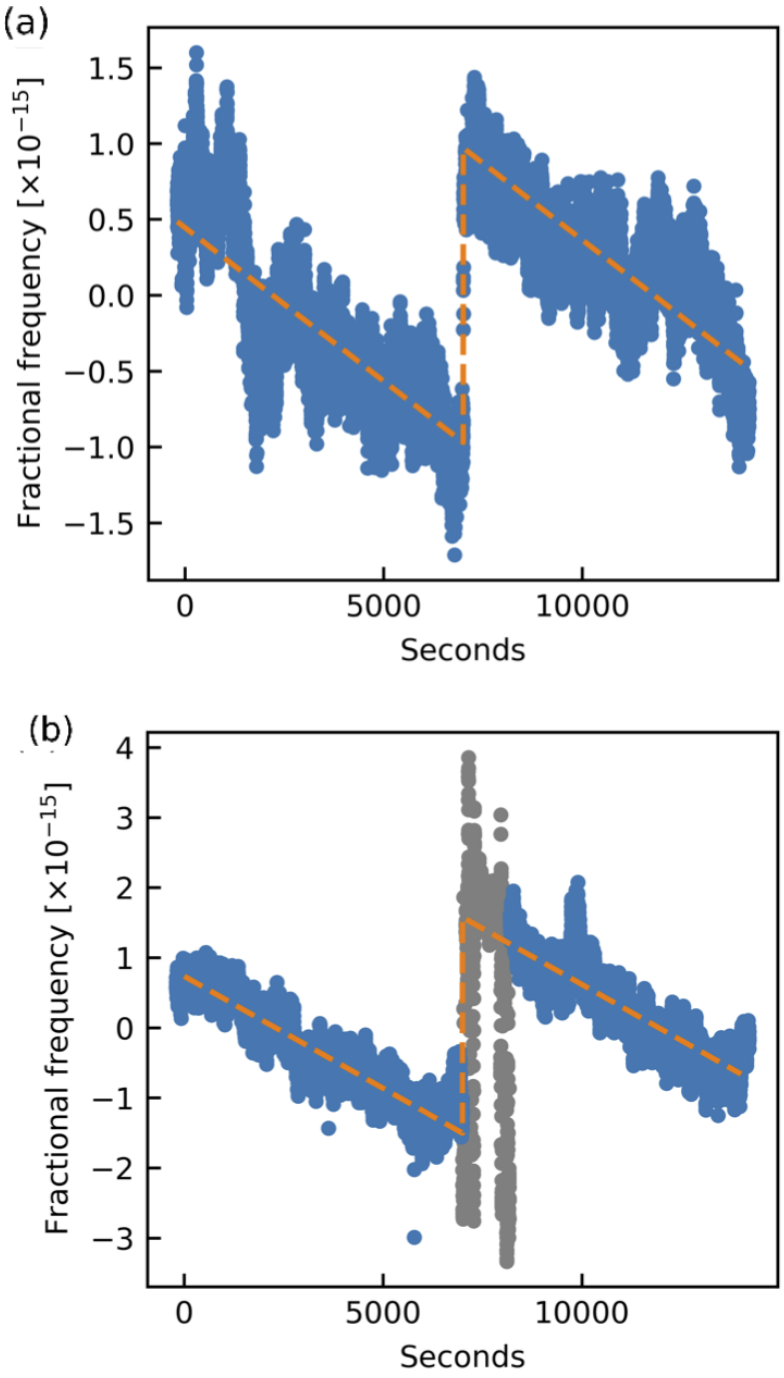

Figure 4.11: Frequency jumps in the difference frequency between the OLO and a reference ultrastable laser based on a 4 K Si cavity. The data are fit to a linear plus Heaviside function to determine the time and magnitude of the jump. The two frequency steps are fit to 1.94×10^{-15} and 3.08×10^{-15} respectively. Data colored in grey in panel **(b)** corresponding to the interval when the RAM servo was being debugged is omitted to avoid biasing the fit.

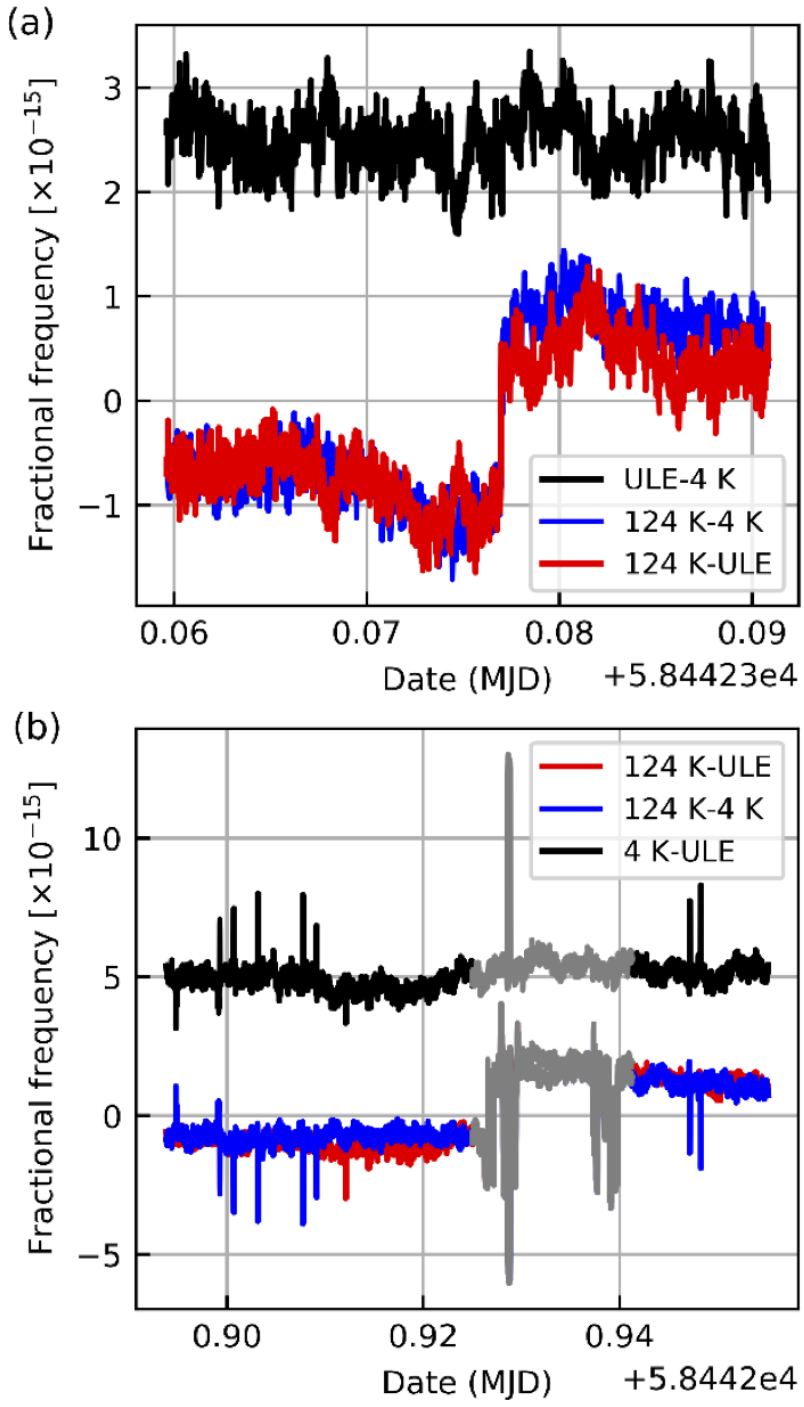

Figure 4.12: Three-cornered hat analysis of the OLO frequency jumps presented in Fig. 4.11. Examining all three beats, the frequency jumps are clearly attributable to the time scale local oscillator (124 K).

feedback to lock on the opposite side of the error signal. This allowed us to relock the servo without significantly changing the temperature of the electro-optic modulator as any changes in temperature inside the enclosure housing the ultrastable laser can degrade its stability. After relocking, an offset in the OLO frequency was observed. Over a 20 minute interval, the sign of the feedback was changed several times to investigate this effect. When fitting the frequency step in Fig. 4.11, only the data outside of this time period is used. The blue data corresponds to the data considered in the fit, while the grey data taken during the locking process was omitted. This second frequency excursion had a magnitude of 3.08×10^{-15}. A corresponding correction was applied to all data after each frequency step to account for the measured frequency excursion.

We note that the occurrence of such a jump when the clock is offline can still be corrected for in real time using this approach. If the jump is identified prior to calculating the Kalman filter prediction for epoch n, a constant frequency shift may be added to $\hat{k}_0[n|n-1]$ in Eq. 4.1. The time error introduced by a jump in the frequency of the OLO depends on the time required to identify the jump and apply an appropriate correction to the predictive model to compensate for it. Due to the excellent short-term stability of the three ultrastable lasers, this can happen almost immediately. Under the assumption that these two jumps, on average, are identified and corrected for within 1000 s we would anticipate an additional time error of only 5 ps.

4.3 Outlook

By combining an improved local oscillator with an accurate high-uptime optical clock, we have demonstrated a novel time scale architecture with enhanced stability. Additional technical upgrades of our silicon cavity can further improve our optical time scale stability, including greater passive thermal isolation, shorter optical path lengths and operation closer to the silicon coefficient of thermal expansion zero crossing. In addition, reducing the optical power incident on the cavity offers the capability to reduce the linear drift [153].

Future efforts will leverage existing time transfer infrastructure in Boulder, CO to incorporate this optical technology into the UTC(NIST) time scale. An underground fiber network is in place to support phase-stabilized optical signal transfer from JILA to NIST with negligible excess noise [163, 167]. Using a femtosecond frequency comb [162, 168], our optical time scale signal will be linked to UTC.

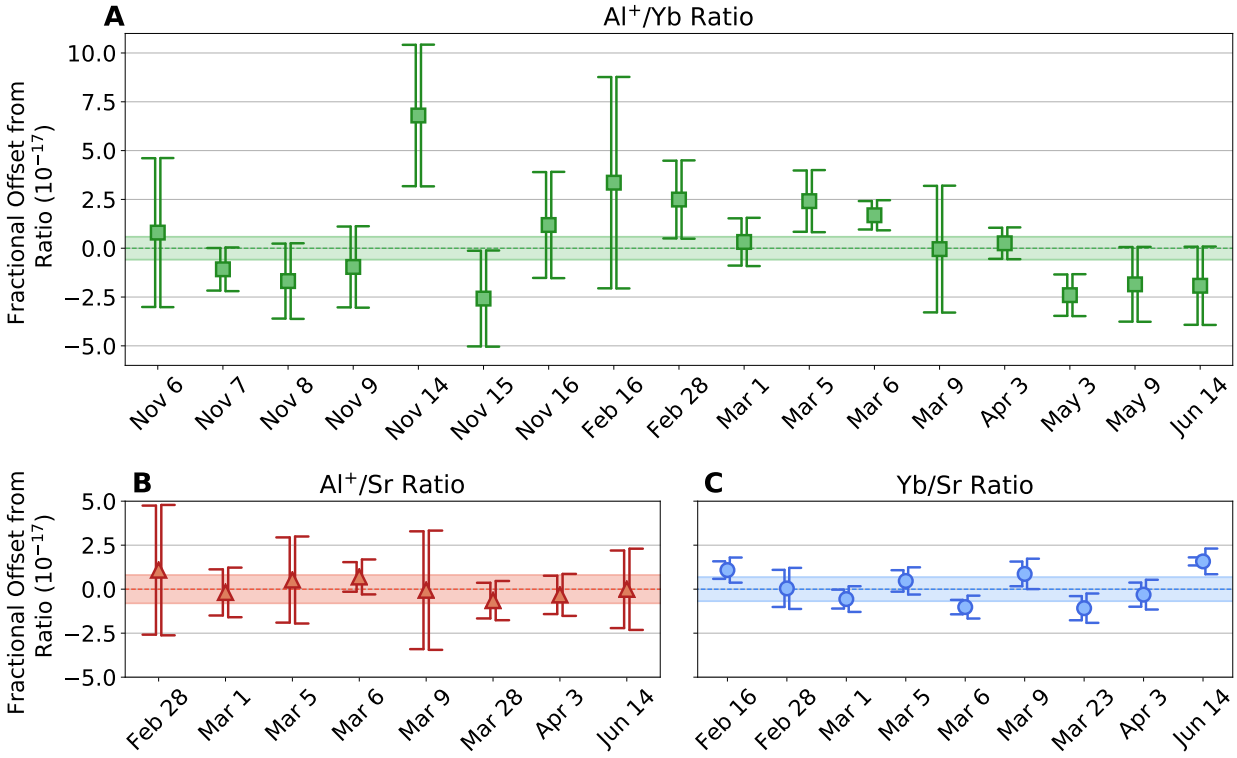

Figure 4.13: Frequency ratio measurements between optical clocks at NIST and JILA. Error bars to the left side of each data point represent statistical uncertainty, whereas error bars on the right represent the quadrature sum of statistical and systematic uncertainties. Lightly shaded regions correspond to the final uncertainty (1 standard deviation) of each ratio: 5.9×10^{-18}, 8.0×10^{-18} and 6.8×10^{-18}, for Al^+/Yb, Al^+/Sr and Yb/Sr, respectively. Figure reproduced from [169]

.

4.3.1 Applications

In this section, we briefly describe two experiments using the infrastructure from our optical timescale work. The first example is realizing an optical clock network in Boulder

for frequency ratio measurements with 18 digits of both precision and accuracy. Comparisons between optical clocks can circumvent the accuracy and stability limitations of microwave clocks to measure frequency ratios at unprecidented precision and accuracy. These measurements, currently undergoing worldwide [170], are an important step towards the redefinition of the second [25]. To compare clocks between JILA and NIST, microwave and optical signals must be transferred between labs with high fidelity. This was achieved using the infrastructure plotted in Fig. 4.7.Over the course of $\approx$ 6 months, measurements were made comparing our strontium clock frequency with the NIST Yb optical lattice clock and Al^+ ion clock as plotted in Fig. 4.13. These measurements culminated in the following ratios: $Al^+/Yb = 2.16288712751666 3703(13)$, $Al^+/Sr = 2.61170143178146302(21)$, $Yb/Sr = 1.207507039343337 8482(82)$.

In addition to forming an novel optical timescale, the data in Fig. 4.3 was used to place bounds on coupling to dark matter at low energy [19]. The details of this analysis are described in detail in the following Ph.D. theses [171, 172], so I will just provide a few conceptual remarks here. There are theoretical proposals that ultralight dark matter can couple to oscillations of the fine structure constant α [173]. Many of the components of our clock also depend directly on α, including our ^{87}Sr clock transition frequency, the oscillation frequency of a hydrogen maser, and even the lattice constant of our silicon cavity. As displayed in Fig. 4.14, comparisons of our silicon cavity frequency with either a hydrogen maser or our ^{87}Sr clock provide differential sensitivity to α. Given the comparison is made to the free-running silicon cavity, the excellent long-term stability of Si3 was critical to place competitive dark matter bounds.

4.3.2 Future improvements

There are a number of technical upgrades that may further improve the long-term stability of our silicon cavity apparatus. First we will discuss the principles of etalons and strategies to mitigate their effects. Parasitic etalons are a known source of instability in

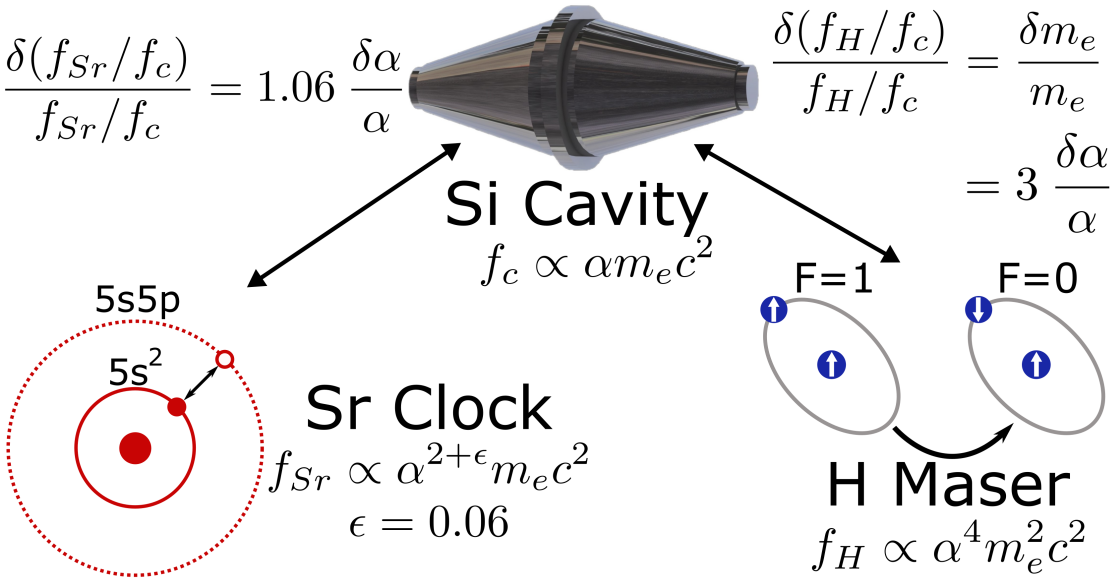

Figure 4.14: The ^{87}Sr clock transition frequency, the oscillation frequency of a hydrogen maser, and the lattice constant of our silicon cavity all depend directly on the fine structure constant α. Via atom-cavity comparisons, we realize differential α sensitivity to place bounds on the coupling of ultralight dark matter. Figure reproduced from [19]

.

optical experiments that have stringent noise requirements at low Fourier frequencies. Etalon effects can degrade the performance of a number of subsystems used in optical frequency metrology including ultrastable lasers, optical frequency combs, and fiber optic links as well as the sensitivity of advanced interferometric gravitational wave detectors [174, 175, 176]. To illustrate this concept, we consider the case of laser intensity modulation due to a parasitic etalon, though we note that this effect can also lead to phase noise and residual amplitude modulation (RAM).

$$\delta P(t) = P_{\mathrm{C}} + P_{\mathrm{E}} + 2\sqrt{P_{\mathrm{C}} P_{\mathrm{E}}} \cos\left(\frac{2\pi \delta x(t)}{\lambda}\right) \tag{4.5}$$

Here P_{C} is the optical power in the carrier, P_{E} is a portion of the total power that traverses a slightly different path than the carrier due to scattering off a rough optical surface or an undesired back reflection off of a transmissive optic or photodiode, and $\delta x(t)$ is the time-

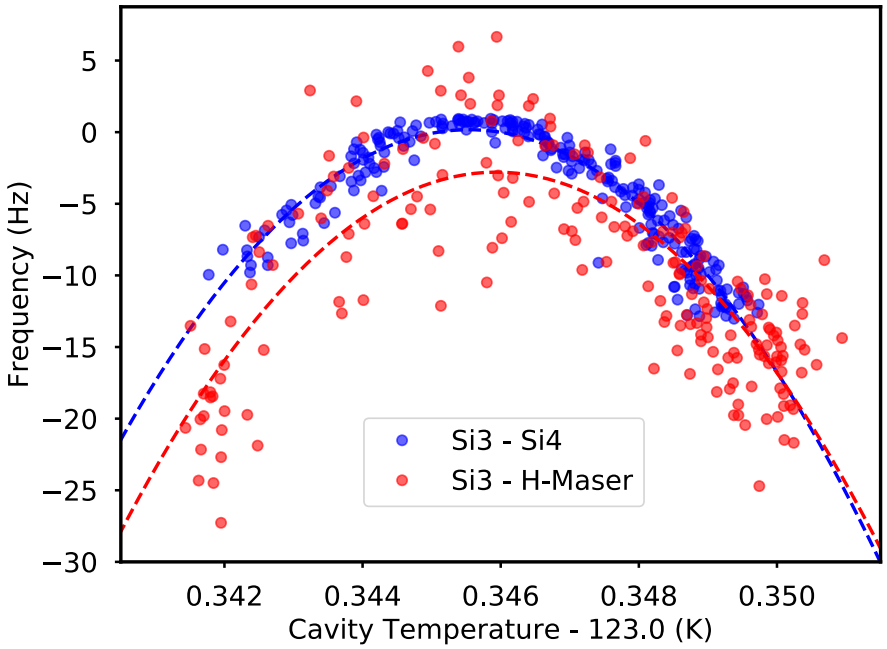

Figure 4.15: Measurement of the coefficient of thermal expansion (CTE) zero crossing. The temperature of Si3 was stepped by ∼10 mK and the cavity frequency was monitored by both the direct Si3/Si4 beat and the Si3/H-Maser comparison via a frequency comb.

varying path length difference between the two interfering fields. One sees immediately that this effect can be mitigated by reducing either P_{E} or $\delta x(t)$. To limit P_{E} in our optical setup, we used superpolished mirrors and lenses to reduce optical scatter to < 10 ppm per surface. To limit back reflections from photodiodes, Faraday isolators were installed in front of each detector and their optical windows were removed. Active temperature stabilization of our vacuum chamber was also added to improve the stability of the optical path length between the laser and reference cavity.

When characterizing the OLO prior to beginning this experiment, a strong correlation between slow drift in the optical power incident on the cavity and the laser frequency measured with the Sr clock was observed over a week long measurement. To address this, a photodetector was installed in transmission and a servo was added to stabilize the transmitted optical power.

The sensitivity of the Si reference cavity to temperature fluctuations is minimized by operating as close as possible to the temperature where the coefficient of thermal expansion (CTE) crosses through zero. Shortly after the completion of the data campaign, a measurement of the zero crossing temperature similar to that described in [154] revealed that we were operating approximately 4.5 mK above the optimal temperature. The data from this measurement is plotted in Fig. 4.15. The parabolic behavior of the cavity frequency is simple to intuit: one sweeps from a negative CTE coefficient to a positive value, with a zero crossing in the middle corresponding to the vertex of the parabola. Further details of this measurement are outlined in [171]. Using the measured temperature fluctuations on the innermost cryogenic shield, the thermal transfer function between this shield and the cavity, and the measured offset from the CTE zero crossing, one may estimate the temperature induced frequency instability of the OLO during the data campaign. As shown in Fig. 4.16, we estimate a contribution that is roughly consistent with the measured cavity noise term shown in Fig. 4.5. However, no clear temporal correlation between the estimated cavity temperature fluctuations and the frequency residuals from Fig. 4.3b was observed. Though this

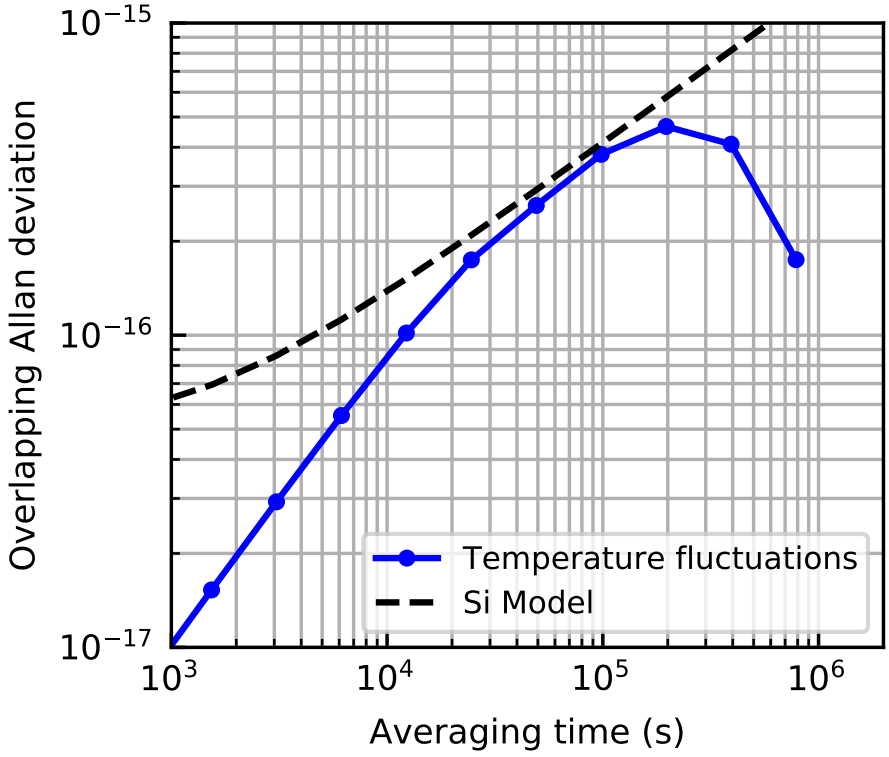

Figure 4.16: Frequency instability arising due to temperature fluctuations assuming an offset of 4.5 mK from the zero-crossing temperature for the Si coefficient of thermal expansion. The data agrees well with the cavity model from Fig. 4.5 between $10^4 - 10^5$s.

analysis is inconclusive, it suggests that operating closer to the CTE zero crossing will likely be required to significantly improve the OLO stability at averaging times which determine the Dick effect limit of the time scale stability ($10^3 - 10^5$ s).

Finally, we also discuss the possibilities of realizing optical cavities with frequency drift improved beyond the values reported in this work. Although the exact mechanisms for drift in crystalline cavities is still speculative, the optical power dependence revealed in [153] provided some hints. After waiting for a settling time long compared to any thermal time constant, the drift of Si4 showed a strong dependence on the circulating optical power. Given that Si4 used amorphous SiO_2/Ta_2O_5 dielectric coatings, there was great interest in studying the drift properties of the all-crystalline Si6 cavity using $Al_{1-x}Ga_xAs/GaAs$ coatings [177]

and test if the small but finite drift was due to properties of the mirror coatings. As shown in Fig. 4.17, preliminary drift studies show that Si6 displays an even reduced drift compared to Si3. Thermal engineering at cryogenic temperatures to achieve the same frequency stability at long averages times poses a challenge [152], however these initial studies show a very promising future for continuing to advance optical timekeeping. Work on Si6 is currently ongoing to improve upon the cavity drift and timescale results reported in this chapter. Additionally the use of multiple silicon cavities will add the necessary redundancy to address occasional downtime from lasers unlocking.

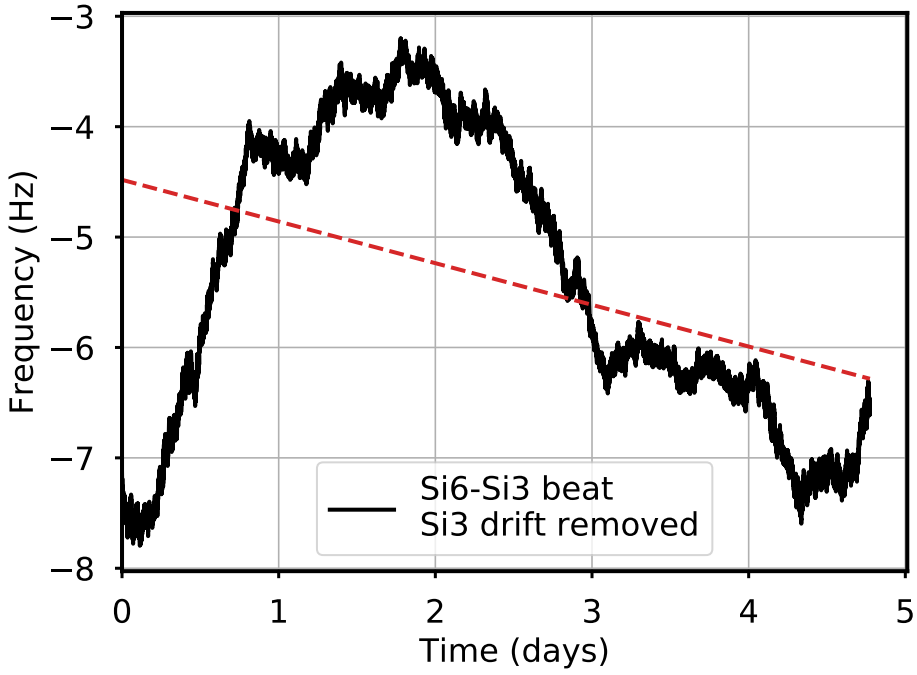

Figure 4.17: Measurement of the drift of the all-crystalline cavity Si6 including $Al_{1-x}Ga_xAs/GaAs$ coatings. The Si3 drift is determined from daily measurements with our ^{87}Sr clock and already subtracted from the black data. We fit a linear drift of -2.3×10^{-20}/s plotted in red. Figure adapted from [172].

Chapter 5

Operating optical clocks at high density

The research in this chapter is reported in the following publication: W. R. Milner, L. Yan, R. B. Hutson, C. Sanner, and J. Ye, *Phys. Rev. A* **107**, 063313 (2023).

5.1 Introduction

Enabled by the combination of ultralow temperature and three-dimensional confinement, when Sr2 first came online in 2017 there was a initial set of very exciting results. First, it was revealed that upon achieving state-insensitive trapping in a 3D lattice record atom-light coherence times were observed [33]. Interaction studies next showed the emergence of many-body interactions shifts substantially richer and more complicated than simply summing pairwise interactions [71]. All of these results were realized using an elegant spectroscopy technique relying on *in situ*, high resolution imaging to resolve differential frequency shifts on both spatial and spectral energy scales [178]. As highlighted in Fig. 5.1, images of ground and excited state atomic distributions provides a map for spatial variations of the clock frequency to be precisely measured. This *self-synchronous* clock comparison allows for rejection of clock laser noise and common-mode clock shifts (e.g. BBR temperature gradients) to achieve QPN-limited stability.

For future experiments, our eyes were ambitiously set on studying minute, unexplored clock shifts occurring at high atomic density. The foremost experiment was probing dipolar interactions, occurring at mHz energy scales between neighboring atoms [23, 179, 180, 24].

More broadly, operation of our ultracold ^{87}Sr clock platform at high density would open the door to a slew of new, exciting research directions. For example, spin-orbit coupling generated from clock addressing will enable explorations of cluster state generation and tunable spin models [181, 68]. Lattice thermometry [182] and studies of novel physics such as SU(N) magnetism [123, 183] are also enabled by our 10 nuclear spin components. Finally, there was reason to believe preparing insulating states in our 3D lattice where tunneling is inhibited could suppress motional dephasing effects [72, 70].

From the state-preparation work described in Chapter 2, we were confident we could prepare nuclear spin-polarized samples with a necessarily low temperature ($T/T_F < 0.2$) to achieve high filling ($na^3 > 0.9$). Following spin polarization [107, 184], the Pauli exclusion principle mandates there is at most one atom per lattice site in the ground motional state. To ensure this ground state motional occupation during lattice loading we operate with $k_BT < k_BT_F < \hbar\omega_{bg}$, where T, T_F, $\hbar\omega_{bg}$ refers to the atomic temperature, Fermi temperature and lattice bandgap respectively [132]. At the highest density affordable with one fermion per lattice site, this system realizes an insulating state of matter where tunnelling is suppressed [72, 185].

However, one important technical hurdle lay in our way: the imaging spectroscopy techniques reported in [178] cannot be trivially applied at high density. In our lattice where the average distance between atoms ($\lambda_{magic}/2 = 407$ nm) is comparable to the probe wavelength ($\lambda_{image} = 461$ nm), imaging with a weak, resonant probe is strongly perturbed. Both collective effects mediated by dipolar interactions [186] and density-dependent effects such as lensing of the probe beam [187, 188] introduce errors to the reconstructed density distribution at high density.

5.1.1 Imaging spectroscopy

To mitigate these systematic effects, different techniques can be used to reduce the absorption cross section and make the cloud 'optically thin'. These techniques can be broadly

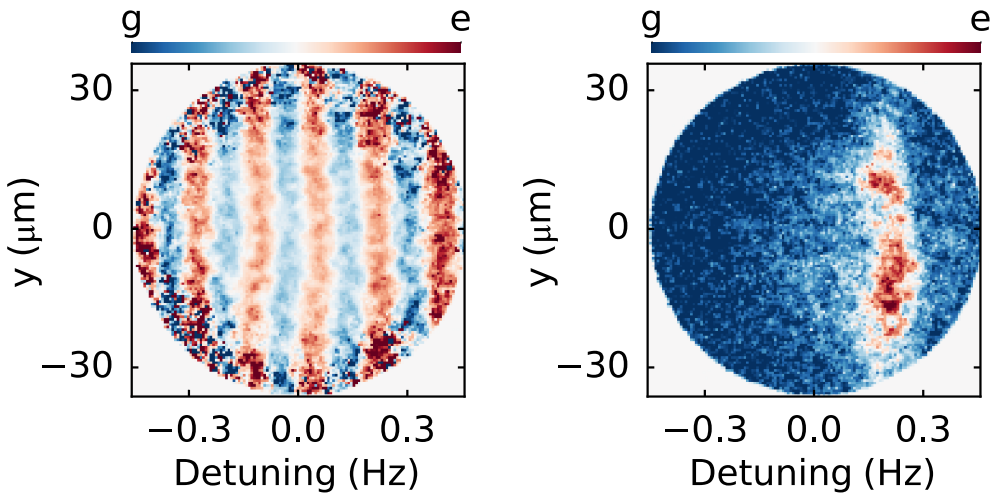

Figure 5.1: Imaging spectroscopy. *In situ* images of ground and excited state atoms following **left** Ramsey and **right** Rabi spectroscopy reveal spatially-differential frequency shifts. A magnetic field gradient (0.26 G/cm) was intentionally applied, so the atomic resonance frequency matches the clock laser frequency in a narrow spatial region. Reproduced from Ref. [178].

divided into two categories: dispersive imaging at large detuning from resonance [189, 190, 191] and saturated imaging at high intensity [192, 193, 194, 195].

5.1.2 Background on imaging techniques

We provide a brief overview of different imaging techniques for cold atoms in this section. The discussion here is based largely on the following seminal text in Ref. [187]. Essentially all information about cold atoms is retrieved from analyzing their interactions with coherent light fields [196, 197]. The relevant physics emerges from a semi-classical picture where one may consider the complex index of refraction:

$$n_R = 1 + \frac{\sigma_0 n \lambda}{4\pi}\left(\frac{i}{1+\delta^2+I/I_{sat}} - \frac{\delta}{1+\delta^2+I/I_{sat}}\right) \tag{5.1}$$

where δ is the normalized detuning in half linewidths ($\delta = \frac{\nu-\nu_0}{\Gamma/2}$), n is the atomic density, and σ_0 is the two-level absorption cross section $\sigma_0 = \frac{3\lambda^2}{2\pi}$.

For a plane wave $E_0 e^{ik_0 z}$ incident on our atom cloud, the k-vector is modified by

$k = k_0 n_R$. This has two immediate consequences: the light is attenuated (corresponding to the imaginary part of n_R) and also phase shifted (corresponding to the real part of n_R). So $E \rightarrow tE_0 e^{i\phi}$, where $t = \exp(-\frac{\tilde{n}\sigma_0}{2}\frac{1}{1+\delta^2+I/I_{sat}})$, $\phi = -\frac{\tilde{n}\sigma_0}{2}\frac{\delta}{1+\delta^2+I/I_{sat}}$ and $\tilde{n} = \int n \; dz$ is the integrated column density along the imaging axis z. Information encoded in the atomic density $\tilde{n}$ may thus be extracted by studying the phase shift or attenuation of the probe beam.

First we discuss 'absorption' imaging. Absorption imaging is historically the standard imaging technique employed on ultracold atom platforms and was used for the discoveries of the Bose-Einstein Condensate [198, 199] and degenerate Fermi gas [122]. The attractiveness of absorption imaging is rooted in its simplicity, requiring only a single beam, and its capability to achieve a high signal-to-noise ratio without the constraint of a high numerical aperture (NA) as demanded in fluorescence imaging. For essentially any measurement probing dilute ensembles in time-of-flight, absorption imaging is the technique of choice. Absorption imaging extracts the column density $\tilde{n}$ by analyzing of missing photons from our probe beam and relating it to the attenuation parameter t. Thus, one operates on-resonance so $\delta = 0$ and $\phi = 0$ and $E \rightarrow tE_0$ so the intensity on camera is $I_{abs} = |E|^2/2 = I_0 t^2$. In the low-saturation regime ($I/I_{sat} \ll 1$), the column density is simply logarithmically related to the transmission and $I = I_0 e^{-\tilde{n}\sigma_0}$ referred as the Beer-Lambert law in chemistry textbooks. The full equation to extract $\tilde{n}$ including saturation effects as discussed in Eq. 5.5. In summary, at high saturation each atom scatters photns at a rate $\Gamma/2$ and instead there is a linear relation between atom number and missing photons. The full expression accounts for both effects and $\tilde{n} = \frac{1}{\sigma_0}\Big[\log(s_0/s_1) + (s_1 - s_0)\Big]$ where s_0 (s_1) are the saturation intensities in images (with) without atoms.

As seen in the paragraph above, even if our probe beam $tE_0 e^{i\phi}$ contains phase sensitive information a simple image of the beam on our camera will only reveal spatial variations of t^2. Retrieving this phase information requires spatially filtering the scattered and unscattered components of the probe beam as displayed in Fig. 5.2. A simple technique to achieve this

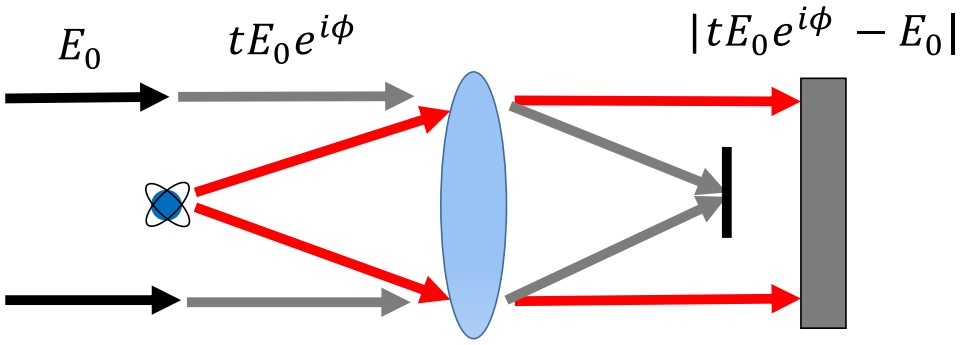

Figure 5.2: Schematic for *Dark Ground* imaging. The scattered field $tE_0e^{i\phi}$ and the unscattered field E_0 are separated in the Fourier plane, so the signal on the CCD is sensitive to the ϕ^2 in Eq. 5.2.

is employing *Dark Ground* (DG) imaging, where the unscattered field in blocked the Fourier plane. Perhaps surprisingly, just blocking this unscattered component of the beam gives a phase sensitive signal.

$$I_{DG} = |E - E_0|^2/2 = I_0/2\left(1 + t^2 - 2\,t\,\cos(\phi)\right). \tag{5.2}$$

At large detuning $\delta \gg 1$, we can approximate $t \approx 1$ and $\cos(\phi) \approx (1 - \frac{1}{2}\phi^2)$. Then, $I_{DG} \approx I_0\phi^2$ and we realize a method to directly examine phase shifts of our probe beam. We note this dispersive imaging technique is slightly simpler than *phase contrast* imaging, which requires phase shifting the unscattered beam by $\pi/2$ radians.

Our first measurements for *in situ* imaging at high density used DG imaging. The measurements are shown in Fig. 5.3. The gray line is the atom number measured with time-of-flight absorption imaging, where the optical density is sufficiently low that systematic errors can be ignored. While we were satisfied to see that the apparent atom number saturated at high detuning and was in reasonable agreement with dilute absorption imaging, there were still residual doubts about this technique. First, using DG imaging demanded precise fabrication and alignment of custom optics developed by the Keck lab at JILA. Thus, we found that using this technique required a painstaking alignment procedure for operation

that was susceptible to systematic drifts. Additionally, careful studies of dispersive imaging had shown that residual systematic effects at finite detuning are non-negligible and required using differential measurement schemes at opposite detuning to be addressed [200].

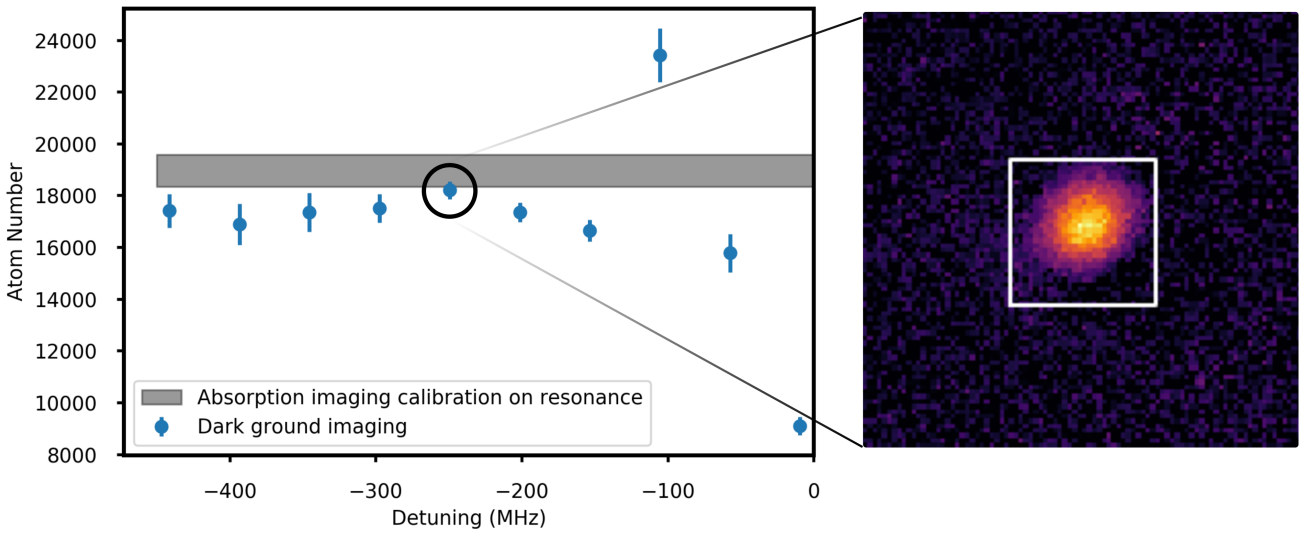

Figure 5.3: Dark-ground imaging measurements. **Left:** Atom count appears to saturate at large detuning. Anomalously large atom number at ≈ -100 MHz was repeatable, but never investigated. **Right:** Image of atomic distribution in Fermi gas via dark-ground imaging is plotted.

A much simpler strategy to overcome these systematic errors at high density, which was ultimately used for the main results reported in this chapter, is to use resonant, highly saturated imaging techniques to make the cloud optically thin. For fluorescence imaging, this is particularly attractive as the signal-to-noise ratio does not degrade as one strongly increases the probe intensity. Rather in fluorescence imaging the signal-to-noise is entirely determined by the number of collected photons, which is practically limited by the NA. Thus operating with an $I/I_{sat} >> 1$ the scattering rate is homogeneous for all atoms and largely immune to beam intensity, frequency, and pointing fluctuations. The details of this measurement scheme are outlined in Section 5.2.

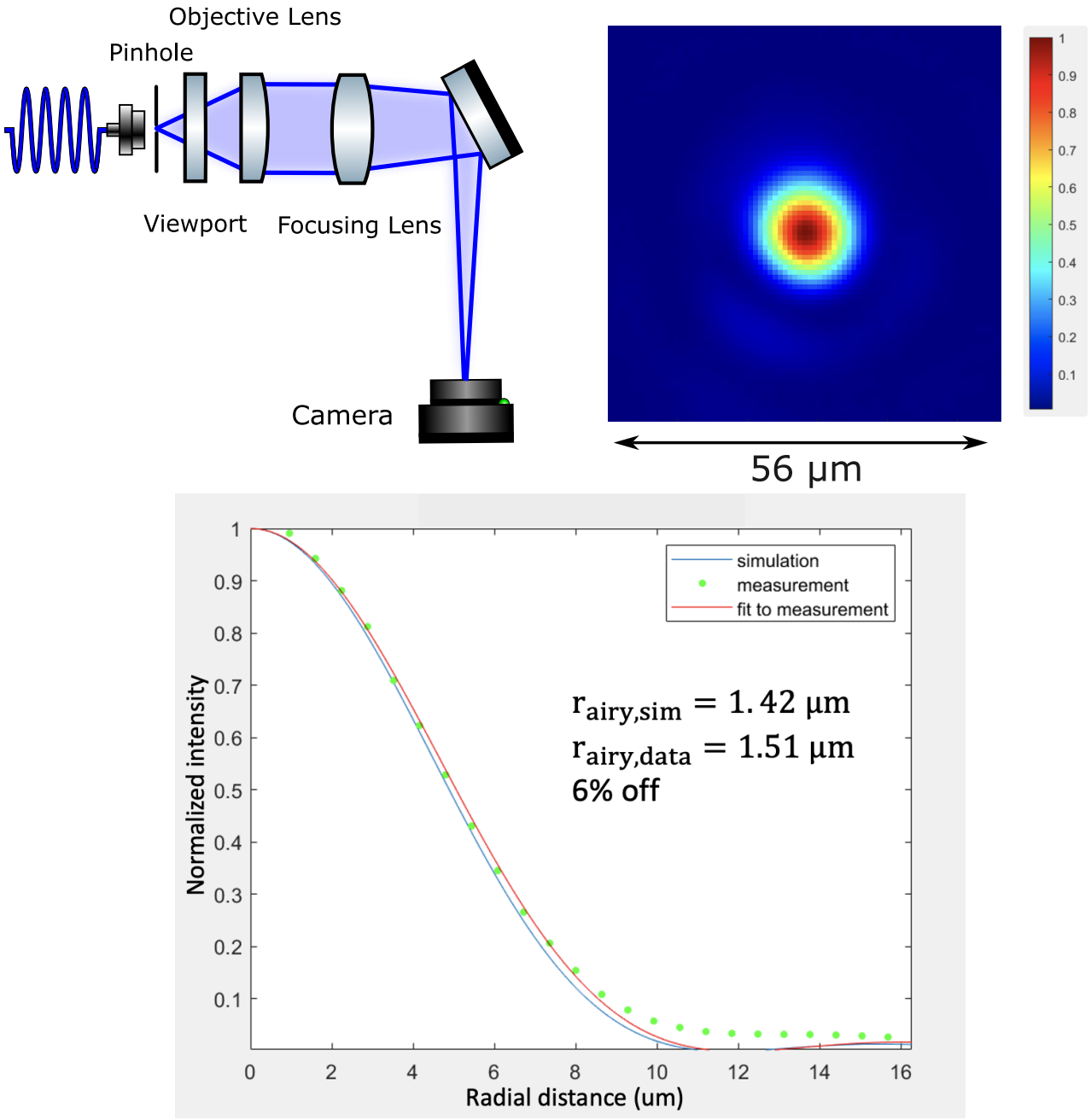

Figure 5.4: Imaging system calibration. **Top left:** We measured the point-spread-function (PSF) using an illuminated pinhole propagating through a mock imaging system including our objective lens and experiment viewport. Magnification of imaging system can be changed with the 'focusing lens' in the diagram. **Top right:** The image of our PSF is shown. **Bottom:** We plot the azimuthal average of the imaged PSF in green dots. We compare to the calculated PSF (blue) and to an Airy disk fit (red) of the data. We observe a 6% disagreement between the fitted and calculated radii.

5.1.3 Imaging system

While systematic errors at high density may place challenges on imaging, there is a far more strict restriction that must first be addressed: the diffraction limit. The spatial resolution of an imaging system is fundamentally limited by the Numerical Aperature $NA = n\sin(\theta)$ where θ is the half-angle of the maximum cone of light that can enter the imaging system. In geometric terms, one needs to 'collect' the large k-vectors of light to study fine spatial structure. Practically, one must also reduce all aberrations of the imaging system to be 'diffraction-limited'.

Imaging system calibration is shown in Fig. 5.4[1] . We measured the point-spread-function (PSF) using an illuminated pinhole propagating through a mock imaging system including our objective lens and experiment viewport. This was compared with calculated Airy disk distribution $I(x) \propto \left(\frac{2\mathcal{J}_1(x)}{x}\right)^2$ where $x \equiv ka\sin\theta$. Here, k is the standard wavenumber, a is the aperture size, and θ is the angle of observation. We observe a 6% disagreement between the fitted and calculated radii.

A schematic of our vertical imaging is shown in Fig. 5.5. The details of the interface with the vertical clock laser and optical lattice are detailed in Chapter 3. The most important optical element in our imaging system, which sets our imaging resolution, is our objective lens. We use a commercial Thorlabs AL50100G aspheric lens with $f_{obj.} = 100$ mm and $NA = 0.20$. Diffraction limited performance is achieved with this lens in an 'infinite conjugate ratio' configuration. This means the lens is designed to collimate light from a point source and thus the lens is placed $f_{obj.}$ away from the atoms. Despite being inexpensive, it works quite well and the custom AR coating from LaserOptik is plotted in Fig. 3.15. A lens from Thorlabs ACT508-400-A-ML with $f_{int.} = 400$ mm is used to form an intermediate imaging plane. The magnification of imaging system is now $f_{int.}/f_{obj.} \approx 4$. When designing our imaging system, we wanted to have the flexibility to quickly change the imaging system magnification without

[1] Thanks to Jonathan Friduss for taking these measurements.

having to move our camera or re-align optics. Mitutoyo sell lens systems with a fixed image-object distance, in this case 280 mm. Thus one can swap in different lens systems and enjoy variable magnification while the image-object distance does not change. To ensure the imaging resolution is not compromised, the NA of this magnification stage needs to be larger than or equal to the primary objective NA (i.e. so we don't 'throw away' the high k-vectors with our secondary imaging stage). For the images in this chapter, we used a Mitutoyo $375-039$ with magnification $10\times$ and $NA = 0.21$.

As outlined in Chapter 3, we also wanted to have the flexibility to tilt our imaging system to avoid etalons of our imaging beam or superlattices with our vertical lattice formed between the viewports. The historical vertical imaging system, whose details are in [101], featured a clever design where the vertical lattice was *reflected* off the objective lens. However, we found that achieving the simultaneous conditions of diffraction-limited imaging and a stable vertical lattice were practically not feasible. One could form a deep, well retro-reflected vertical lattice, then observe severely distorted imaging and vice-versa. Thus, having the capability to adjust the imaging system orientation and vertical lattice retro-reflector independently was direly needed.

As seen in Fig. 5.5, the JILA shop constructed a very nice mount that achieved this condition. Now, the vertical lattice is *transmitted* through the objective and reflected off a dichoic mounted on the 2 inch Polaris mount. The HR coating of the dichoic is plotted in Fig. 3.15. However, we still needed to determine what degree of tilt was tolerable to remain diffraction-limited. Aberrations from tilting the imaging beam are depicted Fig. 5.6 as simulated in the ray-tracing software OSLO. These simulations consider the full imaging system including the viewport, which crucially breaks the symmetry of the imaging system. The black circle is the diffraction-limited spot size. Given this ray-tracing software does not account for diffraction, we want to just be in the regime where the aberrations are small compared to the diffraction-limit. A tilt $\theta < 0.5^\circ$ appears to be safe. While all this engineering may seem like overkill, having all the degrees of freedom to optimize this juncture

of beams was fairly critical.

5.2 Saturated imaging at high density

Using highly saturated imaging to mitigate imaging errors, with a saturation parameter far greater than the optical depth, we accurately confirm the density distribution in our 3D optical lattice in good agreement with thermodynamic calculation. We extend previous work using high intensity fluorescence imaging [192], confirming the accuracy of this imaging technique in a new high density regime with a degenerate Fermi gas of ^{87}Sr [107, 201]. With atomic densities as high as 6×10^{14} atoms/cm^3, we observe systematic agreement with atom counts obtained via time-of-flight absorption imaging and identify the range where the extracted atomic density distribution is not blurred by our imaging pulse.

Our high intensity imaging scheme is outlined in Fig. 5.7. The combination of atomic level structure and relatively large mass of ^{87}Sr is particularly well suited for our imaging technique, providing a cycling transition with a large scattering rate while avoiding significant motional effects from the imaging pulse. The transition from $^1S_0$ to $^1P_1$ with linewidth $\Gamma = 2\pi \times 30.2$ MHz provides a large photon scattering rate with minimal depumping to dark states during the imaging time [202]. During a 1 μs pulse at full saturation about 100 photons per atom are scattered and the atoms accelerate at $a = \frac{\hbar k \Gamma}{2m}$ where k is the imaging light wavenumber and m is the atomic mass. The net momentum transfer amounts to a Doppler shift of $ka\tau = 2.8$ MHz which is much less than the transition linewidth $\Gamma/2\pi$. Finally, the linear displacement for a 1 μs pulse at full saturation is just $\frac{a\tau^2}{2} = 0.6$ μm. This linear displacement and corresponding Doppler shift can be largely cancelled in fluorescence imaging by retroreflecting the incident beam. The spread in transverse position due to random momentum transfer from spontaneous emission is $\frac{\hbar k}{6m} t^{3/2} \sqrt{\Gamma/2} < 0.1$ μm over a 1 μs pulse duration and small compared to our 1.3 μm imaging resolution [203]. Using highly saturated absorption imaging, we measure the column density distribution $\tilde{n}$ in our optical lattice in Fig. 5.7a. Accounting for the lattice spacing $a = 407$ nm corresponding to the ^{87}Sr

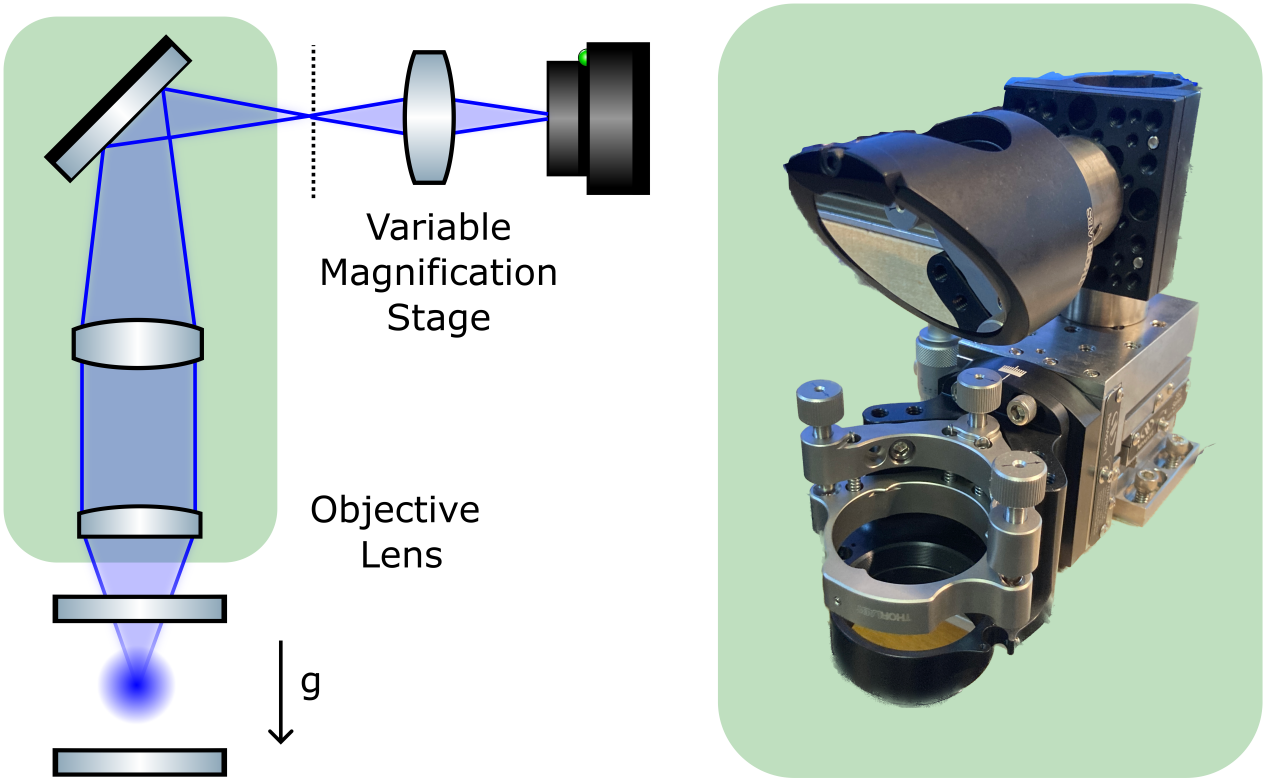

Figure 5.5: **Left:** Vertical imaging system schematic is shown. Objective lens with $NA = 0.2$ and variable magnification stage are depicted. **Right:** Mount constructed by JILA machine shop is shown. Tilt meter can precisely determine the degree that the objective is tilted with respect to the viewports.

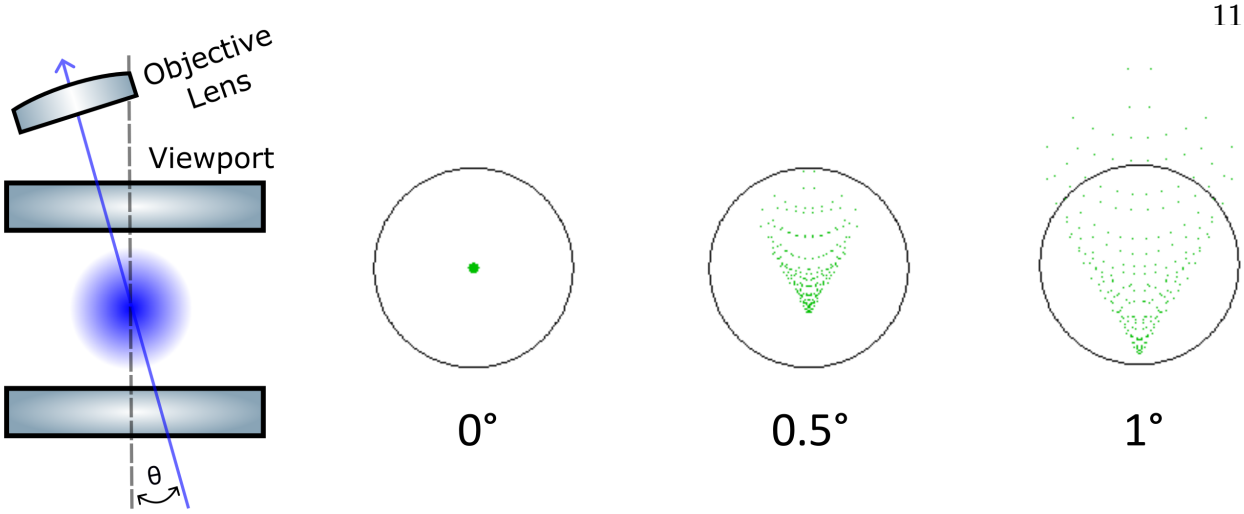

Figure 5.6: **Left:** Tilt of imaging beam with respect to viewports causes aberrations. **Right:** Aberrations from tilting probe beam simulated in OSLO. Note these aberrations arise from the relative angle between the probe beam and viewports, and thus cannot be compensated by adjusting the objective lens. Operating $\leq 0.5°$ is necessary to strongly avoid these aberrations.

magic wavelength at 813 nm, the scaled column density $\tilde{n}a^2$ is plotted.

Saturated absorption and fluorescence imaging are beneficial in comparison to standard imaging techniques in a number of ways. In this highly saturated regime the scattering rate is largely immune to beam intensity, frequency, and pointing fluctuations. Given the saturation intensity $I_{sat} = 40$ mW/cm^2 for the imaging transition, a Gaussian probe beam with 20 mW of optical power and a 100 μm waist corresponds to a peak intensity of $I \sim 3000$ I$_{sat}$, within the typical constraints of a standard imaging laser system. Given that the probe beam is attenuated through the atom cloud, a saturation parameter I/I_{sat} much greater than the optical depth is required to fully saturate the imaging transition. We note parallels between fluorescence and absorption imaging at high saturation. In both cases, the extracted atom number is determined by a single variable. For fluorescence imaging, this corresponds to the number of collected photons per atom and for saturated absorption imaging the number of missing photons per atom in the probe beam. Thus, both fluorescence and saturated absorption imaging can be calibrated via a single absolute atom number measurement. For images

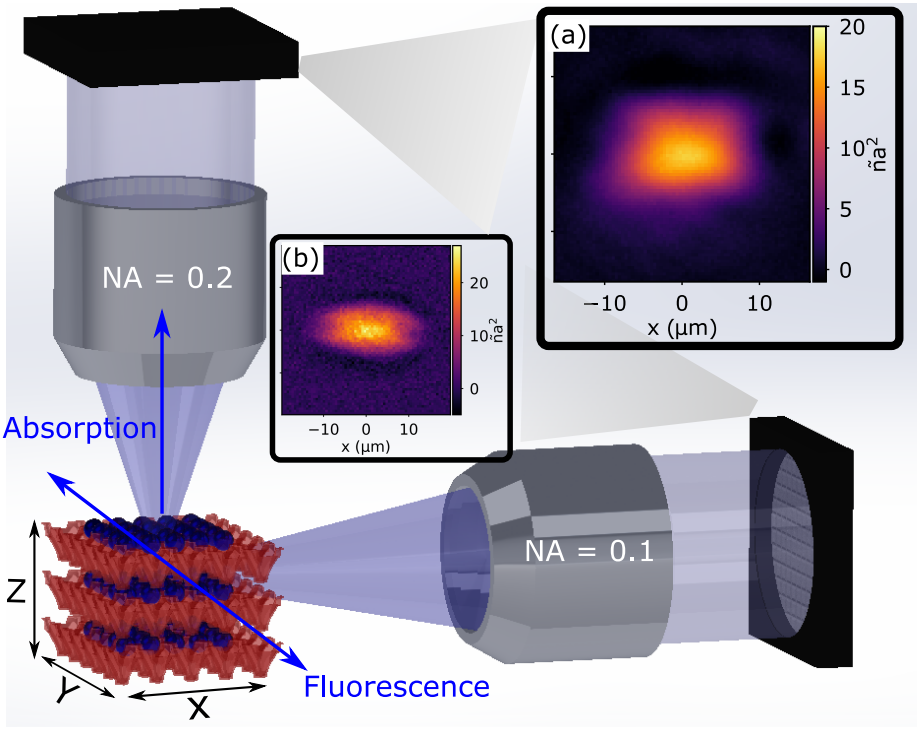

Figure 5.7: Schematic of our clock platform. Vertical and horizontal imaging systems with numerical apertures of 0.2 and 0.1 respectively provide measurements of the 2D density distribution $\tilde{n}$. Accounting for the lattice spacing $a = 407$ nm, $\tilde{n}a^2$ is determined from highly saturated absorption imaging. To mitigate imaging errors, the atoms are highly saturated and each scatters photons with a maximum rate of $\Gamma/2$. Measurements from our high resolution imaging system integrated along gravity are presented in panel **(a)**, where the density distribution is extracted for thermodynamic modeling. Images from the horizontal imaging system in panel **(b)** are just used to determine our atom cloud aspect ratio for our inverse Abel transform.

in our 3D lattice, we determine our atom number via clock excitation fraction fluctuations arising from quantum projection noise (QPN) [29].

For fluorescence imaging, only a single image of collected fluorescence in an arbitrary direction is required, minimizing fringing and simplifying image processing substantially. Fluorescence imaging also avoids limited dynamic range issues suffered from high intensity absorption imaging. Strategies such as multiple measurements at varying intensity to determine the atomic density in different regions of the cloud may be taken to confront this issue [194, 195]. The primary disadvantage of fluorescence imaging in comparison to absorption imaging is that the signal-to-noise is generally worse. To optimize signal-to-noise ratio (SNR) in fluorescence imaging, the photon collection efficiency and therefore the numerical aperture (NA) of the imaging system, must be maximized. In our experiment, the vertical and horizontal imaging systems have numerical apertures of 0.2 and 0.1, corresponding to collection efficiencies of approximately 1% and 0.25%. Alternatively, if spatial resolution is not required then the pulse duration can be extended enhancing the number of detected photons.

5.2.1 In situ imaging characterization

To initially benchmark our saturated imaging techniques used for Fig. 5.8, we probe an uncharacterized Fermi gas via extremely-high intensity fluorescence to guarantee that complete saturation is achieved and collective effects are negligible. In this extreme regime, the absorption imaging signal-to-noise is very poor. For later measurements to achieve optimal signal-to-noise, we employ a more reasonable intensity for absorption imaging, although still under the operating condition of $I/I_{sat} \gg OD$. Absorption imaging at $\mathrm{I} \sim \mathrm{I}_{sat}$ and high intensity fluorescence imaging are presented side-by-side for comparison. To study these systematic errors at high density, we prepare a sample with optical depth > 200 by producing a degenerate Fermi gas with 10 nuclear spin components, $\approx 2 \times 10^5$ atoms and a T/T_F of approximately 0.1 in a crossed dipole trap. The errors associated with low intensity

absorption imaging can be seen twofold. First, the reconstructed optical depth from absorption detection in Fig. 5.8a is far too low, two orders of magnitude less than the expected value of ~ 200. This erroneously low optical depth is attributed to effects such as enhanced forward emission and lensing of probe light [187]. Secondly, the reconstructed optical depth in Fig. 5.8b increases after a 500 μs time-of-flight expansion conclusively demonstrating the density dependence of these observed systematic errors.

In comparison, saturated fluorescence imaging yields a far larger reconstructed optical depth and diffuses following expansion as expected. We compare this reconstructed 2D density distribution with the expected distribution corresponding to a Fermi gas. Using independently measured experimental values, we calculate this distribution with no free parameters [204]. The total atom number and reduced temperature T/T_F are determined from time-of-flight absorption imaging at low density with an optical density ~ 1. The trapping frequencies are extracted from parametric confinement modulation. Using these parameters, we calculate both an *in situ* and 500 μs time-of-flight Fermi gas profile for comparison with our measurements. We observe qualitative agreement between measurement and calculation in Fig. 5.8c and Fig. 5.8e at these extremely high optical depths.

Intrigued by the measurements presented in Fig. 5.8, we undertake a quantitative study on the fidelity of our saturated imaging technique. We present a calibration method for fluorescence detection, using the total number of collected fluorescence photons for comparison with an accurate atom number reference. Absorption imaging at low density following time-of-flight expansion serves as an appropriate calibration. Following expansion for 7 ms, the optical depth is ~ 1 and systematic imaging errors can be safely ignored. To independently calibrate the atom number in our 10 spin Fermi gas, we prepare a thermal sample and use measured density fluctuations to determine the effective absorption cross section [205, 206, 207]. In Fig. 5.9a we ensure this calibration shows agreement with a simple linear model for atom numbers ranging from 0.5×10^5 to 4×10^5, varied by controlling our final evaporation trap depth. For the 3 μs pulse duration used, the fitted calibration is in rea-

sonable agreement with independent calculation using the measured quantum efficiency and imaging system numerical aperture. To ensure that the imaging transition is fully saturated, the laser intensity at 1 μs pulse duration is increased until the collected photon number plateaus, as seen in the figure inset.

To perform accurate spatially resolved measurements, we must also determine the blurring induced by our imaging pulse. Just as collective effects introduce errors to the reconstructed density distribution, any systematic changes to $\tilde{n}$ introduced by our imaging pulse must be determined. To calibrate this blurring in Fig. 5.9b, we extend the fluorescence pulse duration and examine the peak column density as atoms diffuse. The inset shows averaged images from 500 ns and 2 μs pulse durations. We note that we observe no atom loss or molecular formation over the full 2 μs range, confirmed by the detected photon count increasing linearly with pulse duration. To minimize blurring, we carefully retroreflect our probe beam by optimizing the backcoupled light through the probe optical fiber. At pulse durations up to 1 μs, we confirm that the peak column density decreases by $< 5\%$.

5.2.2 Band insulator demonstration

Motivated by the calibration reported in Fig. 5.9, we directly determine the 3D density distribution in a deep optical lattice via saturated *in situ* absorption imaging. We form a cubic lattice with trap depths of approximately 60, 70, and 50 E_r in three orthogonal directions, where E_r is the lattice photon recoil energy $\approx h \times$ 3.5 kHz. Following forced evaporation with 10 nuclear spin states we spin polarize using a focused beam detuned from the $^3P_1$ intercombination line to form a state-dependent potential, removing nearly all but the m_F = -9/2 atoms [107, 184]. Clock spectroscopy confirms $\approx 90\%$ spin purity. An additional step of spin purification is applied by coherently driving the m_F = -9/2 atoms into the excited clock state and removing any residual spins with a resonant imaging pulse. Absorption imaging directly provides us with the column density distribution $\tilde{n}$, integrated through the vertical axis along gravity as depicted in Fig. 5.7a. Based on our Fig. 5.9b

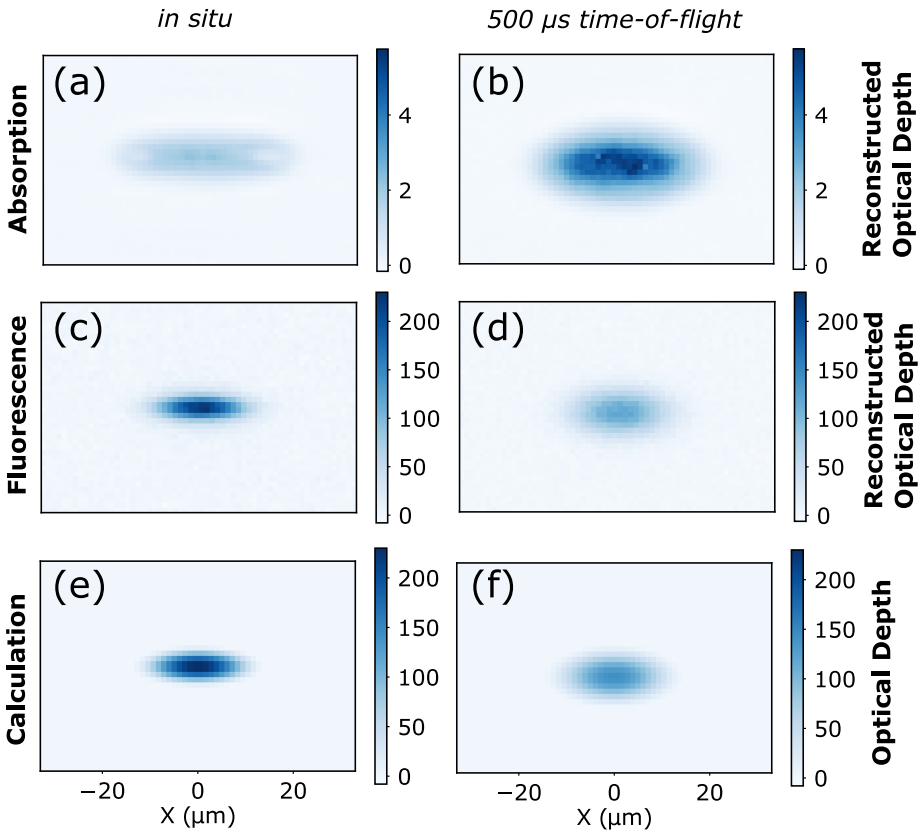

Figure 5.8: A comparison of high intensity fluorescence and standard absorption imaging ($I \sim I_{sat}$) at optical depths exceeding 200 in our highly degenerate Fermi gas is shown. *In situ* absorption imaging at low intensity yields strikingly erroneous measurements at high density. The calculated 2D Fermi gas distribution according to our experimental parameters is shared for comparison in qualitative agreement.

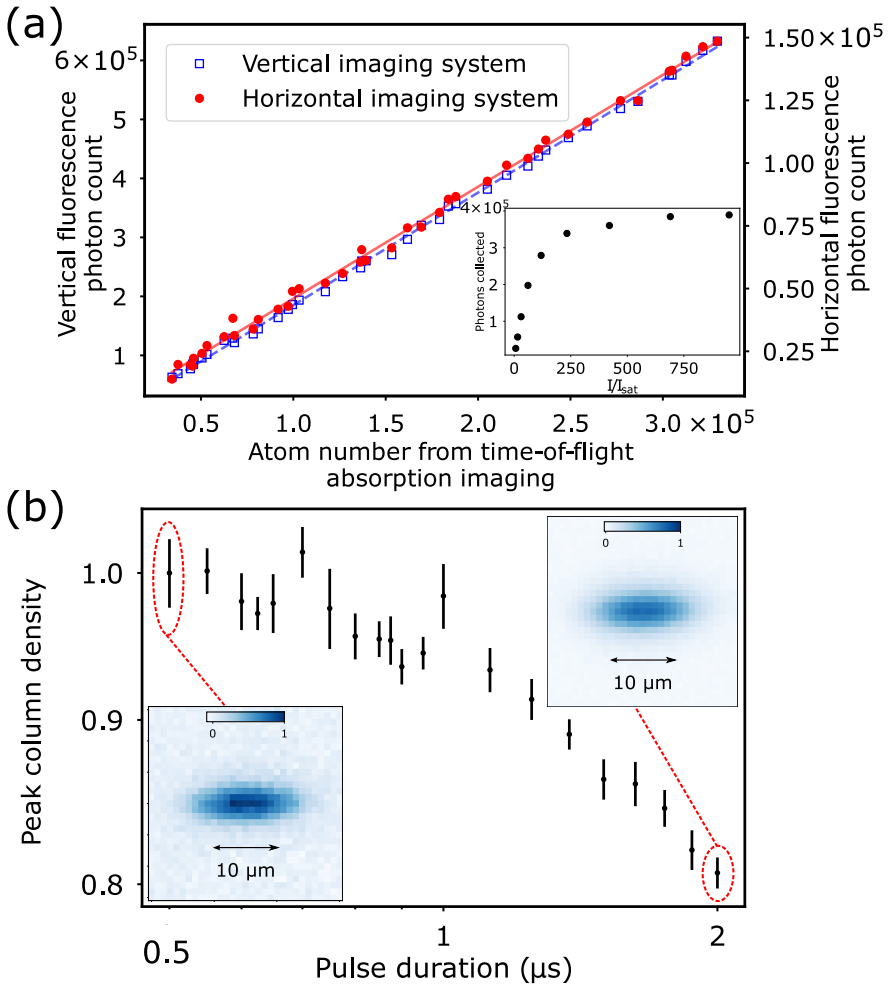

Figure 5.9: **(a)** Calibration method for *in situ* fluorescence detection using atom counts from time-of-flight absorption imaging. Collected photon counts from both the vertical and horizontal imaging systems are plotted, with solid and dashed lines representing fits to the horizontal and vertical measurements respectively. Inset: Collected photon count with vertical imaging system as a function of I/I_{sat} at 1 μs pulse duration. **(b)** Peak column density as a function of fluorescence pulse duration. Measurements are normalized by 1.9×10^{11} atoms/cm^2, the column density at the shortest pulse duration of 500 ns. Images at 500 ns and 2 μs in inset are plotted for comparison. The error bars denote the standard error of the mean.

analysis, we choose a pulse duration of 1 μs to minimize blurring and a saturation intensity of 54(4), substantially larger than peak optical density of ~ 15. To spatially probe the band insulator plateau we use an imaging magnification of 38.8 to achieve an effective pixel size of 412 nm, roughly equal to the lattice constant $a = 407$ nm. We note that our effective pixel

size is smaller than our optical resolution of 1.3 μm, thus our imaging system is optically oversampled. To extract the 3D density distribution, we use an inverse Abel transform [208]. Given our vertical imaging is not along an axis of cylindrical symmetry, n must be appropriately scaled by the aspect ratio of the spatial density distribution. The aspect ratio is independently calibrated using the absorption imaging measurement in Fig. 5.7b.

At this high magnification, the SNR in fluorescence imaging for a 1 μs pulse duration is limited by a combination of read noise and photon shot noise. We found that even after extensive averaging the extracted 3D density distribution using an inverse Abel transform was sensitive to small fluctuations in $\tilde{n}$. Thus, saturated absorption imaging with a superior SNR provides a more robust technique to characterize the 3D density distribution. This extracted 3D density distribution is plotted in Fig. 5.10a.

To judge the fidelity of our measured 3D density distribution, we compare the line cut at both $z = 0$ and $y = 0$ with calculation in Fig. 5.10b. To estimate the density distribution, we use a thermodynamic calculation in the local density approximation. [182, 183]. The ingredients of this calculation include values for the entropy-per-particle, harmonic confinement, and total atom number. Given the density distribution only depends on the ratio of the respective harmonic confinements, the measured aspect ratios from Fig. 5.7 are used for our thermodynamic calculation. The total atom number N is determined from quantum projection noise measurements. To estimate the entropy-per-particle including heating from lattice loading, we perform a "round-trip" measurement where we load the atoms from our optical dipole trap into the three-dimensional optical lattice and then reverse the sequence to load them back into the dipole trap [182, 71]. Measuring a reduced temperature in time-of-flight of $T/T_F = 0.151(4)$ and $0.179(7)$ before and after lattice loading respectively, we determine an entropy-per-particle increase of $0.25(6)\ k_B$. Inferring half of that entropy increase in the actual lattice loading, we estimate an entropy-per-particle $s/k_B = 1.56(6)$ in the lattice. From the data in Fig. 5.10b, we fit $s/k_B = 1.49$ in good agreement with prediction. Although we did not perform a cross-dimensional thermalization measurement to directly

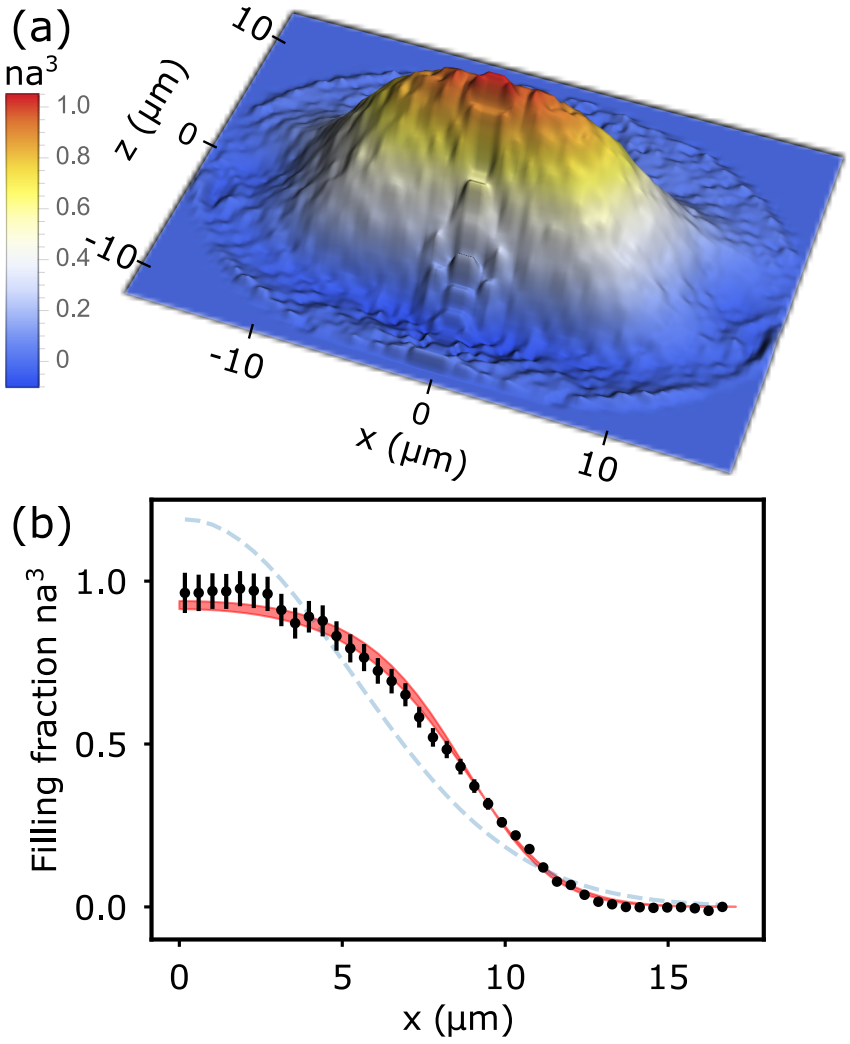

Figure 5.10: **(a)** The three-dimensional density distribution and the corresponding lattice filling fraction are determined from *in situ* absorption image in Fig. 5.7a and the use of an inverse Abel transformation. **(b)** A linecut along $z = 0$ and $y = 0$ provides the data points in circles. Errorbars are both the statistical uncertainty of the Abel transformation and atom number uncertainty added in quadrature. We start with a prediction based on thermodynamic calculation, using independently measured values for the entropy-per-particle, atom number, and harmonic confinement. The best fit to the data results in a 10% reduction of the measured aspect ratio ω_y/ω_x and 5% reduction of the predicted entropy-per-particle. The red line captures this fit, with entropy-per-particle uncertainty in the shaded band. The blue dashed line is a fit to Gaussian in qualitative disagreement with na^3.

verify thermal equilibrium, the uncertainty in our predicted entropy-per-particle is included in the shaded band of the thermodynamic calculation in Fig. 5.10b [209, 210]. We note that the extended plateau region is larger than our 1.3 μm imaging resolution. We compare na^3 to a Gaussian fit and observe strong disagreement near the center of the cloud owing to the fermionic nature of the atoms in our optical lattice.

5.2.3 Density diffusion

Here we provide supplemental analysis to the data presented in Fig. 5.9b. In panel A of Fig. 5.11, we plot the integrated counts along the x axis of each image. We see an asymmetry emerge along the direction of the probe beam as the pulse duration is extended. This asymmetry suggests that the observed density diffusion may arise from inhomogeniety between the incident and retroreflected beams. While the power is certainly mismatched, this could also be due to either imperfect spatial alignment or mode mismatch given the divergence of the probe beam.

We also plot the total counts in each image as a function of pulse duration in panel B. The linear character of the counts over the full pulse duration range suggests that we do not observe appreciable atom loss or pumping to dark states. The counts at each pulse duration are normalized to the counts at 500 ns. The inset shows the Gaussian RMS width of the cloud as a function of pulse duration.

5.2.4 Signal-to-noise comparison between imaging techniques

In the main text of the paper we refer to both saturated absorption and fluorescence imaging. We provide a quantitative comparison of the signal-to-noise ratio (SNR) between the two techniques here. We express our signal-to-noise for a detection pixel in terms of the normalized variance $\mathbb{V}(N)/N$, where N denotes the number of atoms within the respective detection region. For fluorescence imaging the SNR is simply determined by the shot noise associated with the number of detected photons. To calculate the total atom number, we

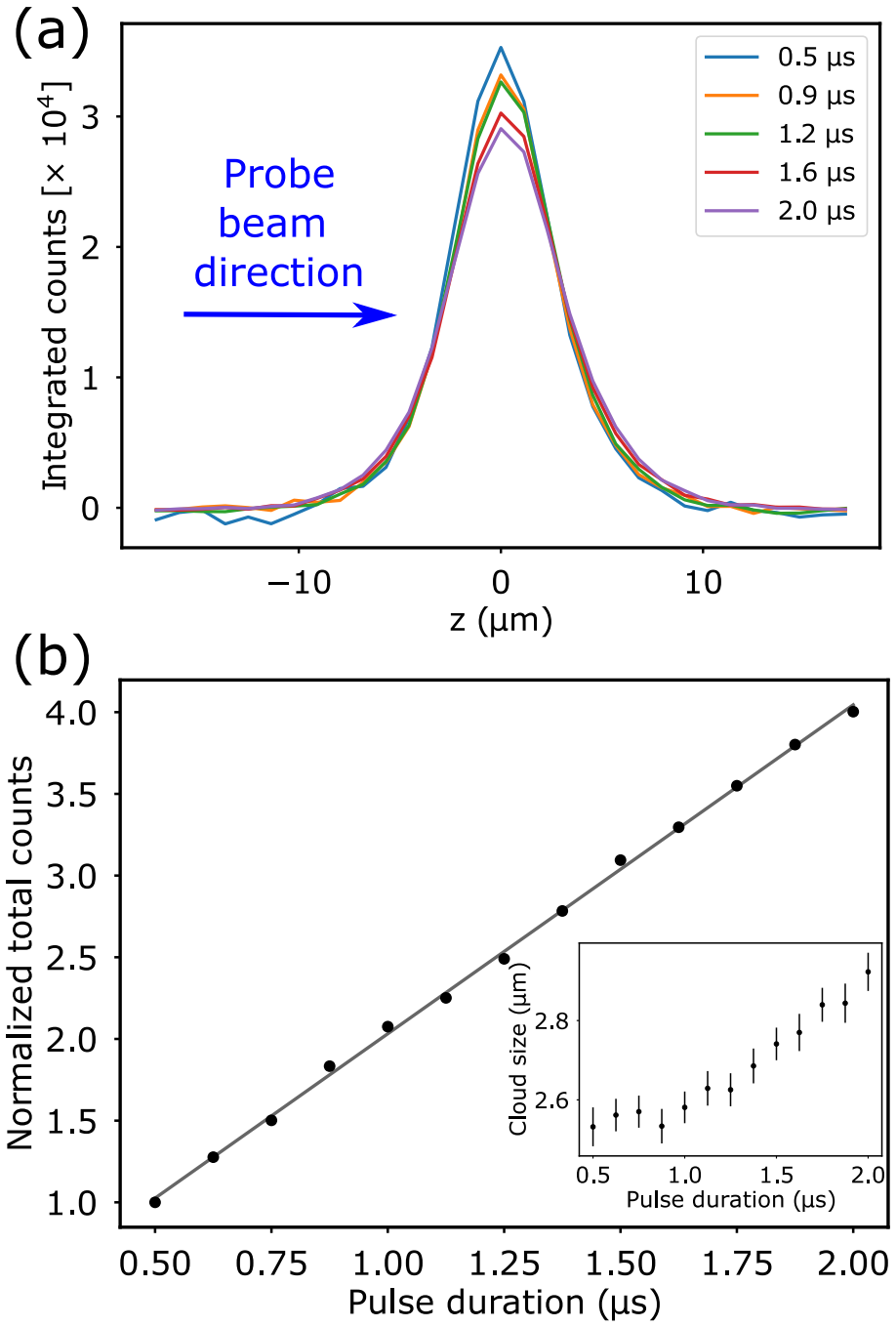

Figure 5.11: Panel **(a)** shows the integrated counts from the images in Fig. 5.9b of the main text along the x axis as a function of pulse duration. The total counts at each pulse duration is plotted in panel **(b)**, normalized by the counts at 500 ns. Given the detected photon count increases linearly with pulse duration, we observe minimal atom loss or molecular formation over the full 2 μs range. The inset shows the Gaussian RMS width of the cloud as a function of pulse duration.

first convert the fluorescence counts detected on our camera to the number of collected photons. Then, using the collection efficiency of our imaging system and scattering rate of our atomic transition we determine the conversion of detected photons per atom. On our CCD camera, we measure n_a counts in a given pixel. Using the quantum efficiency q of the imaging system, and the camera conversion gain g in units of counts per photo electron, we infer $\frac{n_a}{qg}$ photons. At full saturation, the atomic scattering rate is $\frac{\Gamma}{2}$ and the number of photons scattered per atom is $P_{sc} = \frac{\Gamma}{2} \times \tau$, where τ is the pulse duration. Finally, we denote the collection efficiency as Y, determined by the numerical aperture of our imaging system and by radiation pattern anisotropies. Combining terms, the total atom number is $N = \frac{n_a}{gqYP_{sc}}$. Using error propagation, we determine the variance $\mathbb{V}_{Fl}(N)$.

$$\mathbb{V}_{Fl}(N) = \left(\frac{\partial N}{\partial n_a}\right)^2 \mathbb{V}(n_a) = \left(\frac{1}{gqYP_{sc}}\right)^2 g n_a \tag{5.3}$$

Here, we have used the fact that the distribution of generated photo electrons n_e is Poissonian. Thus, $\mathbb{V}(n_a) = \mathbb{V}(g \times n_e) = g^2 \mathbb{V}(n_e) = g^2 n_e = g n_a$. Combining terms:

$$\mathbb{V}_{Fl}(N)/N = \frac{1}{qYP_{sc}}. \tag{5.4}$$

The SNR associated with absorption imaging is more complicated given the formula for the atom number in Eq. 5.5 has both logarithmic and linear terms and involves two images n_a and n_b with and without atoms present. Here, A and σ_0 refer to the effective pixel size accounting for the imaging system magnification and effective atomic absorption cross section, respectively. Similar to fluorescence imaging, an appropriate error propagation of the n_a and n_b terms determines Eq. 5.6 and Eq. 5.7. We summarize the formulas here and point a reader to reference [211] for a full derivation.

$$N = \frac{A}{\sigma_0} \log\left(\frac{n_b}{n_a}\right) + \frac{2}{\Gamma \tau g q}(n_b - n_a) \tag{5.5}$$

$$\mathbb{V}_{Abs}(N) = g\tilde{A}^2\left(\frac{1}{n_a} + \frac{1}{n_b}\right) + g\tilde{B}^2(n_a + n_b) + 4g\tilde{A}\tilde{B} \tag{5.6}$$

$$\tilde{A} = \frac{A}{\sigma_0}, \tilde{B} = \frac{2}{qg\tau\Gamma} \tag{5.7}$$

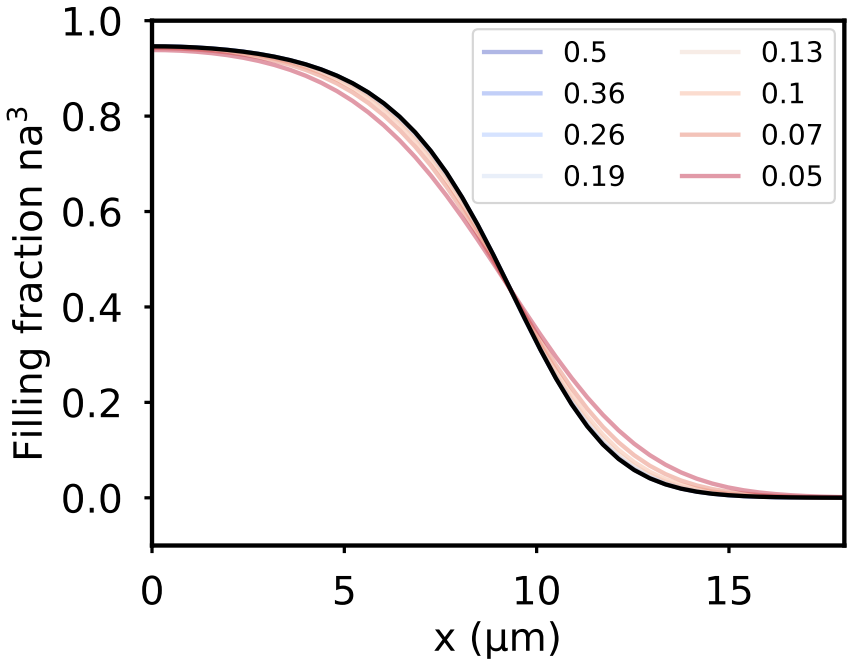

Figure 5.12: Numerical aperture dependence on density distribution. Black curve is the actual density distribution. Depends very weakly on NA. For our NA (0.2), low-pass filtering is minimal. Thus, these measurements provide a fairly robust probe for temperature in the lattice.

We compare the different techniques in Fig. 5.13 using the experimentally relevant parameters for our imaging system. In both cases, a 1 μs resonant pulse is used with a numerical aperture of 0.2 and a quantum efficiency of 85%. For the fluorescence SNR in blue, the transition is assumed to be fully saturated and scatters photons with a rate of $\Gamma/2$. For the $I/I_{sat} = \sim 55$ we use for our inverse Abel measurements, the SNR in absorption imaging is superior to fluorescence imaging in regions where the column density is higher than 2 atoms/a^2. Particularly given our peak density of $\tilde{n}a^2 = \sim 20$ in Fig. 5.7a, absorption imaging provides a better SNR in the regions of high density where we extract our peak filling fraction. At a critical OD of 0.17, fluorescence detection under our experimental

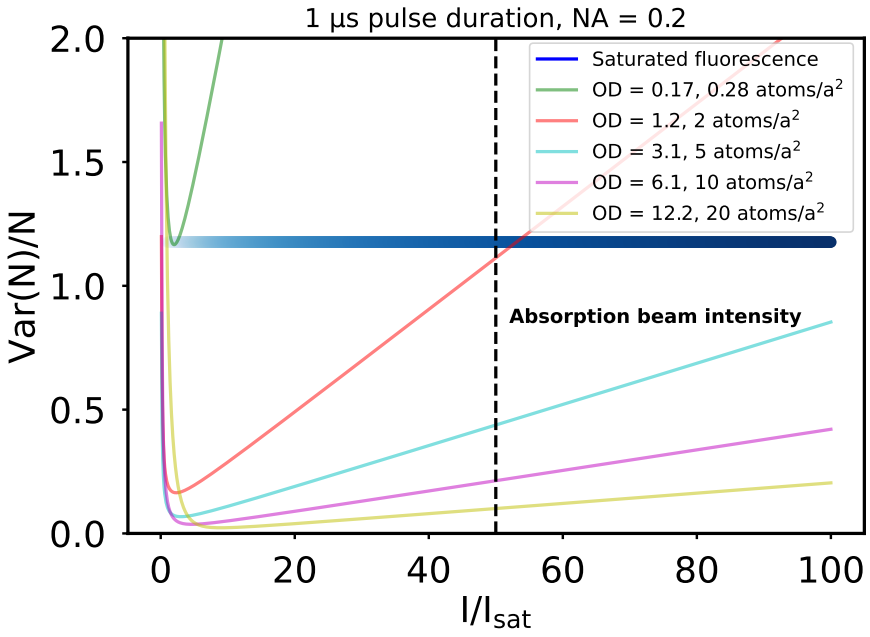

Figure 5.13: SNR comparison between absorption and fluorescence imaging. The relevant imaging parameters from the main figures of the paper are used for this calculation. For absorption imaging the atom count variance scales inversely proportional with intensity in the non-saturated limit $I \ll I_{sat}$, and proportional with intensity in the high saturation limit. The variance is for both imaging methods proportional to $1/\tau$. In the fully saturated regime (and assuming no technical noise) the normalized variance for fluorescence imaging is independent of atomic column density. To avoid imaging defects at the high densities used in clock operation, an $I/I_{sat} > 50$ was used in all imaging measurements. The black dashed line indicates the intensity used for our inverse Abel measurements.

parameters provides a superior SNR at all imaging intensities. We note these calculations neglect technical noise, in particular camera readout noise, which can be accounted for by offsetting $\mathbb{V}(n_a)$ accordingly. This contribution will disproportionately reduce the SNR of fluorescence imaging, as the fluorescence counts are substantially lower than the absorption counts.

To probe fine spatial details in our atomic cloud, an imaging resolution smaller than the length scale of these spatial features is required. To achieve this condition, a sufficiently large numerical aperture imaging system must be utilized and aberrations must be minimized. In

this case, the imaging resolution is fundamentally limited by diffraction. We verified the diffraction-limited performance of our $NA = 0.2$ objective lens by propagating a point source at 461 nm through a test setup (including all imaging path optics and vacuum viewports) and measuring the point-spread function.

While absorption and fluorescence imaging rely on the same light scattering process (they only collect different parts of the scattered EM field [187]), the signal amplitudes for these two methods scale differently with the NA. When collecting fluorescence, the solid angle coverage of the imaging system proportionally affects the signal down to the lowest spatial frequencies. This is not the case for absorption imaging, where the amplitude of spatial frequency components below the NA-dependent bandwidth is constant as the NA is further increased (assuming the lens fully covers the probe beam). In other words, for fluorescence imaging, most of the signal light gets collected in the outer ring fraction of the lens aperture, which renders it particularly susceptible to lens imperfections.

5.2.5 Density distribution calculation

To accurately model the density distribution in our 3D lattice, we use a thermodynamic calculation in the local density approximation. The general Hamiltonian for SU(N) symmetric fermions in a 3D lattice in the atomic limit takes the following form:

$$H_{AL} = \frac{U}{2} \sum_{i,\sigma \neq \sigma'} \hat{n}_{i,\sigma} \hat{n}_{i,\sigma'} + \sum_{i,\sigma} V_i \hat{n}_{i,\sigma}. \tag{5.8}$$

Here for a fermion with number operator $\hat{n}$ and spin index σ on a lattice site i, there are just two competing energy scales: an interaction energy U between particles and a position dependent energy offset V_i according to the harmonic confinement. By using the local density approximation $\mu = \mu_0 - V(x, y, z)$, where $V(x, y, z) = \frac{1}{2} m(\omega_x^2 x^2 + \omega_y^2 y^2 + \omega_z^2 z^2)$ and μ_0 corresponds to the peak chemical potential in the lattice. For the spin-polarized system in this work, U = 0 and $\sigma = 0$ so the calculations are substantially simplified.

Ultimately, we want to express the density distribution $n(\mu, T)$ in terms of the chemical potential, atomic temperature, and position in the lattice. On a lattice site i, we express the Grand partition function $\mathcal{Z}$ and Grand potential Ω :

$$\mathcal{Z}(\mu, T) = 1 + e^{\beta\mu}, \tag{5.9}$$

$$\Omega = -k_B T \ln(\mathcal{Z}).$$

From here, we determine the entropy and occupancy per lattice site i:

$$s(\mu, T) = -\frac{\partial \Omega}{\partial T} = k_B \ln(\mathcal{Z}) + \Delta s,$$

$$\Delta s = -\frac{k_B}{\mathcal{Z}} \beta\mu e^{\beta\mu}, \tag{5.10}$$

$$n(\mu, T) = -\frac{\partial \Omega}{\partial \mu} = \frac{1}{\mathcal{Z}} e^{\beta\mu}. \tag{5.11}$$

We accurately determine the total atom number N_{lat} from in situ absorption imaging and total entropy S_{lat} via time-of-flight fitting to a non-interacting Fermi-Dirac profile. From these two quantities we determine the predicted entropy-per-particle s/k_B. Similarly, we express the entropy s and occupation n on a given lattice site using Eq. 5.10 and Eq. 5.11 expressed in terms of T and μ. Given the density distribution only depends on the ratio of the respective harmonic confinements, the measured aspect ratios from Fig. 5.7 are used for our thermodynamic calculation. We then determine global parameters T and μ_0 to ensure the integrated entropy and occupancy over all lattice sites equals our experimentally measured values of S_{lat} and N_{lat}. A linecut of $n(\mu, T)$ at $z = 0$ and $y = 0$ is plotted in Fig. 5.10b.

5.2.6 Inverse Abel transform

A generic inverse Abel transform assumes cylindrical symmetry and uses a 2D projection to reconstruct the 3D distribution. Limited to this analysis, constraints are placed on both the geometry of our trapping potential and the choice of imaging axis to ensure cylindrical symmetry. Borrowed from similar alkaline-earth experiments realizing highly efficient evaporation, we use a crossed dipole trapping geometry to provide a strong vertical confinement [212, 213]. Imaging along this axis of vertical confinement is preferable as the corresponding optical depth is the smallest and the imaging resolution is enhanced by the vertical imaging system.

We outline our reconstruction procedure here using measurements of the atomic cloud aspect ratios and an inverse Abel transform. A similar trapping geometry and reconstruction procedure was used in prior work [182]. To understand our density reconstruction along an axis without cylindrical symmetry, we treat our system as an ellipsoid with radii r_x, r_y, r_z. With N total atoms, the volume of this system is $V_{lat} = \frac{4}{3}\pi r_x r_y r_z$ and thus the density is $n_{lat} = N/V_{lat}$. We extract the inverse Abel transform using the data in Fig. 5.7a imaged along the vertical direction. We take the y axis as a symmetry axis, given the largest Band insulator plateau will occur along the x axis with the weakest harmonic confinement. The modification to our reconstruction procedure occurs here, where the density distribution must be appropriately rescaled to reflect the actual volume and therefore density of our atomic sample. The inverse Abel transform taking the y axis as a symmetry axis produces a density distribution corresponding to volume of $V_{Abel} = \frac{4}{3}\pi r_x r_x r_y$ and density $n_{Abel} = N/V_{Abel}$. This density distribution n_{Abel} must then be rescaled by V_{Abel}/V_{lat} to reflect the actual volume V_{lat}. Here, $V_{Abel}/V_{lat} = r_x/r_z$. We fit the Fig. 5.7b image from our horizontal imaging system to a 2D Gaussian function and determine $r_x/r_z = 2.11$. Given excess noise around the origin, the $x = 0$ point is interpolated with the neighboring point in Fig. 5.10a. This reconstruction procedure was cross-checked with simulated density distributions to ensure its fidelity. The

three-point Abel transform method was used for this work, which has been independently studied to verify its fidelity [214].

5.3 Atom number calibration

To calibrate our atom number, we analyze quantum projection fluctuations using the narrow-linewidth clock transition between the $^1S_0$ and $^3P_0$ states in ^{87}Sr. Using a clock laser stabilized to our 8 mHz linewidth silicon reference cavity, rotation noise due to laser instability can be neglected in these measurements [215]. Additionally, fluctuations in total counts are $< 2\%$ and not a limiting systematic for determining the atom number calibration.

5.3.1 Quantum projection noise

Referenced in many texts [29], by preparing atoms in a superposition of $^1S_0$ to $^3P_0$ the variance $\mathbb{V}$ of the measured excitation fraction is related to the mean atom number $\bar{N}$ and mean excitation $\bar{p}_e$ by:

$$\mathbb{V}_{QPN} = \frac{\bar{p}_e(1-\bar{p}_e)}{\bar{N}}. \tag{5.12}$$

To determine this variance, we do many subsequent measurements of p_e under identical operating conditions. For a measurement i to determine p_e^i, two fluorescence counts $\tilde{C}_g^i$ and $\tilde{C}_e^i$ are read off a region of interest of our camera including our atoms. These counts are subtracted by two averaged dark frames $\bar{B}_g$ and $\bar{B}_e$ to yield $C_g^i = \tilde{C}_g^i - \bar{B}_g$, $C_e^i = \tilde{C}_e^i - \bar{B}_e$. We would like to determine the coefficient a that satisfies $N_e^i = aC_e^i/\tau$, $N_g^i = aC_g^i/\tau$. We can immediately see that the excitation fraction has no dependence on this coefficient:

$$p_e^i = \frac{\cancel{a}C_e^i}{\cancel{a}C_e^i + \cancel{a}C_g^i}. \tag{5.13}$$

However, the total atom number $N^i = a(C_e^i + C_g^i)/\tau = aC_t^i/\tau$ does. Rewriting Eq. 10, we see a measurement of the variance $\mathbb{V}_{QPN}$, the mean excitation $\bar{p}_e$, and the mean total

counts $\bar{C}_t$ can determine a.

$$\mathbb{V}_{QPN} = \frac{\bar{p}_e(1-\bar{p}_e)}{a\bar{C}_t/\tau} \tag{5.14}$$

The coefficient a can be interpreted as the "atoms per count per pulse duration". In principle, with knowledge of the quantum efficiency, gain, scattering rate, numerical aperture, and radiation pattern one could calculate this value. Practically, assumptions about the radiation pattern based on the quantization axis and probe light polarization make this calculation more difficult. In practice, it is much more straightforward to directly measure a than to individually measure each of these values with high accuracy.

The observed variance of the excitation fraction $\mathbb{V}_{p_e}$ has contributions from quantum projection noise (QPN), photon shot noise (PSN), and camera readout noise (RN):

$$\mathbb{V}_{p_e} = \mathbb{V}_{QPN} + \mathbb{V}_{PSN} + \mathbb{V}_{RN}. \tag{5.15}$$

Here g is the detector gain in units of counts per electron.

$$\mathbb{V}_{PSN} = \frac{\bar{p}_e(1-\bar{p}_e)}{\bar{C}_t} \times g, \tag{5.16}$$

$$\mathbb{V}_{RN} = \frac{\mathcal{R}^2}{\bar{C}_t{}^2}(2\bar{p}_e^2 - 2\bar{p}_e + 1). \tag{5.17}$$

$\mathbb{V}_{PSN}$ can be understood intuitively considering the ratio $\mathbb{V}_{QPN}/\mathbb{V}_{PSN}$. The number of signal electrons (equivalently the number of collected photons multiplied by the camera quantum efficiency) per atom determines the relative scaling of $\mathbb{V}_{QPN}$ and $\mathbb{V}_{PSN}$.

$$\frac{\mathbb{V}_{QPN}}{\mathbb{V}_{PSN}} = \frac{1}{g \times a} \tag{5.18}$$

To determine a we need to accurately calibrate $\mathbb{V}_{RN}$ and $\mathbb{V}_{PSN}$. We see at $p_e = 1$, $\mathbb{V}_{PSN}$, $\mathbb{V}_{QPN} = 0$. Thus, measuring $\mathbb{V}_{p_e}$ at $p_e = 1$ will independently determine $\mathbb{V}_{RN}$.

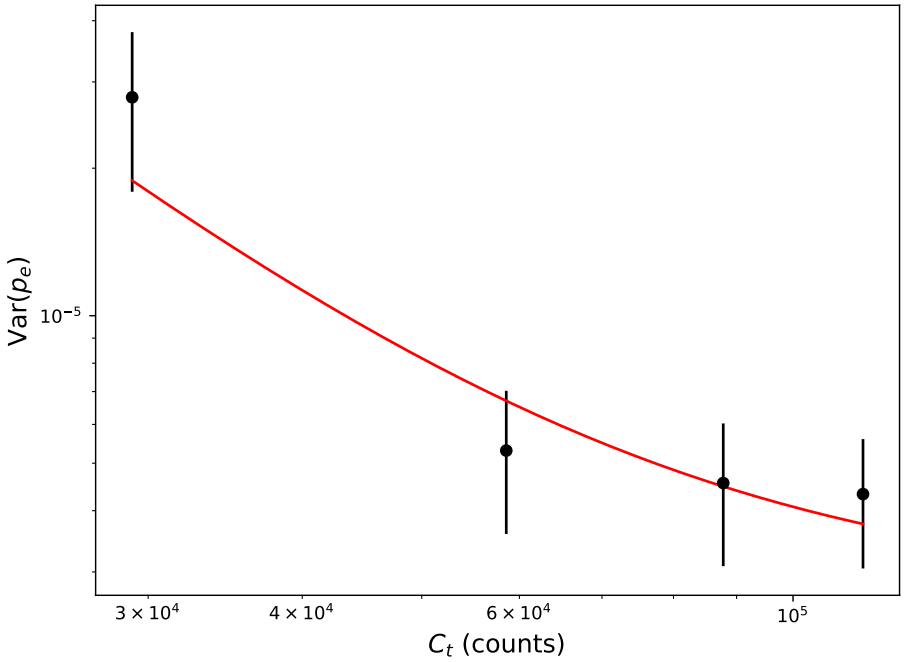

Figure 5.14: Readout noise calibration. A π pulse on our optical clock transition is used so $p_e \approx 1$ and $\mathbb{V}_{p_e} = \frac{\mathcal{R}^2}{\bar{C_t}^2} + C$. We use 4 pulse durations between 5 and 20 μs to vary C_t. We fit $\mathcal{R} = 100.2 \pm 24.6$ and $C = 2.73 \times 10^{-6} \pm 1.02 \times 10^{-6}$.

We wish to fit $\mathcal{R}$ and ensure it is consistent with the cameras specified readout noise. To extract this value, we use 4 pulse durations between 5 and 20 μs to vary C_t. This is illustrated in Fig. 5.14. In practice, we fit

$$\mathbb{V}_{p_e} = \frac{\mathcal{R}^2}{\bar{C_t}^2} + C. \tag{5.19}$$

We fit $\mathcal{R} = 100.2 \pm 24.6$ and $C = 2.73 \times 10^{-6} \pm 1.02 \times 10^{-6}$. For our circular ROI there are $X = 889$ pixels in the masked radius. For the calibrated gain $g = 1.59$ counts/e- and readout noise $r = 2.4$ e- respectively , $\mathcal{R}_{calc} = \sqrt{Xgr} = 94.7$ in agreement with $\mathcal{R} = 100.2 \pm 24.6$. We note that the gain and readout noise of the camera are close to specification. Dark counts over our 30 ms exposure are $< .1$ e- and considered negligible.

Next, we wish to determine a_{QPN}. To do so, we perform a second measurement at $p_e = 0.5$. The variance of this dataset contains contributions from $\mathbb{V}_{QPN}$, $\mathbb{V}_{PSN}$, and $\mathbb{V}_{RN}$.

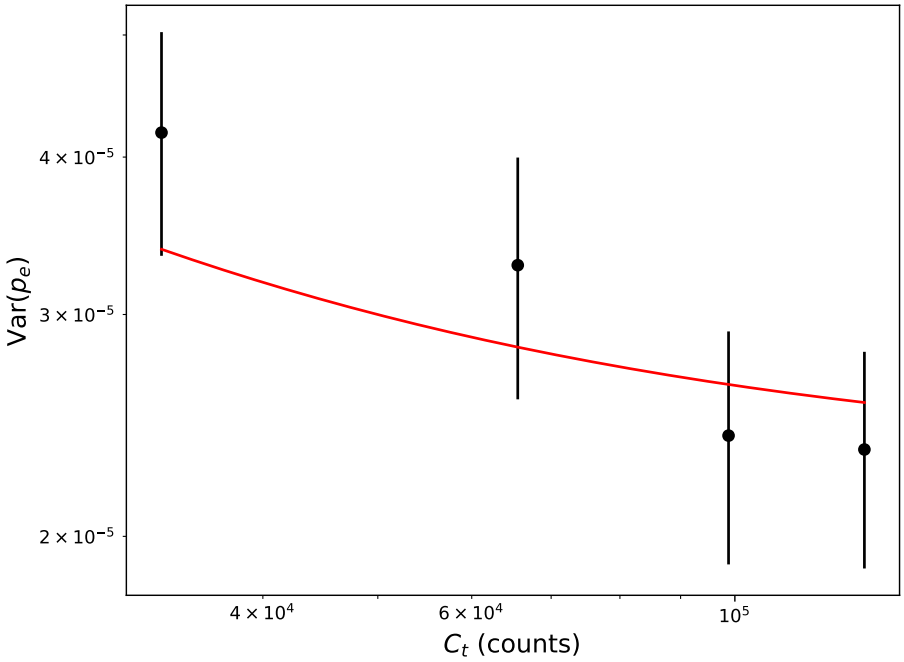

Figure 5.15: a_{QPN} calibration. The atoms in our optical lattice are placed in a superposition of the ground and clock states with a $\pi/2$ pulse so $p_e \approx 0.5$ for these measurements and $\mathbb{V}_{p_e}$ is fit to Eq. 18. We determine $a_{QPN} = 1.72 \pm 0.16$.

Using the measured $\mathcal{R}$ value, we subtract the $\mathbb{V}_{RN}$ contribution. Next, we fit the data in Fig. 5.15 to:

$$\mathbb{V}_{p_e} = \frac{0.5(1-0.5)}{a\bar{C}_t/\tau} + \frac{0.5(1-0.5)}{\bar{C}_t} \times g. \tag{5.20}$$

We fit $a_{QPN} = 1.72 \pm 0.16$. This is in reasonable agreement with the calculated value of 1.43 assuming $\Gamma/2$ scattering into 4 π while also accounting for the measured quantum efficiency.

5.3.2 Readout noise

Here, we derive the readout noise term used in our variance measurements. The expressions used are somewhat different than other literature, given that we use averaged dark frames $\bar{B}_e$ and $\bar{B}_g$. Recall, $p_e = \frac{C_e}{C_e+C_g}$. To determine the readnoise contribution to the

excitation fraction, we perform standard error propagation:

$$\mathbb{V}_{RN} = \left(\frac{\partial p_e}{\partial C_e}\right)^2 \mathbb{V}(C_e) + \left(\frac{\partial p_e}{\partial C_g}\right)^2 \mathbb{V}(C_g). \tag{5.21}$$

Here,

$$\frac{\partial p_e}{\partial C_g} = \frac{C_e}{(C_e + C_g)^2} = \frac{p_e}{(C_e + C_g)}, \tag{5.22}$$

$$\frac{\partial p_e}{\partial C_e} = \frac{C_g}{(C_e + C_g)^2} = \frac{1 - p_e}{(C_e + C_g)}. \tag{5.23}$$

To determine $\mathbb{V}(C_e)$ consider an X pixel region-of-interest for which we extract C_g, C_e in two separate measurements. Each pixel contains r read noise in electrons. The single pixel read noise in units of counts is thus $g \times r_i$. The total noise in this region of interest is summed in quadrature pixel-by-pixel $\mathbb{V}(C_g), \mathbb{V}(C_e) = \sum_X (r_i \times g)^2 = X r^2 g^2 = \mathcal{R}^2$. Plugging terms in Eq. 5.21:

$$\mathbb{V}_{RN} = \frac{\mathcal{R}^2}{\bar{C_t}^2}(2\bar{p}_e^2 - 2\bar{p}_e + 1). \tag{5.24}$$

5.3.3 Imaging system parameters for Fig. 5.9a

In Table 5.1 and Table 5.2 is a summary of the imaging parameters for the measurements in Fig. 5.9a. For Fig. 5.7 and Fig. 5.10, a 1 μs pulse duration was used. In Fig. 5.9b, we vary the pulse length between 500 ns and 2 μs. Atom number fluctuations in time-of-flight absorption imaging for these measurements have a standard deviation less than 2 %.

5.3.4 Outlook

In conclusion, we report on the observation of a spin-polarized, band insulating state in our 3D optical lattice clock. This has been enabled by characterizing saturated *in situ* imaging techniques to accurately determine our density distribution. Broadly, the saturated imaging techniques in this work will be applicable for studies of SU(N) magnetism

Parameter	Value
Numerical aperture	0.23
Pulse duration	3 μs
Total photons scattered per atom at full saturation	287
Collection efficiency	1.3 %
Camera quantum efficiency	0.85
Imaging system quantum efficiency	0.65
Calculated photon count per atom	2.06
Measured photon count per atom	1.91(1)

Table 5.1: Vertical imaging system parameters.

Parameter	Value
Numerical aperture	0.10
Pulse duration	3 μs
Total photons scattered per atom at full saturation	287
Collection efficiency	0.25 %
Camera quantum efficiency	0.78
Imaging system quantum efficiency	0.72
Calculated photon count per atom	0.402
Measured photon count per atom	0.445(3)

Table 5.2: Horizontal imaging system parameters.

and thermodynamics in the Mott-insulating regime [71, 216]. With the high filling fraction demonstrated in this work, many-body states arising from dipolar interactions can be generated between atoms on neighboring lattice sites [23, 179].

Chapter 6

Observing coherent superexchange interactions

The research in this chapter is reported in the publication: W. R. Milner, S. Lannig, M. Mamaev, L. Yan, A. Chu, B. Lewis, M. N. Frankel, R. B. Hutson, A. M. Rey, and J. Ye, arXiv (2024).

6.1 Introduction

The introduction to this thesis emphasized the importance of improving clock precision to advance the capabilities of optical lattice clocks. As we already stated, this requires probing as many atoms as possible while maintaining a long coherent interrogation time T. The challenge to the experimenter is thus to balance many different dephasing factors to find the optimal operating conditions. In this chapter we provide a detailed study of coherence times in our 3D optical lattice, building upon prior investigations [72]. In 1D lattice clocks, coherence times have been extensively studied and a spin model has been developed that successfully captures interaction-based dephasing [59]. In this regime, the key factor is the interplay of s and p-wave interactions: At shallow lattice, atoms are delocalized and can interact with distinguishable fermions on neighboring sites via s-wave interactions. At deep lattice, atoms are confined to a single lattice site and interact solely via p-wave channels [60].

In our 3D optical lattice where atoms are strongly confined in all 3 directions, s-wave interactions increase to the kHz level and are the dominant interaction energy scale. In the Mott-insulating regime ($U \gg t$) at high filling, doubly-occupied sites are energetically

unfavorable and motion is restricted. Dephasing in this regime arises from spin-exchange processes known as *superexchange*. We provide an intuitive description of these interactions in the following sections and detail an experimental study of their effects on clock spectroscopy.

6.1.1 Single-particle dephasing

We can broadly divide dephasing mechanisms in two-classes: *single-particle* dephasing mechanisms that do not depend on the atomic density and *interaction*-based dephasing mechanisms that do. We will start with single-particle dephasing mechanisms, which are necessarily simpler. The fundamental single-particle dephasing mechanism is the $^3P_0$ excited state lifetime, with the most recent experimental study determining a lifetime of 118(3) s [217].[1] In some sense achieving spectroscopy times limited by the natural lifetime is the ultimate goal, although one could envision Pauli-blocking [201, 218, 219] or erasure-style schemes [220] to overcome this limitation.

Unsurprisingly, other single particle effects kick in at comparatively shorter timescales. The predominant single-particle dephasing mechanism is Raman scattering of lattice photons from our 813 nm magic wavelength trap, affecting both the $^1S_0$ ground and $^3P_0$ clock states. As depicted in Fig. 6.1, although our lattice laser frequency ω_k is hundreds of THz detuned from dipole allowed transitions, off-resonant scattering processes still occur at rates approaching Hz-level in hundreds of E_R deep lattices. For $^1S_0$ ($^3P_0$), the dominant contributing state is $^1P_1$ ($^3S_1$).

The effects of Raman scattering on clock coherence were carefully studied on Sr2 by previous graduate student Ross Hutson and reported in Ref. [72, 221]. We briefly overview the key findings of his measurements here, before diving into our own study building upon those results. A simple benchmark of Raman scattering is to first examine the excited state decay loss. Here, the atoms are shelved in $|e = {}^3P_0\rangle$ and the time-dependent decay to $|g = {}^1S_0\rangle$ was examined as a function of lattice depth. The measurements are plotted in

[1] Studies to directly determine the clock state lifetime on 1D lattice clock platforms are ongoing.

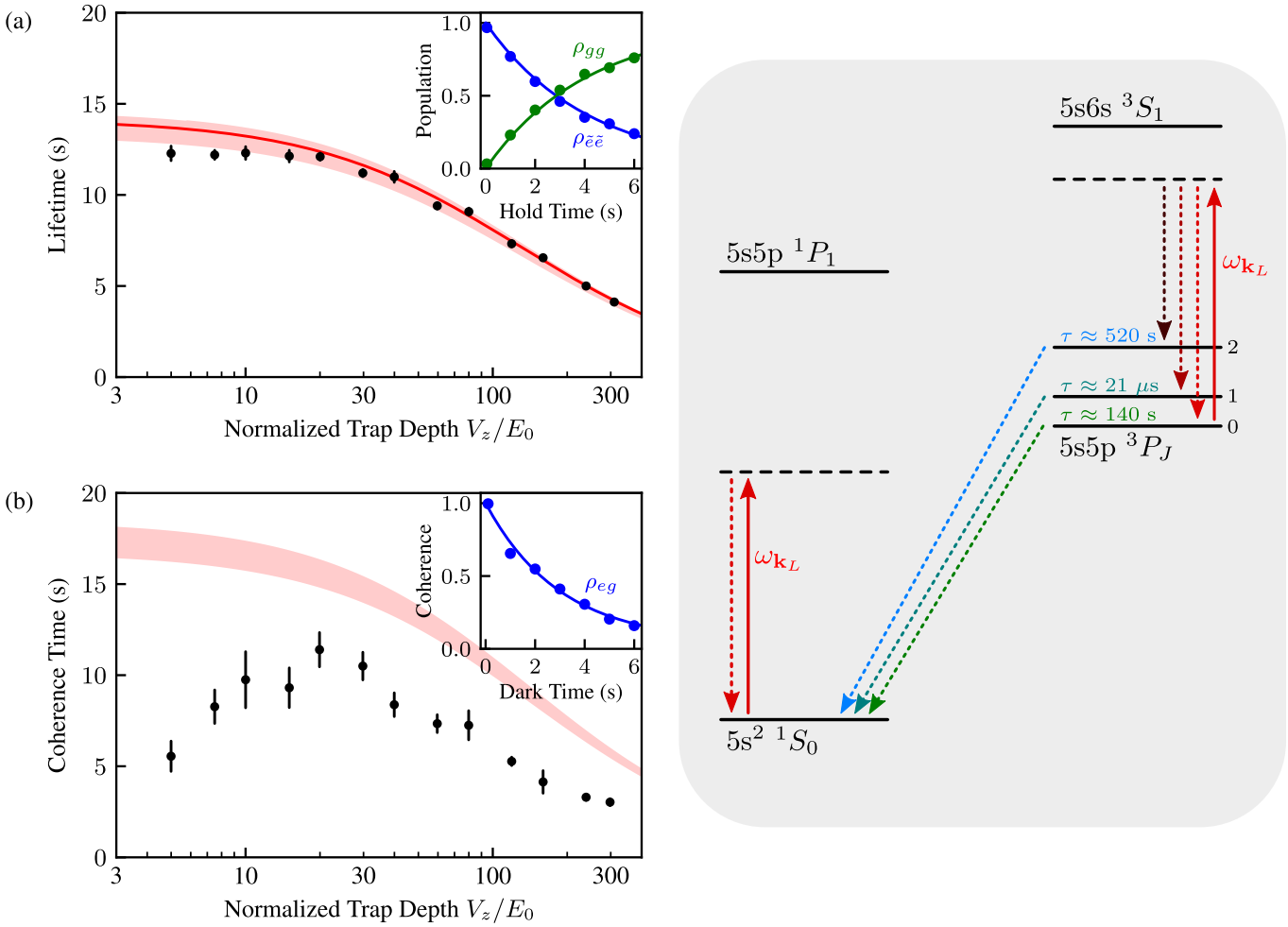

Figure 6.1: Coherence time study on Sr2. **Top left:** Excited state lifetime measurements agree well with Raman scattering-limited theory. **Bottom left:** Coherence time measurements qualitatively agree with lattice scattering-limited dephasing at deep trap depths within prefactors of ≈ 2. At shallow lattice, dephasing rates strongly increase likely due to motional effects. **Right:** Although our lattice laser frequency ω_k is hundreds of THz detuned from dipole allowed transitions, off-resonant scattering processes still occur at $\approx$ mHz rates. Figure reproduced from Ref. [72].

Fig. 6.1(a). This data is very well modelled by the calculated decay rate in red:

$$\Gamma_{ee} = \sum_i \Gamma'_{ee} V_i (1 - \sqrt{E_R/4V_i}) + \Gamma^0_{ee}. \tag{6.1}$$

Here, $\Gamma'_{ee} = 5.7(3) \times 10^{-4}$ s^{-1} E$_\mathrm{R}^{-1}$ and $\Gamma^0_{ee} = 9(1) \times 10^{-3}$ s^{-1}. Γ'_{ee} is due to Raman scattering. Γ^0_{ee} is predominantly due to spontaneous emission from $^3P_0$ and BBR-induced pumping via $^3D_1$. These decay coefficients are also tabulated in Ref. [222]. V_i are the lattice depths in direction of the 3D lattice in units of E_R.

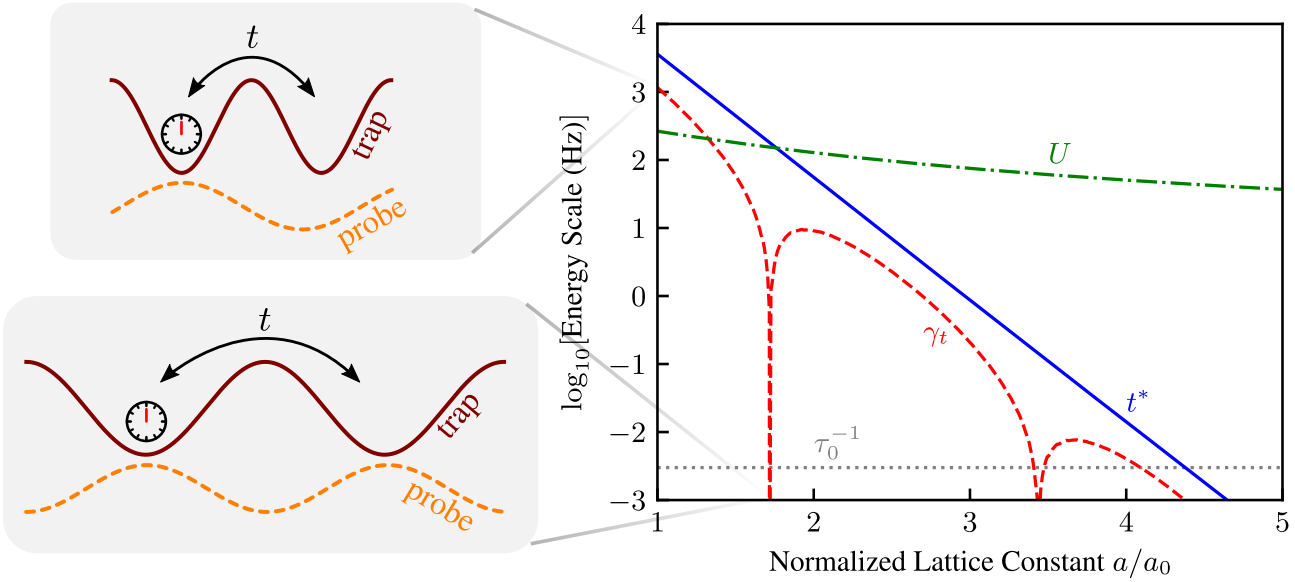

Figure 6.2: **Left:** Motional dephasing arises due to *spin-orbit coupling* from incommensurate lattice and probe wavelengths. **Right:** Dephasing rates are plotted. If the lattice spacing a is commensurate with clock laser wavelength, dephasing rate γ_t is strongly minimized. Sufficiently large lattice spacing via tunable spacing accordion lattices can strongly reduce tunneling t, also minimizing γ_t. Figure adapted from Ref. [72].

With Raman scattering benchmarked, the next task was to study the effects of lattice-induced scattering on clock coherence. Instead of monitoring the decay of populations, atoms are put in a superposition state $|\psi\rangle = (|g\rangle + |e\rangle)/2$ and the evolution of coherences over time are detected via Ramsey spectroscopy. Here, a final $\pi/2$ pulse in the spectroscopy sequence maps the coherences into populations that can be readily measured with resonant imaging

light. The 'coherence time', or $1/e$ time for loss in contrast, is plotted in Fig. 6.1(b). The red line is the calculated dephasing rate according to:

$$\Gamma_{eg} = \sum_i \Gamma'_{eg} V_i (1 - \sqrt{E_R/4V_i}) + \Gamma^0_{eg}. \tag{6.2}$$

Here, $\Gamma'_{eg} = 4.0(2) \times 10^{-4}$ s^{-1} E$_\mathrm{R}^{-1}$ and $\Gamma^0_{eg} = 1.2(1) \times 10^2$ s^{-1}. The coherence time measurements qualitatively agree with lattice scattering at deep trap depths within prefactors of ≈ 2.

At shallow lattice depths, the coherence times are substantially smaller than expected from Raman scattering. This discrepancy was attributed to motional dephasing effects due to tunneling. This motional dephasing mechanism is shown in Fig. 6.2. In our clock operating conditions, the clock and lattice wavelengths of $\lambda_{clk} = 698$ and $\lambda_{magic} = 813$ nm are incommensurate. Thus on each site in our cubic lattice, indexed j and separated by a lattice constant $a = \lambda_{magic}/2$, the initial superposition state prepared is $|\psi\rangle_j = \left(|g\rangle + {}^{i\varphi j} |e\rangle \right)/\sqrt{2}$ with a *spin-orbit coupled* (SOC) phase $\varphi = 2\pi a/\lambda_{clk}$ [70]. The analogy of SOC comes from the coupling of spin and motion, although describing this as a discretized Doppler shift is probably more intuitive for a clock person. Explicitly the dephasing is described according to a Bessel function relation $C(T) = \mathcal{J}_0\big(4\,t\,T\,\sin(\varphi/2)\big)$ [73].[2] It is also sensible define a motional dephasing rate as the argument of this function $\gamma_t \equiv 4\,t\,|\sin(\varphi/2)|$. Here, t and U are the tunneling coupling and on-site interaction strength respectively as detailed in Chapter 3.

The interplay of Raman scattering and motional dephasing thus places a limitation on clock coherence time: At deep lattices one is limited by Raman scattering and at shallow lattices limited by tunneling. We note as pointed out in [72], operating in a blue-detuned lattice at ≈ 390 nm does not substantially improve decoherence rates. Two strategies are clear to address this challenge:

First, one could use accordion lattices to dynamically tune a the lattice constant. As

[2] This Bessel function relation is derived in [223].

depicted in Fig. 6.2, if a is sufficiently large ($\gg \lambda_{magic}/2$), t and thus γ_t becomes negligibly small. Alternatively, one could make choose a lattice spacing to make a and λ_{clk} commensurate. Here, all atoms behave as indistinguishable fermions turning off both s-wave interactions and tunneling induced dephasing. In other words, at high density the system is in the *band-insulating*[3] rather than *Mott-insulating* regime where motion and interactions are Pauli blocked at *full filling*. While this is certainly a promising research direction that we will likely ultimately pursue, it requires installing an accordion lattice and it is unclear how one references the phase of the clock laser to the lattice.[4]

Secondly, one could envision tuning parameters of our Fermi-Hubbard Hamiltonian to improve coherence times. The calculations in Fig. 6.2 are in the single particle limit in a homogeneous lattice and make no assumptions about interactions or local-disorder. By very definition, a Mott-insulator is a many-body state that behaves as an insulator due to interactions, despite having a band structure that admits conductivity [224]. Thus one would expect that operating the Mott-insulating regime ($U \gg t$), one might be able to make the lattice sufficiently shallow to avoid Raman scattering and still suppress tunneling from interactions.

Additionally, experiments from the Ye lab Wannier-Stark, 1D lattice clock [21] and the Kaufman lab tweezer clock [225] showed that long coherence times of 52.8(1.5) and 48(8) seconds respectively could be achieved. In both systems, the largely negligible tunneling coupling between sites strongly minimizes dephasing and raised the broader question of how local disorder between lattice sites could further improve our 3D clock. That is, operating in the regime where the site-to-site energy shift $\equiv \Delta E$ is much larger than the tunnel coupling t, one would also expect to strongly suppress motional dephasing.

[3] It might be more appropriate to call this many-body state a *Pauli* insulator.

[4] Although as we will detail in the coming sections, this is not explicitly required for extracting the atomic coherence time.

6.1.2 Interaction-based dephasing

In summary, while Ross' study provided ingenious ideas moving forward it also highlighted that both the coherence times on Sr2 somewhat mysteriously fell short of expectation and that a quantitative understanding of interactions are a key next step. The single particle limit is not so meaningful in a 3D lattice at high density!

In the next section, we give an overview of the relevant interactions in our 3D lattice. We begin with the canonical *Fermi-Hubbard model.* We then show that at half-filling in the repulsive limit, the Fermi-Hubbard Hamiltonian can be mapped to the *Heisenberg* Hamiltonian. Finally, we show that with our SOC phase, our dynamics can be generalized to an XXZ Hamiltonian exhibiting anisotropy.

6.1.2.1 Fermi-Hubbard Hamiltonian

In a 3D lattice filled with a degenerate Fermi gas of spin-polarized ^{87}Sr atoms in the motional ground state [107], the system can be modelled with the Fermi-Hubbard Hamitonian where ground and excited state atoms on the same lattice site interact via the Hubbard interaction parameter U, and motion is captured by a parameter t_z for tunneling along the z direction. We start from the two-well Fermi-Hubbard Hamiltonian with a energy tilt ΔE between sites,

$$\hat{H}_{\mathrm{FH}} = -t_z \sum_{\sigma\in\{g,e\}} (\hat{\tilde{c}}^{\dagger}_{0,\sigma}\hat{\tilde{c}}_{1,\sigma} + H.c.) + U \sum_{j\in\{0,1\}} \hat{n}_{j,e}\hat{n}_{j,g} + \frac{\Delta E}{2}(\hat{n}_1 - \hat{n}_0), \tag{6.3}$$

Here, $\hat{\tilde{c}}^{\dagger}_{j,\sigma}(\hat{\tilde{c}}_{j,\sigma})$ creates (annihilates) a fermion on site j with spin σ in the lab frame. We define $\hat{n}_{j,\sigma} = \hat{\tilde{c}}^{\dagger}_{j,\sigma}\hat{\tilde{c}}_{j,\sigma}$, and $\hat{n}_j = \hat{n}_{j,e} + \hat{n}_{j,g}$. To be explicit regarding the notation conventions in this section: x, y, z refers to *spatial* directions with respect to the lab frame for all operators in this chapter. The $\sim$ above operators emphasizes that they are in the lab frame, rather than the rotated spiral frame explained in Section 6.1.2.3. Capitalized values X, Y, Z refers to *spin* orientations on the Bloch sphere. Finally, we index sites according to j. Calculations

in the following sections are confined to the z spatial direction, in which our clock is launched and thus the SOC phase is imprinted.

The Fermi-Hubbard Hamiltonian is formed with the basis states for $|\text{site } j=1, \text{site } j=2\rangle$: $|eg,0\rangle, |0,eg\rangle, |e,e\rangle, |g,g\rangle, |e,g\rangle, |g,e\rangle$. In matrix form:

$$H_{FH}/h = \begin{pmatrix} U-\Delta E & 0 & 0 & 0 & -t_z & t_z \\ 0 & U+\Delta E & 0 & 0 & -t_z & t_z \\ 0 & 0 & 0 & 0 & 0 & 0 \\ 0 & 0 & 0 & 0 & 0 & 0 \\ -t_z & -t_z & 0 & 0 & 0 & 0 \\ t_z & t_z & 0 & 0 & 0 & 0 \end{pmatrix} \tag{6.4}$$

The eigenvalues are plotted in Fig. 6.3. Next, the eigenstates and eigenvectors are derived in the Mott-insulating limit $U \gg t_z$ where we will be working. For simplicity, we set $\Delta E = 0$. The ground and most excited state are Taylor expanded to first order in t_z. Ordering the states by energy:

Energy	Eigenenergy	Eigenvector
E_1	$\approx$ -$4t_z^2/U$	$\approx (\|g,e\rangle - \|e,g\rangle)/\sqrt{2}$ - $t_z/U(\|eg,0\rangle + \|0,eg\rangle)$
E_2	0	$(\|e,g\rangle + \|g,e\rangle)/\sqrt{2}$
E_3	0	$\|e,e\rangle$
E_4	0	$\|g,g\rangle$
E_5	U	$(\|0,eg\rangle - \|eg,0\rangle)/\sqrt{2}$
E_6	$\approx$ U + $4t_z^2/U$	$\approx (\|eg,0\rangle + \|0,eg\rangle)/\sqrt{2} + t_z/U(\|g,e\rangle - \|e,g\rangle)$

We see that the ground state E_1 is approximately a singlet state ($|s\rangle \equiv (|g,e\rangle - |e,g\rangle)/\sqrt{2}$). The states $|e,e\rangle$ and $|g,g\rangle$ are non-interacting due to the Pauli exclusion principle. Other states are either a triplet state $|t\rangle \equiv (|g,e\rangle + |e,g\rangle)/\sqrt{2})$ with $E = 0$ or separated by an energy gap approximately equal to U. As we will detail in the next section,

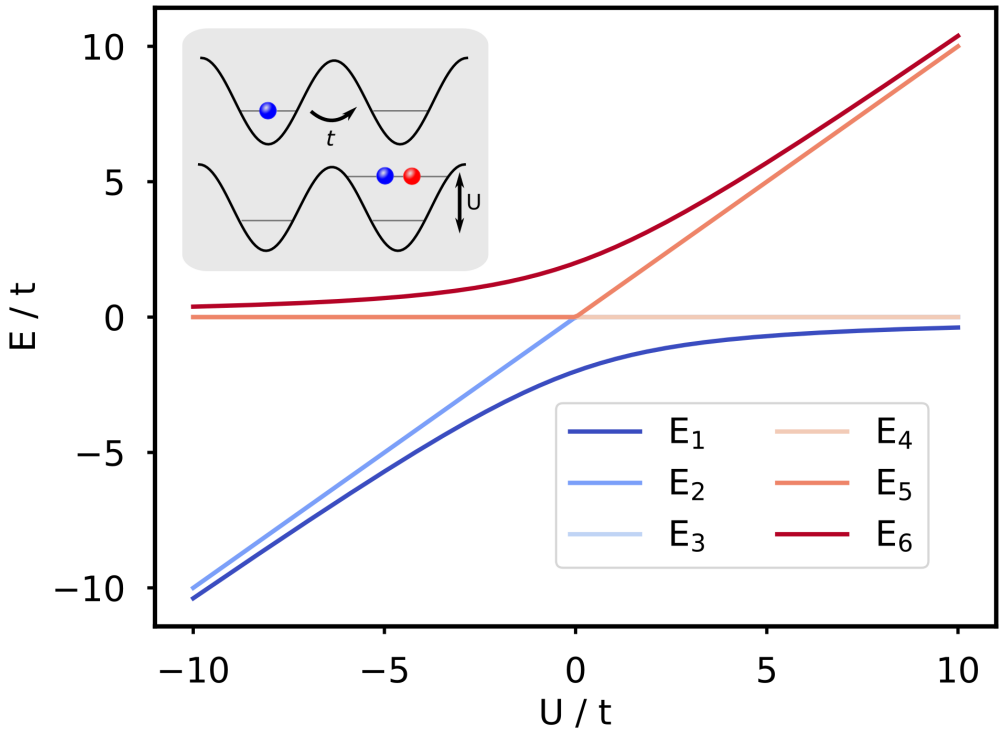

Figure 6.3: Eigenstates of the two-site Fermi-Hubbard model ($\Delta E = 0$). The ground state in the Mott-insulating limit $U \gg t_z$, approximately a 'singlet' state, is $4t^2/U$ lower than the $E = 0$ 'triplet' states. Higher-lying states are separated by an energy gap U. At $U = 0$, the energy seperation of the highest and lowest eigenstates is set by tunneling bandwidth $4t$.

this separation of energy scales forms the basis for modelling the system as the *Heisenberg Hamiltonian.*

It is also instructive to plot the solutions of the non-interacting Fermi-Hubbard Hamiltonian ($U = 0$). As a function of tilt (ΔE), the energy spectrum is plotted in Fig. 6.4. In the limit of large tilt $|\Delta E| \gg t_z$, the energy spectrum is dominated by doubly occupied states.

6.1.2.2 Heisenberg Hamiltonian

In the Mott-insulating limit $U \gg t_z$, the double-occupied states are separated by a large energy gap $\sim U$, which allows for restriction of dynamics in the single-occupied states via second-order perturbation theory. We get the effective Hamiltonian for superexchange

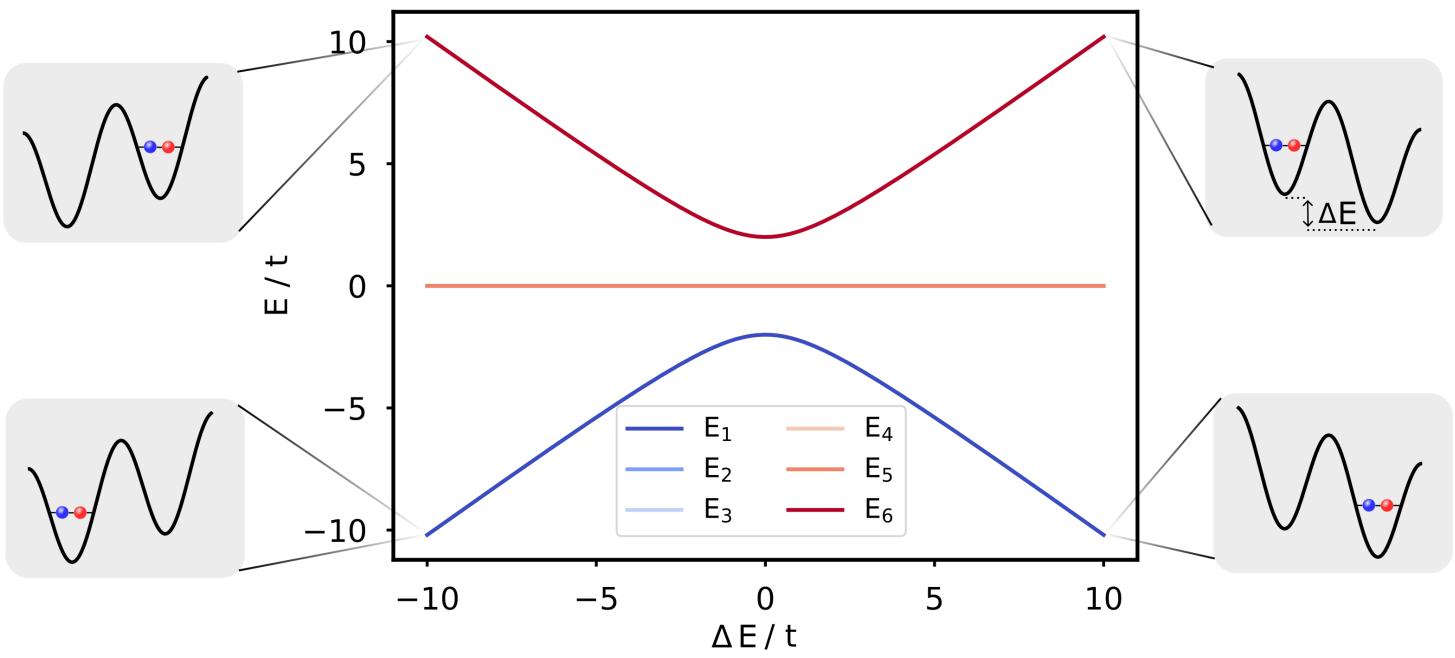

Figure 6.4: Non-interacting Fermi-Hubbard model ($U = 0$). As the the energy offset ΔE is increased, the ground state becomes a doubly-occupied state. Note at $\Delta E = 0$, energy is again set by tunneling bandwidth $4t$.

interaction,

$$\hat{H}_{\text{eff}} = J_{\text{SE}}\left(\hat{\tilde{\mathbf{s}}}_0 \cdot \hat{\tilde{\mathbf{s}}}_1 - \frac{1}{4}\right), \tag{6.5}$$

where

$$J_{\text{SE}} = \frac{4t_z^2}{U}\frac{1}{2}\left(\frac{1}{1-\Delta E/U} + \frac{1}{1+\Delta E/U}\right) = \frac{4t_z^2 U}{U^2 - \Delta E^2}. \tag{6.6}$$

Here the spin operators are defined as $\hat{\tilde{\mathbf{s}}}_j = \sum_{\alpha\beta=\{e,g\}} \hat{\tilde{c}}^{\dagger}_{j,\alpha}\boldsymbol{\sigma}_{\alpha\beta}\hat{\tilde{c}}_{j,\beta}/2$, where $\boldsymbol{\sigma}_{\alpha\beta}$ are Pauli matrices. $\hat{\tilde{s}}^{\alpha}_j$ for $\alpha \in \{X, Y, Z\}$ refers to spin-1/2 matrices describing atoms on sites j in the lab frame.

Expanding $\hat{\tilde{\mathbf{s}}}_0 \cdot \hat{\tilde{\mathbf{s}}}_1 = (\hat{\tilde{\mathbf{s}}}_0 + \hat{\tilde{\mathbf{s}}}_1)^2/2 - 3/4$, we obtain triplet states ($|d\rangle \equiv |g,g\rangle$, $|u\rangle \equiv |e,e\rangle$,$|t\rangle \equiv (|g,e\rangle + |e,g\rangle)/\sqrt{2}$) with zero energy, and the singlet state ($|s\rangle \equiv (|g,e\rangle - |e,g\rangle)/\sqrt{2}$) with energy $-J_{\text{SE}}$ with respect to the triplet states. We note that with four basis states this Hamiltonian is simpler than the Fermi-Hubbard Hamiltonian.

This is a convenient point to next understand how interactions affect our Ramsey fringe

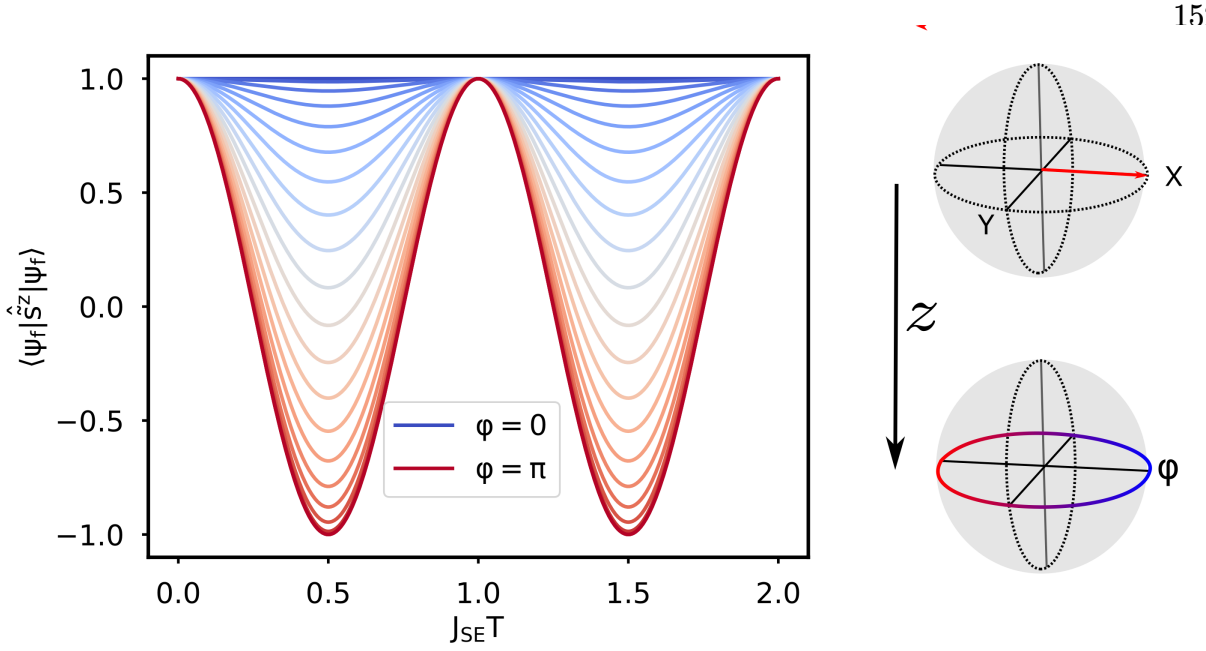

Figure 6.5: Contrast oscillations versus spin-orbit coupled phase φ. Maximum oscillation amplitude occurs at $\varphi = \pi$. Note this condition is not so different than our operating parameter $2\pi a/\lambda_{clk} \approx 7\pi/6$.

contrast. The oscillation of the contrast can be understood based on the time evolution of the initial state generated by the first Ramsey pulse. This state has a spiral phase $e^{ij\varphi}$ imprinted by the clock laser with Rabi frequency Ω, $\hat{H}_{\text{clock}}(\theta)/\hbar = \frac{1}{2}\sum_j(|\Omega|e^{i\theta} \times \hat{\vec{s}}_j^{+} e^{ij\varphi} + H.c.)$, where θ controls the rotation axis. We consider the initial state generated by the first Ramsey pulse with $|\Omega|T_1 = \pi/2$,

$$\begin{aligned} |\psi_{\text{init}}\rangle &= e^{-i\hat{H}_{\text{clock}}(\theta=\pi/2)T_1/\hbar} |g\rangle_0 \otimes |g\rangle_1 \\ &= \frac{1}{\sqrt{2}}(|g\rangle_0 + |e\rangle_0) \otimes \frac{1}{\sqrt{2}}(e^{-i\varphi/2}|g\rangle_1 + e^{i\varphi/2}|e\rangle_1) \\ &= \frac{1}{2}\left[e^{-i\varphi/2}|d\rangle + e^{i\varphi/2}|u\rangle + \sqrt{2}\cos(\varphi/2)|t\rangle + i\sqrt{2}\sin(\varphi/2)|s\rangle\right]. \end{aligned} \tag{6.7}$$

The dynamics in the dark time can be described by the singlet state $|s\rangle$ acquiring a phase $e^{iJ_{\text{SE}}T/\hbar}$. Then we apply the second Ramsey pulse with $|\Omega|T_2 = \pi/2$ with the same θ, and

get the final state

$$|\psi_f\rangle = -ie^{i\varphi/2}\sin(J_{\mathrm{SE}}T/2\hbar)\sin^2(\varphi/2)\,|d\rangle + \frac{1}{4}e^{-i\varphi/2}\Big(3e^{-iJ_{\mathrm{SE}}T/2\hbar} + (1-\cos(\varphi))e^{iJ_{\mathrm{SE}}T/2\hbar} + \cos(\varphi)\Big)\,|u\rangle$$
$$+ \frac{i}{\sqrt{2}}\sin(J_{\mathrm{SE}}T/2\hbar)\sin(\varphi/2)\sin(\varphi)\,|t\rangle - \frac{1}{\sqrt{2}}\sin(J_{\mathrm{SE}}T/2\hbar)\cos(\varphi/2)\sin(\varphi)\,|s\rangle\,. \tag{6.8}$$

In this case the Ramsey fringe contrast is given by $C = 2|\langle\psi_f|\hat{\tilde{s}}^z|\psi_f\rangle|/N$, where $\hat{\tilde{s}}^z = \hat{\tilde{s}}^z_1 + \hat{\tilde{s}}^z_2$. The contrast will thus undergo oscillatory dynamics,

$$C(T) = \left|\cos^2\left(\frac{\varphi}{2}\right) + \sin^2\left(\frac{\varphi}{2}\right)\cos(J_{\mathrm{SE}}T/\hbar)\right|. \tag{6.9}$$

These contrast oscillations $\langle\psi_f|\,\hat{\tilde{s}}^z\,|\psi_f\rangle$ are plotted in Fig. 6.5.

6.1.2.3 XXZ Hamiltonian

While dynamics for small system sizes can be exactly solved with the two spin models above, it relies on preparing a complicated initial state with SOC on each site, then solving the ensuing dynamics with a fairly simple Hamiltonian. To gain intuition about the dynamics, it is attractive to do a basis rotation where the initial state is simpler. As depicted in Fig. 6.6, we rotate into a "spiral" frame where the initial state is uniform (all atoms in the same superposition state) and the site-dependent laser phase φ on a site j is absorbed into the spin operators across the lattice, $\hat{s}^{\pm}_j = \hat{\tilde{s}}^{\pm}_j e^{\pm ij\varphi}$, $\hat{s}^Z_j = \hat{\tilde{s}}^Z_j$. Thus, we obtain a superexchange spin Hamiltonian in the spiral frame

$$\hat{H}_{\mathrm{SE}} = \sum_j J_{\mathrm{SE}}(j)\left[\frac{1}{2}\left(e^{i\varphi}\hat{s}^+_j\hat{s}^-_{j+1} + H.c.\right) + \hat{s}^Z_j\hat{s}^Z_{j+1}\right]. \tag{6.10}$$

Once again, the superexchange interaction strength is $J_{\mathrm{SE}}(j) = 4t_z^2U/(U^2 - \Delta E_j^2)$, which is inhomogeneous due to the local potential difference between adjacent sites ΔE_j, including gravity and the lattice Gaussian confinement. We see this interaction Hamiltonian is anisotropic, as it exhibits exchange-symmetric XXZ-style anisotropy and an antisymmetric spin exchange term. Observables such as atomic coherence reveal collective quantum dynamics on timescales of the averaged $\bar{J}_{\mathrm{SE}}$ over the ensemble, which is tuned by controlling the inhomogeneity and the lattice depth.

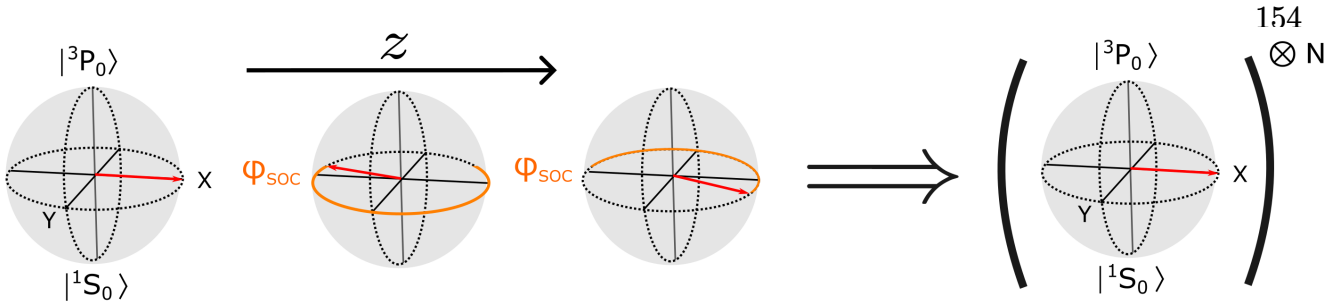

Figure 6.6: Spiral basis transformation. The site-dependent laser phase φ is absorbed into the spin operators: $\hat{s}_j^{\pm} = \hat{\tilde{s}}_j^{\pm} e^{\pm ij\varphi}$, $\hat{s}_j^{Z} = \hat{\tilde{s}}_j^{Z}$. Thus, the initial state in this transformed basis is polarized state on the collective Bloch sphere.

We also give a brief overview of the 1D lattice interaction model. Given this interaction model has been extensively studied in optical lattice clocks [59, 216], we use it as a benchmark, given that the 3D model is comparatively less explored. The corresponding interaction dynamics are well described by a collective spin model that includes both on-site p-wave interactions between atoms in different radial modes and off-site s-wave interactions. Both s- and p-wave interactions contribute to decoherence and atom loss, and their contributions can be balanced to optimize coherence times. A more detailed summary of the 1D spin model including the relevant terms in the Hamiltonian is provided in Section 6.2.4.4.

Finally, we provide some broader context regarding why superexchange interactions are relevant before diving into our experimental study [74, 75, 76]. The physics of superexchange is central in describing magnetic phenomena such as antiferromagnetism [77, 78] and is believed to play a role in superconductivity [79]. Several ultracold atom experiments have employed optical lattices to explore low-temperature bosonic ferromagnetic and fermionic antiferromagnetic correlations induced by superexchange [80, 81, 82, 83, 3, 84, 85, 86], as well as some non-equilibrium superexchange-driven quantum dynamics in local density probes [226, 227, 228, 229, 230]. In clocks, such interactions can also be directly employed for the generation of large scale quantum entanglement over the entire 3D lattice system [87, 88, 89, 68]. Thus, we can engineer a large, coherent spin ensemble with inter-

action precisely controlled to introduce and optimize quantum coherence, correlation, and entanglement to advance the frontier of quantum metrology [231, 64, 232, 233].

6.1.3 Ramsey fringe contrast measurements

In this section, we overview the basic experimental techniques and analysis to extract the Ramsey contrast. The experimental schematic is depicted in Fig. 6.7A. After evaporation, we confine the atoms in a retroreflected, cubic lattice operating at the magic wavelength of $\lambda_{magic} = 813$ nm with lattice constant $a \approx 407$ nm [33]. Beginning with a nuclear-spin polarized Fermi gas with a temperature $T/T_F \approx 0.2$, the atoms are adiabatically loaded into the ground band of the 3D lattice [107, 33]. The lattice depth $\left(V_\perp\right)$ of the transverse (horizontal with respect to gravity) confinement is tuned independently from the depth of the vertical confinement $\left(V_z\right)$ by adjusting the optical power in the corresponding lattice beams. Our two-level spin system is established between the ground ${}^1S_0$ $\left(|g\rangle\right)$ and metastable electronic 'clock' state ${}^3P_0$ $\left(|e\rangle\right)$. We coherently drive the clock transition $|g, m_F = -9/2\rangle \leftrightarrow |e, m_F = -9/2\rangle$ at $\lambda_{clk} \approx 698$ nm with a vertical laser beam using an optical local oscillator locked to an ultrastable silicon cavity [39].

To confine the atoms in our 3D lattice, we adiabatically ramp all lattice beams in three 150 ms steps. Starting at 0 E_R, we ramp to 2.5 E_R, then 10 E_R, before ramping to our final trap depth V_F for clock spectroscopy. Here, $E_R = h^2/8ma^2 \approx h \times 3.5$ kHz is the lattice photon recoil energy, For measurements with $V_F \leq 10$ Er, we ramp $0E_R \rightarrow 2.5E_R \rightarrow V_F$ then hold. To prepare for clock spectroscopy in our magic wavelength lattice, we ramp off the XODT trap over 100 ms, while leaving the lattice depths at V_F.

After loading the lattice, we put the atoms into a superposition of $|g\rangle$ and $|e\rangle$ and perform Ramsey spectroscopy. For detection, *in situ* absorption imaging along the vertical direction is employed and approximately 100 photons per atom are scattered over a 1 μs pulse duration with minimal blurring compared to the diffraction-limited point-spread function of 1.3 μm [234, 24]. Two images of the ground and clock state atoms, their numbers denoted

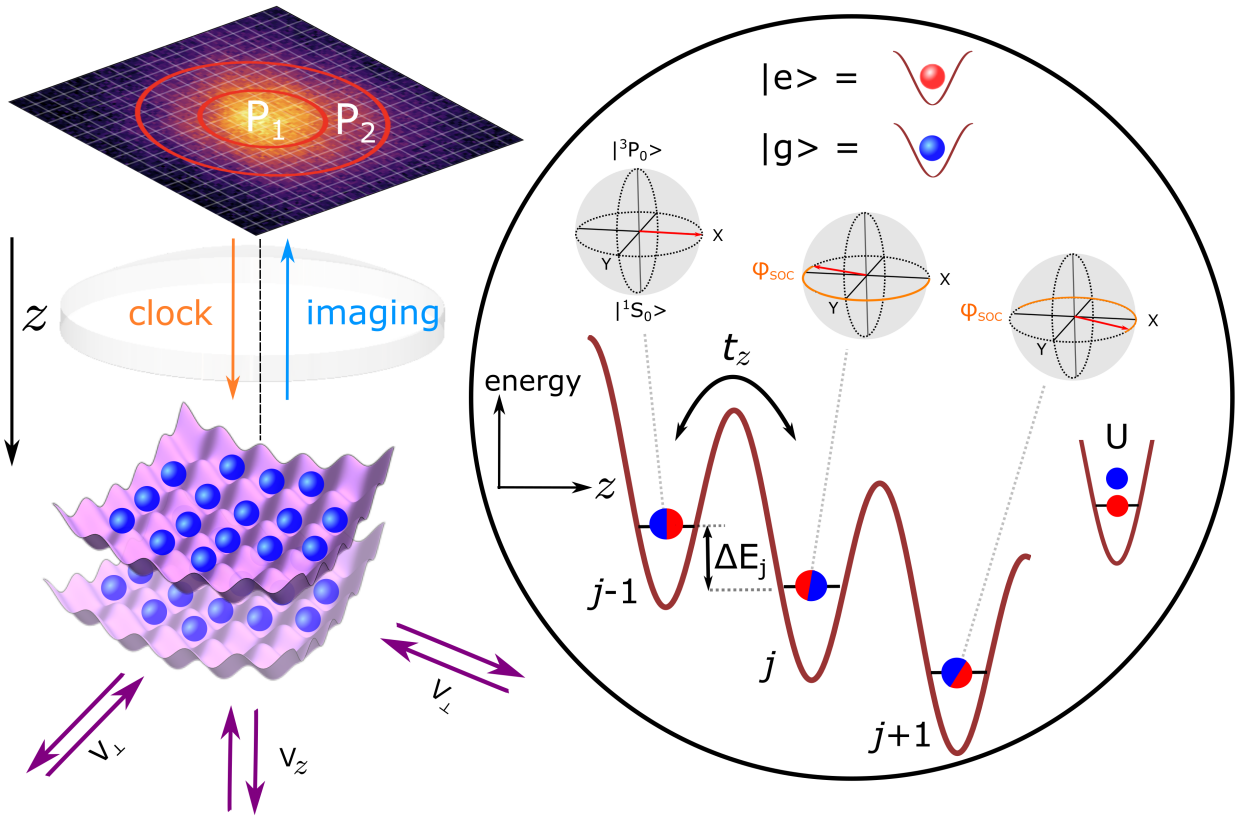

Figure 6.7: **Left**: Ultracold fermions are confined in the ground band of a three-dimensional optical lattice with tunable confinement. Lattice depths can be independently varied by changing the optical power of retro-reflected beams in the transverse $V_\perp$ or vertical direction V_z. *In situ* imaging allows to spatially resolve interactions and dephasing via imaging spectroscopy [178]. **Right**: Dynamics are described via the Fermi-Hubbard model with tunneling t_z, interaction energy U, and a site-to-site energy shift ΔE_j from the lattice Gaussian confinement. Atoms along the z axis on sites indexed $j-1, j$ are initialized in a superposition state of the ground state $|g = {}^1S_0\rangle$ and the metastable electronic state ('clock' state) $|e = {}^3P_0\rangle$, where the clock laser imprints local phase shift φ due to spin-orbit coupling. Dephasing of the coherence is proportion to an effective superexchange rate: $4t_z^2 U/(U^2 - \Delta E_j^2)$.

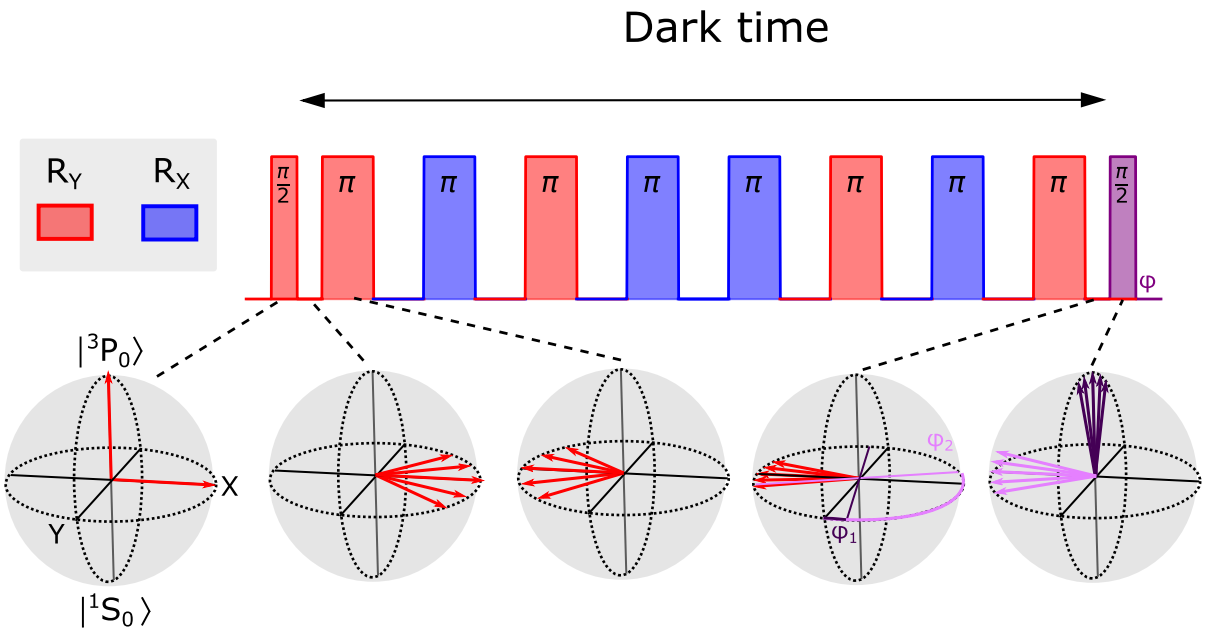

Figure 6.8: Ramsey spectroscopy is employed to study the coherence time. An XY8 pulse sequence is used to mitigate single-particle dephasing. The dephasing and rephasing of individual spins is depicted on the Bloch sphere during the echo sequence. For the final $\pi/2$ pulse two choices of the randomized phase $\varphi_{1,2}$ are shown (light and dark purple) to illustrate the spread of resulting excitation fractions in individual realizations.

N_g and N_e, are taken to determine the excitation fraction $p_e = N_e/(N_e + N_g)$. For a chosen region-of-interest P_A of our imaged density distribution, we record the local excitation fraction $p_e^A = N_e^A/(N_e^A + N_g^A)$. This is shown in Fig. 6.7A, where the excitation fractions are evaluated in spatially separate regions P_1 and P_2 to determine both the Ramsey fringe contrast and relative atomic coherence using imaging spectroscopy [178].

To evaluate atomic coherence at different lattice confinement, we measure the Ramsey fringe contrast for varying dark time T. An XY8 sequence consisting of eight π pulses along the two orthogonal rotation axes in the equatorial place of the Bloch sphere is used to remove single particle dephasing as depicted in Fig. 6.8 [235, 236]. To decouple the atomic coherence measurement from the finite atom-light coherence time (~3 s) [39], the phase of the final Ramsey $\pi/2$ pulse is randomized. Parametric plots of the excitation fractions

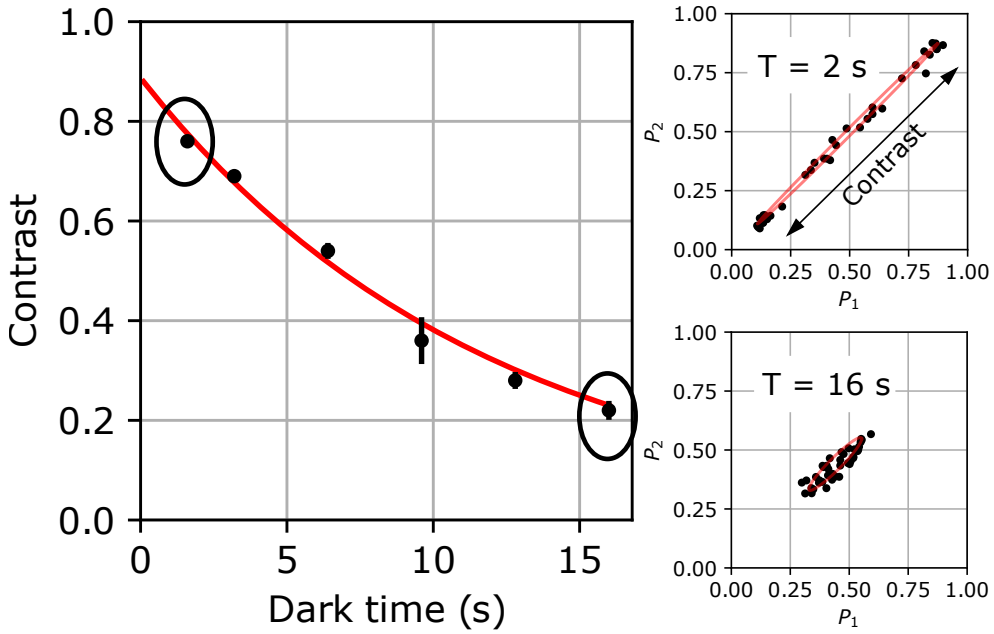

Figure 6.9: To determine the coherence time T_2, the contrast decay is fit to an exponential $C(T) = C_0 e^{-(T/T_2)}$ as a function of dark time T. The contrast is determined via parametric plots of excitation fractions in regions P_1 and P_2 of the ensemble as depicted in Fig. 6.7. Error bars are 1σ (standard deviation) obtained from jackknifing.

from concentric regions P_1 and P_2 ($P_1 < 6\mu$m and $6\ \mu\text{m} < P_2 < 12\mu$m with respect to the trap center) are used to determine the contrast as shown in Fig. 6.9. These parametric plots show ellipses, where a maximum likelihood estimator determines the ellipse contrast and jackknifing is used to extract 1σ (standard deviation) errorbars for all Ramsey contrast measurements [178]. The system is sufficiently homogeneous in the spatial regions P_1 and P_2 that the contrast C is approximately the same. No statistically significant phase shift between P_1 and P_2 is measured, indicating that the XY8 pulse sequence largely removes any spatially varying frequency shift.

Our saturated imaging procedure using our high-resolution (NA = 0.2) vertical imaging system is detailed in Chapter 5. We extract the contrast of our atomic ensemble using imaging spectroscopy where the local excitation fractions in two spatially separated regions

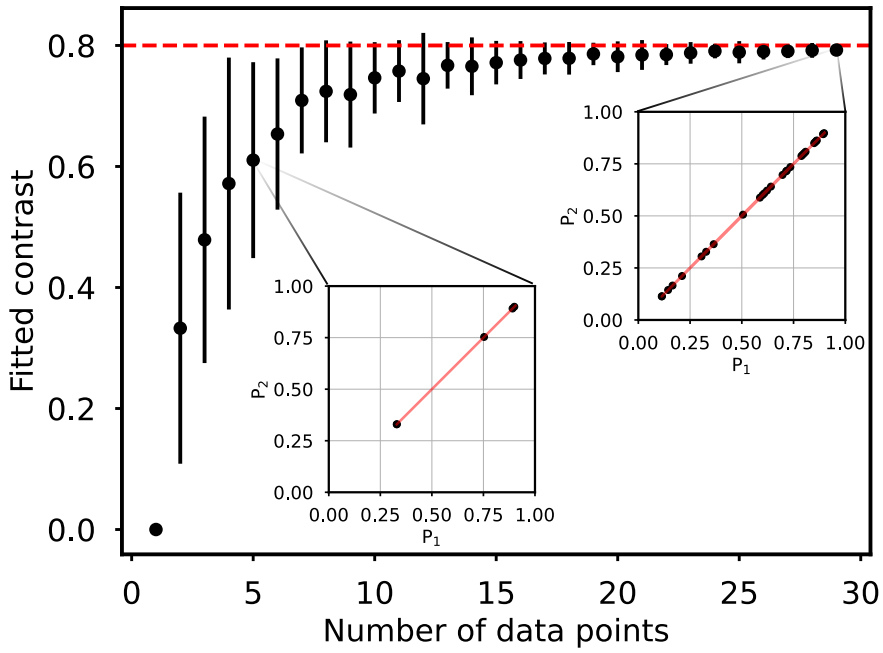

Figure 6.10: Simulated ellipse fitting fidelity. We sample data from a known distribution $(C = 0.80, \phi = 0)$, anc examine the convergence of the fitted contrast as a function of data points. Single realizations of simulation are plotted as callouts. We see contrast measurements are biased and thus one can underestimate contrast is not enough data is collected. $\gtrsim 40$ data points were taken for reported measurements in this chapter to ensure than these systematic errors are minimal.

are compared. Ellipse fitting is used, where parametric plots in regions P_1, P_2 trace an ellipse $= \frac{1}{2} + \frac{C}{2}\cos\Big(2\pi f_{1,2} T + \phi_0\Big)$ [178]. The differential frequency shift $f_{1,2}$ between spatial regions of interest following our XY8 decoupling sequence is consistent with zero. This is illustrated in Fig. 6.9, where the parametric plots show a straight line with no opening angle. We use jackknifing to determine the 1σ (standard deviation) contrast error bars. For n excitation fraction measurements at a given dark time T, we first determine the contrast $\bar{C}$ using all data points. Next, we cycle through all n datapoints and recompute the contrast $C_{\neq i}$ excluding the i-th data point. Summing all contributions we estimate the uncertainty: $\mathrm{Var}(C) = \frac{n-1}{n} \sum_i^n (\bar{C} - C_{\neq i})^2$

It is useful to determine the necessary data to experimentally measure the contrast

with low uncertainty. To evaluate this, we simulate our ellipse fitting fidelity. We sample data from a known distribution ($C = 0.80, \phi = 0$), and examine the convergence of the fitted contrast as a function of data points as plotted in Fig. 6.10. We see that contrast measurements are biased and thus one can underestimate contrast is not enough data is collected. $\gtrsim 40$ data points were taken for reported measurements in this chapter to ensure than these systematic errors are minimal.

6.2 Observing coherent superexchange interactions

Combining an understanding of the various dephasing mechanisms and spectroscopy sequences detailed above, we next describe our study of the effects of interactions on our clock spectroscopy. In the current experiment we independently vary the lattice confinement to explore the 1D and 3D lattice spin models, including the crossover between the two regimes. To do so we load a degenerate Fermi gas of ^{87}Sr atoms into a 3D lattice with tunable confinement, allowing us to vary the interaction strength and tunneling rates. The interaction effects on spin coherence between the ground and metastable clock state are directly recorded on Ramsey fringes. In a vertical 1D lattice, we achieve coherence times of $\sim$20 s when minimizing the contribution of s and p-wave interactions. As a weak transverse confinement is turned on, s-wave interactions are increased by orders of magnitude and very fast dephasing is observed. At deep transverse confinement, favorable coherence times are partially recovered, and coherent superexchange interactions are manifested directly in oscillations of the Ramsey fringe contrast persisting over a timescale of multiple seconds.

Before quantitatively modelling the different dephasing mechanisms, we wished to broadly scan over a large interaction parameter space by varying $V_\perp$ and V_z. The extracted quality factor $Q = \pi C_0 T_2 \nu$ is plotted in Fig. 6.11, where ν is the clock transition frequency $\approx$ 429 THz. We identify two interesting regimes to investigate further: (1) In the 1D lattice regime with no transverse confinement the longest coherence times are observed; (2) With deep transverse confinement where the average $\bar{J}_{\mathrm{SE}}/h \gtrsim 1$ Hz, coherent superexchange

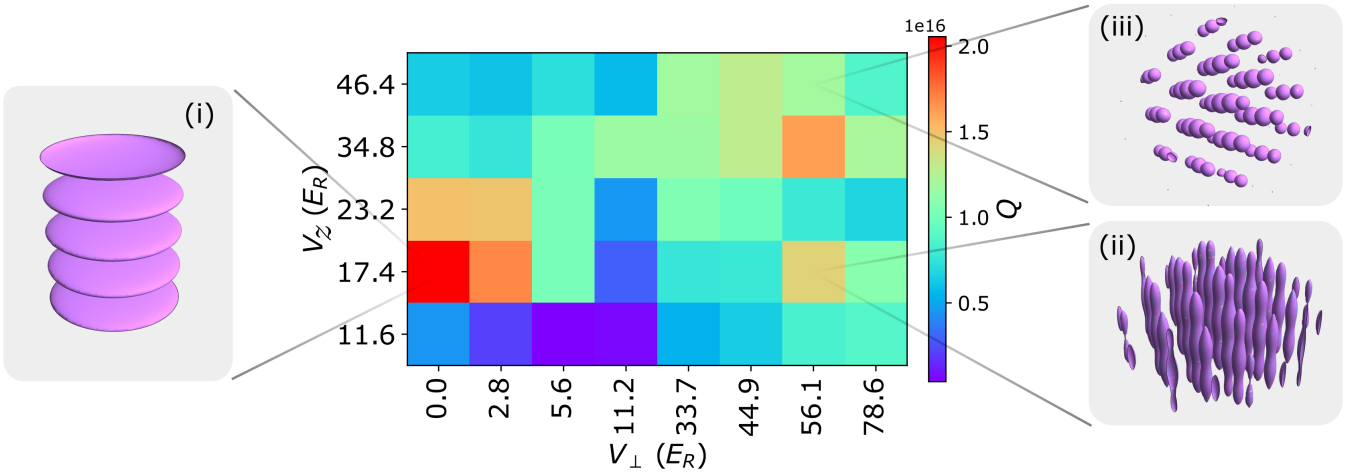

Figure 6.11: The quality factor $Q = \pi C_0 T_2 \nu$ where $\nu \approx 429$ THz is plotted over a wide range of transverse and vertical confinement. Two candidate regimes are identified to investigate further. The weak or zero transverse confinement regime (i), where the longest optical lattice clock T_2 times have been reported [21]. Regime (ii), where fast initial contrast decay is observed due to superexchange interactions. The deep 3D lattice regime (iii) was studied on this platform in [72] where the coherence time is limited by Raman scattering of lattice photons.

dynamics are observed on the Ramsey fringe contrast over a timescale of seconds. As previously reported [72], the deep 3D lattice regime (3) where $\bar{J}_{\mathrm{SE}}/h \ll 1$ Hz reveals a limit on the coherence time primarily due to Raman scattering of lattice photons on $|e\rangle$ atoms. The dark times in this study ($T < 16$ s) are short compared to both the $^1S_0$ lattice lifetime and vacuum lifetime as plotted earlier in Ch. 3.8.

6.2.1 3D lattice study: Superexchange interactions

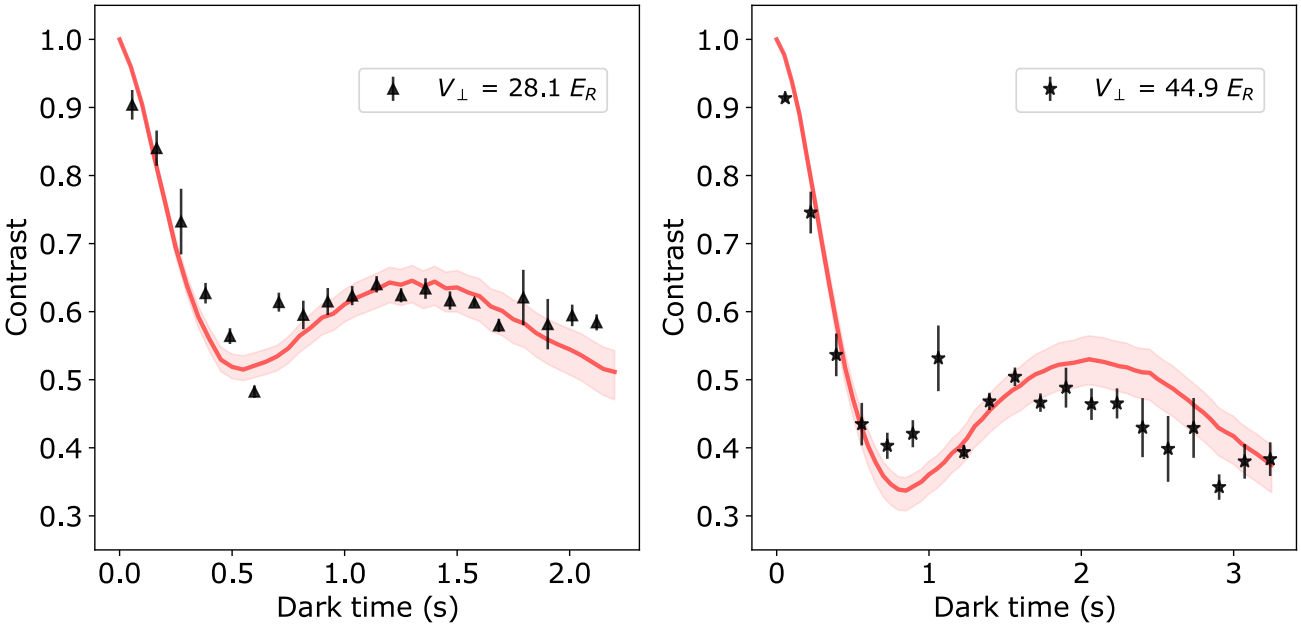

Figure 6.12: Ramsey contrast decay is studied in a 3D lattice at fixed $V_z = 17.4\ E_R$ and thus t_z, while $V_\perp$ is varied between approximately 70 and 20 E_R primarily modifying U. Decay curves at $V_\perp = 28.1\ E_R$ **left**, and 44.9 E_R **right**, are plotted. Error bars are 1σ (standard deviation). Red lines are theory, averaging contrast decay in 1D chains initialized from a thermal distribution of the 3D cloud with fitted temperatures of 350(14) nK for $V_\perp = 28.1$ E_R and 322(17) nK for $V_\perp = 44.9\ E_R$. The error bands stem from the uncertainty on the temperature and T_2.

In Fig. 6.12, we show the contrast decay as a function of dark time for $V_\perp > V_z$, finding a clear oscillatory feature on timescales of the superexchange rate $\bar{J}_{\mathrm{SE}}$. For these measurements V_z is fixed to $17.4E_R$ at which $t_z \approx h \times 14.2$ Hz, where $E_R = h^2/8ma^2 \approx h \times 3.5$ kHz is

the lattice photon recoil energy. $\bar{J}_{\mathrm{SE}}$ is tuned by varying $V_\perp$ between 19.7 and 67.4E_R, thus varying U/h from 1.2 to 2.3 kHz. In the $V_\perp \gg V_z$ regime, the system is comprised of isolated vertical tubes along z as shown in Fig. 6.11. We assume all atoms within each tube are pinned in place even for non-unity filling, since the local potential difference is much stronger than tunneling ($\Delta E_j \gg t_z$). We further assume that every uninterrupted chain of neighbouring atoms within a given tube undergoes evolution under the superexchange Hamiltonian $\hat{H}_{\mathrm{SE}}$. Their evolution is independent of other chains, and the contrast is an average over all chains. The curves in Fig. 6.12 show numerical predictions averaging over the full 3D system using calibrated experimental parameters, an optimized temperature and include the overall slow decay in contrast reported in Fig. 6.11, which find good agreement with the measurements. The extracted temperatures indicates that our experiments operate at a central filling fraction of ≈ 0.5 atoms per lattice site.

To extract the superexchange rates, we vary $V_\perp$ and fit the experimentally measured contrast decay to the function $C_{\mathrm{SE}}(T) = Ae^{-T/T_2} + B\cos(2\pi f T)e^{-T/T_{\mathrm{osc}}} + D$. In Fig. 6.13 the measured oscillation frequencies f are first compared to results derived from the same full many-body Hamiltonian used to generate the theory curves in Fig. 6.12 (empty red squares). Here, the oscillation frequencies are extracted in the same way as for the measurement data. Additionally, we are also comparing to a simplified theoretical model that averages over contributions of two-site pairs (blue line), which is expected to be valid for low to intermediate filling fractions where long chains are unlikely. This calculation includes higher-order interaction effects such as bond-charge corrections to the tunneling rate t_z. The agreement with both theoretical models is excellent for intermediate $V_\perp$ between 22.5 and 45 E_R. For the deepest $V_\perp$, the experimentally measured rate appears to be higher-frequency. Numerical calculations suggest this could arise from additional interaction inhomogeneity or light-scattering effects [237] that favor higher frequency contributions. At shallow $V_\perp < 20E_R$ where $V_\perp \approx V_z$, our theoretical approximation of isolated vertical tubes breaks down and in-plane interactions become relevant. In Fig. 6.13, the dark times of the contrast decay data

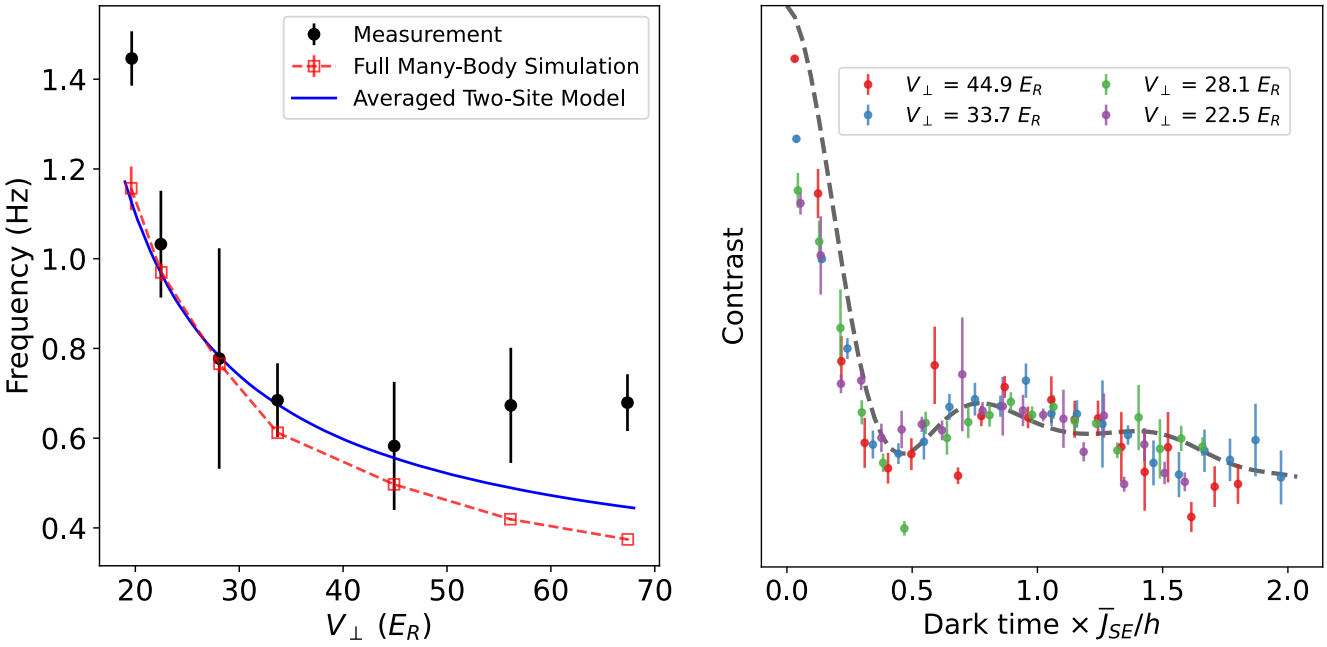

Figure 6.13: **Left**: Fitted contrast oscillation frequencies (black points) are compared to the fit results obtained from the full simulations as shown in panels A, B (red empty squares) and calculated superexchange frequency (blue line) including bond-charge corrections to t_z, which averages the expected oscillations with local ΔE_j and U along the imaging direction. Error bars are 1σ (standard deviation) uncertainty of the fitted frequency. **Right**: Contrast curves approximately collapse when dark times are rescaled by the calculated oscillation frequency (blue line). A simple simulation sampling spin chains with different lengths and coupling strengths (gray dashed line) is overlaid.

are rescaled by the calculated superexchange rate from the two-site model (blue line). The rescaled data collapse to a single curve, reflecting the underlying superexchange dynamics in all measurements. This is also in agreement with a more general theoretical model that attempts to capture the effects of finite temperature and trap inhomogeneity without explicitly invoking experimental details. Instead, the superexchange couplings and chain lengths are randomly sampled from probability distributions that aim to capture the experimental parameters and inhomogeneity. We do not expect perfect rescaling due to varying $J_{\mathrm{SE}}(j)$ inhomogeneity owing to a change in lattice curvature as a function of $V_\perp$.

For additional confirmation of the superexchange oscillations, we explored using other

decoupling pulse sequences than just XY8. The Ramsey fringe contrast for both XY8 and a single π pulse are plotted in Fig. 6.14. We see that the oscillation dynamics are not so different for the different sequences. Exploring driven superexchange dynamics could be an interesting research direction for future studies. Additionally, the atom loss in these measurements is plotted in Fig. 6.15. We clearly see that we are in the regime where superexchange dynamics J_{SE} are much quicker than the atom loss rate $1/\tau$ where $\tau = 19(1)$ s is the fitted $1/e$ time constant. This is promising step for future quantum simulation studies, as atom loss strongly hinders the fidelity of these experiments.

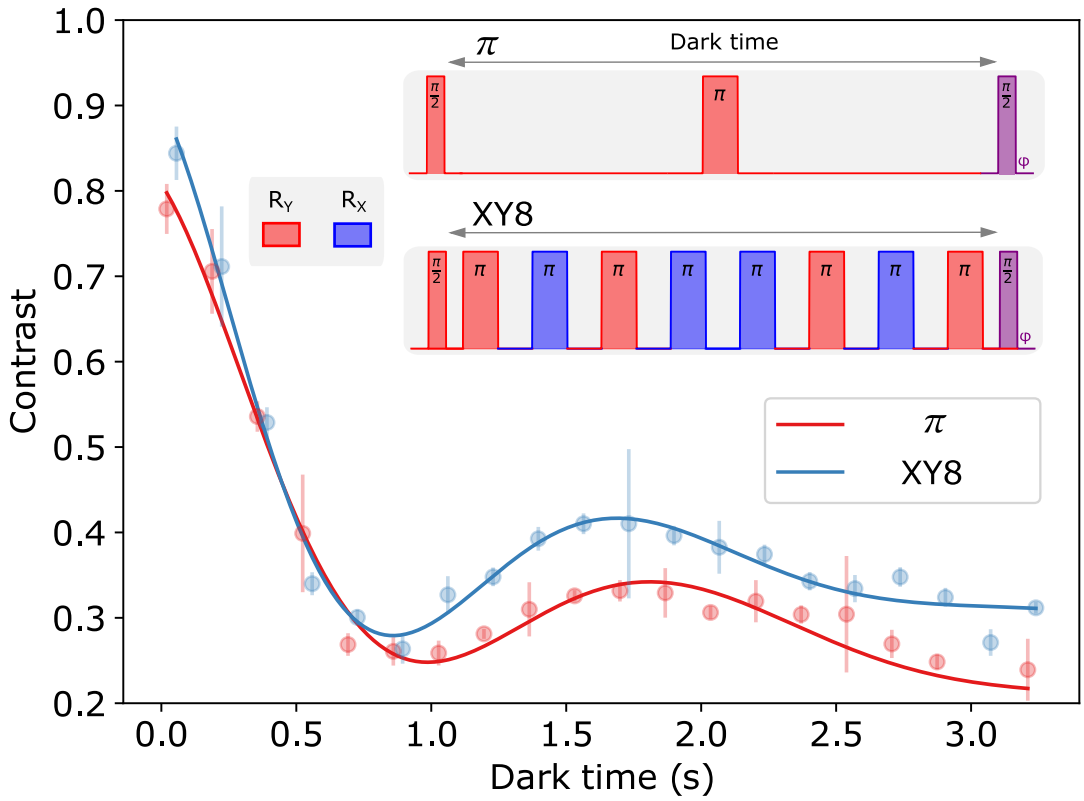

Figure 6.14: We explored contrast decay using both an XY8 decoupling sequence and a standard spin echo sequence with a single π pulse. The solid lines are fits using the model $C_{\mathrm{SE}}(T)$.

In order to study the properties of the interactions further, we vary the lattice filling and the energy offsets ΔE_j of the local lattice tilt in Fig. 6.16. First, the fraction of atoms

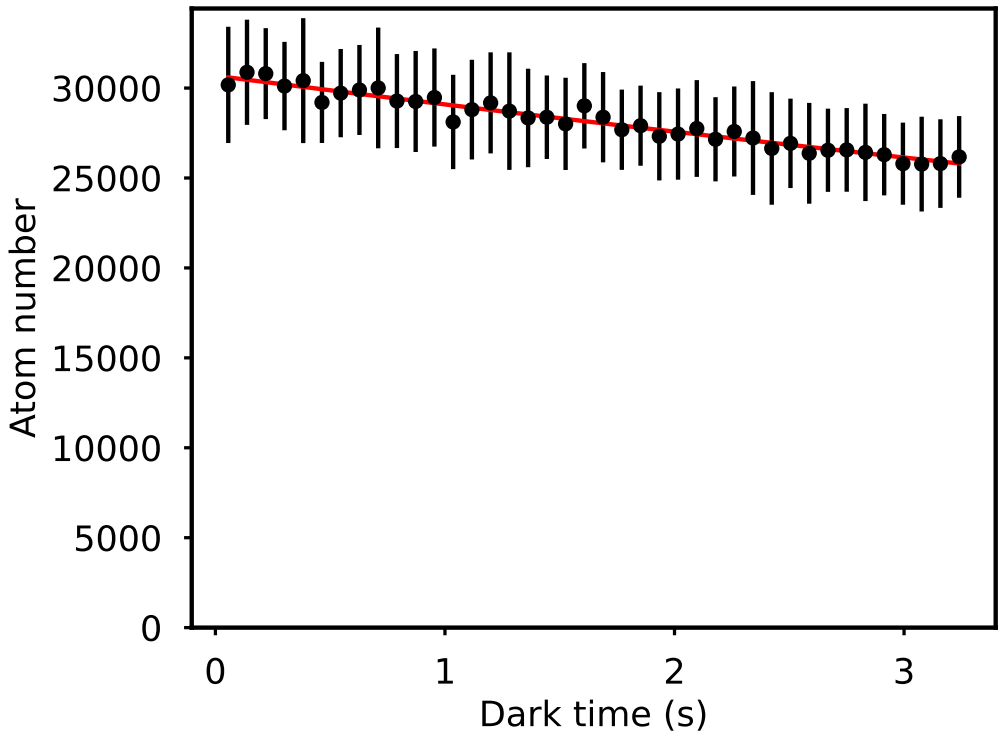

Figure 6.15: Atom loss in superexchange regime. For atom loss, we fit a 1/e time constant $\tau = 19(1)$ seconds with $V_\perp = 44.9E_R$ and $V_z = 17.4E_R$ conditions. Statistical errorbars in this measurement are susceptible to long term drifts of the total atom number.

participating in superexchange is reduced by imprinting holes in the lattice. Beginning with maximum filling, before Ramsey spectroscopy a variable clock laser pulse duration is used to shelve atoms in $|e\rangle$ with spatially uniform probability, and subsequently the remaining $|g\rangle$ atoms are removed with resonant light at 461 nm. The ensuing contrast decay as a function of the total atom number N is plotted in Fig. 6.16. The oscillation amplitude, reflecting the fraction of atoms participating in superexchange, is strongly decreased as N is reduced due to the increasing number of holes. Due to the reduced filling fraction at the wings of the atom cloud, this effect is also observed when choosing the region of interest to be an annulus and increasing its radius compared to P_2 as shown in Fig. 6.18.

As the position of the atoms in the combined potential of gravity and the lattice confinement is shifted vertically the site-to-site energy shift ΔE_j, and consequently the su-

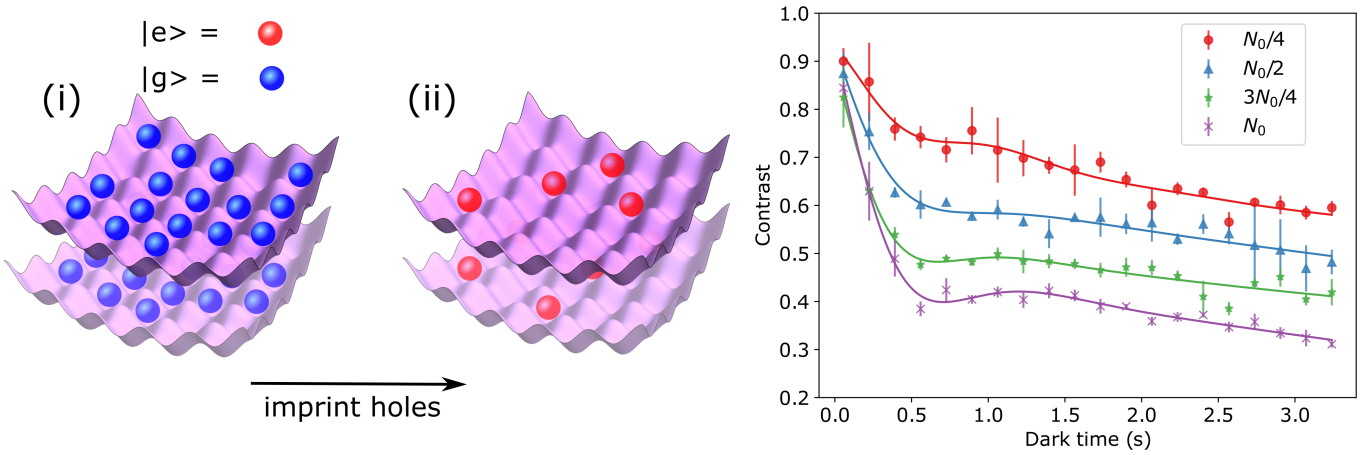

Figure 6.16: All measurements presented here are performed at trap depths $V_z = 17.4\ E_R$ and $V_\perp = 44.9\ E_R$. The fraction of atoms participating in superexchange is modified by reducing the filling fraction via uniformly adding holes as depicted in **left** panel. In (i), the initial state is a near unity filled sample of ground state atoms. Next, atoms are placed in a superposition state with tunable pulse area. Light resonant with $|^1S_0\rangle$ is turned on to imprint holes, with the remaining atoms in $|^3P_0\rangle$ as shown in (ii). The contrast decay is plotted in **right** as the clock pulse area and thus total atom number N is reduced compared to the initial atom number N_0. The solid lines shown in **right** panel are fits using the model $C_{\mathrm{SE}}(T)$. Error bars are 1σ (standard deviation).

perexchange interaction strength, is strongly modified. We precisely move the cloud position at the μm scale. Figure 6.17 displays these oscillations as a function of cloud position z. We compare the oscillation frequency with a heuristic simulation analogous to Fig. 6.13 of the Ramsey contrast in Fig. 6.17 (red line). Averaging the Ramsey signal along the z-direction during imaging strongly suppresses the effect of locally enhanced $J_{\mathrm{SE}}(j)$ where $U = \Delta E_j$. The asymmetry of the background trap gradient around $z = 0$ leads to a reduction of the oscillation frequency at large z where $\Delta E_j > U$. The frequency of the simulation shows qualitative agreement with the measured oscillation.

For the measurements in Fig. 6.17, we displace the position of the atoms in the lattice potential to locally change ΔE_j. This requires precise adjustment of the density distribution at the µm level. To accomplish this, we use our horizontal imaging system with imaging parameters in [234]. We used a commercial, piezo actuated mirror that moves the XODT

beam to adjust the center position of the atomic density distribution.

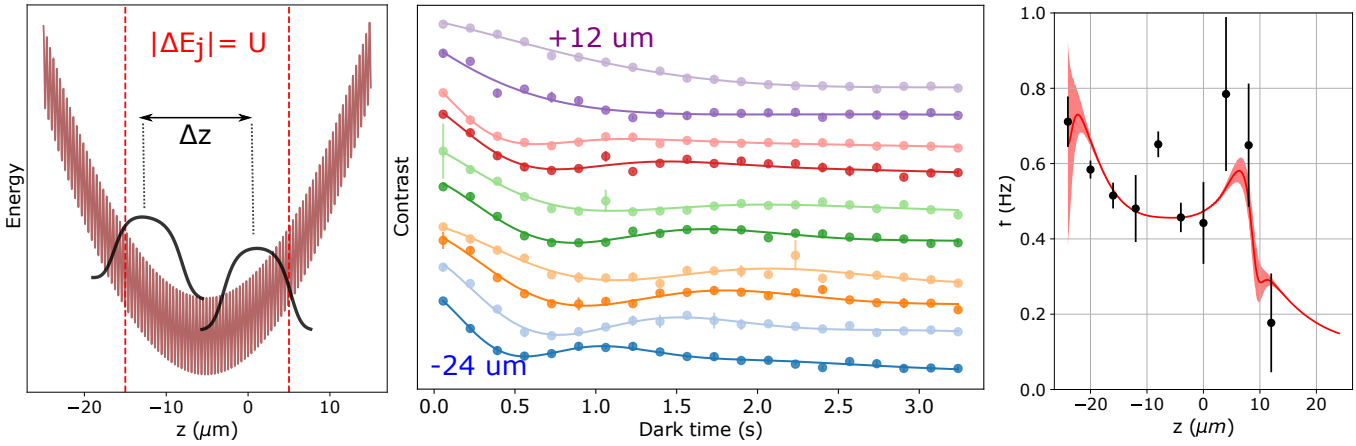

Figure 6.17: In **left** panel, the superexchange coupling is modified by changing the position of the atoms in the lattice potential varying the site-to-site energy shift ΔE_j. At the positions indicated by vertical red lines tunneling becomes resonant and strongly enhances the local $J_{\mathrm{SE}}(j)$. However, averaged over the whole cloud this only slightly modifies the oscillation frequencies. Oscillations in contrast at different vertical positions z are shown in **middle** panel; curves are shifted vertically according to z position. These measured oscillation frequencies are compared with a heuristic superexchange simulation (red line) of the Ramsey contrast in **right** panel.

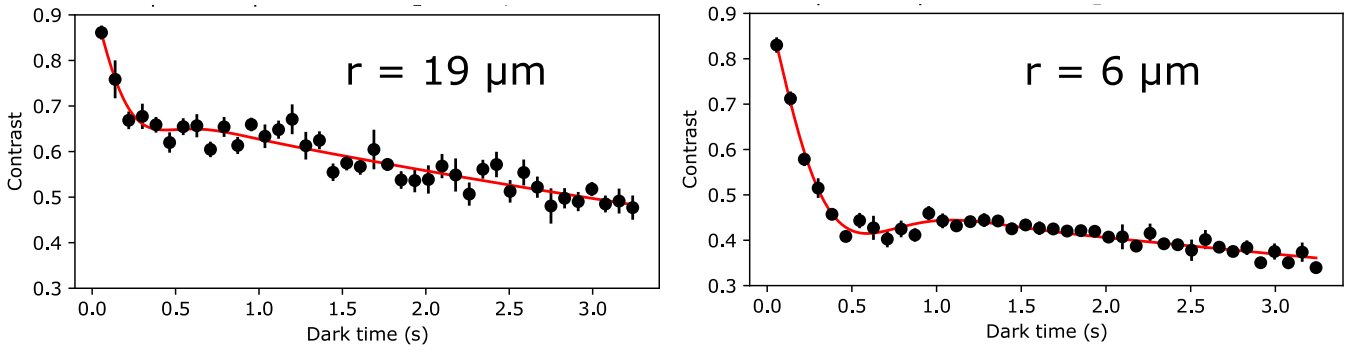

Figure 6.18: Contrast decay in two regions of interest using annulus' with thickness 2 px (0.8 μm) and radii 14 px (6 μm), 48 px (19 μm) are plotted. $V_\perp = 44.9\ E_R$ and $V_Z = 17.4\ E_R$ was used for these measurements. Error bars are 1σ (standard deviation) uncertainty of the Ramsey contrast obtained from jackknifing. The sparsely filled region (19 μm) has higher contrast due to the lower filling fraction compared to near the center of the cloud (6 μm).

6.2.2 1D lattice study: s and p-wave interactions

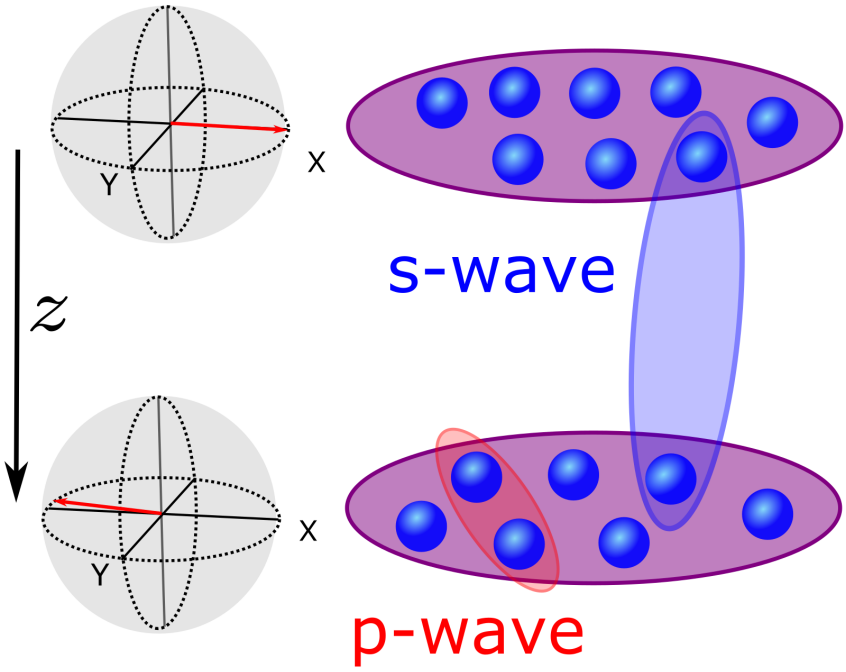

Figure 6.19: In the weak transverse confinement regime, both off-site s-wave interactions, induced by the SOC phase between lattice sites, and on-site p-wave interactions between atoms contribute to dephasing [60]. Their strength is controlled by the vertical confinement V_z and transverse confinement $V_\perp$, strongly influencing the observed coherence time T_2.

In the previous section, we detailed the study of superexchange interactions in our 3D lattice. Modelling the system via an XXZ Hamiltonian is only valid in the regime $V_z \ll V_\perp$, for which the system acts as individual vertical tubes and each site with an atom acts as a spin-1/2 particle. In this section we detail studies in our 1D lattice, along with the crossover regime to 3D. Prior work [60] has also shown that in the 1D lattice confinement along z ($V_\perp = 0$), interactions are weak and instead single-particle eigenstates defined in terms of vertical Wannier-Stark eigenstates (eigenstates of the 1D lattice and gravity) and transverse

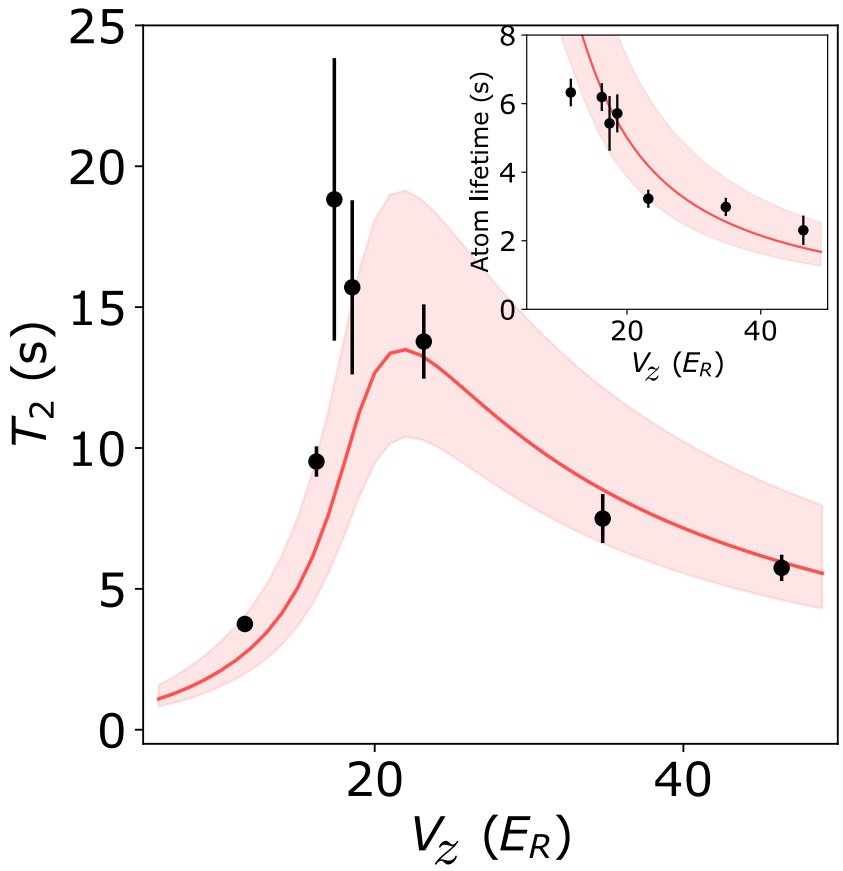

Figure 6.20: T_2 is measured without transverse confinement ($V_\perp = 0$). In the inset the atom lifetime τ, limited by inelastic p-wave loss, is plotted as a function of V_z. Theory modeling Ramsey contrast decay based on the 1D spin Hamiltonian using experimental measured parameters is overlaid in red. The error bands are based on the uncertanties of the experimental parameters. Error bars are 1σ (standard deviation) uncertainty of the fitted T_2 and τ values.

eigenmodes create an energy lattice where atoms remain frozen. In this 1D limit, on-site interactions favor spin alignment between atoms, locking them into large collective spins of Wannier-Stark level n along gravity , $\hat{S}_n^\alpha$, whose dynamics is described by the same type of spin Hamiltonian as superexchange but with modified couplings and an additional onsite term. $\hat{H}_{\mathrm{LS}} = \hat{H}_{\mathrm{on-site}} + \hat{H}_{\mathrm{off-site}}$. Here, $\hat{H}_{\mathrm{on-site}} \sim \sum_n \hat{S}_n^Z \hat{S}_n^Z$ describes the on-site p-wave interactions (see Fig. 6.19), and $\hat{H}_{\mathrm{off-site}}$ includes the off-site s-wave interactions and takes the same form as $\hat{H}_{\mathrm{SE}}$ by replacing the spin-1/2 operators with large-spin operators. In this

work, we bridge these two regimes by varying the transverse lattice confinement $V_\perp$. We extend the theoretical description of Ref. [60] to the regime $V_z \gg V_\perp$, where in each pancake the weak transverse lattice defines a new set of transverse eigenmodes with renormalized spin couplings.

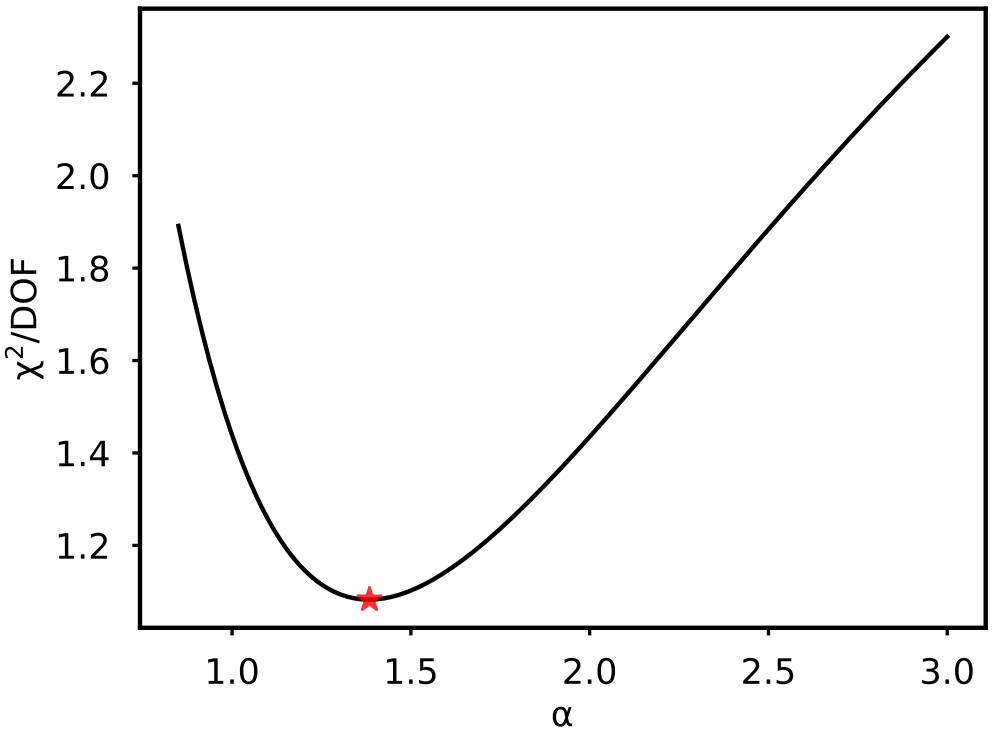

Figure 6.21: All 1D lattice measurements are fit to a stretched exponential $Ce^{(-T/T_2)^\alpha}$ where α is fixed. We re-fit the data varying α and plot the χ^2/DOF for each fitting iteration. χ^2 is minimized for $\alpha = 1.38$ (starred point).

In 1D ($V_\perp = 0$), both on-site p-wave and off-site s-wave interactions contribute to the contrast decay (see Fig. 6.19). The observed T_2 coherence time and atom lifetime are plotted as a function of V_z in Fig. 6.20. Varying V_z provides two distinct regimes to probe the physics of contrast decay. At large V_z, atoms become localized in Wannier orbitals along the z-lattice and interact predominantly via on-site Ising-type p-wave interactions that contribute to slow contrast decay with $T_2 \sim 1/\sqrt{N_s}$ (N_s is the atom number per pancake), as observed in previous studies [59]. As V_z decreases, the reduced p-wave interaction leads to slower

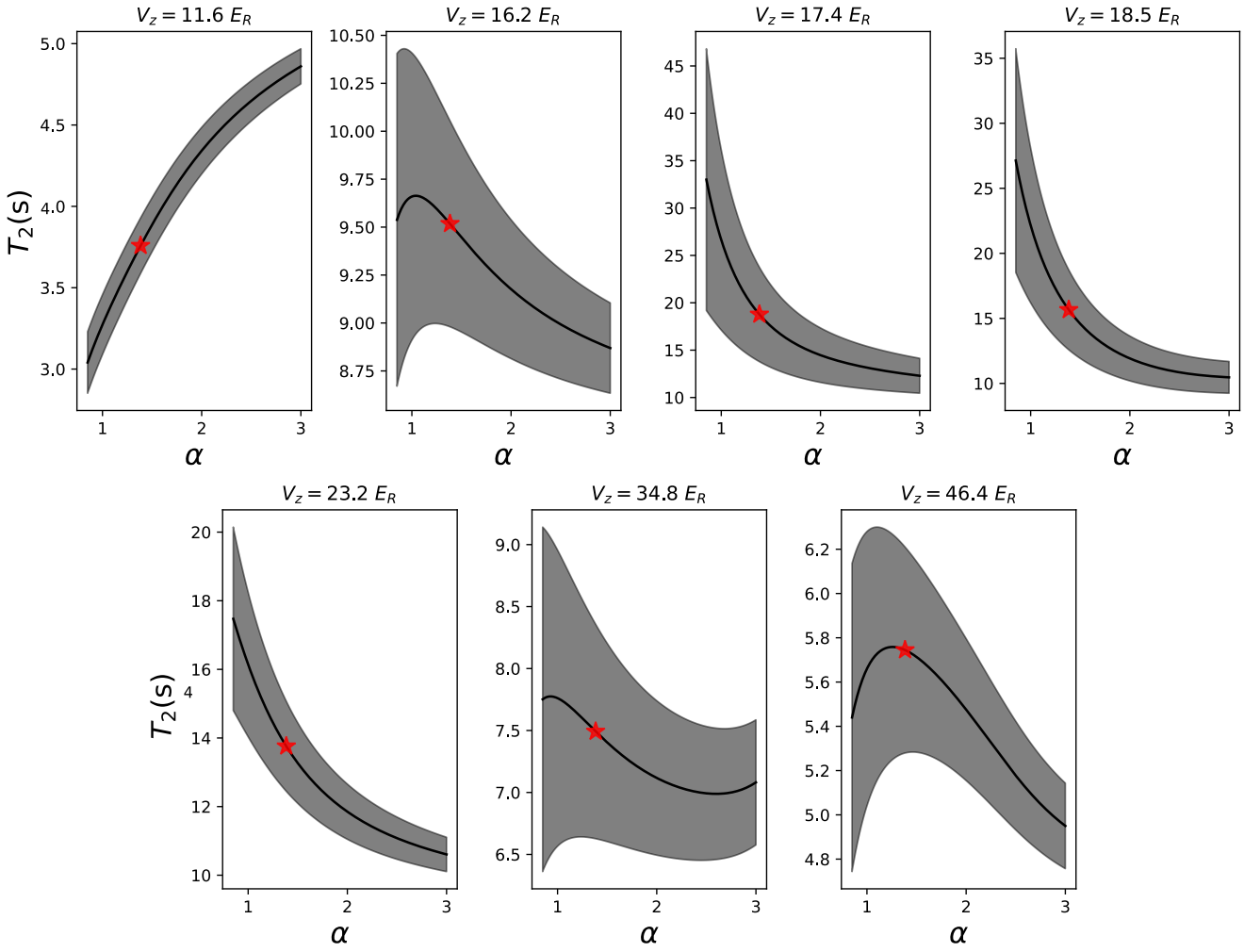

Figure 6.22: T_2 dependence on stretched exponential parameter α. Red star corresponds to the fitted $\alpha = 1.38$.

decoherence rate. However, the Wannier-Stark states become increasingly delocalized along z and atoms experience progressively stronger off-site s-wave interactions. The interplay between s-wave and p-wave interactions leads to spin wave instabilities that contribute to fast contrast decay with $T_2 \sim 1/N_s$. With increasing s-wave interaction strength, this instability rate increases as V_z decreases. The crossover between these two mechanisms occurs around $V_z = 17.4E_R$, with a correspondingly longest coherence time of 19(5) s. While experiment and theory largely agree with each other, the discrepancy at long coherence times could arise from unexpected reduction of the s-wave interaction strength from re-thermalization

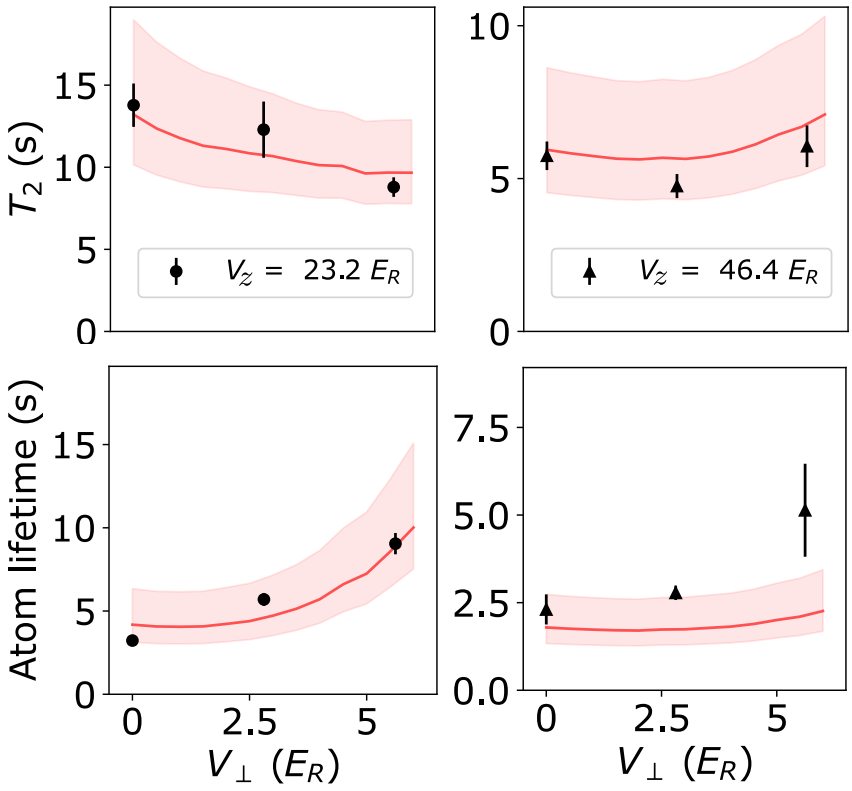

Figure 6.23: A weak transverse confinement $V_\perp$ is applied. This leads to increased atom lifetime τ, as well as a reduction of T_2 at intermediate $V_z = 23.2E_R$ and a enhancement of T_2 at deep $V_z = 46.4E_R$.

processes neglected in the theory. The 1D lattice employed in this study operates with a much higher density than previous studies [21, 60]. Thus, the atom lifetimes (see Fig. 6.20 inset), limited by inelastic p-wave loss are correspondingly much shorter [21].

For the $V_\perp = 0$ measurements in Fig. 6.11, as a function of dark time T, a stretched exponential function $C_0 e^{-(T/T_2)^\alpha}$ is fit to the Ramsey contrast to extract a T_2 coherence time for $T > 1$ s. For $V_\perp = 0$, we expect intra-site, all-to-all p-wave interactions to lead to Gaussian decoherence. We extract a single value $\alpha = 1.38$ by minimizing the combined χ^2 for all measurements for $V_\perp = 0$. χ^2 as a function of α is plotted in Fig. 6.21. The fitted T_2 time for each α value is plotted in Fig. 6.22. For all other measurements with $V_\perp > 0$, we

set $\alpha = 1$ when fitting T_2.

Upon introduction of a weak transverse confinement ($V_\perp \ll V_z$), the increasing localization of the transverse modes in the x-y plane leads to enhancement of s-wave interactions. Additionally, due to decreased overlap of transverse modes, p-wave interactions are suppressed, which in turn substantially improves atom lifetimes as shown in Fig. 6.23. Meanwhile, different trends in the coherence time are observed between the intermediate $V_z = 23.2E_R$ and deep $V_z = 46.4E_R$ lattices. For $V_z = 23.2E_R$, the weak transverse confinement increases s-wave interactions within pancakes, enhancing the population of unstable spin wave modes, and a subsequent decrease of T_2. For $V_z = 46.4E_R$, the system remains in the quasi-stable Ising dominated regime and T_2 increases as p-wave interactions decrease.

6.2.3 Lattice inhomogeneties

In this section, we describe the role of spatial inhomogeities in our 3D lattice on our observed contrast oscillations. The superexchange coupling strength $J_{\mathrm{SE}}(j)$ depends on the site-to-site energy shift ΔE_j between atoms on lattice sites j along the clock axis z. Calculating ΔE_j requires determining the atom's location in the lattice Gaussian confinement during clock spectroscopy. Thus, understanding the details of our lattice loading procedure is key. First, we consider the trapping potential in the XODT before lattice loading. The XODT potential including the gravitational tilt is $U_{XODT}(j)/\hbar = (1/2\, m\omega_{XODT}^2 a^2)(j - j_{\mathrm{XODT}})^2 + mgaj$, where j is a dimensionless position in units of the lattice spacing, j_{XODT} is the center position of the XODT beam, and $\omega_{XODT} = 2\pi \times 250$ Hz, thus $U_{XODT}(j)/\hbar = (44.7\text{ Hz})\ (j - j_{\mathrm{XODT}})^2 + (873.1\text{ Hz})\ j$. The bottom of this displaced parabola is at j_{s}, where the atomic density distribution is centered.

Next, we consider the potential of the optical lattice. We align the center of the lattice beams to the atom cloud in the XODT. Thus, the center of the transverse lattice beams is located at j_{s}. After ramping down the XODT beams, the offset of the vertical lattice potential, generated by the two transverse lattice beams, is therefore $U_{\mathrm{lat}} =$

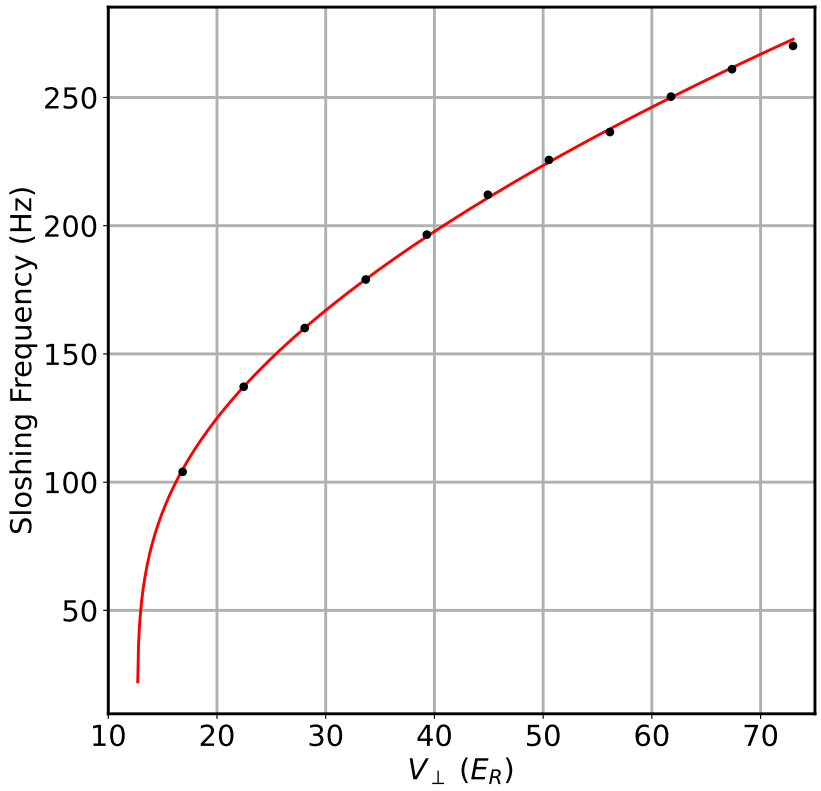

Figure 6.24: Lattice Gaussian confinement calibration. The trap frequency is measured for atoms solely confined in both horizontal lattice beams, each at a power equivalent to the trap depth $V_\perp$. The oscillations are initiated by rapidly switching off the superimposed horizontal dipole trap. We note, that for the evaluation the gravitational sag needs to be taken into account, and that employing a harmonic approximation for estimating the sag induces discernible errors in the beam parameters. Numerical evaluation of the Gaussian beam curvature at the position of the atomic sag allows the construction of a fit function from which the beam waist radius is extracted to be $w = 62.2(14)\,\mu\text{m}$.

$-2V_\perp \exp(-2a^2(j-j_\text{s})^2/w^2) + mgaj$, where w is the transverse lattice beam waist radius extracted in Fig. 6.24. Thus, the minimum of U_lat is at $j < j_\text{s}$. Because we turn off the 1064 nm trap in a deep lattice where tunneling is frozen, the atom position is centered at j_s throughout the Ramsey spectroscopy. Therefore, the cloud is significantly displaced from the center of the lattice potential, as depicted in Fig. 6.17.

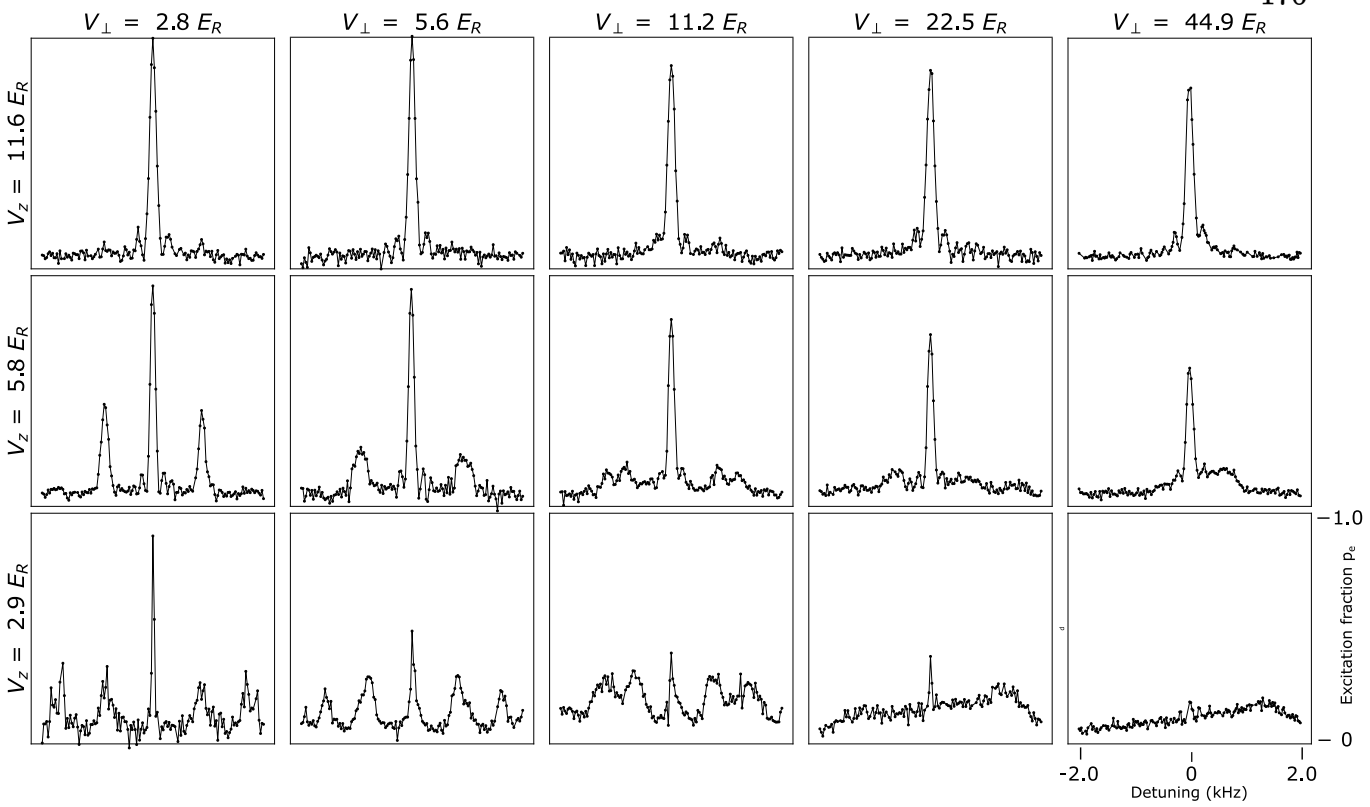

Figure 6.25: Rabi spectroscopy in shallow lattice confinement is studied. The detuning span in each measurement is -2 kHz to 2 kHz. The Rabi pulse duration was optimized for each measurement to maximize the excited state fraction at zero detuning.

The XODT trap frequency ν_{XODT} is calibrated via sloshing measurements, where the atoms are displaced in the dipole trap and their spatial oscillations at ν_{XODT} are measured. We do a similar measurement to determine the Gaussian confinement from the lattice beams. Here, the atoms are loaded from the XODT into a 2D lattice formed by both transverse lattice beams. As depicted in Fig. 6.24, the oscillation frequency is plotted as a function of transverse trap depth $V_\perp$.

The effects of this inhomogeneity can be readily observed with coarse Rabi spectroscopy in a fairly shallow lattice. As seen in Fig. 6.25, as the lattice confinement is varied the carrier and apparent 'sideband' transitions are strongly modified. At shallow transverse lattice depths where the Gaussian confinement is weak, Wannier-Stark peaks at approximately

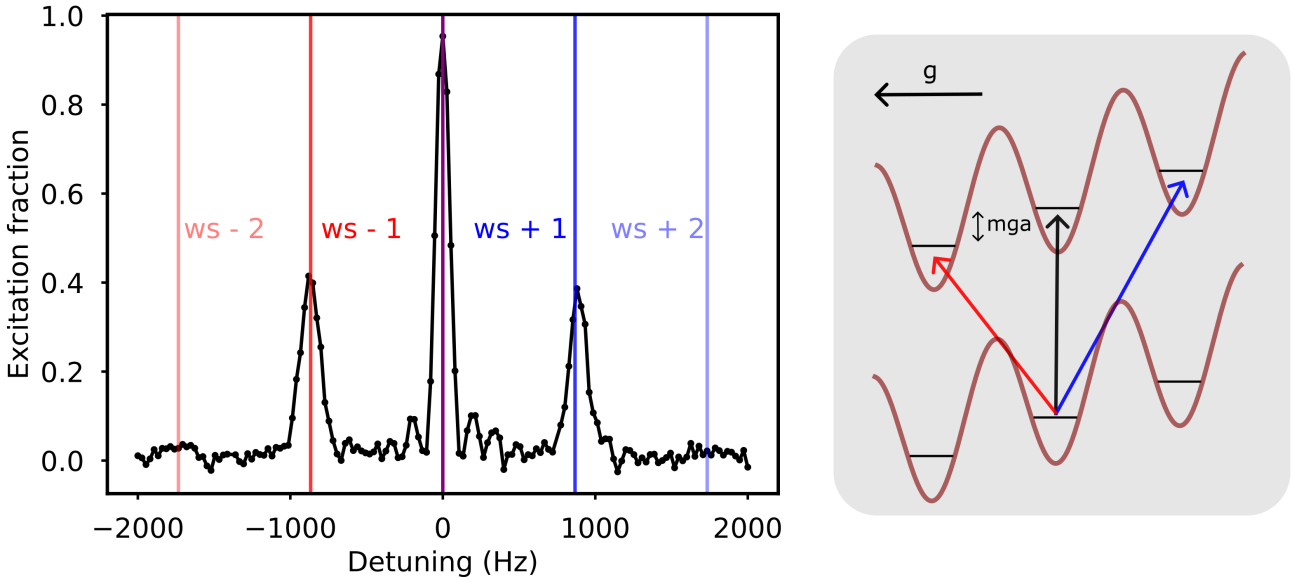

Figure 6.26: **Left:** Rabi spectroscopy for $V_\perp = 2.8\ E_R$ and $V_z = 5.8\ E_R$. Wannier-Stark transitions are clear, as depicted in schematic on **right**. Note, this picture is only correct when neglecting the harmonic confinement of the lattice as $V_\perp \to 0$.

mga are observed as shown in Fig. 6.26. As the transverse confinement, and thus the inhomogeneity, is increased these peaks are broadened. Finally, we checked spatial Rabi frequency inhomogeneity as shown in Fig. 6.27. It is minimal over the region-of-interest < 40 px used in these measurements.

6.2.4 Modelling

In this section we provide details of the modelling used to compare theory and data.[5] Using the spin model explained in Section 6.1.2.3, and accounting for the inhomoegeities outlined in the previous section, the contrast oscillations in our 3D lattice can be well modelled. Additionally, the coherence times and atom loss in the 1D lattice are well captured using the canonical 1D spin model [60, 59].

[5] This section was written with tight collaboration from theorist Ana Maria Rey, and her students Mikhail Mamaev and Anjun Chu, along with Stefan Lannig.

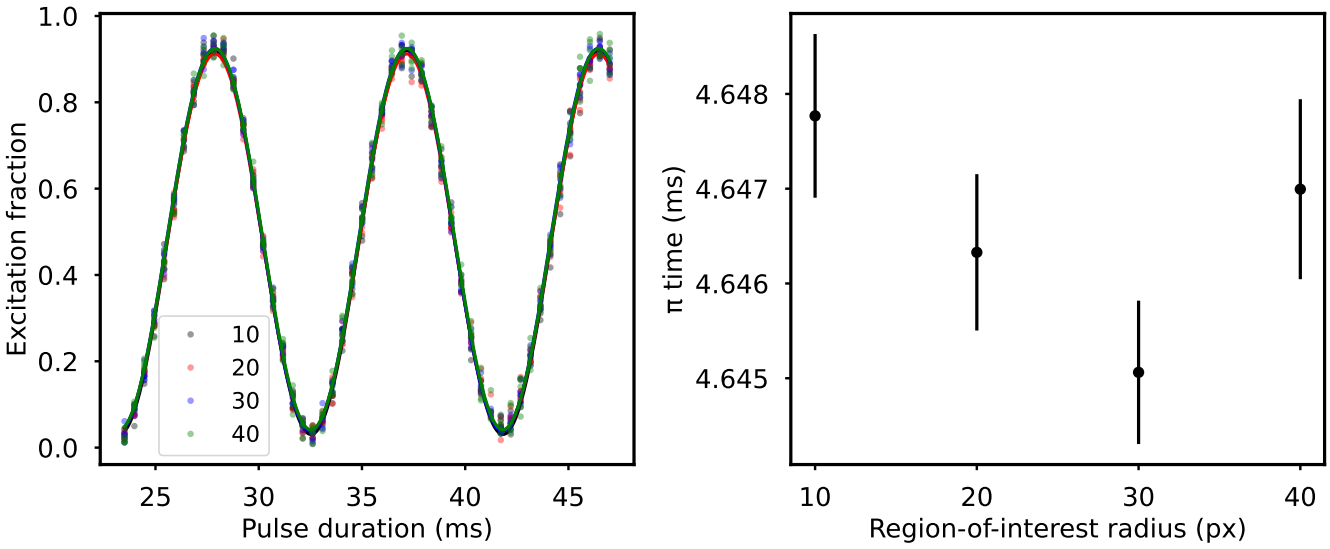

Figure 6.27: **Left**: Rabi flopping is plotted depending on region-of-interest (ROI). Here, the ROI are thin rings of thickness 2 px with corresponding radii in legend. **Right**: Fitted π time as a function of ROI. Rabi drive is homogeneous within experimental uncertainty over the spatial extent of the atomic distribution.

6.2.4.1 Heuristic averaging of superexchange dynamics

In our experiment operating under the conditions $V_z \ll V_\perp$, we ignore tunneling in the transverse directions and consider superexchange dynamics only along the z direction. To capture the superexchange dynamics, we need to include a spatially varying superexchange rate $J_{\mathrm{SE}}(j)$, due to the tilt generated by gravity and the confinement generated by the Gaussian profile of the lattice beam. In addition to the site-to-site energy shift ΔE_j, the reduction of the transverse lattice power at $|j - j_{\mathrm{s}}| \gtrsim w/a$ (with lattice constant a) also decreases the on-site interactions U_j and therefore induces a weak j-dependence. Instead of applying Eq. (6.6), to avoid artifacts from the divergence present in this approximation, we obtain $J_{\mathrm{SE}}(j)$ from an independent diagonalization of Eq. (6.3) at each lattice site j. For simplicity, we focus on the region with uniform density in the x-y plane and therefore consider the variation of J_{SE} only in vertical direction.

Here we assume the oscillatory dynamics are mainly generated by two-atom chains.

So we can heuristically generalize Eq. (6.9) to average over all possible local one-atom and two-atom chains in our system. We define $n(j)$ as the local filling fraction of lattice sites labelled by j, such that the total atom number in each vertical tube is $N_{\mathrm{tube}} = \sum_j n(j)$. In the following, two adjacent lattice sites along z direction are considered but all quantities are given with respect to individual lattice sites. The probability to have only one atom in these two lattice sites is $p^{(1)}(j) = n(j)[1 - n(j)]$, and the probability to have two atoms is $p^{(2)}(j) = [n(j)]^2$. Here, the magnetization of a one-atom chain is $\langle \tilde{s}^{z,(1)}(j) \rangle = \langle \psi_f | \hat{\tilde{s}}^z | \psi_f \rangle = 1/2$, and in a local two-atom chain $\langle \tilde{s}^{z,(2)}(j) \rangle = \{\cos^2(\varphi/2) + \sin^2(\varphi/2)\cos[J_{\mathrm{SE}}(j)T/\hbar]\}/2$ (see Eq. (6.9)) and thus the average magnetization per size is $\langle \tilde{s}^z(j) \rangle = \sum_k p^{(k)} \langle \tilde{s}^{z,(k)} \rangle$. We then average over all spatial positions to obtain the Ramsey contrast

$$\begin{aligned} C(T) &= \frac{1}{N_{\mathrm{tube}}} \left| \sum_j 2 \langle \tilde{s}^z(j) \rangle \right| \\ &= \left| 1 - \sum_j \frac{[n(j)]^2}{N_{\mathrm{tube}}} \sin^2\left(\frac{\varphi}{2}\right) + \sum_j \frac{[n(j)]^2}{N_{\mathrm{tube}}} \sin^2\left(\frac{\varphi}{2}\right) \cos(J_{\mathrm{SE}}(j)T/\hbar) \right|. \end{aligned} \tag{6.11}$$

By fitting a function of the from $Ae^{-T/\tau_{\mathrm{osc}}} \cos(\bar{J}_{\mathrm{SE}} T/\hbar)$ to the oscillatory term in $C(T)$ we obtain the oscillation frequency $\bar{J}_{\mathrm{SE}}/h$, which is the basis for the solid red lines in Figs. 6.13 and 6.17. The bond-charge corrections Δt_z taken into account for the blue line in Fig. 6.13 are scaled with U_j to account for the inhomogeneity across the atom cloud. The error bands are derived from the uncertainty of this fit parameter. We choose a temperature of $\sim 370\,\mathrm{nK}$ to roughly match the peak-to-peak oscillation amplitude of $2\sin^2(\varphi/2)\sum_j [n(j)]^2/N_{\mathrm{tube}} \sim 0.7$ observed in most measurements (as displayed in Figs. 6.17 and 6.12).

We note that this approach of estimating the oscillation frequency does not provide a comprehensive and quantitative model for the coherence as it neglects effects from longer chains and the dynamical decoupling pulse sequence. These are taken into account in the following section.

6.2.4.2 Superexchange contrast dynamics

Now we generalize Eq. (6.5) to the case of many-atoms. Here we work in a "spiral" frame where the initial state is uniform (all atoms in the same superposition state) and the site-dependent laser phase φ is absorbed into the spin operators across the lattice, $\hat{s}_j^{\pm} = \hat{\tilde{s}}_j^{\pm} e^{\pm ij\varphi}$, $\hat{s}_j^Z = \hat{\tilde{s}}_j^Z$, where j is the lattice index along z direction.

This transformation lead to the following 1D spin-spin interaction Hamiltonian [68],

$$\begin{aligned} \hat{H}_{\mathrm{SE}} &= \sum_{j=1}^{L-1} J_{\mathrm{SE}}(j) \left[\cos(\varphi) \left(\hat{s}_j^X \hat{s}_{j+1}^X + \hat{s}_j^Y \hat{s}_{j+1}^Y \right) + \hat{s}_j^Z \hat{s}_{j+1}^Z + \sin(\varphi) \left(\hat{s}_j^X \hat{s}_{j+1}^Y - \hat{s}_j^Y \hat{s}_{j+1}^X \right) \right], \\ J_{\mathrm{SE}}(j) &= \frac{4 t_z^2 U}{U^2 - \Delta E_j^2}, \end{aligned} \tag{6.12}$$

where L is the number of sites, and $J_{\mathrm{SE}}(j)$ the superexchange interaction strength. The latter depends on both the on-site Hubbard interactions and the local potential difference $\Delta E_j = \frac{1}{2} m \omega_{lat}^2 a^2 [(j+1-j_0)^2 - (j-j_0)^2]$, where j_0 is the bottom of the lattice confining potential.

The first three terms act as an XXZ Hamiltonian with spin anisotropy $\sim \sec(\varphi)$, which induces contrast decay. The last two terms are a Dzyaloshinskii-Moriya (DM) type interaction, which breaks exchange symmetry due to the chirality of the imprinted clock laser phase. The latter has been studied in the context of exotic chiral properties such as skyrmions. At the collective mean-field level such an interaction has no effect. In our case since the interaction strengths $J_{\mathrm{SE}}(j)$ are inhomogeneous, the DM interaction will also generate contrast decay, as each atom will feel an unequal force from its left and right neighbours due to the lack of exchange symmetry.

The Ramsey decay dynamics are modeled by initializing a product state of all spins in a uniform superposition state following the first Ramsey pulse as written above,

$$|\psi_{\mathrm{init}}\rangle = e^{-i\frac{\pi}{2}\sum_j \hat{s}_j^Y} \bigotimes_j |{\downarrow}\rangle_j \,. \tag{6.13}$$

The chain then undergoes time-evolution under the Hamiltonian, interspersed with echo

pulses during the XY8 sequence. For a sequence including a single echo pulse we write,

$$|\psi_f(t)\rangle = e^{-i\hat{H}_{\rm SE}t/2}e^{-i\pi\sum_j \hat{s}_j^X}e^{-i\hat{H}_{\rm SE}t/2}\,|\psi_{\rm init}\rangle\,. \tag{6.14}$$

An XY8 sequence instead applies eight pulses about different axes as depicted in the main text Fig. 6.8. After time-evolving the state, a final Ramsey pulse with an arbitrary phase θ is performed,

$$|\psi_{f,\theta}(t)\rangle = e^{-i\frac{\pi}{2}\sum_j\left[\cos(\theta)\hat{s}_j^Y+\sin(\theta)\hat{s}_j^X\right]}\,|\psi_f(t)\rangle\,. \tag{6.15}$$

The contrast of the uninterrupted chain is obtained by measuring the excited state fraction,

$$N_\theta(t) = \langle\psi_{f,\theta}(t)|\left[\sum_j\left(\hat{s}_j^Z+\frac{1}{2}\right)\right]|\psi_{f,\theta}(t)\rangle\,. \tag{6.16}$$

For a single independent chain, contrast is obtained via,

$$C(t) = \frac{1}{L}\left[\max_\theta N_\theta(t) - \min_\theta N_\theta(t)\right]. \tag{6.17}$$

If there are multiple independent chains, their contributions to the excited state fraction $N_\theta(t)$ must be summed together for each angle θ before performing the maximization and minimization above.

A single site $L = 1$ has unity contrast $C = 1$ at all times. Chains with few sites will exhibit persistent oscillations of contrast, whereas chains with many sites will undergo decay, with revivals only occuring on timescales $\sim 1/L$. Inhomogeneity in the superexchange couplings $J_{\rm SE}(j)$ will also wash out revivals or oscillatory dynamics at longer times. The contrast dynamics from many summed, disordered chains thus generally exhibits only one or two oscillations before saturating to a constant value determined by how many of the chains had isolated single sites.

We compare this theory to the experiment by using specific lattice parameters, interaction coupling coefficients, and averaging over the 3D distribution which yields a theoretically predicted contrast $C(T)$. Since the experiment also finds a slower decay on timescale $\sim 1/T_2$ measured in Fig. 6.11, we normalize the resulting contrast obtained from numerical simulation of the superexchange Hamiltonian by a further factor $C(T) \to C(T)e^{-T/T_2}$. The

resulting theoretically predicted contrast is shown as solid lines in Fig. 6.12 of the main text, which is in good agreement with the measurements. The shaded region on the theory curves corresponds to an uncertainty of ± 2 s for the T_2 in this adjustment factor (in line with the T_2 measurement uncertainty). The corresponding calibrated parameters used in these simulations are given in Table 6.1.

$V_\perp$ $[E_R]$	N	ω_{lat}/h [Hz]	$j_0 - j_s$ $[a]$	U/h [kHz]	T_2 [s]
19.6	22,100	12.4	35	1.17	5.7
22.5	13,000	14.3	31	1.27	6.9
28.1	14,800	17.8	25	1.44	9.1
33.7	17,700	21.4	20	1.59	11.4
44.9	22,500	28.5	15	1.86	10.4

Table 6.1: Parameters for 3D lattice simulations. For transverse lattice depth $V_\perp$ we provide the atom number N, the lattice harmonic confinement frequency ω_{lat} along the z direction, the position of the cloud $j_0 - j_s$ relative to the minimum of the lattice confinement (in units of lattice spacing), the on-site Hubbard repulsion U at the center of the lattice, and the lifetime of atomic coherence T_2 (beyond decay caused by superexchange).

In addition, we provide a more simple theoretical prediction without invoking explicit experimental conditions. We randomly sample a large number of chains with lengths L drawn from a Poisson distribution $P(\lambda)$ with low Poisson parameter $\lambda < 1$, appropriate for an initial thermal distribution. The coupling strengths V_j in each chain are drawn from a Gaussian distribution of mean $J_{\mathrm{SE}}(j)$ and standard deviation $\epsilon J_{\mathrm{SE}}(j)$, with ϵ meant to capture inhomogeneity in the superexchange interactions. As ϵ increases, the contrast oscillations reduce in amplitude to the profile observed in the experiment. The curve in Fig. 6.13 of the main text shows the prediction for Poisson parameter $\lambda = 0.25$ and $\epsilon = 0.4$. This curve is also adjusted by a factor of $e^{-\frac{1}{5}T\overline{J}_{\mathrm{SE}}/h}$ to account for slower atomic decay, using an effective lifetime of five superexchange cycles, which is in line with the experimental lifetimes and yields good agreement with all measured data.

6.2.4.3 Corrections to Fermi-Hubbard Parameters

Due to wavefunction overlap with adjacent sites, additional interaction and tunneling terms are present in the Fermi-Hubbard Hamiltonian. We identify the main contributions to be bond-charge type effects [238] and an admixture of higher bands due to the gravitational tilt.

Bond-charge interactions are those with interactions between adjacent sites and additionally an exchange of the particles. This can be cast into the form of a tunneling term, thus directly correcting the tunneling energy $t_z' = t_z + \Delta t_z$ with

$$\Delta t_z = -\frac{4\pi\hbar^2 a_{eg}^-}{m} \int d^3x \, \psi_0^3 \psi_1, \tag{6.18}$$

where $\psi_j = \psi(x, y, z - ja)$ describes the ground band Wannier function ψ at lattice site j. For lattice depths of $V_z = 17.4\ E_R$ and $V_\perp = 44.9\ E_R$ we obtain $\Delta t \approx h \times 1.2\,\mathrm{Hz}$, which corresponds to an increase of about 8% with respect to the bare value of $t_z \approx h \times 14.2\,\mathrm{Hz}$.

A direct calculation of the Wannier-Stark wavefunction suggests an additional correction to the tunneling energy on the order of $\sim 10\%$. However, the exact calculation of the full contribution remains challenging because we estimate that all higher bands would be needed to be taken into account for a faithful quantification [71]. Because these effects are barely above our experimental uncertainty we are mostly neglecting these corrections in this work.

6.2.4.4 1D large-spin Hamiltonian

To model the contrast decay in Fig. 6.19 and Fig. 6.20 we describe the $V_z \gg V_\perp$ regime in 3D optical lattice clocks using the assumption that the spins in each pancake are locking into a large spin based on Ref. [60, 59], which leads to the following 1D large-spin

Hamiltonian:

$$\begin{aligned}\hat{H}_{\mathrm{LS}} &= \hat{H}_{\mathrm{on-site}} + \hat{H}_{\mathrm{off-site}},\\ \hat{H}_{\mathrm{on-site}}/\hbar &= \sum_n \Big[J_{0,n}\hat{\mathbf{S}}_n \cdot \hat{\mathbf{S}}_n + \chi_{0,n}\hat{S}_n^Z\hat{S}_n^Z + C_{0,n}\hat{N}_n\hat{S}_n^Z \Big],\\ \hat{H}_{\mathrm{off-site}}/\hbar &= \sum_n \Big[J_{1,n}\hat{\mathbf{S}}_n \cdot \hat{\mathbf{S}}_{n+1} + \chi_{1,n}\hat{S}_n^Z\hat{S}_{n+1}^Z + D_{1,n}(\hat{S}_n^X\hat{S}_{n+1}^Y - \hat{S}_n^Y\hat{S}_{n+1}^X) \Big].\end{aligned} \tag{6.19}$$

The collective spin operators are defined as $\hat{\tilde{\mathbf{S}}}_n = \sum_{n_x n_y}\sum_{\alpha\beta=\{e,g\}} \hat{\tilde{c}}^\dagger_{n_x n_y n,\alpha}\boldsymbol{\sigma}_{\alpha\beta}\hat{\tilde{c}}_{n_x n_y n,\beta}/2$ in the lab frame, where $\boldsymbol{\sigma}_{\alpha\beta}$ are Pauli matrices, $\hat{\tilde{c}}_{n_x n_y n,\alpha}$ are fermionic annihilation operators for radial mode labelled by (n_x, n_y) assuming separable potential in pancakes, Wannier-Stark level n along gravity and internal state α. $\hat{N}_n$ is the atom number operator for Wannier-Stark level n. We transform into the "spiral" frame by unitary transformation $\hat{S}_n^{\pm} = e^{\pm in\varphi}\hat{\tilde{S}}_n^{\pm}$ and $\hat{S}_n^z = \hat{\tilde{S}}_n^z$. The interaction parameters are

$$\begin{aligned} J_{0,n} &= \eta_0(V_{eg}^{n,n} - U_{eg}^{n,n})/2, \quad \chi_{0,n} = \eta_0(V_{ee}^{n,n} + V_{gg}^{n,n} - 2V_{eg}^{n,n})/2,\\ C_{0,n} &= \eta_0(V_{ee}^{n,n} - V_{gg}^{n,n})/2, \quad J_{1,n} = -\eta_1 U_{eg}^{n,n+1}\cos\varphi,\\ \chi_{1,n} &= -\eta_1 U_{eg}^{n,n+1}(1-\cos\varphi), \quad D_{1,n} = -\eta_1 U_{eg}^{n,n+1}\sin\varphi. \end{aligned} \tag{6.20}$$

where $\varphi = 2\pi a/\lambda_{clk}$ is the spin-orbit-coupled clock phase between nearest-neighbor sites of the lattice, with a the lattice spacing. η_0 and η_1 are dimensionless overlap integrals for on-site and nearest-neighbor interaction respectively,

$$\eta_{|n-m|} = \frac{\sqrt{2\pi}}{k_L}\left(\frac{V_z}{E_R}\right)^{-1/4}\int \mathrm{d}z\,[W_n(z)]^2[W_m(z)]^2, \tag{6.21}$$

where $E_R = \hbar^2 k_L^2/2m$ is the lattice recoil energy, with wave number $k_L = \pi/a$, and $W_n(z)$ is the wave function of a Wannier-Stark state centered at site n.

The s-wave ($U_{\alpha\beta}$) and p-wave ($V_{\alpha\beta}$) interaction strengths ($\alpha,\beta = \{g,e\}$) are calculated by averaging a Fermi-Dirac distribution over radial modes,

$$\begin{aligned} U_{\alpha\beta}^{n,m} &= \frac{8\pi\hbar a_{\alpha\beta}}{m}\frac{k_L}{\sqrt{2\pi}}\left(\frac{V_z}{E_R}\right)^{1/4}\sum_{n_x m_x n_y m_y} s_{n_x m_x}s_{n_y m_y}\frac{N_{n_x n_y n}}{N_{n,\mathrm{init}}}\frac{N_{m_x m_y m}}{N_{m,\mathrm{init}}},\\ V_{\alpha\beta}^{n,m} &= \frac{6\pi\hbar b_{\alpha\beta}^3}{m}\frac{k_L}{\sqrt{2\pi}}\left(\frac{V_z}{E_R}\right)^{1/4}\sum_{n_x m_x n_y m_y}(p_{n_x m_x}s_{n_y m_y} + s_{n_x m_x}p_{n_y m_y})\frac{N_{n_x n_y n}}{N_{n,\mathrm{init}}}\frac{N_{m_x m_y m}}{N_{m,\mathrm{init}}}, \end{aligned} \tag{6.22}$$

where $a_{\alpha\beta}$ is the elastic s-wave scattering length, and $b^3_{\alpha\beta}$ is the elastic p-wave scattering volume. As the atoms are nuclear-spin polarized ($m_F = \pm 9/2 \rightarrow m'_F = \pm 9/2$ transition between $^1S_0$ and $^3P_0$ states), to fully anti-symmeterize the wavefunction the following scattering lengths are required $a_{eg} = a^-_{eg}$, $b^3_{eg} = (b^+_{eg})^3$ [60, 216]. Defining the wave function for a radial mode (n_x, n_y) is $\phi_{n_x}\phi_{n_y}$, we have $s_{nm} = \int \mathrm{d}x\, [\phi_n(x)]^2[\phi_m(x)]^2$, $p_{nm} = \int \mathrm{d}x\, [(\partial_x\phi_n(x))\phi_m(x) - \phi_n(x)(\partial_x\phi_m(x))]^2$. Here $N_{n_xn_yn}$ are the initial population in radial mode (n_x, n_y) and lattice site n under a Fermi-Dirac distribution, $N_{n_xn_yn} = \left[\exp[(\epsilon_{n_xn_y} - \mu_n)/k_BT_R] + 1\right]^{-1}$, where the chemical potential for each lattice site μ_n is chosen to match the initial atom number for each Wannier-Stark level $N_{n,\mathrm{init}} = \sum_{n_xn_y} N_{n_xn_yn}$, and T_R is the radial temperature. Errorbands in Fig. 6.19 and Fig. 6.20 include the uncertainty of s-wave and p-wave scattering parameters, $0.5E_R$ uncertainty of lattice depth, as well as 20% uncertainty in radial temperature.

Apart from unitary evolution under $\hat{H}_{\mathrm{LS}}$, inelastic on-site p-wave e-e collision can lead to two-body loss of the atom number as observed in previous studies [59, 216]. We describe the atom loss based on the following Lindblad master equation,

$$\hbar\frac{d}{dT}\hat{\rho} = -i[\hat{H}_{\mathrm{LS}}, \hat{\rho}] + \sum_n \Gamma_{0,n}\mathcal{L}_n(\hat{\rho}), \tag{6.23}$$

where $\hat{H}_{\mathrm{LS}}$ is the Hamiltonian given in Eq. (6.19). The Liouvillian for e-e loss is given by

$$\mathcal{L}_n(\hat{\rho}) = \sum_{n_xn_ym_xm_y}\left[\hat{L}_{n_xn_ym_xm_y}\hat{\rho}\hat{L}^\dagger_{n_xn_ym_xm_y} - \frac{1}{2}\{\hat{L}^\dagger_{n_xn_ym_xm_y}\hat{L}_{n_xn_ym_xm_y}, \hat{\rho}\}\right], \tag{6.24}$$

where $\hat{L}_{n_xn_ym_xm_y} = \hat{\tilde{c}}_{n_xn_yn,e}\hat{\tilde{c}}_{m_xm_yn,e}$. We use the averaged e-e loss rate over the radial modes to maintain the large-spin description,

$$\Gamma_{0,n} = \eta_0\tilde{V}^{n,n}_{ee}/4, \tag{6.25}$$

where we replace the elastic p-wave scattering volume b^3_{ee} in $V^{n,m}_{ee}$ by inelastic p-wave scattering volume β^3_{ee} to get $\tilde{V}^{n,m}_{ee}$. For simplicity, we assume $U^{n,m}_{\alpha\beta}$, $V^{n,m}_{\alpha\beta}$ and $\tilde{V}^{n,m}_{ee}$ approximately unchanged under atom loss. Due to the XY8 pulse sequence, one can assume the atom loss

for ground and excited states is symmetric, and obtain the following equation for atom loss,

$$\frac{d}{dT}N_n = -\frac{\Gamma_{0,n}}{2}N_n^2, \tag{6.26}$$

which gives an exact solution

$$N_n(T) = \frac{N_{n,\text{init}}}{1+\Gamma_{0,n}N_{n,\text{init}}T/2}. \tag{6.27}$$

We fit the total atom number measured in the experiment integrating through all lattice layers with the fitting function $A/(1+BT)$ using fitting parameters A, B to extract the atom loss rate, and then compare with the analytic solution above.

We perform numerical simulation based on truncated Wigner approximation (TWA) [239]. The key idea is to solve the mean-field equations of Eq. (6.23) with random sampling of initial conditions. For the initial state ("spiral" frame) with all the spins pointing towards $+X$ direction, we set $S_n^X(0) = N_{n,\text{init}}/2$, $N_n(0) = N_{n,\text{init}}$, and sample $S_n^Y(0)$ and $S_n^Z(0)$ using a Gaussian distribution $\mathcal{N}(\mu = 0, \sigma^2 = N_{n,\text{init}}/2)$.

In the case of $V_\perp = 0$, we consider the radial modes as harmonic oscillator modes with trapping frequency $\omega_R = \sqrt{4V_z/mw_L^2}$, where w_L is the Gaussian beam waist of the vertical lattice. We determine the radial temperature T_R by comparing the density distribution projected to the x-y plane between theory and experiment at $17.4E_R$, which leads to $T_R =$ 250nK at this lattice depth. Since the lattice depth is ramping up adiabatically, the ratio $k_BT_R/\hbar\omega_R$ should be roughly a constant, we use $T_R(\text{nK}) = 60 \times \sqrt{V_z/E_R}$ to generate atom distribution in radial modes.

In the case of $V_\perp > 0$, the radial modes are generated by the potential of a 2D lattice with lattice depth $V_\perp$ plus harmonic oscillator with trapping frequency $\omega_R = \sqrt{4(V_z+V_\perp)/mw_L^2}$, where we assume the Gaussian beam waist is nearly the same for all lattice beams, i.e. $w_L \approx w$. The compression step in the loading sequence leads to a lower temperature compared to the case of $V_\perp = 0$, and we use radial temperature $T_R(V_\perp > 0) = 0.42 \times T_R(V_\perp = 0)$ to generate atom distribution in radial modes.

The validity of the 1D spin model is based on the frozen-mode approximation [60, 111], which is to assume all the atoms are fixed in their single-particle eigenstates due to negligible effects of interaction on the single-particle energy spectrum, ensured by $N_{n,\mathrm{init}} J_{0,n} \ll \hbar\omega_R$ and $N_{n,\mathrm{init}} J_{0,n} \ll mga$. We restrict our calculation within $V_\perp \leq 6E_R$ to avoid the breakdown of this approximation.

6.2.5 Conclusion

In conclusion, we have used our degenerate Fermi gas 3D optical lattice clock with anisotropic and tunable tunneling rates in the presence of spin-orbit coupling to directly probe different regimes of interaction effects described by the Fermi-Hubbard Hamiltonian. Superexchange interactions are identified as an important systematic effect that degrade the precision of optical lattice clocks operating with high filling at timescales $h/\bar{J}_{\mathrm{SE}}$. We demonstrate that we can both microscopically model and control these interactions in the 3D optical lattice.

For clock metrology, we can either reduce the magnitude or control the form of the superexchange interactions to enhance clock performance. For example, we can increase the lattice constant a sufficiently large to reduce the tunneling rate to a negligible value [72]. Alternatively, a variable lattice spacing can be used to make a commensurate with λ_{clk} to achieve $\varphi \bmod 2\pi = 0$. Without SOC ($\varphi \bmod 2\pi = 0$) the isotropic Heisenberg Hamiltonian $\sum_j J_{\mathrm{SE}}(j)\hat{\mathbf{s}}_j \cdot \hat{\mathbf{s}}_{j+1}$ is recovered, and any coherent spin state becomes an eigenstate accumulating only a trivial global phase. On the other hand, collective superexchange interactions can be used to produce spin entanglement for quantum enhanced sensing [91]. At intermediate in-plane tunnelling rates, these isotropic, Heisenberg interactions couple the single particles within each plane to collective spins [89]. Thus, by reducing single-particle inhomogeneities via potential shaping or layer selection [240], the collective spins across all planes can be squeezed by SOC-induced XXZ interactions investigated here.

Chapter 7

Outlook

Over the course of the past three Chapters, we discussed different studies on our experimental platform all geared towards both furthering our understanding and advancing the performance of optical lattice clocks. This included improvements to the long-term stability of our optical local oscillator for timekeeping purposes, imaging studies to enable clock operation at high density, and explorations of our clock coherence revealing oscillations in the Ramsey fringe contrast arising from superexchange interactions. These studies fulfill the promise of Chapter 1, aiming to understand the fundamental interactions between constituent particles in our optical lattice clock. These studies revealed that in both our superexchange and dipole-dipole studies, the experimental observables of interest were very well captured by the spin models presented in Chapter 1. Harnessing these anisotropic spin models opens the door to both novel many-body physics studies and employing spin entanglement to achieve clock stability below the standard quantum limit. In this chapter, we outline some preliminary forays in these research directions.

7.1 Superexchange enhanced metrology

Building upon the results in Chapter 6, it is enticing to next outline a plan to use these superexchange interactions for enhanced metrology. The proposal here is inspired by theory work from Ana Maria Rey's group [89]. To both model and realize spin squeezing, it is often advantageous to have highly collective states where the system can be well-approximated as

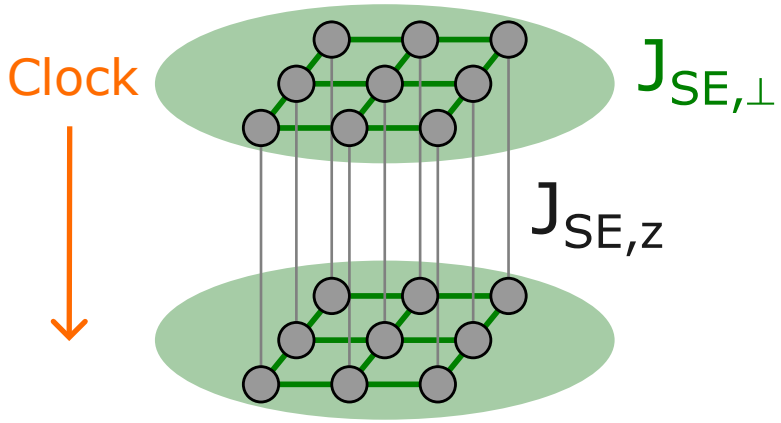

Figure 7.1: Contact interaction-based spin squeezing. Using $V_z \gg V_\perp$, so $J_{SE,z} \ll J_{SE,\perp}$, atoms on each layer of the 3D lattice interact strongly via intralayer Heisenberg interactions $J_{SE,\perp}$ and behave as collective spins. These collective spins, on different layers, interact via $J_{SE,z}$ under the same interaction Hamiltonian in Chapter 6. Figure adapted from [89].

a state oriented on the generalized Bloch sphere. The metrological improvement of this state over a coherent spin state[1] is characterized by the Wineland parameter ξ^2 [241]:

$$\xi^2 = N\frac{\langle \Delta \mathbf{S}_\perp \rangle}{|\mathbf{S}|^2}. \tag{7.1}$$

ξ^2 depends on the spin variance perpendicular to the orientation of the Bloch vector $\langle \Delta S_\perp \rangle$ and the length of Bloch vector $|\mathbf{S}|$ proportional to the Ramsey contrast. The experimental challenge is generally to engineer interactions to induce squeezing and reduce $\langle \Delta S_\perp \rangle$ while minimizing loss of contrast from these operations.

With this philosophy in mind, we present the squeezing scheme depicted in Fig. 7.1. From the results in Chapter 6, we realize an XXZ-style, anisotropic Hamiltonian along the clock direction. As pointed out in [89], this Hamiltonian can be modelled as a one-axis twisting Hamiltonian and is expected to admit spin-squeezing. To address contrast loss, we plan to engineer strong, intralayer Heisenberg interactions so $J_{SE,z} \ll J_{SE,\perp}$. This can

[1] Using the notation from Chapter 6, $|\psi_{CSS}\rangle = e^{-i\frac{\pi}{2}\sum_j \hat{s}_j^Y} \bigotimes_j |\downarrow\rangle_j$

be accomplished by tuning $V_z \gg V_\perp$. This interactions lock the constituent spins in each plane into large collective spins, which then interact between different layers via the XXZ Hamiltonian presented in Chapter 6.

A promising parameter regime for implementing this strategy is around region (1) identified in Fig. 6.11. Although in the 1D limit with $V_\perp = 0$ we obtain the maximal value of the coherence time T_2, the amount of usable entanglement in this regime is limited [59] due to the presence of strong p-wave loss. However, we observe that the transition from pancakes to "waffles" by introducing a weak transverse corrugation of $V_\perp \gtrsim 5E_R$ strongly reduces the atom loss by increasingly localizing the atoms in the transverse directions. Due to the lack of clock-induced SOC within each waffle, the in-plane superexchange leads to isotropic Heisenberg interactions, which feature energy gaps between sectors with different total spin length. These collective spins are expected to be robust to holes and loss, as numerically modelled in [89]. Inhomogeneous superexchange coupling[2] in our optical lattice will likely need to be reduced to minimize the contrast loss detailed in Chapter 6. The predominant contribution to this inhomogeneous coupling is variations of the site-to-site energy ΔE arising from the lattice Gaussian confinement. To address this, box potentials [240] or even significantly increasing the waist of our lattice beams should strongly suppress these energy shifts.

Reducing the lattice external confinement will also pay dividends for potential future studies of SU(N) physics. The repulsive SU(N) Fermi-Hubbard model is expected to exhibit interesting phases at integer filling and low temperature: The SU(2) model has already been studied extensively and exhibits antiferromagnetic ordering [77, 78]. The SU(3) model is expected to show striped ordering [242]. More exotic phases are expected for $N > 3$, where intuiting a simple picture of ordering is more challenging compared to lower dimensions. Consider the density distribution depicted in Fig. 7.2, where we now load all 10 nuclear spins denoted σ into our 3D lattice. Given we are no longer nuclear spin-polarized, doubly

[2] $J_{\mathrm{SE}}(j) \neq J_{\mathrm{SE}}(j+1)$

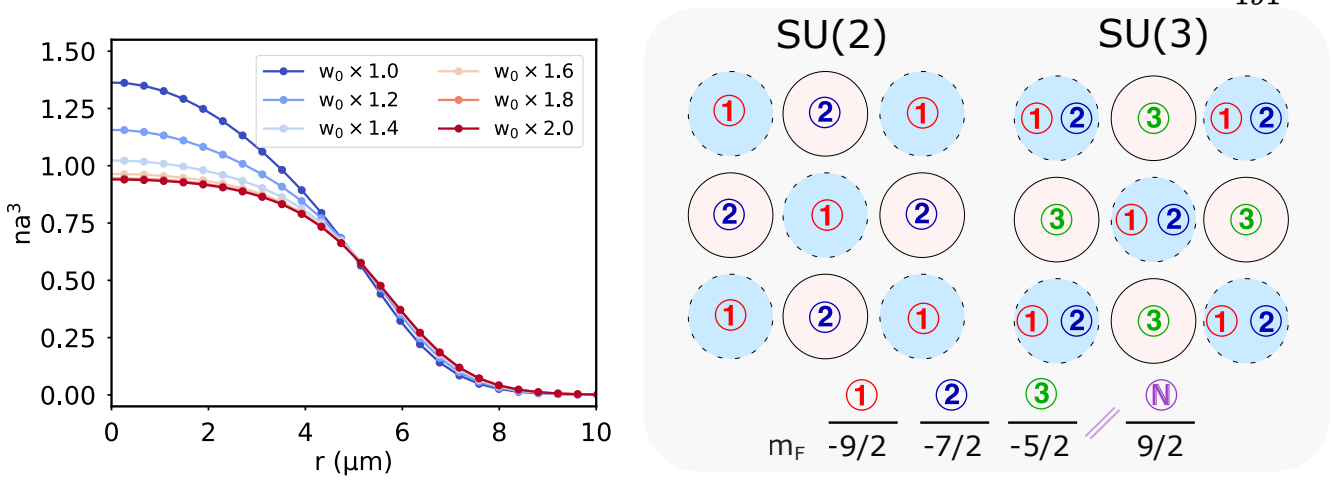

Figure 7.2: **Left**: Lattice filling fraction versus optical lattice beam waists as dictated by the SU(10) repulsive Fermi-Hubbard Hamiltonian. This calculation is in the 'atomic limit', where $U/t \approx 10$ and thus tunneling is neglected in the Hamiltonian in Eq. 7.2. This calculation is using the current experimental beam waists w_0, which are approximately 60 μm in each direction. In this calculation, $T/T_F = 0.20$, and the total atom number N $= 10^4$ atoms. **Right**: At unit filling, the repulsive SU(N) model is expected to exhibit novel ordering. The SU(2) model exhibits antiferromagnetic correlations and the SU(3) model is expected to show striped ordering. Figure reproduced from [242].

occupied sites are not suppressed by the lattice bandgap as prescribed by the band insulating regime. The filling fraction is still determined by the partition function $\mathcal{Z}$, modified from Eq. 5.9 in Chapter 5 to now include a repulsive interaction strength U:

$$\mathcal{Z}(\mu, T) = \sum_{\sigma=0}^{N} \binom{N}{\sigma} e^{-\beta\left(\frac{U}{2}\sigma(\sigma-1)-\mu\sigma\right)}. \tag{7.2}$$

Given strontium does not possess a magnetic Feshbach resonance allowing the capability to independently tune the s-wave scattering length, simultaneously achieving the Mott insulating condition $U/t \approx 10$ and not having an excessively large chemical potential μ is challenging. The parameters U, t are dictated by the optical lattice depth and μ is largely determined by the lattice beam waist. Thus one needs to operate at the lattice depth where $U/t \approx 10$, which corresponds to $\approx 9E_R$, then select a sufficiently large beam waist that μ is sufficiently small to minimize doubly occupied sites. As we see in Fig. 7.2, with lattice

beam waists $\times 2$ larger than our current setup we expect to realize this condition. Currently experiments are ongoing to probe these SU(N) phases [243], including schemes to employ spin-resolved imaging on the $^3P_1$ transition [244] similar to the methods described in Chapter 2.

7.2 Enhanced dipole-dipole interactions

Up to this point in this thesis, all interactions between atoms in the lattice have been mediated by collisions. This strongly constraints the length scale of interactions, given the wavefunctions of particles need to strongly overlap for any appreciable interaction strength. In our superexchange interaction study, we thus only considered on-site, s-wave collisions and neglected next-nearest neighbor contributions which are many orders of magnitude smaller. In this final thesis section, we present a new paradigm in our three-dimensional optical lattice: electric dipole-dipole interactions. These interactions exhibit qualitatively different behavior. Although their interaction strength is $\approx 100\times$ smaller, they possess *long-range* character including terms in the dipolar Hamiltonian that scale as $1/r$ and depend strongly on the lattice geometry. Just like the superexchange interactions, an anisotropic spin model emerges from these dipolar interactions that opens the door for spin-squeezing and novel many-body physics studies. Finally we discuss strategies to magnify these dipolar interactions, with the aim of making their strength is commensurate with the Hz-scale superexchange coupling.

Trapped atoms in optical lattices provide a powerful interface for probing atom-light interactions [245]. These studies build upon Dicke's seminal work revealing that at sufficiently high atomic densities, where the mean atom-atom distance d is considerably smaller than the probe wavelength λ, atoms behave as a 'super-atom' and exhibit superradiance [246]. Using lattices to trap many quantum emitters in periodic arrays, while having the capability to tune this ratio d/λ, is expected to open the door to a host of cooperative phenomena [247]. One exciting direction is the creation of 'subradiant' states, where destructive interference between oscillating atomic dipoles can extend the collective lifetime of the system beyond the

single-particle spontaneous emission rate Γ [67]. Akin to Pauli blocking, one could envision that as clock coherence times approach the natural $^3P_0$ lifetime these subradiant states could see use [248]. Additionally, these atom-light studies can aid our microscopic understanding of optics phenomena like the apparent maximum index of refraction observed in materials [249]. The long-lived clock state in ^{87}Sr offers the capability to probe the many-excitation regime where the population $\langle s_i^Z \rangle$ can be coherently tuned spectroscopically to any projection on the Bloch sphere. We note this is in the stark contrast to Alkali species, where the absence of long-lived electronic states makes coherently preparing states with any appreciable population in the excited state ($\langle s_i^Z \rangle \gg -N/2$) infeasible. In principle all dynamics ranging from subradiance to cooperative frequency shifts can be exactly solved via the quantum master equation, where the temporal evolution of the populations and coherences is encoded in the density matrix $\hat{\rho}$:

$$\frac{d\hat{\rho}}{dt} = -\frac{i}{\hbar}[\hat{H}_0 + \hat{H}_{\mathrm{DD}}, \hat{\rho}] + \mathcal{L}[\hat{\rho}] \tag{7.3}$$

$$= \frac{1}{i}\sum_i \left[\frac{\omega_0}{2} s_i^Z, \hat{\rho}\right] - \frac{i\Gamma}{2}\sum_{i\neq j} g(k|\mathbf{r}_{ij}|)\left[s_i^+ s_j^-, \hat{\rho}\right] - \frac{\Gamma}{2}\sum_{i,j} f(k|\mathbf{r}_{ij}|)\left[\left\{s_i^+ s_j^-, \hat{\rho}\right\} - 2 s_j^- \hat{\rho} s_i^+\right]. \tag{7.4}$$

$$f(\mathbf{v}) = \frac{3}{2}\left[\sin^2\theta \frac{\sin \mathbf{v}}{\mathbf{v}} + (3\cos^2\theta - 1)\left(\frac{\sin \mathbf{v}}{\mathbf{v}^3} - \frac{\cos \mathbf{v}}{\mathbf{v}^2}\right)\right], \tag{7.5}$$

$$g(\mathbf{v}) = -\frac{3}{2}\left[\sin^2\theta \frac{\cos \mathbf{v}}{\mathbf{v}} + (3\cos^2\theta - 1)\left(\frac{\cos \mathbf{v}}{\mathbf{v}^3} + \frac{\sin \mathbf{v}}{\mathbf{v}^2}\right)\right]. \tag{7.6}$$

The elastic and dissipative portions of the dipole-dipole interactions are captured by the formulae $g(\mathbf{v})$ and $f(\mathbf{v})$ respectively. One sees that the Hermitian portion of the Hamiltonian $g(\mathbf{v})[s_i^+ s_j^-, \hat{\rho}]$ corresponds to the exchange of photons between atoms and the non-Hermitian part of the Hamiltonian, denoted $\mathcal{L}[\hat{\rho}]$, corresponds to dissipative effects (i.e. independent and cooperative emission). Here, $\mathbf{r}_{ij} = \mathbf{r}_i - \mathbf{r}_j$ is the vector that connects sites i and j in lattice and θ denotes the angle between the quantization axis and $\mathbf{r}_{ij}$. From a metrology

perspective, deleterious frequency shifts that would compromise our clock accuracy would manifest in the coherences $\langle s_i^+ \rangle$, requiring a solution of Eq. 7.3. The equations of motion for any observable can be calculated by the relation $\frac{dA}{dt} = \mathrm{Tr}[\frac{d\hat{\rho}}{dt}A]$. Following the treatment from Ref. [23], we find:

$$\frac{d\langle s_i^+ \rangle}{dt} = -i\Delta\langle s_i^+ \rangle - \frac{\Gamma}{2}\langle s_i^+ \rangle + \frac{\Gamma}{2}\Big[f(k|\mathbf{r}_{ij}|) - ig(k|\mathbf{r}_{ij}|)\Big]\langle s_i^Z s_j^+ \rangle. \tag{7.7}$$

Here, Δ is the detuning of the clock laser from the atomic resonance. The first two terms in Eq. 7.7 are single-particle terms apparent in all Ramsey spectroscopy. We see that the dipole-dipole frequency shift is proportional to the term $\langle s_i^Z s_j^+ \rangle$ in the density matrix. Solving $\frac{d\langle s_i^Z s_j^+ \rangle}{dt}$ is quite involved, as the Hilbert space for the full density matrix scales as 2^N making exact calculations for the 10^4 particles in our optical lattice intractable. However determining $\frac{d\langle s_i^Z s_j^+ \rangle}{dt}$ can be dramatically simplified by making a perturbative expansion for small ΓT, so the calculation is effectively reduced to summing pairwise interactions corresponding to $N(N-1)$ polynomial complexity[3] [23]. The total frequency shift δ, determined by summing the aggregate shift on each atom i from all other atoms $j \neq i$ is:

$$\frac{\delta}{\Gamma} \approx \frac{1}{N}\sum_i \sum_{i \neq j} U_{ij}\frac{1}{2}\cos 2\Omega T, \tag{7.8}$$

$$U_{ij} = g(k|\mathbf{r}_{ij}|)\cos k\mathbf{x}_{ij} - f(k|\mathbf{r}_{ij}|)\sin k\mathbf{x}_{ij}. \tag{7.9}$$

We emphasize that Eq. 7.8 is only valid in the regime that $\Gamma T \ll 1$. Thus we assume that $\langle s_i^Z \rangle$ is unchanged during our Ramsey dark time. The next higher order correction to Eq. 7.8 is $\propto U_{ij}\Gamma T$ and can be understood as $\langle s_i^Z \rangle$ being modified due to the decay rate Γ from the excited state. For Eq. 7.9 the clock is assumed to be oriented along the x direction, so $\mathbf{x}_{ij}$ is the projection of $\mathbf{r}_{ij}$ in the x direction and $k\mathbf{x}_{ij}$ corresponds to the spin-orbit-coupled phase from Chapter 6.

[3] For each one of the N total atoms, we need to sum the interaction contributions from the $N-1$ other atoms.

There are a few qualitative remarks to make about Eq. 7.8. First, the interaction strength U_{ij} and thus the ensuing frequency shift δ depends on the array geometry. The terms in $g(\mathbf{v})$ and $f(\mathbf{v})$ can strongly interfere either constructively or destructively. Secondly, the net shift δ directly depends on the initial pulse area ΩT and thus excitation angle. For standard Ramsey spectroscopy a $\pi/2$ pulse area with $\Omega T = \pi/4$ is used, corresponding to $\delta = 0$. The largest frequency shifts[4] thus occur at initial pulse areas of $\pi/4$ and $3\pi/4$. Finally, within prefactors U_{ij} resembles the interaction energy between two classical dipoles oscillating out of phase with the exact same trigonometric terms $g(\mathbf{v})$ and $f(\mathbf{v})$ [250].

To gain some intuition about the spatial dependence of U_{ij} and δ, we plot these functions in Fig. 7.3. For this calculation, we vary the orientation of our clock laser k-vector with respect to the lattice spacing along x and y, and we use a 200×200 square of atoms. In the 'forward' direction we observe constructive interference, consistent with the intuition that an emitted photon will propagate co-linearly, in-phase with the clock k-vector. We additionally plot the frequency shift δ, determined by summing over all other atoms $j \neq i$. When the clock laser is oriented near a 'Bragg' condition satisfying $\psi = \arccos \pi/ka \approx 31°$, constructive interference occurs for far-field $1/r$ terms corresponding to the largest frequency shifts.

We quantitatively studied these dipole-dipole frequency shifts on our 3D lattice clock as reported in Refs. [24, 221]. The findings of this study are briefly summarized in Fig. 7.4, and we point the reader to these references for a more detailed description. Experimental parameters that strongly modify the clock frequency δ are the initial excitation angle, the choice of electronic transition, and the clock laser orientation. First, we varied the initial pulse area ΩT for our Ramsey interferometer and observed that our clock frequency shift δ is proportional to $\cos 2\Omega T$ as expected from Eq. 7.8. Characterized by the Clebsch-Gordan (CG) coefficients, the coupling strength varies strongly between different clock states as plotted in Fig. 2.3. We explored this dependence by driving the π and σ^+ transitions, whose

[4] This is also consistent with the value $|\langle s_i^Z s_j^+ \rangle|$ being maximal at $\pi/4$ and $3\pi/4$.

CG coefficients differ by nearly an order of magnitude. Finally, we studied the dependence of frequency shifts on the orientation of our clock laser with respect to the optical lattice. As expected, we observed that clock shifts were dramatically increased at the Bragg angle compared to normal incidence.

These first studies were in the perturbative regime, where the coherent interrogation times T were much shorter than the interaction timescale $1/\Gamma$. Using dressing lasers to mix states with larger dipole moments enables entering the regime $\tilde{\Gamma}T \approx 1$. The modelling of these dynamics in this regime becomes much richer, as effects like excited state decay changing the $\langle s^Z \rangle$ projection can no longer be ignored.

Our dressing scheme is conceptually depicted in Fig. 7.5. As first proposed in [251], a dressing laser at 1354 nm addressing the ${}^3P_0 \rightarrow {}^1P_1$ state is turned on to strongly enhance the dynamics of our ${}^1S_0 \rightarrow {}^3P_0$ clock transition. To gain some insight of the single-particle dynamics, we write down the Schrödinger equation following the derivation in [251].[5] The states for our three-level system are defined above in Fig. 7.5.

$$\begin{aligned} i\dot{c}_2(t) &= \frac{\Omega_d}{2} c_3(t), \\ i\dot{c}_3(t) &= \frac{\Omega_d}{2} c_2(t) - i\frac{\Gamma_3}{2} c_3(t) - \Delta c_3(t). \end{aligned} \tag{7.10}$$

Given $\Gamma \gg \Omega_d$, the excited state $|3\rangle$ can be adiabatically eliminated $\dot{c}_3(t) = 0$. Thus, $c_3(t) = \frac{\Omega_d}{2\Delta + i\Gamma_3} c_2(t)$. We form a dressed state $|\tilde{2}\rangle = |2\rangle + \alpha\,|3\rangle$, where the mixing angle $\alpha = \frac{\Omega_d}{2\Delta + i\Gamma_3}$. Plugging $c_3(t)$ into the top equation in Eq. 7.10, we arrive at $i\dot{c}_2(t) = \frac{\Omega_d^2}{2} \frac{2\Delta - i\Gamma_3}{4\Delta^2 + \Gamma_3^2} c_2(t) = (\tilde{\Delta} - i\tilde{\Gamma}/2) c_2(t)$. We define an effective detuning $\tilde{\Delta}$ and an effective decay rate $\tilde{\Gamma}$ from our dressed state $|\tilde{2}\rangle$.

$$\begin{aligned} \tilde{\Delta} &= \frac{\Delta \Omega_d^2}{4\Delta^2 + \Gamma_3^2}, \\ \tilde{\Gamma} &= \frac{\Gamma_3 \Omega_d^2}{4\Delta^2 + \Gamma_3^2}. \end{aligned} \tag{7.11}$$

[5] Postdoc Ben Lewis wrote helpful notes that I reference for this derivation.

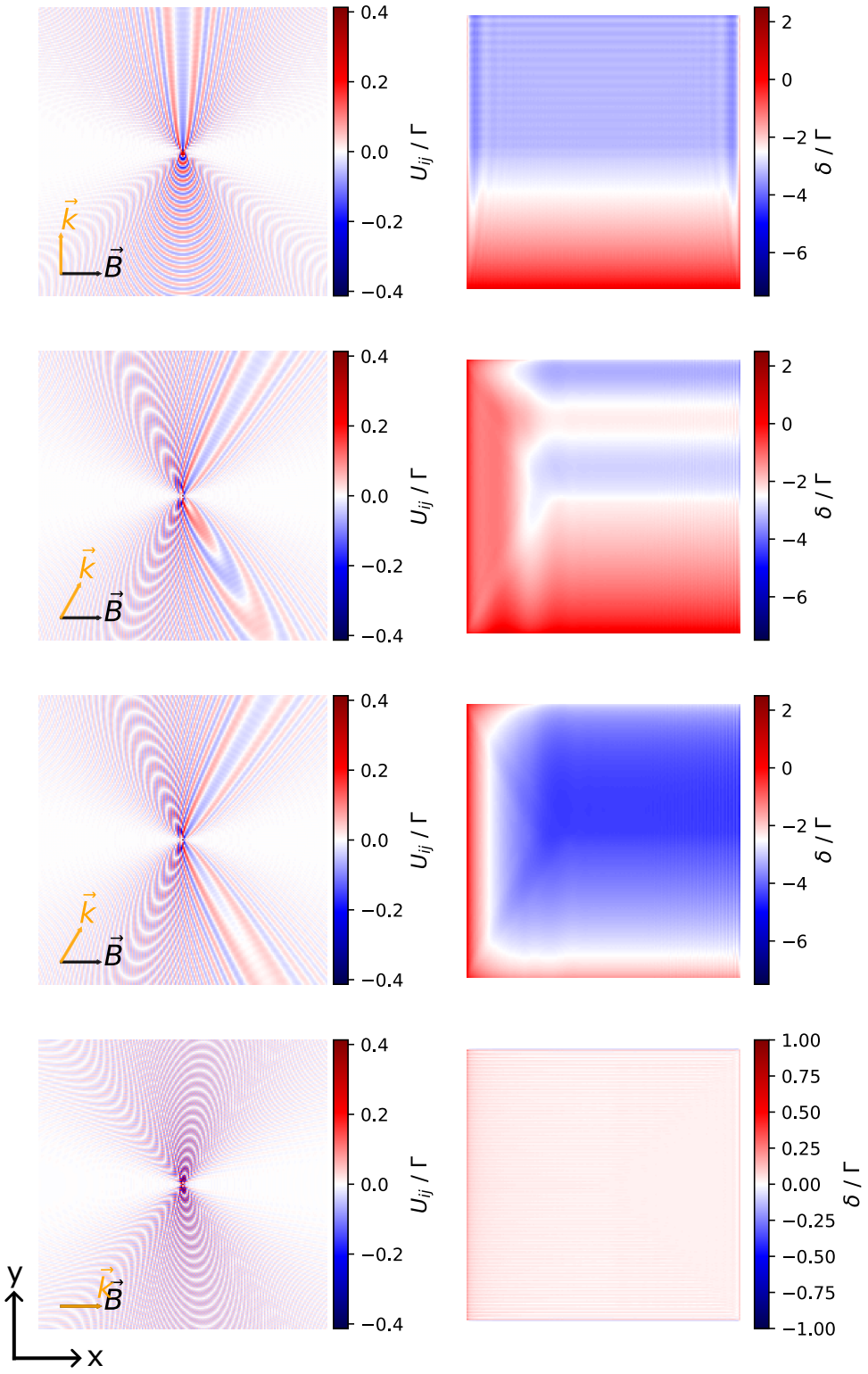

Figure 7.3: Calculated dipole-dipole interactions for a 200×200 square of atoms. The optical lattice is oriented along the x and y directions. $\vec{k}$ indicates the k-vector of the clock laser, while the quantization axis $\vec{B}$ is fixed for all calculations. The Clebsch-Gordan coefficient will depend on the clock m_F states chosen and is set to unity for this calculation. **Left**: We plot the function U_{ij} from Eq. 7.9. **Right**: We plot the frequency shift δ stemming from Eq. 7.8.

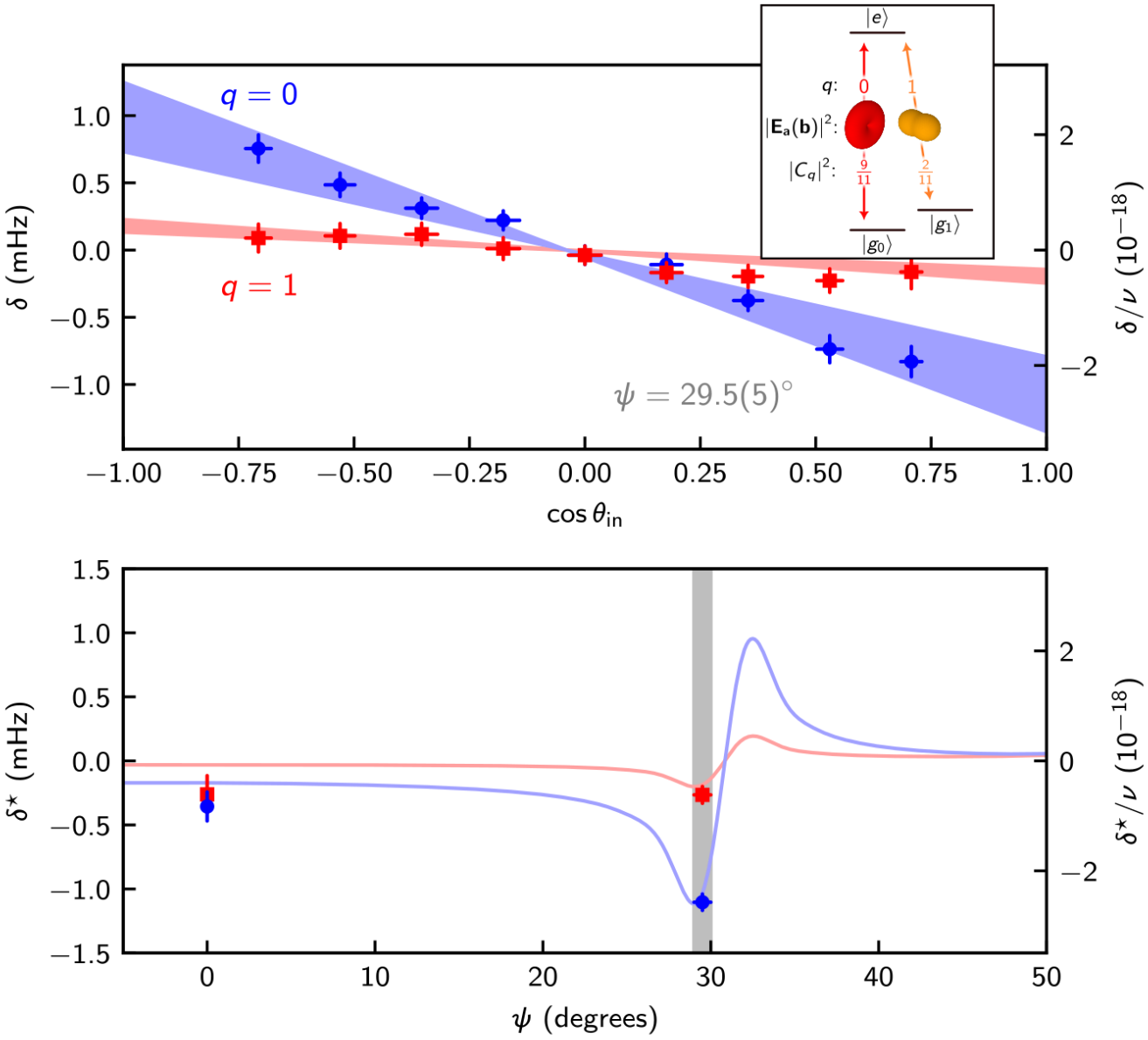

Figure 7.4: Probing dipole-dipole frequency shifts in our optical clock. **Top**: We vary the initial excitation angle in our Ramsey interferometer, modifying δ from Eq. 7.9. We also drive the π and σ^+ transitions with markedly different Clebsch-Gordan coefficients. **Bottom**: We vary the orientation of our clock laser with respect to the optical lattice. As expected, we observe the largest frequency shift near the Bragg resonance as displayed in Fig. 7.8. Figure adapted from [24].

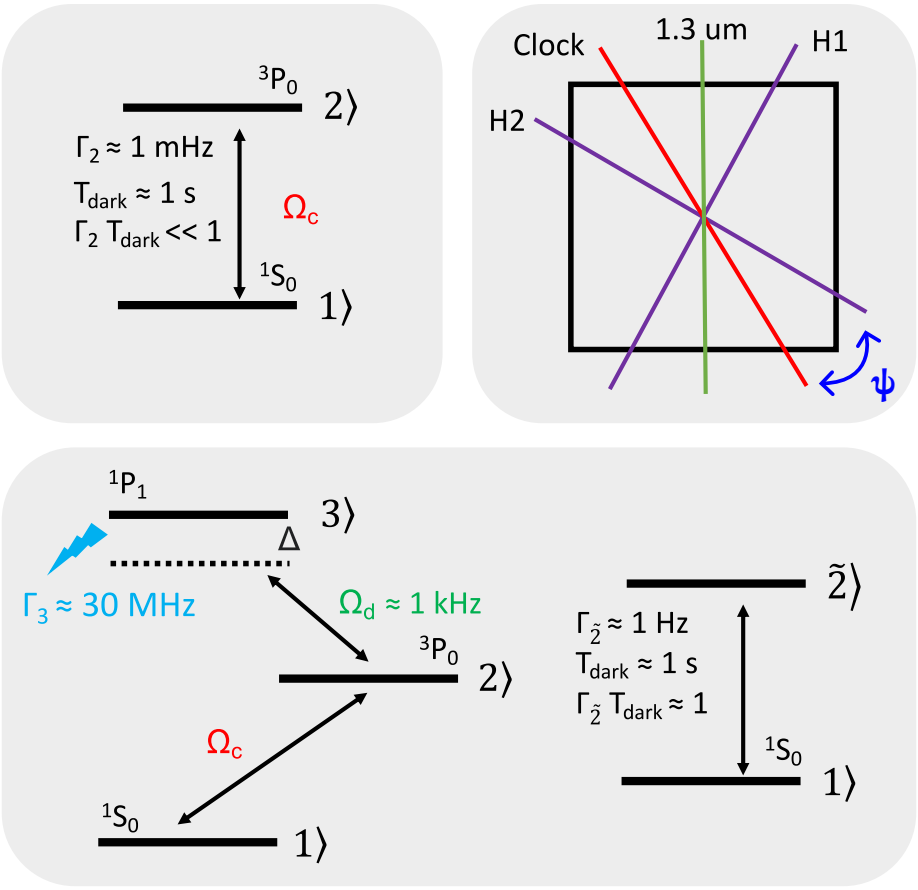

Figure 7.5: **Upper left:** Our $^1S_0 \rightarrow {}^3P_0$ clock transition, used for the dipolar studies in Fig. 7.4. **Upper right:** Laser orientations for lattice, clock laser, and dressing beams. The clock laser is oriented near a 'Bragg' condition satisfying $\psi = \arccos \pi/ka \approx 30.8°$. **Lower:** Electronic states for our three-level dressing scheme. As calculated in Eq. 7.11, a dressed state is formed with an effective decay rate $\tilde{\Gamma}$.

The effective decay rate $\tilde{\Gamma}$ is of particular relevance for the studies here. Using Eq. 7.11 with realistic beam parameters with our dressing laser, we expect a peak AC stark shift $\tilde{\Delta} = 8$ mHz at $\Delta = \Gamma_3/2$ and a peak decay rate of $\tilde{\Gamma} = 0.5$ Hz on resonance ($\Delta = 0$). We note this is $^3P_0 \rightarrow {}^1P_1$ transition is an 'M1' transition, where the relevant dipole matrix element is $\mu \cdot B$ and B is the magnetic component of the dressing laser.

In Fig. 7.6, we share Rabi and Ramsey spectroscopy probing these single-particle effects. To our surprise, our first AC stark measurements revealed an shift of 4.33(7) Hz,

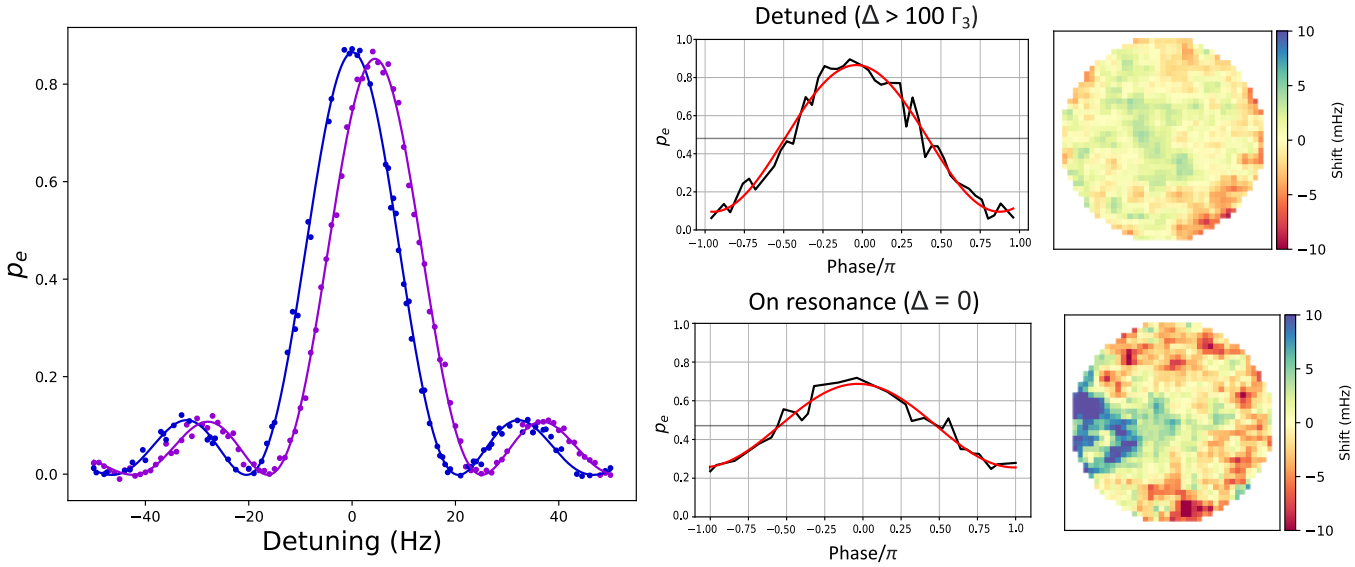

Figure 7.6: **Left:** Rabi spectroscopy on $^1S_0 \rightarrow {}^3P_0$ clock transition with the dressing laser on (off) plotted in purple (blue). A 4.33(7) Hz shift is measured with dressing laser on resonance. **Right:** Ramsey spectroscopy ($T_{dark} = 2$ s) with the dressing laser highly detuned and on resonance. When highly detuned, we see minimal contrast loss. On resonance, we observe contrast loss and the emergence of spatial frequency shifts.

much larger than expected. This larger shift is actually due to off-resonant E1 effects. Similar to Raman scattering of lattice photons at 813 nm as discussed in Ch. 6, lasers hundreds of THz detuned from any resonance can still have non-negligible effects for Hz-level clock spectroscopy. An additional feature is no increase of the clock Rabi frequency Ω_c. A single dressing beam driving $^3P_0 \rightarrow {}^1P_1$ induces a dipole moment oscillating at hundreds of THz that is effectively 'integrated away'. As pointed out in the initial proposal [251], an EIT scheme using two phase-coherent lasers simultaneously driving $^3P_0 \rightarrow {}^1P_1$ and $^1S_0 \rightarrow {}^1P_1$ should coherently induce an enhanced dipole moment for the $^1S_0 \rightarrow {}^3P_0$ clock transition. We additionally explored Ramsey spectroscopy ($T_{dark} = 2$ s) with the dressing laser. When highly detuned from resonance, we see minimal contrast loss. On resonance, we observe contrast loss and the emergence of intriguing spatial frequency shifts.

To try to gain some intuition about the spatial frequency shifts we observed in Fig. 7.6, we employed a spectroscopy scheme similar to our first dipolar study in [24]. We tune three

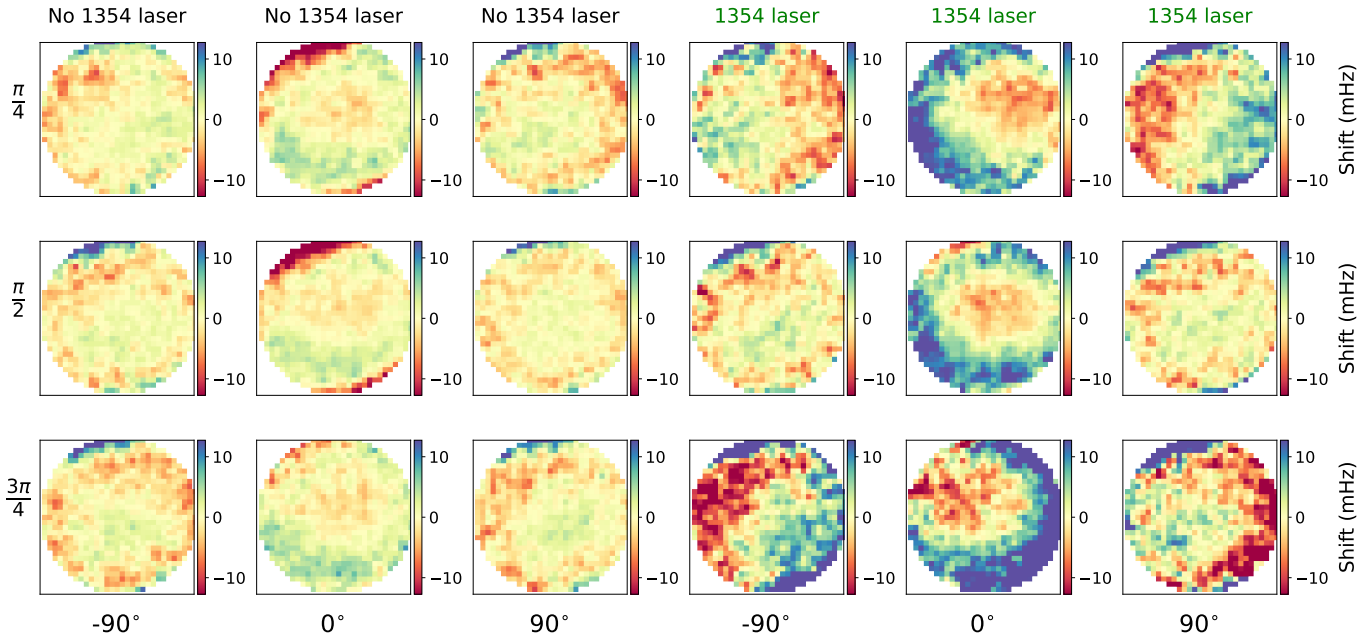

Figure 7.7: Probing enhanced dipole-dipole interactions via Ramsey spectroscopy. We strongly enhance the dipolar coupling via applying a dressing laser at 1354 nm addressing the ${}^3P_0 \rightarrow {}^1P_1$ state In this study we vary three experimental parameters: (1) We perform spectroscopy with our dressing laser at 1354 nm on and off. (2) We change the initial excitation angle angle between $\pi/4$, $\pi/2$, and $3\pi/4$. (3) We vary the readout angle ϕ of our final $\pi/2$ pulse at the output of our Ramsey interferometer.

experimental parameters: (1) Turning our dressing laser at 1354 nm on and off, (2) Varying the initial excitation angle, and (3) Changing the readout angle ϕ at the output of our Ramsey interferometer. The intuition for each of these parameters is the following: (1) governs whether or not we prepare a dressed state. (2) is motivated by the fact we expect the strongest dipole-dipole interactions for a $\pi/4$ and $3\pi/4$ excitation angle. Finally for (3), it is insightful to vary the angle ϕ of the final Ramsey $\pi/2$ pulse as the selected readout quadrature determines whether the atomic coherences and populations of the density matrix $\hat{\rho}$ are measured. Here, $\phi = \pm 90°$ corresponds to the 'side of fringe' and is thus directly proportional to the atomic coherences.

The results of our study are plotted in Fig. 7.7. As aligned with out intution, we indeed see the largest frequency shifts occur at $\pi/4$ and $3\pi/4$, $\phi = \pm 90°$ and when the dressing laser is turned on. This strongly suggests the observation of enhanced dipole-dipole shifts. Work is ongoing to modify Eq. 7.8 to appropriately model the frequency shifts observed in Fig. 7.7. A key piece missing to make this study fully conclusive is an understanding of the spatial dependence of these observed shifts. Given that these dipole-dipole shifts dependent strongly on the system geometry, changing the dressing laser orientation will be an important addition to this study to confirm these results.

In conclusion, we report a set of novel studies on the three-dimensional optical lattice clock at JILA and outline a number of interesting research directions building upon these results to pursue next. Hopefully just like the author, a reader feels the same excitement for the vista of physics opportunities lying ahead on the horizon.

Bibliography

[1] T. M. Graham, Y. Song, J. Scott, C. Poole, L. Phuttitarn, K. Jooya, P. Eichler, X. Jiang, A. Marra, B. Grinkemeyer, M. Kwon, M. Ebert, J. Cherek, M. T. Lichtman, M. Gillette, J. Gilbert, D. Bowman, T. Ballance, C. Campbell, E. D. Dahl, O. Crawford, N. S. Blunt, B. Rogers, T. Noelm, and M. Saffman, *Multi-qubit entanglement and algorithms on a neutral-atom quantum computer*, Nature (London) **604**, 457 (2022).

[2] D. Bluvstein, S. J. Evered, A. A. Geim, S. H. Li, H. Zhou, T. Manovitz, S. Ebadi, M. Cain, M. Kalinowski, D. Hangleiter, J. Pablo Bonilla Ataides, N. Maskara, I. Cong, X. Gao, P. S. Rodriguez, T. Karolyshyn, G. Semeghini, M. J. Gullans, M. Greiner, V. Vuletić, and M. D. Lukin , *Logical quantum processor based on reconfigurable atom arrays*, Nature (London) **626**, 58 (2024).

[3] A. Mazurenko, C. S. Chiu, G. Ji, M. F. Parsons, M. Kanász-Nagy, R. Schmidt, F. Grusdt, E. Demler, D. Greif, and M. Greiner, *A cold-atom Fermi–Hubbard antiferromagnet*, Nature (London) **545**, 462 (2017).

[4] J.-Y. Choi, S. Hild, J. Zeiher, P. Schauss, A. Rubio-Abadal, T. Yefsah, V. Khemani, D. A. Huse, I. Bloch, and C. Gross, *Exploring the many-body localization transition in two dimensions*, Science **352**, 1547 (2016).

[5] T. S. Roussy, L. Caldwell, T. Wright, W. B. Cairncross, Y. Shagam, K. B. Ng, N. Schlossberger, S. Y. Park, A. Wang, J. Ye, E. A. Cornell, *A new bound on the electron's electric dipole moment*, Science **46**, 1547 (2023).

[6] ACME Collaboration, *Improved limit on the electric dipole moment of the electron*, Nature (London) **562**, 355 (2018).

[7] L. Morel, Z. Yao, P. Cladé, and S. Guellati-Khélifa , *Determination of the fine-structure constant with an accuracy of 81 parts per trillion*, Nature (London) **588**, 61 (2020).

[8] A. Browaeys and T. Lahaye, *Many-body physics with individually controlled Rydberg atoms*, Nat. Phys. **16**, 132 (2020.

[9] L. Chomaz, I. Ferrier-Barbut, F. Ferlaino, B. Laburthe-Tolra, B. L. Lev, and T. Pfau, *Dipolar physics: a review of experiments with magnetic quantum gases*, Rep. Prog. Phys. **86**, 026401 (2023).

[10] M. Greiner, O. Mandel, T. Esslinger, T. W. Hänsch, and Immanuel Bloch , *Quantum phase transition from a superfluid to a Mott insulator in a gas of ultracold atoms*, Nature (London) **415**, 39 (2002.

[11] I. Bloch, J. Dalibard, and W. Zwerger, *Many-body physics with ultracold gases*, Rev. Mod. Phys. **80**, 885 (2008).

[12] L. Pezzè, A. Smerzi, M. K. Oberthaler, R. Schmied, and P. Treutlein, *Quantum metrology with nonclassical states of atomic ensembles*, Rev. Mod. Phys. **90**, 035005 (2018).

[13] E. Altman, K. R. Brown, G. Carleo, L. D. Carr, E. Demler, C. Chin, B. DeMarco, S. E. Economou, M. A. Eriksson, K. C. Fu, M. Greiner, K. R. A. Hazzard, R. G. Hulet, A. J. Kollár, B. L. Lev, M. D. Lukin, R. Ma, X. Mi, S. Misra, C. Monroe, K. Murch, Z. Nazario, K.-K. Ni, A. C. Potter, P. Roushan, M. Saffman, M. Schleier-Smith, I. Siddiqi, R. Simmonds, M. Singh, I. B. Spielman, K. Temme, D. S. Weiss, J. Vuckovic, V. Vuletic, J. Ye, and M. Zwierlein, *Quantum Simulators: Architectures and Opportunities*, PRX Quantum **2**, 017003 (2021).

[14] P. Kómár, E. M. Kessler, M. Bishof, L. Jiang, A. S. Sørensen, J. Ye, and M. D. Lukin, *A quantum network of clocks*, Nat. Phys. **10**, 582 (2014).

[15] J. Ye, and P. Zoller, *Essay: Quantum Sensing with Atomic, Molecular, and Optical Platforms for Fundamental Physics*, Phys. Rev. Lett. **132**, 190001 (2024).

[16] C. L. Degen, F. Reinhard, and P. Cappellaro, *Quantum sensing*, Rev. Mod. Phys. **89**, 035002 (2017).

[17] S. Kolkowitz, I. Pikovski, N. Langellier, M. D. Lukin, R. L. Walsworth, J. Ye, *Gravitational wave detection with optical lattice atomic clocks*, Phys. Rev. D **94**, 124043 (2016).

[18] C. Sanner, N. Huntemann, R. Lange, C. Tamm, E. Peik, M. S. Safronova, and S. G. Porsev, *Optical clock comparison for Lorentz symmetry testing*, Nature (London) **567**, 204 (2019).

[19] C. J. Kennedy, E. Oelker, J. M. Robinson, T. Bothwell, D. Kedar, W. R. Milner, G. E. Marti, A. Derevianko, and J. Ye, *Precision Metrology Meets Cosmology: Improved Constraints on Ultralight Dark Matter from Atom-Cavity Frequency Comparisons*, Phys. Rev. Lett. **125**, 201302 (2020).

[20] M. Takamoto, I. Ushijima, N. Ohmae, T. Yahagi, K. Kokado, H. Shinkai, and H. Katori, *Test of general relativity by a pair of transportable optical lattice clocks*, Nat. Photonics **14**, 411 (2020).

[21] T. Bothwell, C. J. Kennedy, A. Aeppli, D. Kedar, J. M. Robinson, E. Oelker, A. Staron, and J. Ye, *Resolving the gravitational redshift across a millimetre-scale atomic sample*, Nature (London) **602**, 420 (2022).

[22] D. F. J. Kimball, D. Budker, T. E. Chupp, A. A. Geraci, S. Kolkowitz, J. T. Singh, and A. O. Sushkov, *Probing fundamental physics with spin-based quantum sensors*, Rev. Mod. Phys. **108**, 010101 (2023).

[23] D. E. Chang, J. Ye, and M. D. Lukin, *Controlling dipole-dipole frequency shifts in a lattice-based optical atomic clock*, Phys. Rev. A **69**, 023810 (2004).

[24] R. B. Hutson, W. R. Milner, L. Yan, J. Ye, C. Sanner, *Observation of millihertz-level cooperative Lamb shifts in an optical atomic clock*, Science **383**, 384 (2024).

[25] N. Dimarcq, M. Gertsvolf, G. Mileti, S. Bize, C. W. Oates, E. Peik, D. Calonico, T. Ido, P. Tavella, F. Meynadier, G. Petit, G. Panfilo, J. Bartholomew, P. Defraigne, E. A. Donley, P. O. Hedekvist, I. Sesia, M. Wouters, P. Dubé, F. Fang, F. Levi, J. Lodewyck, H. S. Margolis, D. Newell, S. Slyusarev, S. Weyers, J.-P. Uzan, M. Yasuda, D.-H. Yu, C. Rieck, H. Schnatz, Y. Hanado, M. Fujieda, P.-E. Pottie, J. Hanssen, A. Malimon, and N. Ashby, *Roadmap towards the redefinition of the second*, Metrologia **61**, 012001 (2024).

[26] A. D. Ludlow, M. M. Boyd, J. Ye, E. Peik, and P. O. Schmidt, *Optical atomic clocks*, Rev. Mod. Phys. **87**, 637 (2015).

[27] D. W Allan, *Statistics of atomic frequency standards*, Proc. IEEE **54**, 221 (1966).

[28] H. Dehmelt, *A Single Atomic Particle Forever Floating at Rest in Free Space: New Value for Electron Radius*, Phys. Scr. **1988**, 102 (1988).

[29] W. M. Itano, J. C. Bergquist, J. J. Bollinger, J. M. Gilligan, D. J. Heinzen, F. L. Moore, M. G. Raizen, and D. J. Wineland, *Quantum projection noise: Population fluctuations in two-level systems*, Phys. Rev. A **47**, 3554 (1993).

[30] N. F Ramsey, *Molecular Beams*, Oxford University Press (1985).

[31] S. M. Brewer, J.-S. Chen, A. M. Hankin, E. R. Clements, C. W. Chou, D. J. Wineland, D. B. Hume, and D. R. Leibrandt, *$^{27}Al^{+}$ quantum-logic clock with a systematic uncertainty below* 10^{-18}, Phys. Rev. Lett. **123**, 033201 (2019).

[32] A. Aeppli, K. Kim, W. Warfield, M. S. Safronova, and J. Ye, *Clock with* 8×10^{-19} *systematic uncertainty*, Phys. Rev. Lett. **133**, 023401 (2024).

[33] S. L. Campbell, R. B. Hutson, G. E. Marti, A. Goban, N. Darkwah Oppong, R. L. McNally, L. Sonderhouse, J. M. Robinson, W. Zhang, B. J. Bloom, and J. Ye, *A Fermi-degenerate three-dimensional optical lattice clock*, Science **358**, 90 (2017).

[34] F. Levi, D. Calonico, C. E Calosso1, A. Godone1, S. Micalizio, and G. A Costanzo, *Accuracy evaluation of ITCsF2: a nitrogen cooled caesium fountain*, Metrologia **51**, 270 (2014).

[35] V. Gerginov, N. Nemitz, S. Weyers, R. Schröder, D. Griebsch, and R. Wynands, *Uncertainty evaluation of the caesium fountain clock PTB-CSF2*, Metrologia **47**, 65 (2009).

[36] B. C. Young, F. C. Cruz, W. M. Itano, and J. C. Bergquist, *Visible Lasers with Subhertz Linewidths*, Phys. Rev. Lett **82**, 3799 (1999).

[37] A. D. Ludlow, X. Huang, M. Notcutt, T. Zanon-Willette, S. M. Foreman, M. M. Boyd, S. Blatt, and J. Ye, *Compact, thermal-noise-limited optical cavity for diode laser stabilization at* 1×10^{-15}, Opt. Lett **32**, 641 (2007).

[38] Y. Y. Jiang, A. D. Ludlow, N. D. Lemke, R. W. Fox, J. A. Sherman, L.-S. Ma, and C. W. Oates, *Making optical atomic clocks more stable with* 10^{-16}*-level laser stabilization*, Nat. Photonics **5**, 158 (2011).

[39] D. G. Matei, T. Legero, S. Häfner, C. Grebing, R. Weyrich, W. Zhang, L. Sonderhouse, J. M. Robinson, J. Ye, F. Riehle, and U. Sterr, 1.5 μm *Lasers with Sub-10 mHz Linewidth*, Phys. Rev. Lett. **118**, 263202 (2017).

[40] E. Oelker, R. B. Hutson, C. J. Kennedy, L. Sonderhouse, T. Bothwell, A. Goban, D. Kedar, C. Sanner, J. M. Robinson, G. E. Marti, D. G. Matei, T. Legero, M. Giunta, R. Holzwarth, F. Riehle, U. Sterr, and J. Ye, *Demonstration of* 4.8×10^{-17} *stability at 1 s for two independent optical clocks*, Nat. Photonics **13**, 714 (2019).

[41] T. Udem, J. Reichert, R. Holzwarth, and T. W. Hänsch, *Accurate measurement of large optical frequency differences with a mode-locked laser*, Opt. Lett **24**, 881 (1999).

[42] S. A. Diddams, D. J. Jones, J. Ye, S. T. Cundiff, J. L. Hall, J. K. Ranka, R. S. Windeler, R. Holzwarth, T. Udem, and T. W. Hänsch, *Direct Link between Microwave and Optical Frequencies with a 300 THz Femtosecond Laser Comb*, Phys. Rev. Lett **84**, 5102 (2000).

[43] J. Stenger, H. Schnatz, C. Tamm, and H. R. Telle, *Ultraprecise Measurement of Optical Frequency Ratios*, Phys. Rev. Lett **88**, 073601 (2002).

[44] S. T. Cundiff, and J. Ye, *Colloquium: Femtosecond optical frequency combs*, Rev. Mod. Phys. **75**, 325 (2003).

[45] J. L. Hall, *Nobel Lecture: Defining and measuring optical frequencies*, Rev. Mod. Phys. **78**, 1279 (2006).

[46] T. W. Hänsch, *Nobel Lecture: Passion for precision*, Rev. Mod. Phys. **78**, 1297 (2006).

[47] C. Zhang, S. B. Schoun, C. M. Heyl, G. Porat, M. B. Gaarde, and J. Ye, *Noncollinear Enhancement Cavity for Record-High Out-Coupling Efficiency of an Extreme-UV Frequency Comb*, Phys. Rev. Lett **125**, 093902 (2020).

[48] A. Cingöz, D. C. Yost, T. K. Allison, A. Ruehl, M. E. Fermann, I. Hartl, and J. Ye, *Direct frequency comb spectroscopy in the extreme ultraviolet*, Nature (London) **482**, 68 (2012).

[49] J. Tiedau, M. V. Okhapkin, K. Zhang, J. Thielking, G. Zitzer, E. Peik, F. Schaden, T. Pronebner, I. Morawetz, L. Toscani De Col, F. Schneider, A. Leitner, M. Pressler, G. A. Kazakov, K. Beeks, T. Sikorsky, and T. Schumm, *Laser Excitation of the Th-229 Nucleus*, Phys. Rev. Lett. **123**, 182501 (2024).

[50] P. G. Thirolf, B. Seiferle, and L. von der Wense,, *The 229-thorium isomer: doorway to the road from the atomic clock to the nuclear clock*, J. Phys. B **52**, 203001 (2019).

[51] S. Kraemer, J. Moens, M. Athanasakis-Kaklamanakis, S. Bara, K. Beeks, P. Chhetri, K. Chrysalidis, A. Claessens, T. E. Cocolios, J. G. M. Correia, H. De Witte, R. Ferrer, S. Geldhof, R. Heinke, N. Hosseini, M. Huyse, U. Köster, Y. Kudryavtsev, M. Laatiaoui, R. Lica, G. Magchiels, V. Manea, C. Merckling, L. M. C. Pereira, S. Raeder, T. Schumm, S. Sels, P. G. Thirolf, S. Malven Tunhuma, P. Van Den Bergh, P. Van Duppen, A. Vantomme, M. Verlinde, R. Villarreal, and U. Wahl, *Observation of the radiative decay of the ^{229}Th nuclear clock isomer*, Nature (London) **617**, 706 (2023).

[52] C. Zhang, T. Ooi, J. S. Higgins, J. F. Doyle, L. von der Wense, K. Beeks, A. Leitner, G. Kazakov, P. Li, P. G. Thirolf, T. Schumm, J. Ye, *Frequency ratio of the ^{229m}Th isomeric transition and the ^{87}Sr atomic clock*, Nature (In Press) (2024).

[53] C. Monroe, D. M. Meekhof, B. E. King, W. M. Itano, and D. J. Wineland, *Demonstration of a Fundamental Quantum Logic Gate*, Phys. Rev. Lett. **75**, 4714 (1995).

[54] A. Sørensen and K. Mølmer, *Quantum Computation with Ions in Thermal Motion*, Phys. Rev. Lett. **82**, 1971 (1999).

[55] D. Kielpinski, C. Monroe, and D. J. Wineland, *Architecture for a large-scale ion-trap quantum computer*, Nature (London) **417**, 709 (2002).

[56] J. Keller, T. Burgermeister, D. Kalincev, A. Didier, A. P. Kulosa, T. Nordmann, J. Kiethe, and T. E. Mehlstäubler, *Controlling systematic frequency uncertainties at the 10^{-19} level in linear Coulomb crystals*, Phys. Rev. A **9**, 1971 (2019).

[57] J. Zhang, G. Pagano, P. W. Hess, A. Kyprianidis, P. Becker, H. Kaplan, A. V. Gorshkov, Z.-X. Gong, and C. Monroe, *Observation of a many-body dynamical phase transition with a 53-qubit quantum simulator*, Nature (London) **551**, 601 (2017.

[58] G. K. Campbell, M. M. Boyd, J. W. Thomsen, M. J. Martin, S. Blatt, M. D. Swallows, T. L. Nicholson, T. Fortier, C. W. Oates, S. A. Diddams, N. D. Lemke, P. Naidon, P. Julienne, J. Ye , and A. D. Ludlow, *Probing Interactions Between Ultracold Fermions*, Science **324**, 360 (2009).

[59] M. J. Martin , M. Bishof, M. D. Swallows, X. Zhang, C. Benko, J. Von-Stecher, A. V. Gorshkov, A. M. Rey , and J. Ye, *A quantum many-body spin system in an optical lattice clock*, Science **341**, 632 (2013).

[60] A. Aeppli, A. Chu, T. Bothwell, C. J. Kennedy, D. Kedar, P. He, A. M. Rey, and J. Ye, *Hamiltonian engineering of spin orbit–coupled fermions in a Wannier-Stark optical lattice clock*, Science Advances **8**, eadc9242 (2022).

[61] J. Ye, H. J. Kimble, and H. Katori, *Quantum State Engineering and Precision Metrology Using State-Insensitive Light Traps* , Science **320**, 1734 (2008).

[62] K. Kim, A. Aeppli, T. Bothwell, and J. Ye, *Evaluation of Lattice Light Shift at Low* 10^{-19} *Uncertainty for a Shallow Lattice Sr Optical Clock*, Phys. Rev. Lett **130**, 113203 (2023).

[63] W. R. Milner, J. M. Robinson, C. J. Kennedy, T. Bothwell, D. Kedar, D. G. Matei, T. Legero, U. Sterr, F. Riehle, H. Leopardi, T. M. Fortier, J. A. Sherman, J. Levine, J. Yao, J. Ye, and E. Oelker, *Demonstration of a Timescale Based on a Stable Optical Carrier*, Phys. Rev. Lett **123**, 173201 (2019).

[64] J. M. Robinson, M. Miklos, Y. M. Tso, C. J. Kennedy, T. Bothwell, D. Kedar, J. K. Thompson, and J. Ye, *Direct comparison of two spin squeezed optical clocks below the quantum projection noise limit*, Nat. Phys. **20**, 208 (2024).

[65] M. Zych, F. Costa, I.Pikovski, and Č. Brukner , *Quantum interferometric visibility as a witness of general relativistic proper time*, Nat. Comm. **2**, 505 (2011).

[66] I.Pikovski, M. Zych, F. Costa, and Č. Brukner , *Universal decoherence due to gravitational time dilation*, Nat. Phys. **11**, 668 (2015).

[67] J. Rui, D. Wei, A. Rubio-Abadal, S. Hollerith, J. Zeiher, D. M. Stamper-Kurn, C. Gross, and I. Bloch , *A subradiant optical mirror formed by a single structured atomic layer*, Nature (London) **583**, 369 (2020),.

[68] M. Mamaev, I. Kimchi, R. M. Nandkishore, and A. M. Rey, *Tunable-spin-model generation with spin-orbit-coupled fermions in optical lattices*, Phys. Rev. Res. **3**, 013178 (2021).

[69] S. Murmann, A. Bergschneider, V. M. Klinkhamer, G. Zürn, T. Lompe, and S. Jochim, *Two fermions in a double well: Exploring a fundamental building block of the Hubbard model*, Phys. Rev. Lett. **114**, 080402 (2015).

[70] S. Kolkowitz, S. L. Bromley, T. Bothwell, M. L. Wall, G. E. Marti, A. P. Koller, X. Zhang, A. M. Rey, and J. Ye , *Spin-orbit-coupled fermions in an optical lattice clock*, Nature (London) **542**, 66 (2017).

[71] A. Goban, R. B. Hutson, G. E. Marti, S. L. Campbell, M. A. Perlin, P. S. Julienne, J. P. D'Incao, A. M. Rey, and J. Ye, *Emergence of multi-body interactions in a fermionic lattice clock*, Nature (London) **563**, 369 (2018).

[72] R. B. Hutson, A. Goban, G. E. Marti, L. Sonderhouse, C. Sanner, and J. Ye, *Engineering quantum states of matter for atomic clocks in shallow optical lattices*, Phys. Rev. Lett. **123**, 123401 (2019).

[73] S. L. Bromley, S. Kolkowitz, T. Bothwell, D. Kedar, A. Safavi-Naini, M. L. Wall, C. Salomon, A. M. Rey, and J. Ye, *Dynamics of interacting fermions under spin-orbit coupling in an optical lattice clock*, Nat. Phys. **14**, 399 (2018).

[74] L.-M. Duan, E. Demler, and M. D. Lukin, *Controlling spin exchange interactions of ultracold atoms in optical lattices*, Phys. Rev. Lett. **91**, 090402 (2003).

[75] M. Lewenstein, A. Sanpera, V. Ahufinger, B. Damski, A. Sen De, and U. Sen, *Ultracold atomic gases in optical lattices: mimicking condensed matter physics and beyond*, Advances in Physics **56**, 243 (2007).

[76] S. Trotzky, P. Cheinet, S. Fölling, M. Feld, U. Schnorrberger, A. M. Rey, A. Polkovnikov, E. A. Demler, M. D. Lukin, and I. Bloch, *Time-resolved observation and control of superexchange interactions with ultracold atoms in optical lattices*, Science **319**, 295 (2008).

[77] E. Manousakis, *The spin-*1/2 *Heisenberg antiferromagnet on a square lattice and its application to the cuprous oxides*, Rev. Mod. Phys. **63**, 1 (1991).

[78] A. Auerbach, *Interacting electrons and quantum magnetism*, Springer Science & Business Media (2012).

[79] P. A. Lee, N. Nagaosa, and X.-G. Wen, *Doping a Mott insulator: Physics of high-temperature superconductivity*, Rev. Mod. Phys. **78**, 17 (2006).

[80] D. Greif, T. Uehlinger, G, Jotzu, L. Tarruell, and T. Esslinger, *Short-range quantum magnetism of ultracold fermions in an optical lattice*, Science **340**, 1307 (2013).

[81] R. A. Hart, P. M. Duarte, T.-L. Yang, X. Liu, T. Paiva, E. Khatami, R. T. Scalettar, N. Trivedi, D. A. Huse, and R. G. Hulet , *Observation of antiferromagnetic correlations in the Hubbard model with ultracold atoms*, Nature (London) **519**, 211 (2015).

[82] M. Boll, T. A. Hilker, G. Salomon, A. Omran, J. Nespolo, L. Pollet, I. Bloch, and C. Gross, *Spin-and density-resolved microscopy of antiferromagnetic correlations in Fermi-Hubbard chains*, Science **353**, 1257 (2016).

[83] L. W. Cheuk, M. A. Nichols, K. R. Lawrence, M. Okan, H. Zhang, E. Khatami, N. Trivedi, T. Paiva, M. Rigol, and M. W. Zwierlein, *Observation of spatial charge and spin correlations in the 2D Fermi-Hubbard model*, Science **352**, 1260 (2016).

[84] M. Takahashi, *Thermodynamics of one-dimensional solvable models*, Cambridge University and Press (2005).

[85] S. Taie, E. Ibarra-García-Padilla, N. Nishizawa, Y. Takasu, Y. Kuno, H.-T. Wei, R. T. Scalettar, K. R. A. Hazzard, and Y. Takahashi, *Observation of antiferromagnetic correlations in an ultracold SU(N) Hubbard model*, Nat. Phys. **18**, 1356 (2022).

[86] M. Gall, N. Wurz, J. Samland, C. Fai Chan, and M. Köhl , *Competing magnetic orders in a bilayer Hubbard model with ultracold atoms*, Nature (London) **589**, 40 (2021).

[87] P. He, M. A. Perlin, S. R. Muleady, R. J. Lewis-Swan, R. B. Hutson, J. Ye, and A. M. Rey, *Engineering spin squeezing in a 3D optical lattice with interacting spin-orbit-coupled fermions*, Phys. Rev. Res. **1**, 033075 (2019).

[88] T. Hernández Yanes, M. Płodzień, M. Mackoit Sinkevičienė, G. Žlabys, G. Juzeliūnas, and E. Witkowska, *One-and two-axis squeezing via laser coupling in an atomic Fermi-Hubbard model*, Phys. Rev. Lett. **129**, 090403 (2022).

[89] M. Mamaev, D. Barberena, and A. M. Rey, *Spin squeezing in mixed-dimensional anisotropic lattice models*, Phys. Rev. A **109**, 023326 (2024).

[90] C. Qu. and A. M. Rey, *Spin squeezing and many-body dipolar dynamics in optical lattice clocks*, Phys. Rev. A **100**, 041602(R) (2019).

[91] M. A. Perlin, C. Qu, and A. M. Rey, *Spin squeezing with short-range spin-exchange interactions*, Phys. Rev. Lett. **125**, 223401 (2019).

[92] M. M. Boyd, *High Precision Spectroscopy of Strontium in an Optical Lattice: Towards a New Standard for Frequency and Time*, Ph.D. Thesis (2007).

[93] A. D. Ludlow, *The Strontium Optical Lattice Clock: Optical Spectroscopy with Sub-Hertz Accuracy*, Ph.D. Thesis (2008).

[94] H. A. Bethe and E. E. Salpeter, *Quantum Mechanics of One and Two Electron Atoms*, (Academic Press, New York, 1957).

[95] D. A. Steck, *Quantum and Atom Optics*, (2017).

[96] P. C. Srivastava, V. Kumar, M. J. Ermamatov, *High-spin structure of ^{87}Sr and ^{87}Zr nuclei: shell model interpretation*, Act. Phys. Pol. B **47**, 2151 (2016).

[97] G. zu Putlitz, *Bestimmung des elektrischen Kernquadrupolmomentes des ungeraden stabilen Strontium-87-Kerns*, Z. Phys. **175**, 542 (1963).

[98] H. Kluge and H. Sauter, *Levelcrossing experiments in the first excited $^1P_1$ states of the alkaline earths*, Z. Phys. **270**, 295 (1974).

[99] M. S. Safronova, M. G. Kozlov, W. R. Johnson, and D. Jiang, *Development of a configuration-interaction plus all-order method for atomic calculations*, Phys. Rev. A **80**, 012516 (2009).

[100] M. M. Boyd, T. Zelevinsky, A. D. Ludlow, S. Blatt, T. Zanon-Willette, S. M. Foreman, and J. Ye, *Nuclear spin effects in optical lattice clocks*, Phys. Rev. A **76**, 022510 (2007).

[101] S. L. Campbell, *A Fermi-degenerate three-dimensional optical lattice clock*, Ph.D. Thesis (2017).

[102] M. Yasuda, T. Kishimoto, M. Takamoto, and H. Katori, *Photoassociation spectroscopy of ^{88}Sr: Reconstruction of the wave function near the last node*, Phys. Rev. A **73**, 011403(R) (2006).

[103] T. L. Nicholson, S. L. Campbell, R. B. Hutson, G. E. Marti, B. J. Bloom, R. L. McNally, W. Zhang, M. D. Barrett, M. S. Safronova, G. F. Strouse, W. L. Tew, and J. Ye , *Systematic evaluation of an atomic clock at 2 × 10^{-18} total uncertainty*, Nat. Comm. **6**, 6896 (2015).

[104] M. J. Holland, B. DeMarco, and D. S. Jin, *Evaporative cooling of a two-component degenerate Fermi gas*, Phys. Rev. A **61**, 053610 (2000).

[105] T. Binnewies, G. Wilpers, U. Sterr, F. Riehle, J. Helmcke, T. E. Mehlstäubler, E. M. Rasel, and W. Ertmer, *Doppler Cooling and Trapping on Forbidden Transitions* , Phys. Rev. Lett. **87**, 123002 (2001).

[106] S. Stellmer, B. Pasquiou, R.Grimm, and F. Schreck, *Laser Cooling to Quantum Degeneracy*, Phys. Rev. Lett. **110**, 263003 (2013).

[107] L. Sonderhouse, C. Sanner, R. B. Hutson, A. Goban, T. Bilitewski, L. Yan, W. R. Milner, A. M. Rey, and J. Ye , *Thermodynamics of a deeply degenerate SU(N)-symmetric Fermi gas*, Nat. Phys. **16**, 1216 (2020).

[108] R. Grimm, M. Weidemüller, and Y. B. Ovchinnikov, *Optical Dipole Traps For Neutral Atoms*, Adv. At. Mol. Opt. Phys. **42**, 95 (2000).

[109] J. Thywissen, *Ultacold Atoms in Optical Lattices*, Lecture Notes (2023).

[110] N. Marzari, A. A. Mostofi, J. R. Yates, I. Souza, and D. Vanderbilt, *Maximally localized Wannier functions: Theory and applications*, Rev. Mod. Phys. **84**, 1419 (2012).

[111] M. J. Martin, *Quantum Metrology and Many-Body Physics: Pushing the Frontier of the Optical Lattice Clock*, Ph.D. Thesis (2013).

[112] F. Le Kien, P. Schneeweiss, and A. Rauschenbeutel, *Dynamical polarizability of atoms in arbitrary light fields: General theory and application to cesium*, Eur. Phys. J. D. **67**, 92 (2013).

[113] P. Julienne, A. Smith, and K. Burnett, *Theory of Collisions between Laser Cooled Atoms*, Adv. At. Mol. Opt. Phys. **30**, 141 (1992).

[114] B. E. A. Saleh and M. C. Teich, *Fundamentals of Photonics*, John Wiley and Sons, (1991).

[115] S. Stellmer, R.Grimm, and F. Schreck, *Production of quantum-degenerate strontium gases*, Phys. Rev. A **87**, 013611 (2013).

[116] M. G. Littman and H. J. Metcalf, *Spectrally narrow pulsed dye laser without beam expander*, App. Opt. **17**, 2224 (1978).

[117] X. Baillard, A. Gauguet, S. Bize, P. Lemonde, Ph. Laurent, A. Clairon, P. Rosenbusch, *Interference-filter-stabilized external-cavity diode lasers*, Opt. Comm. **266**, 609 (2006).

[118] A. Urvoy, Z. Vendeiro, J. Ramette, A. Adiyatullin, and V. Vuletić, *Direct Laser Cooling to Bose-Einstein Condensation in a Dipole Trap*, Phys. Rev. Lett. **122**, 203202 (2019).

[119] J. Hu, A. Urvoy, Z. Vendeiro, V. Crepel, W. Chen , and V. Vuletić, *Creation of a Bose-condensed gas of ^{87}Rb by laser cooling*, Science **358**, 1078 (2017).

[120] L. Sonderhouse, *Quantum gas engineering for atomic clocks*, Ph.D. Thesis (2021).

[121] W. Ketterle, N. J. Van Druten, *Evaporative Cooling of Trapped Atoms*, Adv. At., Mol., Opt. Phys. **37**, 181 (1996).

[122] B. DeMarco and D. S. Jin, *Onset of Fermi Degeneracy in a Trapped Atomic Gas*, Science **285**, 1703 (1999).

[123] A. V. Gorshkov, M. Hermele, V. Gurarie, C. Xu, P. S. Julienne, J. Ye, P. Zoller, E. Demler, M. D. Lukin, and A. M. Rey , *Two-orbital SU(N) magnetism with ultracold alkaline-earth atoms*, Nat. Phys. **6**, 289 (2010).

[124] E. A. Burt, R. W. Ghrist, C. J. Myatt, M. J. Holland, E. A. Cornell, and C. E. Wieman, *Coherence, Correlations, and Collisions: What One Learns about Bose-Einstein Condensates from Their Decay*, Phys. Rev. Lett. **79**, 337 (1997).

[125] S. Giorgini, L. P. Pitaevskii, and S. Stringari, *Theory of ultracold atomic Fermi gases*, Rev. Mod. Phys. **80**, 1215 (2008).

[126] G. M. Bruun and C. W. Clark, *Ideal gases in time-dependent traps* , Phys. Rev. A **61**, 061601(R) (2000).

[127] Y. N. Martinez de Escobar, P. G. Mickelson, P. Pellegrini, S. B. Nagel, A. Traverso, M. Yan, R. Côté, and T. C. Killian, *Two-photon photoassociative spectroscopy of ultracold ^{88}Sr*, Phys. Rev. A **78**, 062708 (2008).

[128] R. W. P Drever, J. L. Hall, F. V. Kowalski, J. Hough, G. M. Ford, A. J. Munley, and H. Ward, *Laser phase and frequency stabilization using an optical resonator*, App. Phys. B **31**, 97 (1983).

[129] A. M. Rey, G. Pupillo, C. W. Clark, and C. J. Williams, *Ultracold atoms confined in an optical lattice plus parabolic potential: A closed-form approach*, Phys. Rev. A **72**, 033616 (2005).

[130] M. Greiner, *Ultracold quantum gases in three-dimensional optical lattice potentials*, Ph.D. Thesis (2003).

[131] S. Blatt, J. W. Thomsen, G. K. Campbell, A. D. Ludlow, M. D. Swallows, M. J. Martin, M. M. Boyd, and J. Ye, *Rabi spectroscopy and excitation inhomogeneity in a one-dimensional optical lattice clock*, Phys. Rev. A **80**, 052703 (2009).

[132] S. Will, *Interacting bosons and fermions in three-dimensional optical lattice potentials*, Ph.D. Thesis (2012).

[133] A. Mazurenko, S. Blatt, F. Huber, M. F. Parsons, C. S. Chiu, G. Ji, D. Greif, and M. Greiner, *Implementation of a stable, high-power optical lattice for quantum gas microscopy*, Rev. Sci. Inst. **90**, 033101 (2019).

[134] L.-S. Ma, P. Jungner, J. Ye, and J. L. Hall, *Delivering the same optical frequency at two places: accurate cancellation of phase noise introduced by an optical fiber or other time-varying path*, Opt. Lett. **19**, 1777 (1994).

[135] A. Einstein, *Zur Elektrodynamik bewegter Körper*, Ann. Phys. (Berlin) **322**, 891 (1905).

[136] A. Bauch, S. Weyers, D. Piester, E. Staliuniene and W. Yang, *Generation of UTC(PTB) as a fountain-clock based time scale*, Metrologia **49**, 180-188 (2012).

[137] G. D. Rovera, S. Bize, B. Chupin, J. Guéna, Ph. Laurent, P. Rosenbusch, P. Uhrich, and M. Abgrall, *UTC*(OP) based on LNE-SYRTE atomic fountain primary frequency standards, Metrologia **53**, S81–S88 (2016).

[138] N. Ashby, *Relativity in the Global Positioning System*, Living Reviews in Relativity **6**, 1 (2003).

[139] B. M. Roberts, G. Blewitt, C. Dailey, M. Murphy, M. Pospelov, A. Rollings, J. A. Sherman, W. Williams, and A. Derevianko, *Search for domain wall dark matter with atomic clocks on board global positioning system satellites*, Nat. Comm. **8**, 1195 (2017).

[140] P. Delva, N. Puchades, E. Schönemann, F. Dilssner, C. Courde, S. Bertone, F. Gonzalez, A. Hees, Ch. Le Poncin-Lafitte, F. Meynadier, R. Prieto-Cerdeira, B. Sohet, J. Ventura-Traveset, and P. Wolf, *Gravitational Redshift Test Using Eccentric Galileo Satellites*, Phys. Rev. Lett. **121**, 231101 (2018).

[141] T. Takano, M. Takamoto, I. Ushijima, N. Ohmae, T. Akatsuka, A. Yamaguchi, Y. Kuroishi, H. Munekane, B. Miyahara, and H. Katori, *Geopotential measurements with synchronously linked optical lattice clocks*, Nat. Photon. **10**, 662 (2016).

[142] M. Lombardi, A. Novick, B. Cooke, and G. Neville-Neil, *Accurate, traceable, and verifiable time synchronization for world financial markets*, Journal of Research of the National Institute of Standards and Technology **121**, 436 (2016).

[143] B. J. Bloom, T. L. Nicholson, J. R. Williams, S. L. Campbell, M. Bishof, X. Zhang, W. Zhang, S. L. Bromley, and J. Ye, *An optical lattice clock with accuracy and stability at the* 10^{-18} *level*, Nature (London) **506**, 662 (2014).

[144] W. F. McGrew, X. Zhang, R. J. Fasano, S. A. Schäffer, K. Beloy, D. Nicolodi, R. C. Brown, N. Hinkley, G. Milani, M. Schioppo, T. H. Yoon, and A. D. Ludlow, *Atomic clock performance enabling geodesy below the centimetre level*, Nature (London) **564**, 87 (2018).

[145] N. Huntemann, C. Sanner, B. Lipphardt, C. Tamm, and E. Peik, *Single-Ion Atomic Clock with* 3×10^{-18} *Systematic Uncertainty*, Phys. Rev. Lett. **116**, 063001 (2016).

[146] H. Hachisu, F. Nakagawa, Y. Hanado, and T. Ido, *Months-long real-time generation of a time scale based on an optical clock*, Sci. Reports **8**, 4243 (2018).

[147] C. Grebing, A. Al-Masoudi, S. Dörscher, S. Häfner, V. Gerginov, S. Weyers, B. Lipphardt, F.Riehle, U. Sterr, and C. Lisdat, *Realization of a timescale with an accurate optical lattice clock*, Optica **6**, 563 (2016).

[148] J. Yao, J. A. Sherman, T. Fortier, H. Leopardi, T. Parker, W. F. McGrew, X. Zhang, D. Nicolodi, R. Fasano, S. Schäffer, K. Beloy, J. Savory, S. Romisch, C. W. Oates, S. A. Diddams, A. D. Ludlow, and J. Levine, *Optical-Clock-Based Time Scale*, Phys. Rev. Applied **12**, 044069 (2019).

[149] M. Schioppo, R. C. Brown, W. F. McGrew, N. Hinkley, R. J. Fasano, K. Beloy, T. H. Yoon, G. Milani, D. Nicolodi, J. A. Sherman, N. B. Phillips, C. W. Oates, and A. D. Ludlow, *Ultrastable optical clock with two cold-atom ensembles*, Nat. Photonics **11**, 48 (2017).

[150] J. Yao, T. E. Parker, N. Ashby, and J. Levine, *Incorporating an Optical Clock into a Time Scale*, IEEE transactions on ultrasonics, ferroelectrics, and frequency control **65**, 127 (2018).

[151] T. Kessler, C. Hagemann, C. Grebing, T. Legero, U. Sterr, F. Riehle, M. J. Martin, L. Chen, and J. Ye , *A sub-40-mHz-linewidth laser based on a silicon single-crystal optical cavity*, Nat. Photon. **6**, 687 (2012).

[152] W. Zhang, J. M. Robinson, L. Sonderhouse, E. Oelker, C. Benko, J. L. Hall, T. Legero, D. G. Matei, F. Riehle, U. Sterr, and J. Ye, *Ultrastable silicon cavity in a continuously operating closed-cycle cryostat at 4 K*, Phys. Rev. Lett. **119**, 243601 (2017).

[153] J. M. Robinson, E. Oelker, W. R. Milner, W. Zhang, T. Legero, D. G. Matei, F. Riehle, U. Sterr, and J. Ye, *Crystalline optical cavity at 4K with thermal-noise-limited instability and ultralow drift*, Optica **6**, 240 (2019).

[154] C. Hagemann, C. Grebing, C. Lisdat, S. Falke, T. Legero, U. Sterr, F. Riehle, M. J. Martin, and J. Ye, *Ultrastable laser with average fractional frequency drift rate below* $5 \times 10^{-19}/s$, Opt. Letters **39**, 5102 (2014).

[155] T. Bothwell, D. Kedar, E. Oelker, J. M. Robinson, S. L. Bromley, W. L. Tew, J. Ye, and C. J. Kennedy, *JILA SrI optical lattice clock with uncertainty of* 2.0×10^{-18} , Metrologia **56**, 065004 (2019).

[156] M. Bishof, X. Zhang, M. J. Martin, and J. Ye , *Optical Spectrum Analyzer with Quantum-Limited Noise Floor*, Phys. Rev. Lett. **111**, 093604 (2013).

[157] J. Levine, *Invited Review Article: The statistical modeling of atomic clocks and the design of time scales*, Rev. Sci. Inst. **83**, 020901 (2012).

[158] J. Yao, T. E. Parker, and J. Levine, *JY1 time scale: a new Kalman-filter time scale designed at NIST*, Meas. Sci. Technol. **28**, 115004 (2017).

[159] I. Sesia, and P. Tavella, *Estimating the Allan variance in the presence of long periods of missing data and outliers*, Metrologia **45**, S134 (2008),.

[160] W. F. McGrew, X. Zhang, H. Leopardi, R. J. Fasano, D. Nicolodi, K. Beloy, J. Yao, J. A. Sherman, S. A. Schäffer, J. Savory, R. C. Brown, S. Römisch, C. W. Oates, T. E. Parker, T. M. Fortier, and A. D. Ludlow, *Towards the optical second: verifying optical clocks at the SI limit*, Optica **6**, 448 (2019).

[161] G. K. Campbell, A. D. Ludlow, S. Blatt, J. W. Thomsen, M. J. Martin, M. H. G. de Miranda, T. Zelevinsky, M. M. Boyd, J. Ye, S. A. Diddams, *The absolute frequency of the ^{87}Sr optical clock transition*, Metrologia **45**, 539 (2008).

[162] H. Leopardi, J. Davila-Rodriguez, F. Quinlan, J. Olson, J. A. Sherman, S. A. Diddams, and T. M. Fortier, *Single-branch Er: fiber frequency comb for precision optical metrology with 10^{-18} fractional instability*, Optica **4**, 879 (2017).

[163] S. M. Foreman, K. W. Holman, D. D. Hudson, D. J. Jones, and J. Ye, *Remote transfer of ultrastable frequency references via fiber networks*, Rev. Sci. Inst. **78**, 021101 (2007).

[164] A. Gelb, *Applied optimal estimation*, The MIT Press (1974).

[165] G. J. Dick, *Local oscillator induced instabilities in trapped ion frequency standards*, Proceedings of 19th Annual Precise Time and Time Interval Meeting, Redondo Beach, U.S. Naval Observatory , 133-147 (1988).

[166] S. Weyers, V. Gerginov, M. Kazda, J. Rahm, B. Lipphardt, G. Dobrev, and K. Gibble, *Advances in the accuracy, stability, and reliability of the PTB primary fountain clocks*, Metrologia **55**, 789 (2018).

[167] S. M. Foreman, A. D. Ludlow, M. H. G. de Miranda, J. E. Stalnaker, S. A. Diddams, and J. Ye, *Coherent Optical Phase Transfer over a 32-km Fiber with 1 s Instability at 10^{-17}*, Phys. Rev. Lett. **99**, 153601 (2007).

[168] T. M. Fortier, A. Bartels, and S. A. Diddams, *Octave-spanning Ti:sapphire laser with a repetition rate >1 GHz for optical frequency measurements and comparisons*, Opt. Letters **31**, 1011 (2019).

[169] BACON collaboration, *Frequency ratio measurements at 18-digit accuracy using an optical clock network*, Nature (London) **591**, 564 (2021),.

[170] N. Nemitz, T. Ohkubo, M. Takamoto, I. Ushijima, M. Das, N. Ohmae, and H. Katori, *Frequency ratio of Yb and Sr clocks with 5×10^{-17} uncertainty at 150 seconds averaging time*, Nat. Photonics **10**, 256 (2016).

[171] J. M. Robinson, *Enhancing optical clocks with ultrastable lasers and spin-squeezing*, Ph.D. Thesis (2023).

[172] D. Kedar, *A Fully Crystalline Cryogenic Reference Cavity*, Ph.D. Thesis (2023).

[173] K. Van Tilburg, N. Leefer, L. Bougas, and D. Budker, *Search for Ultralight Scalar Dark Matter with Atomic Spectroscopy*, Phys. Rev. Lett. **115**, 011802 (2015).

[174] P. Kwee, C. Bogan, K. Danzmann, M. Frede, H. Kim, P. King, J. Pöld, O. Puncken, R. L. Savage, F. Seifert, P. Wessels, L. Winkelmann, and B. Willke, *Stabilized high-power laser system for the gravitational wave detector advanced LIGO*, Opt. Express **20**, 10617 (2012).

[175] E. Oelker, L. Barsotti, S. Dwyer, D. Sigg, and N. Mavalvala, *Squeezed light for advanced gravitational wave detectors and beyond*, Opt. Express **22**, 21106 (2014).

[176] D. J. Ottaway, P. Fritschel, and S. J. Waldman, *Impact of upconverted scattered light on advanced interferometric gravitational wave detectors*, Opt. Express **20**, 8329 (2012).

[177] G. D. Cole, W. Zhang, M. J. Martin, J. Ye, and M. Aspelmeyer, *Tenfold reduction of Brownian noise in high-reflectivity optical coatings*, Nat. Photonics **7**, 644 (2013).

[178] G. E. Marti, R. B. Hutson, A. Goban, S. L. Campbell, N. Poli, and J. Ye, *Imaging optical frequencies with 100 μHz precision and 1.1μm resolution*, Phys. Rev. Lett. **120**, 103201 (2018).

[179] A. Cidrim, A. Piñeiro Orioli, C. Sanner, R. B. Hutson, J. Ye, R. Bachelard, and A. M. Rey, *Dipole-dipole frequency shifts in multilevel atoms*, Phys. Rev. Lett. **127**, 013401 (2021).

[180] S. Krämer, L. Ostermann, and H. Ritsch, *Optimized geometries for future generation optical lattice clocks*, Euro Phys. Lett, **114**, 14003 (2016).

[181] M. Mamaev, R. Blatt, J. Ye, and A. M. Rey, *Cluster state generation with spin-orbit coupled fermionic atoms in optical lattices*, Phys. Rev. Lett. **122**, 160402 (2019).

[182] C. Hofrichter, L. Riegger, F. Scazza, M. Höfer, D. R. Fernandes, I. Bloch, and S. Fölling, *Direct probing of the Mott crossover in the SU(N) Fermi-Hubbard model*, Phys. Rev. X **6**, 021030 (2016).

[183] S. Taie, R. Yamazaki, S. Sugawa, and Y. Takahashi , *An SU(6) Mott insulator of an atomic Fermi gas realized by large-spin Pomeranchuk cooling*, Nat. Phys. **8**, 825 (2012).

[184] S. Stellmer, R. Grimm, and F. Schreck, *Detection and manipulation of nuclear spin states in fermionic strontium*, Phys. Rev. A **84**, 043611 (2011).

[185] U. Schneider, L. Hackermüller, S. Will, Th. Best, I. Bloch , T. A. Costi, R. W. Helmes, D. Rasch, and A. Rosch, *Metallic and insulating phases of repulsively interacting fermions in a 3D optical lattice*, Science **322**, 1520 (2008).

[186] F. Andreoli, M. J. Gullans, A. A. High, A. Browaeys, and D. E. Chang, *Maximum refractive index of an atomic medium*, Phys. Rev. X **11**, 011026 (2021).

[187] W. Ketterle, D. S. Durfee, D. M. Stamper-Kurn, *Making, probing and understanding Bose-Einstein condensates*, arXiv (1999).

[188] S. P. Rath, T. Yefsah, K. J. Günter, M. Cheneau, R. Desbuquois, M. Holzmann, W. Krauth, and J. Dalibard, *Equilibrium state of a trapped two-dimensional Bose gas*, Phys. Rev. A **82**, 013609 (2010).

[189] S. Kadlecek, J. Sebby, R. Newell, and T. G. Walker, *Nondestructive spatial heterodyne imaging of cold atoms*, Opt. Lett. **26**, 137 (2001).

[190] C. C. Bradley, C. A. Sackett, and R. G. Hulet, *Bose-Einstein condensation of lithium: Observation of limited condensate number*, Phys. Rev. Lett. **78**, 985 (1997).

[191] M. R. Andrews, M. O. Mewes, N. J. Van Druten, D. S. Durfee, D. M. Kurn, and W. Ketterle, *Direct, nondestructive observation of a Bose condensate*, Science **273**, 84 (1996).

[192] M. T. DePue, S. L. Winoto, D. J. Han, and D. S. Weiss, *Transient compression of a MOT and high intensity fluorescent imaging of optically thick clouds of atoms*, Opt. Comm. **180**, 73 (2000).

[193] G. Reinaudi, T. Lahaye, Z. Wang, and D. Guéry-Odelin, *Strong saturation absorption imaging of dense clouds of ultracold atoms*, Opt. Lett. **32**, 3143 (2007).

[194] T. Yefsah, R. Desbuquois, L. Chomaz, K. J. Günter, and J. Dalibard, *Exploring the thermodynamics of a two-dimensional Bose gas*, Phys. Rev. Lett. **107**, 130401 (2011).

[195] L. Chomaz, L. Corman, T. Yefsah, R. Desbuquois, and J. Dalibard, *Absorption imaging of a quasi-two-dimensional gas: a multiple scattering analysis*, New. J. Phys. **14**, 055001 (2012).

[196] R. Loudon, *The Quantum Theory of Light*, Oxford Science Publications (2000).

[197] C. Sanner, *Fluctuations in Quantum Degenerate Fermi Gases*, Ph.D. Thesis (2012).

[198] M. H. Anderson, J. R. Ensher, M. R. Matthews, C. E. Wieman, and E. A. Cornell, *Observation of Bose-Einstein Condensation in a Dilute Atomic Vapor*, Science **269**, 198 (1995).

[199] K. B. Davis, M. -O. Mewes, M. R. Andrews, N. J. van Druten, D. S. Durfee, D. M. Kurn, and W. Ketterle, *Bose-Einstein Condensation in a Gas of Sodium Atoms* , Phys. Rev. Lett. **75**, 3969 (1995).

[200] Y.-R. Lee, M.-S. Heo, J.-H. Choi, T. T. Wang, C. A. Christensen, T. M. Rvachov, and W. Ketterle, *Compressibility of an ultracold Fermi gas with repulsive interactions*, Phys. Rev. A **85**, 063615 (2012).

[201] C. Sanner, L. Sonderhouse, R. B. Hutson, L. Yan, W. R. Milner, and J. Ye, *Pauli blocking of atom-light scattering*, Science **374**, 979 (2021).

[202] D. S. Barker, B. J. Reschovsky, N. C. Pisenti, and G. K. Campbell, *Enhanced magnetic trap loading for atomic strontium*, Phys. Rev. A **92**, 043418 (2015).

[203] M. A. Joffe, W. Ketterle, A. Martin, and D. E. Pritchard, *Transverse cooling and deflection of an atomic beam inside a Zeeman slower*, JOSA B. **10**, 2257 (1993).

[204] W. Ketterle, M. Zweirlein, *Making, probing and understanding ultracold Fermi gases*, arXiv (2008).

[205] C. Sanner, E. J. Su, A. Keshet, R. Gommers, Y.-I. Shin, W. Huang, and W. Ketterle, *Suppression of density fluctuations in a quantum degenerate Fermi gas*, Phys. Rev. Lett. **105**, 040402 (2010).

[206] W. G. Tobias, K. Matsuda, G. Valtolina, L. De Marco, J.-R. Li, and J. Ye, *Thermalization and sub-Poissonian density fluctuations in a degenerate molecular Fermi gas*, Phys. Rev. Lett. **124**, 033401 (2020).

[207] T. Müller, B. Zimmermann, J. Meineke, J.-P. Brantut, T. Esslinger, and H. Moritz, *Local Observation of Antibunching in a Trapped Fermi Gas*, Phys. Rev. Lett. **105**, 040401 (2010).

[208] V. Dribinski, A. Ossadtchi, V. A. Mandelshtam, and H. Reisler, *Reconstruction of Abel-transformable images: The Gaussian basis-set expansion Abel transform method*, Rev. Sci. Inst. **73**, 2634 (2002).

[209] C. R. Monroe, E. A. Cornell, C. A. Sackett, C. J. Myatt, and C. E. Wieman, *Measurement of Cs-Cs elastic scattering at T= 30 μK*, Phys. Rev. Lett. **70**, 414 (1993).

[210] G. Valtolina, K. Matsuda, W. G. Tobias, J.-R. Li, L. De Marco, and J. Ye , *Dipolar evaporation of reactive molecules to below the Fermi temperature*, Nature (London) **588**, 239 (2020).

[211] G. E. Marti, *Scalar and Spinor Excitations in a Ferromagnetic Bose-Einstein Condensate*, Ph.D. Thesis (2014).

[212] S. Stellmer, M. K. Tey, B. Huang, R. Grimm, and F. Schreck, *Bose-Einstein Condensation of Strontium*, Phys. Rev. Lett. **103**, 200401 (2009).

[213] T. Fukuhara, S. Sugawa, and Y. Takahashi, *Bose-Einstein condensation of an ytterbium isotope*, Phys. Rev. A **76**, 051604(R) (2007).

[214] D. D. Hickstein, S. T. Gibson, R. Yurchak, D. D. Das, M. Ryazanov, *A direct comparison of high-speed methods for the numerical Abel transform*, Rev. Sci. Insti. **90**, 065115 (2019).

[215] D. G. Matei, T. Legero, Ch. Grebing, S. Häfner, Ch. Lisdat, R. Weyrich, W. Zhang, L. Sonderhouse, J. M. Robinson, F. Riehle, J. Ye, and U. Sterr, *A second generation of low thermal noise cryogenic silicon resonators*, J. Phys.: Conf. Ser. **723**, 012031 (2016).

[216] X. Zhang, M. Bishof, S. L. Bromley, C. V. Kraus, M. S. Safronova, P. Zoller, A. M. Rey, and Ye, J., *Spectroscopic observation of SU(N)-symmetric interactions in Sr orbital magnetism*, Science **345**, 1467 (2014).

[217] J. A. Muniz, D. J. Young, J. R. K. Cline, and J. K. Thompson, *Cavity-QED measurements of the ^{87}Sr millihertz optical clock transition and determination of its natural linewidth*, Phys. Rev. Research **3**, 023152 (2021).

[218] Y. Margalit, Y.-K. Lu, F. Çağrı Top, and W. Ketterle, *Pauli blocking of light scattering in degenerate fermions*, Science **374**, 976 (2021).

[219] A. B. Deb, and N. Kjærgaard, *Observation of Pauli blocking in light scattering from quantum degenerate fermions*, Science **374**, 972 (2021).

[220] Y. Wu, S. Kolkowitz, S. Puri, and J. D. Thompson, *Erasure conversion for fault-tolerant quantum computing in alkaline earth Rydberg atom arrays*, Nat. Comm. **13**, 4657 (2022).

[221] R. B. Hutson, *Probing and Controlling Many-Body Interactions in a Simple Cubic Optical Lattice Clock*, Ph.D. Thesis (2023).

[222] S. Dörscher, R. Schwarz, A. Al-Masoudi, S. Falke, U. Sterr, and C. Lisdat, *Lattice-induced photon scattering in an optical lattice clock* , Phys. Rev. A **97**, 063419 (2018).

[223] S. L. Bromley, *Many-Body Physics in an Optical Lattice Clock*, Ph.D. Thesis (2017).

[224] N. F. Mott, *The Basis of the Electron Theory of Metals, with Special Reference to the Transition Metals*, Proc. Phys. Soc. A, **62**, 416 (1949).

[225] A. W. Young, W. J. Eckner, W. R. Milner, D. Kedar, M. A. Norcia, E. Oelker, N. Schine, J. Ye, and A. M. Kaufman, *Half-minute-scale atomic coherence and high relative stability in a tweezer clock*, Nature (London) **588**, 408 (2020).

[226] R. C. Brown, R. Wyllie, S. B. Koller, E. A. Goldschmidt, M. Foss-Feig, and J. V. Porto, *Two-dimensional superexchange-mediated magnetization dynamics in an optical lattice*, Science **348**, 540 (2015).

[227] P. N. Jepsen, J. Amato-Grill, I. Dimitrova, W. W. Ho, E. Demler, and W. Ketterle, *Spin transport in a tunable Heisenberg model realized with ultracold atoms*, Nature (London) **588**, 403 (2020).

[228] H. Sun, B. Yang, H.-Y. Wang, Z.-Y. Zhou, G.-X. Su, H.-N. Dai, Z.-S. Yuan, and J.-W. Pan, *Realization of a bosonic antiferromagnet*, Nat. Phys. **17**, 990 (2021).

[229] B. Bertini, F. Heidrich-Meisner, C. Karrasch, T. Prosen, R. Steinigeweg, and M. Žnidarič, *Finite-temperature transport in one-dimensional quantum lattice models*, Rev. Mod. Phys. **93**, 025003 (2021).

[230] P. N. Jepsen, Y. K. Lee, H. Lin, I. Dimitrova, Y. Margalit, W. W. Ho, and W. Ketterle, *Long-lived phantom helix states in Heisenberg quantum magnets*, Nat. Phys. **18**, 899 (2022).

[231] E. Pedrozo-Peñafiel, S. Colombo, C. Shu, A. F. Adiyatullin, Z. Li, E. Mendez, B. Braverman, A. Kawasaki, D. Akamatsu, Y. Xiao, and V. Vuletić , *Entanglement on an optical atomic-clock transition*, Nature (London) **588**, 414 (2020).

[232] W. J. Eckner, N. D. Oppong, A. Cao, A. W. Young, W. R. Milner, J. M. Robinson, J. Ye, and A. M. Kaufman , *Realizing spin squeezing with Rydberg interactions in an optical clock*, Nature (London) **621**, 734–739 (2023).

[233] J. Franke, S. R. Muleady, R. Kaubruegger, F. Kranzl, R. Blatt, A. M. Rey, M. K. Joshi, and C. F. Roos , *Quantum-enhanced sensing on optical transitions through finite-range interactions*, Nature **621**, 740 (2023).

[234] W. R. Milner, L. Yan, R. B. Hutson, C. Sanner, and J. Ye, *High-fidelity imaging of a band insulator in a three-dimensional optical lattice clock*, Phys. Rev. A **107**, 063313 (2023).

[235] T. Gullion, D. B. Baker, and M. S. Conradi, *New, compensated Carr-Purcell sequences*, Journal of Magnetic Resonance **89**, 479 (1969).

[236] J.-R. Li, K. Matsuda, C. Miller, A. N. Carroll, W. G. Tobias, J. S. Higgins, and J. Ye, *Tunable itinerant spin dynamics with polar molecules*, Nature (London) **614**, 70 (2023).

[237] M. Foss-Feig, K. R. A. Hazzard, J. J. Bollinger, and A. M. Rey, *Nonequilibrium dynamics of arbitrary-range Ising models with decoherence: An exact analytic solution*, Phys. Rev. A **87**, 042101 (2013).

[238] D.-S. Lühmann, O. Jürgensen, and K. Sengstock, *Multi-orbital and density-induced tunneling of bosons in optical lattices*, New J. Phys. **14**, 033021 (2012).

[239] A. Polkovnikov, *Phase space representation of quantum dynamics*, Annals of Physics **325**, 1790 (2010).

[240] A. L. Gaunt, T. F. Schmidutz, I. Gotlibovych, R. P. Smith, and Z. Hadzibabic, *Bose-Einstein condensation of atoms in a uniform potential*, Phys. Rev. Lett. **110**, 200406 (2013).

[241] D. J. Wineland, J. J. Bollinger, W. M. Itano, F. L. Moore, and D. J. Heinzen, *Spin squeezing and reduced quantum noise in spectroscopy*, Phys. Rev. A **46**, R6797(R) (1992).

[242] C. Honerkamp and W. Hofstetter, *Ultracold Fermions and the SU(N) Hubbard Model*, Phys. Rev. Lett. **92**, 170403 (2004).

[243] G. Pasqualetti, O. Bettermann, N. Darkwah Oppong, E. Ibarra-García-Padilla, S. Dasgupta, R. T. Scalettar, K. R. A. Hazzard, I. Bloch, and S. Fölling, *Equation of State and Thermometry of the 2D SU(N) Fermi-Hubbard Model*, Phys. Rev. Lett. **132**, 083401 (2024).

[244] S. Buob, J. Höschele, V. Makhalov, A. Rubio-Abadal, and L. Tarruell, *A Strontium Quantum-Gas Microscope*, PRX Quantum **5**, 020316 (2024).

[245] D. E. Chang, J. S. Douglas, A. González-Tudela, C.-L. Hung, and H. J. Kimble, *Colloquium: Quantum matter built from nanoscopic lattices of atoms and photons*, Rev. Mod. Phys. **90**, 031002 (2018).

[246] R. H. Dicke, *Coherence in Spontaneous Radiation Processes*, Phys. Rev. **93**, 99 (1954).

[247] A. Asenjo-Garcia, M. Moreno-Cardoner, A. Albrecht, H. J. Kimble, and D. E. Chang, *Exponential Improvement in Photon Storage Fidelities Using Subradiance and "Selective Radiance" in Atomic Arrays*, Phys. Rev. X **7**, 031024 (2017).

[248] L. Henriet, J. S. Douglas, D. E. Chang, and A. Albrecht, *Critical open-system dynamics in a one-dimensional optical-lattice clock*, Phys. Rev. A **99**, 011026 (2019).

[249] F. Andreoli, M. J. Gullans, A. A. High, A. Browaeys, and D. E. Chang, *Maximum Refractive Index of an Atomic Medium*, Phys. Rev. X **11**, 011026 (2021).

[250] J. D. Jackson, *Classical Electrodynamics*, John Wiley, (1999).

[251] R. Santra, E. Arimondo, T. Ido, C. H. Greene, and J. Ye, *High-accuracy optical clock via three-level coherence in neutral bosonic* ^{88}Sr, Phys. Rev. Lett. **94**, 173002 (2005).

[252] The National Institute of Standards and Technology (NIST) database.

[253] T. Ido, T. H. Loftus, M. M. Boyd, A. D. Ludlow, K. W. Holman, and J. Ye, *Precision Spectroscopy and Density-Dependent Frequency Shifts in Ultracold Sr*, Phys. Rev. Lett. 94, 153001 (2005).

[254] BIPM recommended values of standard frequencies.

[255] CRC Handbook of Chemistry and Physics 95th Edition.

[256] D. Kedar, J. Yu, E. Oelker, A. Staron, W. R. Milner, J. M. Robinson, T. Legero, F. Riehle, U. Sterr, and J. Ye, *Frequency stability of cryogenic silicon cavities with semiconductor crystalline coatings*, Optica **10**, 464 (2023).

[257] D. A. Butts, and D. S. Rokhsar, *Trapped Fermi gases*, Phys. Rev. A **55**, 4346 (1997).

[258] R. Jaffe, *Degenerate Fermion Systems*, Lecture Notes (2006).

[259] A. Sommerfeld, *Zur Elektronentheorie der Metalle auf Grund der Fermischen Statistik*, Zeitschrift für Physik **47**, 1 (1928).

Appendix A

^{87}Sr atomic data

This table summarizes the key atomic data for the fermionic strontium isotope ^{87}Sr. Although this information is widely accessible, compiling these values in a single location is designed to be convenient for a curious experimentalist.

Natural abundance	7.00(1)% [252]
Mass	86.9088775(12) amu [252]
Nuclear spin	9/2 [252]
$^1P_1$ Lifetime	5.263(4) ns [102]
$^3D_1$ Lifetime	2.18(1) μs [103]
$^3P_1$ Lifetime	21.28(3) μs [103]
$^3P_0$ Lifetime	118(3) s [217]
$^1P_1$ I_{sat}	40.3 mW/cm^2 [102]
$^3D_1$ I_{sat}	0.32 μW/cm^2 [103]
$^3P_1$ I_{sat}	3.0 μW/cm^2 [103]
$^3P_0$ I_{sat}	0.53 pW/cm^2 [217]
$^1P_1$ Doppler temperature	725 μK [102]
$^1P_1$ Recoil temperature	1.02 μK
$^3P_1$ Doppler temperature	180 nK [103]
$^3P_1$ Recoil temperature	460 nK
$^3P_1$ absolute frequency	434829121312334(38) Hz [253]
$^3P_0$ absolute frequency	429228004229872.99(8) Hz [254]
Scattering length a_{gg}	96.2(1) a_0 [127]
Scattering length a_{eg-}	69.1(9) a_0 [71]
Scattering length a_{eg+}	160.0(2.4) a_0 [71]
Melting point	777 C° [255]
Boiling point	1377 C° [255]
Vapor pressure at 25 C°	1.30×10^{-7} Torr [255]
Vapor pressure at 480 C°	2.84 Torr [255]

Appendix B

List of experiments

Throughout the text of this thesis we refer to the various clock platforms and cavity systems (e.g. Sr2, Si4, etc.). While I try to define this terminology when it first appears, I believe a reference table is useful.

Sr1	One-dimensional optical lattice clock focused towards clock accuracy. The older generation of the experiment was used for the optical timescale [63], dark-matter studies [19], and a 2×10^{-18} accuracy evaluation [155]. Around 2020 Sr1 was upgraded to include an in-vacuum buildup cavity, enabling larger lattice mode volume for far improved coherence times [21, 60].
Sr2	The three-dimensional optical lattice clock platform studied in this thesis. Details of experiment construction are outlined in [101].
Sr3	1D optical lattice clock with cavity QED setup built around 2021. Currently exploring using spin-squeezing to achieve clock stability below the standard quantum limit [64]. Details of experiment construction are outlined in [171].
MJM	40 cm ultra-low-expansion (ULE) cavity endearingly named after Michael J. Martin, the graduate student who commissioned the system. This cavity was the workhorse clock laser system from 2012 until Si3 was installed in 2017. Details of this cavity setup are provided in [111].
Si3	Cryogenic 21 cm silicon cavity operating at 124 K with amorphous SiO_2/Ta_2O_5 dielectric coatings [39]. Installed in 2017, and to this day has the record cavity stability of 4×10^{-17}. Cavity system used for the optical timescale work [63].
Si4	Cryogenic 6 cm silicon cavity with amorphous SiO_2/Ta_2O_5 dielectric coatings. Required novel 4 K cryostat design detailed in [152]. Work to achieve thermal-noise limited stability detailed in [171].
Si6	Same Si4 cryogenic system and silicon cavity spacer design, but using upgraded $Al_{1-x}Ga_xAs/GaAs$ crystalline coatings with lower loss-angle [177]. Details of upgraded cavity system and novel birefringent noise studies in [256, 172].
Si7	Newest silicon cavity with primary aim to achieve better stability than Si3 by using same 21 cm spacer length but operating at 17 K. Using amorphous SiO_2/Ta_2O_5 dielectric coatings to circumvent the birefringent noise discovered on Si6 [256].

Appendix C

Fermi gas overview

One of the central features of our clock experiment is preparing an evaporatively cooled Fermi gas. The purpose if this appendix is to provide a primer of Fermi gas basics. We have a fairly simple, non-interacting Hamiltonian:

$$H = \frac{1}{2m}(p_x^2 + p_y^2 + p_z^2) + \frac{1}{2}m(\omega_x^2 x^2 + \omega_y^2 y^2 + \omega_z^2 z^2) \tag{C.1}$$

The energy levels of this quantum harmonic oscillator are well-know: $\epsilon(n_x, n_y, n_z) = \hbar(\omega_x n_x + \omega_y n_y + \omega_z n_z)$. This trapping potential gives rise to the following density-of-states [257]:

$$g_{3D}(\epsilon) = \frac{\epsilon^2}{2\hbar^3 \omega_x \omega_y \omega_z} \tag{C.2}$$

The occupation of these energy levels is prescribed by the Fermi-Dirac distribution:

$$F(\epsilon, \zeta) = \frac{1}{\frac{1}{\zeta}e^{\beta\epsilon} + 1} \tag{C.3}$$

We express the Fermi-Dirac function in terms of the fugacity $\zeta = e^{\beta\mu}$. Our next task is to turn these microscopic formulae into a thermodynamic treatment where the system can be characterized by state variables (e.g. entropy, pressure) [258]. We define the partition function for ν states:

$$Z = \sum_v e^{-E_\nu \beta} \tag{C.4}$$

Similarly, we define the Grand partition function as:

$$\mathcal{Z} = \sum_N e^{\mu N \beta} Z \tag{C.5}$$

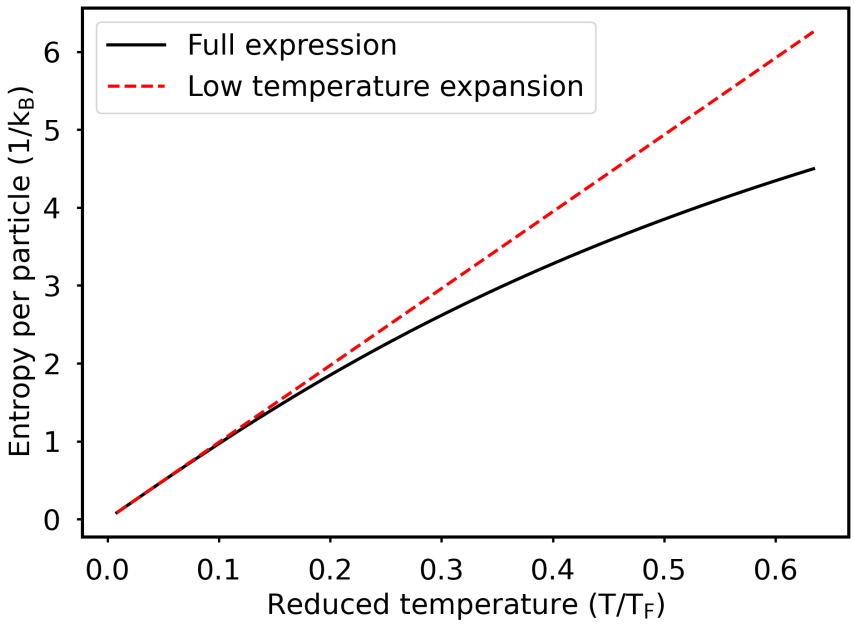

Figure C.1: Entropy per particle in the ODT as a function of reduced temperature. ω_x,ω_y, ω_z, and N are assumed from the table below.

One can interpret $e^{(\mu N - E_\nu)\beta}$ as the probability to find the system with particle number N and energy E_ν. For a fixed T and E_ν, configurations with larger N can be put together in more ways and are thus have higher entropy. Finally, we define a Grand potential:

$$\Omega = -k_B T \ln(\mathcal{Z}) \tag{C.6}$$

These expressions are generalized thermodynamic functions with no underlying assumptions about spin statistics. The next step is to specify these functions for a Fermi gas. If we consider a system of Fermions with energies $E_1, E_2 ... E_j$ with occupations $n_1, n_2 ... n_j$. For j states each with n_j occupation:

$$\mathcal{Z} = \prod_j \sum_{n_j} e^{n_j(\mu - E_j)\beta} \tag{C.7}$$

Considering for Fermions $n_j = 0$ or 1:

$$\mathcal{Z} = \prod_j 1 + e^{(\mu - E_j)\beta} \tag{C.8}$$

Plugging $\mathcal{Z}$ into Ω:

$$\Omega = k_B T \sum_j \ln(1 + e^{(\mu - E_j)\beta}) = k_B T \sum_j \ln(1 - F(E_j, \zeta)) \tag{C.9}$$

To express the Grand potential in a continuous functional form instead of a sum, we write the occupation of a state j in terms the density of states $g(\epsilon)$. Then, this sum can be written as an integral between 0 and ∞.

$$\Omega = k_B T \int_0^\infty g(\epsilon) \ln(1 - F(\epsilon, \zeta)) d\epsilon \tag{C.10}$$

Using Eq. C.2 for $g_{3D}(\epsilon)$ and integrating by parts, we can express Ω in terms of ϵ and $F(\epsilon, \zeta)$, to write Ω in terms of polylogarithms.

$$\Omega = -\frac{1}{6\hbar^3 \omega_x \omega_y \omega_z} \int_0^\infty \epsilon^3 F(\epsilon, \zeta) d\epsilon \tag{C.11}$$

To solve this integral in Eq. C.11, we used the following relation:

$$\int_0^\infty \epsilon^n F(\epsilon,\zeta)d\epsilon = \frac{\Gamma(n+1)Li_{n+1}(-\zeta)}{\beta^{n+1}} \tag{C.12}$$

Here Li_n refers to a polylogarithmic function of order n and $\Gamma = (n-1)!$ as all n are positive integers.

$$\Omega = -\frac{1}{6\hbar^3\omega_x\omega_y\omega_z}\int_0^\infty \epsilon^3 F(\epsilon,\zeta)d\epsilon = \frac{(k_bT)^4}{\hbar^3\omega_x\omega_y\omega_z}Li_4(-\zeta) \tag{C.13}$$

With Ω, most relevant thermodynamic quantities can be determined (ie. $S = \frac{\partial\Omega}{\partial T}$), enjoying some of the derivative properties of polylogarithms:

$$z\frac{\partial \mathrm{Li}_s(z)}{\partial z} = Li_{s-1}(z) \tag{C.14}$$

$$\frac{\partial \mathrm{Li}_s(e^\mu)}{\partial \mu} = Li_{s-1}(e^\mu) \tag{C.15}$$

The entropy S can then be expressed in terms of Ω:

$$S = -\frac{\partial\Omega}{\partial T} = \frac{(k_BT)^3}{\hbar^3\omega_x\omega_y\omega_z}\Big(\mu Li_3(-\zeta) - 4k_bTLi_4(-\zeta)\Big) \tag{C.16}$$

In the low temperature limit ($k_BT << E_F$) one may employ the Sommerfeld expansion [259] so $S \approx k_BN\pi^2T/T_F$. This low temperature expansion, along with the full expression are plotted in Fig. C.1. Additionally, one can express the total atom number N.

$$N = -\frac{\partial\Omega}{\partial\mu} = -\frac{(k_BT)^3}{\hbar^3\omega_x\omega_y\omega_z}\Big(Li_3(-\zeta)\Big) \tag{C.17}$$

Substituting the definition for T_F, one can relate the fugacity ζ to the reduced temperature T/T_F.

$$Li_3(-\zeta) = \frac{-1}{6(T/T_F)^3} \tag{C.18}$$

Eq. C.18 shows an important property: the reduced temperature T/T_F can be related to a single parameter, the fugacity ζ. ζ can be related to the shape of the trapped Fermi gas after ballistic expansion from time-of-flight. Time-of-flight absorption imaging provides

a reliable probe to determine the atom number and reduced temperature, while parametric heating measurements calibrate the trapping frequencies. Rough experimental parameters on Sr2 are shared below.

Typical experimental parameters	
ω_r	100 Hz
ω_z	200 Hz
N	10^4
T	24 nK
T_F	240 nK
ζ	$15,000$